

Global investigation of large earthquakes using long-period seismic data

A thesis submitted to the School of Environmental Sciences of the
University of East Anglia in partial fulfilment of the requirements for the
degree of Doctor of Philosophy

By Konstantinos P. Lentas

October 2013

© This copy of the thesis has been supplied on condition that anyone who consults it is understood to recognise that its copyright rests with the author and that no quotation from the thesis, nor any information derived therefrom, may be published without the author's prior, written consent.

© Copyright 2013

by

Konstantinos P. Lentas

Abstract

Robust earthquake source models provide key information for a wide range of applications in Earth Sciences, such as in global tectonics, natural hazards and tomographic studies. In this thesis, we study large magnitude earthquakes using the Earth's normal modes, which are standing waves resulting from the interference of surface waves travelling in opposite directions. We start by carrying out earthquake source validation tests for a recent source inversion technique (SCARDEC), which shows a tendency for steeper fault dip angles than those reported in the widely used Global CMT catalogue (GCMT), for large magnitude ($M_w \geq 7.5$) shallow thrust earthquakes. We show that SCARDEC source parameters explain normal mode data as well as GCMT, and that SCARDEC dip angles explain body wave data similarly or slightly better than GCMT solutions. SCARDEC dip angles also agree well with results from previous individual earthquake studies and with geophysical subduction zone constraints, suggesting that SCARDEC is a robust technique for rapid source parameter determinations. A new Monte Carlo earthquake source inversion method based on ultra low-frequency normal mode data ($f < 1$ mHz) is then developed, providing an independent way to estimate bulk rupture source parameters (rupture length and duration, magnitude, fault strike, dip and rake) of large magnitude earthquakes. Realistic synthetic tests show the importance of accurately modelling lateral heterogeneity, notably for rake angle, rupture length and duration determinations. Moreover, application of the new technique to five real shallow subduction earthquakes ($M_w \geq 8.5$) of the past decade and a recent normal faulting, deep earthquake using a 3-D Earth mantle model, show clearly the complementary role of the new approach to classical earthquake source techniques, and the advantages of using normal mode data to study very long-duration, slow-slip earthquake sources, such as the 2004 M_w 9.3 Sumatra-Andaman earthquake.

Acknowledgements

First of all, I offer my sincerest gratitude to my supervisor Dr. Ana Ferreira for offering me the great opportunity to carry out this thesis. Without her guidance, encouragement and support this thesis would not have been possible. I also want to thank my secondary supervisor Dr. Paul Burton for useful comments and discussion.

I gratefully acknowledge generous funding from QUEST project which allowed me to focus on my research work and gave me the opportunity to attend several conferences and present my work. However, QUEST was not only about money, but more importantly, it was its people. Through this training network I had the chance to meet some of the head leaders in seismology, and build friendship with other PhD students.

Many thanks to Dr. Martin Vallée for providing me with detailed updated SCARDEC results and for useful discussion. My sincere thanks also goes to Dr. Eric Clévédé for providing me the HOPT source code and Prof. Malcolm Sambridge for providing me the Neighbourhood Algorithm source code.

A big thank you also to our UEA seismology group: Jennie, Sung-Joon, Laura, Ana and Hannah for useful comments and discussion. Last, but not least, I would like to thank my family for encouraging and supporting me all these years.

The research presented in this thesis was carried out on the High Performance Computing Cluster supported by the Research Computing Service at the University of East Anglia.

Contents

Abstract	v
Acknowledgements	vii
1 Introduction	1
1.1 Global earthquakes	2
1.2 Seismological observation of earthquakes: which data?	4
1.3 Determination of earthquake source parameters	8
1.3.1 Early studies	8
1.3.2 Existing global earthquake catalogues	9
1.4 Some current challenges	12
1.5 Motivation and Thesis outline	14
2 Forward modelling of normal mode, body and surface waves: Theoretical background	17
2.1 Summary	17
2.2 Normal modes of the Earth	18
2.3 Normal mode summation for a SNREI model	25
2.4 Normal modes of a rotating, anelastic, elliptical laterally heterogeneous Earth	26
2.5 Higher Order Perturbation Theory (HOPT)	27
2.5.1 The HOPT package	29
2.5.2 Normal mode splitting and coupling	30
2.5.3 The effect of 3-D Earth structure	35
2.6 Spectral element method	37

3 Testing earthquake source models using forward modelling	43
3.1 Summary	43
3.2 Introduction	44
3.3 Subduction earthquakes studied	48
3.4 Normal mode data tests	52
3.5 Body-wave 3-D forward modelling tests	57
3.6 Comparisons with other studies and with geophysical constraints	61
3.7 Frequency dependency of the comparisons	63
3.8 Discussion	65
3.9 Conclusions	72
4 A normal mode earthquake source inversion technique for the determination of spatio-temporal characteristics of large earthquakes	73
4.1 Summary	73
4.2 Introduction	74
4.3 Methodology	76
4.3.1 Theoretical background	76
4.3.2 Forward modelling	78
4.3.3 Source inversion algorithm	78
4.4 Validity of the initial phase modelling	83
4.5 Synthetic tests	86
4.5.1 Selected earthquakes	87
4.5.2 Synthetic data	89
4.5.3 Normal mode multiplet point source inversions	90
4.5.4 Normal mode singlet finite source inversions	100
4.5.5 Misfit function choice	106
4.6 Discussion	107
4.7 Conclusions	113
5 Earthquake source models obtained from ultra low-frequency normal mode data	115
5.1 Summary	115

5.2	Introduction	116
5.3	Method and data	121
5.3.1	Normal mode singlet separation	122
5.4	Analysis of large magnitude earthquakes	123
5.4.1	The 2004 M_w 9.3, 2005 M_w 8.6 and 2007 M_w 8.5 Sumatra earthquakes	125
5.4.2	The 2011 M_w 9.1 Tohoku and 2013 M_w 8.3 Okhotsk Sea earthquakes	137
5.4.3	The 27 February 2010 M_w 8.8 Maule, Chile earthquake	146
5.5	Discussion	149
5.6	Conclusions	156
6	Discussion and conclusions	159
6.1	Earthquake source validation	159
6.2	Spatio-temporal resolution of low frequency normal mode data	161
6.3	Importance of 3-D structure	163
6.4	Source parameter uncertainties	165
6.5	Conclusions	166
6.6	Future work	168
A	Supplementary material for Chapter 3	171
B	Supplementary material for Chapter 4 - Point source inversion synthetic tests	179
C	Supplementary material for Chapter 4 - Finite source inversion synthetic tests	199
D	Supplementary material for Chapter 5	213

List of tables

3.1	List and index codes of the large magnitude ($M_w \geq 7.5$) shallow subduction earthquakes of the past 20 years used in this Chapter. Their GCMT and SCARDEC fault geometries are shown by their beach balls. Earthquakes where GCMT dip angles lay outside of SCARDEC dip angle intervals are shown in bold (earthquakes in red in Figures 3.1–3.3).	49
3.2	Mean misfit values (amplitude misfits and real and imaginary FFT misfits, see equations 3.1–3.2) obtained over all the earthquakes studied in section 3.4 from normal mode comparisons between GCMT and SCARDEC synthetics and real data, for both vertical and transverse components.	57
3.3	Mean waveform misfit values obtained over all the earthquakes studied in section 4 from body wave comparisons between real data and 3-D SEM synthetics using either SCARDEC or GCMT ($m_{SCARDEC(\delta_{GCMT})}^2$) dip angles for both vertical and transverse components (see main text for details).	61
4.1	Results of rupture duration (T_r) and length (L) obtained from linear inversion synthetic tests, with respect to earthquake's latitude and orientation. A simple finite source which is considered as a superposition of three subevents, ruptures unilaterally a line fault of 240 km in 100 s. Rupture duration is always well determined, no matter the latitude of the earthquake or the orientation of the source.	87

4.2 Differences between input models and results of source inversions for strike ϕ , dip δ , rake λ , moment magnitude M_w , obtained from point source inversions using a misfit function involving a combination of the amplitude spectra and FFT observables (97% amplitude – 3% FFT). The top part of the Table shows the effect of the finite source when using point source kernels built with the same Earth model (SAW12D) as the input synthetic data. The bottom part of the Table shows results for the four different artificial earthquakes tested, in three different cases. SAW12D-WN: Synthetic data and excitation kernels are built using SAW12D Earth's model, but white noise is added to the synthetic data, PREM: synthetic data are built using SAW12D Earth's model while excitation kernels are built using PREM model, PREM-WN: synthetic data are built using SAW12D Earth's model while excitation kernels are built using PREM model and white noise is added to the synthetic data. Input models and beachballs are shown on top, and optimal model beachballs and misfits are shown at the bottom.	94
4.3 Same as in Table 4.2, but now for finite source inversions, for the determination of six source parameters (strike ϕ , dip δ , rake λ , moment magnitude M_w , rupture duration T_r , length L).	102
4.4 Differences in optimal source parameters obtained from finite source inversions compared with the input model of Tsai <i>et al.</i> (2005) for the artificial 2004 Sumatra earthquake, with respect to errors in origin time and location that have been introduced to the excitation kernels. Results for an experiment using PREM excitation kernels and adding white noise to the input synthetic data are also shown (PREM-WN). Misfit values and beachballs of the obtained source models are shown at the bottom.	107

5.1	Comparison of the GCMT, W-phase and Tsai <i>et al.</i> (2005) source models for the 2004 Sumatra-Andaman earthquake with point source models obtained from our multiplet point source inversions using: (i) the GCMT location and GCMT depth of $h=28.6\text{km}$ (4^{th} row); (ii) the GCMT location and PDE depth of $h = 10 \text{ km}$ (5^{th} row); and, (iii) the centroid location determined by Tsai <i>et al.</i> (2005) (6^{th} row). Reported uncertainties correspond to solutions with a data misfit not exceeding the minimum misfit value by more than 1%	130
5.2	Initial phase (X_m) estimates for the singlets included in the finite source inversion carried out for the 26 December 2004 Sumatra-Andaman earthquake. Initial phases correspond to the optimal source model determined from the inversion ($\phi = 340.9^\circ$, $T_r = 521.0 \text{ s}$, $L = 1276.8 \text{ km}$) with respect to the PDE location. Singlets' periods (T_m) are also shown for reference.	131
5.3	Comparison of point ($\phi, \delta, \lambda, M_w$) and finite ($\phi, \delta, \lambda, M_w, T_r, L$) source models determined in this study with GCMT, W-phase, SCARDEC and other studies for the 2004 Sumatra-Andaman earthquake. Uncertainties shown correspond to models with misfit values within a 1% tolerance with respect to the optimal misfit.	134
5.4	Comparison of point ($\phi, \delta, \lambda, M_w$) source model determined in this study with GCMT, W-phase, SCARDEC and other studies for the 2005 Nias earthquake. Uncertainties shown correspond to models with misfit values within a 1% tolerance with respect to the optimal misfit.	136
5.5	Comparison of point ($\phi, \delta, \lambda, M_w$) source model determined in this study with GCMT, W-phase, SCARDEC and other studies for the 2007 Bengkulu earthquake. Uncertainties shown correspond to models with misfit values within a 1% tolerance with respect to the optimal misfit.	136
5.6	Initial phase (X_m) estimates for the singlets included in the finite source inversion carried out for the 11 March 2011 Tohoku earthquake. Initial phases correspond to the optimal source model determined from the inversion ($\phi = 197.3^\circ$, $T_r = 151.0 \text{ s}$, $L = 461.0 \text{ km}$) with respect to the PDE location. Singlets' periods (T_m) are also shown for reference.	140

5.7 Comparison of point $(\phi, \delta, \lambda, M_w)$ and finite $(\phi, \delta, \lambda, M_w, T_r, L)$ source models determined in this study with GCMT, W-phase, SCARDEC and other studies for the 2011 Tohoku earthquake. Uncertainties shown correspond to models with misfit values within a 1% tolerance with respect to the optimal misfit.	144
5.8 Comparison of point $(\phi, \delta, \lambda, M_w)$ source model determined in this study with GCMT, W-phase and SCARDEC for the 2013 Okhotsk Sea earthquake. Uncertainties shown correspond to models with misfit values within a 1% tolerance with respect to the optimal misfit.	147
5.9 Comparison of point $(\phi, \delta, \lambda, M_w)$ source model determined in this study with GCMT, W-phase, SCARDEC and other studies for the 2010 Chile earthquake. Uncertainties shown correspond to models with misfit values within a 1% tolerance with respect to the optimal misfit.	149
A.1 SCARDEC source parameters of the subduction earthquakes studied (strike - ϕ , dip - δ , rake - λ , moment magnitude - M_w , depth - Z) and their uncertainties for dip angle ($\Delta\delta$), depth (ΔZ) and moment magnitude (ΔM_w). The index numbers correspond to the earthquakes' GCMT codes (see chapter 3).	172
A.2 Numerical results of the misfit analysis for the GCMT and SCARDEC techniques. Amplitude misfits $m_{Ampl.}^2$, real and imaginary FFT part misfits $m_{Re/Im}^2$ and the number of stations used at each component are shown. . .	173
A.3 GCMT and SCARDEC source models compared with WCMT and other source models found in the literature for the 22 earthquakes with substantial dip angle differences studied in Chapter 3.	174

B.1	Input source parameters (inp.) and parameter space boundaries (min. and max.) over strike (ϕ), dip (δ), rake (λ), moment magnitude (M_w), rupture duration (T_r) and length (L) for the four different earthquakes tested (thrust, strike-slip, normal) in finite source synthetic tests. The parameter space ranges 40° in strike and rake, 30° in dip, 0.6 in moment magnitude, 100 s in rupture duration and 240 km in length. The same parameter space is used in our point source inversion tests for strike, dip, rake and M_w determinations. Input model beachballs are shown on top.	180
D.1	Parameter space boundaries (min. and max.) over strike (ϕ), dip (δ), rake (λ), moment magnitude (M_w), rupture duration (T_r) and length (L) of the six earthquakes studied in this Chapter. The parameter space ranges 40° in strike and rake, 30° in dip, 0.6 in moment magnitude, 100 s in rupture duration and 240 km in length. The same parameter space is used in our point source inversion tests for strike, dip, rake and M_w determinations. . .	214

List of figures

1.1	Global seismicity ($M_w \geq 6.0$) according to the Global Centroid Moment Tensor (GCMT) catalogue for the past 20 years. Red circles show GCMT epicentres and green lines show plate boundaries.	2
1.2	A global map showing the distribution of the current seismic stations included in the GSN network. Figure downloaded from IRIS (http://www.iris.edu/hq/programs/gsn).	5
1.3	An example of three-component seismograms (LHZ: vertical, LHL: longitudinal, LHT: transverse) from the GSN showing ground displacement after the 11 April 2012 M_w 8.6 Sumatra strike-slip earthquake recorded at BFO station at an epicentral distance of 85° and azimuth of 318° . Body waves (P, SV, SH) as well as Rayleigh (R) and Love (L) surface wave arrivals are shown in the seismograms.	6
1.4	Observed vertical component spectra of 240 hours of free oscillations in the 0–1 mHz frequency band recorded at CAN (Canberra, Australia) station for the 26 December 2004 M_w 9.3 Sumatra-Andaman earthquake. Spheroidal and toroidal surface patterns are also shown for some of the gravest free oscillations in the spectra. Figure taken by Park <i>et al.</i> (2005).	8
2.1	Minor and major-arc surface waves that circle the Earth and a three-component seismogram, filtered between 350 s and 150 s, with the seismic wave arrivals for the $M_w = 8.0$ Peru 2007 earthquake. The source is represented as an explosion and the station Flin Flon, Canada (FFC) as a house. R_N and G_N refer to Rayleigh and Love surface waves, respectively. $N=1$ corresponds to minor-arc path, $N=2$ corresponds to major-arc path and $N=3$ involves one great-circle path followed by a minor-arc.	18

2.2	A cartoon illustrating the different types of normal modes. Radial modes (top) ${}_0S_0$ (or so-called the breathing mode) and ${}_1S_0$ involve only radial displacement. Spheroidal modes (middle) ${}_0S_2$ (or so-called the football mode) and ${}_0S_3$ involve both radial and horizontal displacement. Toroidal modes (bottom) ${}_0T_2$ and ${}_0T_3$ involve only horizontal displacement.	22
2.3	The Preliminary Reference Earth Model (PREM) of Dziewonski and Anderson (1981). Density (ρ), compressional (V_P) and shear (V_S) wave velocity variations with depth are indicated in red, black and green, respectively. Transition zone (400–670 km), core-mantle (CMB) and inner-core boundaries (ICB) are highlighted.	23
2.4	Dispersion diagrams for spheroidal (left) and toroidal (right) modes. The degenerate eigenfrequencies for the PREM model are plotted as small circles for angular order up to $l=120$. The fundamental mode, 1^{st} , 2^{nd} and 3^{rd} overtone branches are indicated by the green labels on the right. The corresponding seismic travelling waves are indicated in black (see main text for more details).	24
2.5	PREM degenerate eigenfrequency differences for fundamental spheroidal and toroidal modes. ${}_0f_l^S - {}_0f_{l+1}^T$ differences are plotted using blue circles, in the range $l = 7 - 28$ and ${}_0f_l^S - {}_0f_{l-1}^T$ differences are plotted using green circles, in the range $l = 3 - 6$ and $l = 25 - 36$. The strongest coupling is observed for the quasi-degenerate pairs ${}_0S_{11} - {}_0T_{12}$, ${}_0S_{19} - {}_0T_{20}$ and ${}_0T_{31} - {}_0S_{32}$. The main coupling factor is the Coriolis force, due to the Earth's rotation.	34

2.6	Vertical component acceleration data amplitude and phase spectra (black) for the multiplet ${}_1S_3 - {}_3S_1 - {}_2S_2$ compared to GCMT synthetic amplitude and phase spectra calculated using a self-coupling scheme (red) and a full-coupling scheme (green) for the 2011 Tohoku earthquake. Earth's rotation, ellipticity and 3-D structure (SAW12D) are taken into account in the theoretical spectra calculations. The time window of the time series used is 12–90 hr after the earthquake's occurrence time. Station azimuths, epicentral distances and station names are shown in the left hand side of each diagram.	35
2.7	Vertical component acceleration data amplitude spectra and phase in radians (black) for the multiplet ${}_0S_7 - {}_2S_3$ compared to GCMT synthetic amplitude spectra and phase calculated using a self-coupling scheme (red) and a full-coupling scheme (green) for the 2011 Tohoku earthquake. Earth's rotation, ellipticity and 3-D structure (SAW12D) are taken into account in the theoretical spectra calculations. The time window of the time series used is 5–45 hr after the earthquake's occurrence time. Station azimuths, epicentral distances and station names are shown in the left hand side of each diagram.	36
2.8	3-D SH mantle model SAW12D for four different depth slices (95 km, 755 km, 1500 km, 2500 km). The blue colour indicates areas where the shear wave velocity is higher than the average, while the red colour indicates areas where the shear wave velocity is lower, expressed as a percentage of perturbation from PREM.	37
2.9	Observed vertical component acceleration data amplitude and phase spectra (black) compared to GCMT synthetic amplitude spectra and phase calculated taking into account Earth's rotation and ellipticity using PREM (red) and 3-D SAW12D mantle model (green), for the 2011 Tohoku earthquake for various seismic stations from the Global Seismic Network. A full-coupling scheme is used from 0.2 mHz up to 1.3 mHz. The time window of the time series used is 144h. Station names, epicentral distances and station azimuths are shown in the left hand side.	38

2.10 A visual example of the Earth represented by the cubed sphere, divided in six chunks. In the implementation of SPECFEM3D-GLOBE used in this study, each chunk is subdivided into 5^2 slices of elements, resulting in 150 slices (which corresponds to the number of processors used in the calculations), as shown by different colours. The figure is taken from Komatitsch and Tromp (2002a)	40
3.1 Global map showing the locations and GCMT source mechanisms of the major subduction earthquakes considered in this Chapter. Earthquakes where GCMT dip angles lay outside of SCARDEC dip angle intervals are plotted in red. All the remaining earthquakes are plotted in grey. A detailed list of the earthquakes can be found in Table 3.1 and in Table A.1 of the Appendix A.	48
3.2 Scatter plots of GCMT source parameters versus SCARDEC (strike, dip, rake angles, depth, moment magnitude). Error bars correspond to SCARDEC uncertainties. Red circles correspond to the earthquakes studied, for which GCMT dip angles lay outside of SCARDEC dip angle intervals. Square symbols in the diagram with depth comparisons correspond to earthquakes where the GCMT depth is fixed. All the remaining earthquakes are plotted in grey. A detailed list of the earthquakes can be found in Table 3.1. Mean value (μ) and standard deviation (σ) of the differences between GCMT and SCARDEC parameters are plotted in the top left corner of each diagram.	51
3.3 Scatter plots of GCMT moment tensor components versus SCARDEC. Red circles correspond to the earthquakes studied for which the GCMT and SCARDEC dip angles lay outside of SCARDEC dip angle intervals. All the remaining earthquakes are plotted in grey. Black circle contours indicate negative moment tensor components (all SCARDEC and GCMT moment tensor components compared here have the same signs). Mean value (μ) and standard deviation (σ) of the differences between GCMT and SCARDEC are plotted in the top left corner of each diagram.	53

3.6 Illustrative examples of body wave displacement comparisons for the M_w 8.4 Peru 2001 (GCMT code: 062301E) earthquake in vertical (top, P-waves) and transverse (bottom, SH-waves) components. Data are shown in black, SCARDEC synthetics in green and SCARDEC synthetics with the GCMT dip angle, in magenta. SCARDEC waveform misfits for vertical and transverse components over the total number of stations used (16 for the vertical and 15 for the transverse component) are: $m_Z^2 = 0.22$ and $m_T^2 = 0.16$ for SCARDEC dip angle, and $m_Z^2 = 0.30$ and $m_T^2 = 0.23$ for GCMT dip angle, respectively. Focal mechanisms of the two different source models are shown as beach balls on the right hand side. 59

3.7 Waveform misfits between body wave data and SCARDEC synthetics (green diamonds), and between data and SCARDEC synthetics with the GCMT dip (magenta stars) for all the earthquakes studied. The use of GCMT dip angles yields mean misfit values about 5% larger than SCARDEC for vertical and transverse component data. Earthquakes are plotted in ascending M_w order and their names are written in different colours according to the data used in the GCMT inversions (blue for body and mantle waves, orange for body, mantle and surface waves, purple for mantle waves). 60

3.8 Dip angle comparisons between GCMT (red diamonds) and SCARDEC (green diamonds, including uncertainties) for earthquakes where GCMT dip angles lay outside of the SCARDEC dip angle intervals. Dip angles obtained from individual earthquake studies published in the literature (blue squares), W-phase inversions (cyan stars) and the Slab1.0 subduction zone model (Hayes *et al.*, 2012, orange circles) are also shown, where available. Slab1.0 dip angles correspond to the GCMT locations (latitude and longitude). Slab1.0 depths may differ compared to GCMT depths, with Peru 2007 earthquake having the largest difference (20.8 km). The mean absolute difference is 6.6 km and the median is 5.0 km. Earthquakes are plotted in ascending M_w order and their names are written in different colour according to the data used by GCMT (blue for body and mantle waves, orange for body, mantle and surface waves, purple for mantle waves). 62

3.9 Body-wave (left) and surface-wave (right) comparisons for the $M_w=8.3$ Hokkaido 2003 earthquake for the vertical component of ANTO station. Data (black) and: (i) SCARDEC synthetics convolved with a triangular source time function (red) and (ii) SCARDEC synthetics convolved with the station's relative source time function obtained from SCARDEC (green). The SCARDEC source duration is 72 s. The dominant periods of the waveforms plotted from the top to the bottom are 30 s, 50 s, 70 s, 90 s and 150 s, respectively.	64
3.10 Comparison between SCARDEC average source time functions (green) with rupture durations estimated from individual earthquake studies (blue vertical lines; see main text). For reference, we also show triangular/boxcar source time functions with rupture duration estimated from a constant stress drop scaling relation, as used by the GCMT catalogue (red), for the 34 subduction earthquakes considered in this Chapter. GCMT source time functions are represented as boxcar functions for earthquakes that occurred before 2004. After the 1 st of January 2004 the GCMT source time function is assumed to be triangular (Ekström <i>et al.</i> , 2012). Zero time corresponds to the PDE time of each earthquake. Earthquake names, GCMT magnitudes and codes are shown on top of each plot. Three cases of classical tsunami earthquakes are identified (M_w 7.5 N. Peru 1996 – 022196B, M_w 7.7 Java 2006 – 200607170819A, M_w 7.8 S. Sumatra 2010 – 201010251442A) by SCARDEC, having smoother and longer source time functions than expected from their moment magnitude.	71
4.1 Simple flowchart showing the structure of the new algorithm developed in this Chapter for normal mode earthquake source inversions. The first part of the algorithm carries out all the necessary processing, while the second part is doing the grid search and determines the optimal model. The filtering of and spectra calculations of singlets is followed by the calculation of the phases of the singlets as explained in section 4.4.	79

4.2 (a): A global map showing locations of three sites in different latitudes (north hemisphere, equator, south hemisphere) where line faults with three different orientations are used to generate finite source synthetic data for the experiments presented in section 4.4. Stars in zoom-in maps show locations of three point sources superimposed to build finite source synthetic data with the rupture propagating over 240 km in length towards east (1), southeast (2) and south (3). (b): Earthquake mechanisms of point sources that are used to build synthetic data. (c): Moment rate function of finite synthetic data with a total duration of 100 s. Each of the three point sources is represented as a Gaussian function of 50 s in duration, rupturing every 25 s.	84
4.3 Maps showing centroid locations (blue stars), fault mechanisms, stations' distribution used in the synthetic tests (left), source models and spatio-temporal characteristics (right) used to build the synthetic data for the point and finite source inversion tests. Four earthquakes in different tectonic settings are tested: (a) a thrust earthquake based on the model of Tsai <i>et al.</i> (2005) for the M_w 9.3, 2004 Sumatra earthquake, (b) a strike-slip earthquake for the M_w 8.1, 1998 Antarctic plate earthquake, based on the GCMT source model (rupture model by Nettles <i>et al.</i> (1999)), (c) a normal earthquake based on the GCMT source model of the M_w 8.1, 2007 Kuril earthquake (rupture model based on the model of Lay <i>et al.</i> (2009)), (d) a thrust earthquake based on the model of Delouis <i>et al.</i> (2010) for the M_w 8.8 2010 Chile earthquake.	88
4.4 The effect of uncertainties in the Earth's model as observed on acceleration amplitude spectra of ${}_0S_2$ spheroidal mode singlets and ${}_0S_0$ radial mode. Synthetic data built using SAW12D model (black) are shown in comparison with input model synthetics using PREM (red) for the four earthquakes tested (thrust 1: Sumatra 2004, strike-slip: Antarctic plate 1998, normal: Kuril 2007, thrust 2: Chile 2010). Different earthquakes are plotted column by column. Note the frequency shift observed, especially at ${}_0S_2^0$ and ${}_0S_2^{\pm 1}$ singlets.	91

4.5	480-hr acceleration amplitude spectra and phase of selected spheroidal multiplets excitation kernels (${}_0S_2$, ${}_0S_3$, ${}_0S_0$) for the artificial 2004 Sumatra earthquake, based on the model of Tsai <i>et al.</i> (2005), observed at TLY station at epicentral distance of 45.8° and azimuth of 9.2° . Kernels are presented for the SAW12D Earth model (blue) and PREM (red). All calculations are carried out using HOPT. Rotation, ellipticity and gravity corrections are taken into account in the calculations.	92
4.6	The effect of adding white noise in synthetic data to theoretical acceleration amplitude spectra of ${}_0S_2$ spheroidal mode singlets and ${}_0S_0$ radial mode at station CTAO for the four earthquakes tested (thrust 1: Sumatra 2004, strike-slip: Antarctic plate 1998, normal: Kuril 2007, thrust 2: Chile 2010). Different earthquakes are plotted column by column. Synthetic data with white noise added (black), are shown in comparison with synthetic data without noise added (red). The Earth's model used in both cases is SAW12D.	93
4.7	Results from a point source inversion for the artificial 2004 Sumatra earthquake, using a combination of the amplitude and FFT misfits (97% amplitude and 3% FFT) for the finite source model of Tsai <i>et al.</i> (2005) as the input model ($\phi = 343^\circ$, $\delta = 6.1^\circ$, $\lambda = 107^\circ$, $M_w = 9.31$, $T_r = 545$ s, $L = 1140$ km). SAW12D 3-D model is used to build the synthetic data and the excitation kernels: (a) 480-hr optimal fit amplitude spectra of ${}_0S_2$, ${}_0S_3$, ${}_0S_0$ multiplets, (b) optimal source mechanism, (c) optimal and acceptable range of source parameters (acceptable parameters correspond to source models yielding misfit values not 1% larger than the lowest misfit associated with the optimal source model), (d) misfit function evolution.	96
4.8	Same as in Figure 4.7, but white noise is added to the synthetic data.	97
4.9	Same as in Figure 4.7, but PREM excitation kernels are used in the inversion.	98

4.10 Uncertainties and tradeoffs as shown from ensembles produced by Neighbourhood Algorithm and plotted as pairs of source parameters for the experiments of Figure 4.7 (green), Figure 4.8 (blue) and Figure 4.9 (magenta). Normalized frequency plots are shown at the bottom. The black dashed lines correspond to the input model ($\phi = 343^\circ, \delta = 6.1^\circ, \lambda = 107^\circ, M_w = 9.31$). Green, blue and magenta dashed lines correspond to optimal models determined from the inversions. Mean (μ) and standard deviation (σ) values are also shown.	99
4.11 Results from a finite source inversion for the artificial 2004 Sumatra earthquake, using a combination of the amplitude and FFT misfits (97% amplitude and 3% FFT) for the finite source model of Tsai <i>et al.</i> (2005) as the input model ($\phi = 343^\circ, \delta = 6.1^\circ, \lambda = 107^\circ, M_w = 9.31, T_r = 545$ s, $L = 1140$ km). SAW12D 3-D model is used to build the synthetic data and the excitation kernels. White noise is added to synthetic data: (a) 480-hr optimal fit amplitude spectra of ${}_0S_2^{-2}, {}_0S_2^{-1}, {}_0S_2^0, {}_0S_2^1, {}_0S_2^2, {}_0S_3^{-1}, {}_0S_3^1, {}_0S_0^0$ singlets, (b) optimal source mechanism, (c) optimal and acceptable range of source parameters (acceptable parameters correspond to source models yielding misfit values not 1% larger than the lowest misfit associated with the optimal source model), (d) misfit function evolution.	101
4.12 Same as in Figure 4.11, but without white noise added to synthetic data, while PREM excitation kernels are used in the inversion.	104
4.13 Uncertainties and tradeoffs as shown from ensembles produced by Neighbourhood Algorithm and plotted as pairs of source parameters for the experiments of Figure 4.11 (blue) and Figure 4.12 (magenta). Normalized frequency plots are shown at the bottom. The black dashed lines correspond to the input model ($\phi = 343^\circ, \delta = 6.1^\circ, \lambda = 107^\circ, M_w = 9.31, T_r = 545$ s, $L = 1140$ km). Blue and magenta dashed lines correspond to optimal models determined from the inversions. Mean (μ) and standard deviation (σ) values are also shown.	105

4.14 Optimal source parameters obtained from point source inversions versus true source parameters for the four artificial earthquakes tested (thrust 1: Sumatra 2004, strike-slip: Antarctic plate 1998, normal: Kuril 2007, thrust 2: Chile 2010) using the FFT misfit function (1 st column), the amplitude misfit (2 nd column), the phase misfit (3 rd column) and a combination of the amplitude and FFT (97% amplitude, 3%FFT) misfit functions (4 th column). Synthetic data are built using SAW12D Earth model. Different symbols are associated to different scenarios. Plus signs correspond to excitation kernels built using SAW12D, crosses correspond to synthetic data with white noise added and excitation kernels built using SAW12D, triangles correspond to excitation kernels built using PREM and diamonds correspond to synthetic data with white noise added and excitation kernels built using PREM.	108
4.15 Same as in Figure 4.14, but for finite source inversions. Results are shown for FFT (1 st column), amplitude (2 nd column), phase (3 rd column) and a combination of the amplitude and FFT (97% amplitude, 3%FFT) misfit functions (4 th column).	109
5.1 144-hr acceleration amplitude data (black) and GCMT (red) spectra observed at BFO station for the six earthquakes analysed in this Chapter: (a) 2004 Sumatra-Andaman, (b) 2005 Nias, (c) 2007 Bengkulu, (d) 2011 Tohoku, (e) 2013 Okhotsk Sea, (f) 2010 Chile. Degenerate spheroidal mode eigenfrequencies are plotted in blue for reference.	120
5.2 Singlets separation for ${}_0S_2$ and ${}_0S_3$ multiplets obtained from 480-hr acceleration spectra for the 26 December 2004 M_w 9.3 Sumatra-Andaman earthquake, recorded at CTAO station (black). Finite source model synthetics obtained from the singlets inversion described in subsection 5.4.1.1 are also shown (red) for reference. Top panel shows acceleration amplitude spectra, middle and bottom panels show real and imaginary FFT parts, respectively. Blue dashed lines indicate singlets' eigenfrequencies with respect to Earth's rotation, ellipticity and SAW12D Earth model. . .	124

5.3	Global maps showing the GCMT locations (stars) and beachballs of the six earthquakes analysed in this Chapter: (a) 2004 Sumatra-Andaman, (b) 2005 Nias, (c) 2007 Bengkulu, (d) 2011 Tohoku, (e) 2013 Okhotsk Sea, (f) 2010 Chile. Stations used in the point source inversions are plotted as red squares and those used in the finite source inversions are plotted as cyan triangles.	125
5.4	Map showing the tectonic setting of the 2004, 2005 and 2007 Sumatra earthquakes. Red stars indicate the centroid locations of the mainshocks. Red beachballs correspond to their GCMT source models. Red circles show the seismicity ($M_w \geq 5.5$ in entire GCMT catalogue) of the study area. White dashed lines indicate approximately the rupture areas of historic earthquakes.	126
5.5	Results from a point source inversion for the 2004 Sumatra-Andaman earthquake. The SAW12D 3-D mantle model is used to build excitation kernels for the centroid location of Tsai <i>et al.</i> (2005): (a) 240-hr optimal fit amplitude spectra of ${}_0S_2$, ${}_0S_3$, ${}_0S_4$, ${}_1S_2$, ${}_0S_0$, ${}_0S_5$, ${}_1S_3-2S_2-3S_1$ multiplets; (b) optimal source mechanism; (c) optimal and acceptable range of source parameters (acceptable parameters correspond to source models yielding misfit values not exceeding the minimum misfit value by more than 1%); (d) misfit function evolution as a function of the number of models generated in the parameter search.	129
5.6	Results from a finite source inversion for the 2004 Sumatra earthquake. SAW12D 3-D model is used to build the excitation kernels: (a) 480-hr optimal fit amplitude spectra of ${}_0S_2^{\pm 2}$, ${}_0S_2^0$, ${}_0S_3^{\pm 3}$, ${}_0S_0$ singlets with respect to the PDE location, (b) optimal source mechanism, (c) optimal and acceptable range of source parameters (acceptable parameters correspond to source models yielding misfit values up to 1% larger than the lowest misfit associated with the optimal source model), (d) misfit function evolution.	132

5.7	Tradeoff scatterplots from the ensemble of models produced by the Neighbourhood Algorithm for inversion results of Figure 5.5 (point source inversion; green dots) and Figure 5.6 (finite source inversion; blue dots) for the great 2004 Sumatra-Andaman earthquake. The normalised histograms in the bottom row show the distribution of the inversion results (their mean μ and standard deviation σ values are also shown). Black and red dashed vertical lines correspond to the optimal source parameters obtained from point and finite source inversions, respectively.	133
5.8	Map showing the tectonic setting of the 2011 Tohoku and the 2013 Okhotsk Sea earthquakes. Red stars indicate the centroid locations of the main-shocks. Red beachballs correspond to their GCMT source models. Red circles show the seismicity ($M_w \geq 5.5$ in entire the GCMT catalogue) of the study area. White dotted lines indicate approximately the rupture areas of historic earthquakes.	138
5.9	Results from a point source inversion for the 2011 Tohoku earthquake. The SAW12D 3-D mantle model is used to build the excitation kernels for the GCMT centroid location: (a) 240-hr optimal fit amplitude spectra of ${}_0S_2$, ${}_0S_3$, ${}_0S_4$, ${}_1S_2$, ${}_0S_0$, ${}_0S_5$, ${}_1S_{3-2}S_{2-3}S_1$ multiplets; (b) optimal source mechanism; (c) optimal and acceptable range of source parameters (acceptable parameters correspond to source models yielding misfit values not exceeding the lowest misfit value by more than 1%); (d) misfit function evolution as a function of the number of models generated in the parameter search.	141
5.10	Results from a finite source inversion for the 2011 Tohoku earthquake. The SAW12D 3-D mantle model is used to build the excitation kernels for the PDE location: (a) 480-hr optimal fit amplitude spectra of ${}_0S_2^{\pm 1}$, ${}_0S_2^{\pm 2}$, ${}_0S_3^{\pm 1}$, ${}_0S_3^{\pm 2}$, ${}_0S_3^{\pm 3}$, ${}_0S_0$ singlets; (b) optimal source mechanism; (c) optimal and acceptable range of source parameters (acceptable parameters correspond to source models yielding misfit values not exceeding the lowest misfit value by more than 1%); (d) misfit function evolution as a function of the number of models generated in the parameter search. . .	142

5.11 Tradeoff scatterplots from the ensemble of models produced by the Neighbourhood Algorithm for inversion results of Figure 5.9 (point source inversion; green dots) and Figure 5.10 (finite source inversion; blue dots) for the 2011 Tohoku earthquake. The normalised histograms in the bottom row show the distribution of the inversion results (their mean μ and standard deviation σ values are also shown). Black and red dashed vertical lines correspond to the optimal source parameters obtained from point and finite source inversions, respectively. 143

5.12 Results from a point source inversion for the 2013 Okhotsk Sea earthquake. The SAW12D 3-D mantle model is used to build the excitation kernels for the GCMT centroid location: (a) 48-hr optimal fit amplitude spectra of ${}_0S_3$, ${}_0S_4$, ${}_1S_2$, ${}_0S_0$, ${}_0S_5$, ${}_0T_{5-1}S_{3-2}S_{2-3}S_1$, ${}_0T_3$, ${}_0T_4$ multiplets; (b) optimal source mechanism; (c) optimal and acceptable range of source parameters (acceptable parameters correspond to source models yielding misfit values not exceeding the lowest misfit value by more than 1%); (d) misfit function evolution as a function of the number of models generated in the parameter search. 146

5.13 Tradeoff scatterplots from the ensemble of models produced by the Neighbourhood Algorithm for inversion results of Figure 5.12 for the 2013 Okhotsk Sea earthquake. The normalised histograms in the bottom row show the distribution of the inversion results (their mean μ and standard deviation σ values are also shown). Black dashed vertical lines correspond to the optimal source parameters obtained from the point source inversion. 147

5.14 Map showing the tectonic setting of the 2010 Maule, Chile earthquake. Red star indicates the centroid location of the mainshock. Red beachball corresponds to its GCMT source model. Red circles show the seismicity ($M_w \geq 5.5$ in entire GCMT catalogue) of the study area. Black dotted lines indicate approximately the rupture areas of historic earthquakes. . . 148

5.15 Results from a point source inversion for the 2010 Maule, Chile earthquake. The SAW12D 3-D mantle model is used to build the excitation kernels for the GCMT centroid location: (a) 240-hr optimal fit amplitude spectra of ${}_0S_2$, ${}_0S_3$, ${}_0S_4$, ${}_1S_2$, ${}_0S_0$, ${}_0S_5$, ${}_1S_{3-2}S_{2-3}S_1$ multiplets; (b) optimal source mechanism; (c) optimal and acceptable range of source parameters (acceptable parameters correspond to source models yielding misfit values not exceeding the minimum misfit value by more than 1%); (d) misfit function evolution as a function of the number of models generated in the parameter search.	150
5.16 Tradeoff scatterplots from the ensemble of models produced by the Neighbourhood Algorithm for inversion results of Figure 5.15 for the 2010 Maule, Chile earthquake. The normalised histograms in the bottom row show the distribution of the inversion results (their mean μ and standard deviation σ values are also shown). Black dashed vertical lines correspond to the optimal source parameters obtained from the point source inversion.	151
5.17 Comparisons of source parameters determined in this study (black asterisks – point source, magenta asterisks – finite source) with GCMT (red circles), SCARDEC (green triangles), W-phase (orange circles) and other source models published in the literature (blue squares). Error bars show source parameter uncertainties determined in this study.	153

B.1 Results from a point source inversion for the artificial 1998 Antarctic plate strike slip earthquake, using a combination of the amplitude and FFT misfits (97% amplitude and 3% FFT) using the GCMT location and fault geometry, assuming a total rupture duration of 90 s and rupture length of 240 km, based on the rupture model of Nettles <i>et al.</i> (1999), as the input model ($\phi = 281^\circ, \delta = 84^\circ, \lambda = 17^\circ, M_w = 8.1, T_r = 90$ s, $L = 240$ km). SAW12D 3-D model is used to build the synthetic data and the excitation kernels: (a) 480-hr optimal fit acceleration amplitude spectra of ${}_0S_2$, ${}_0S_3$ and ${}_0S_0$ multiplets, (b) optimal source mechanism, (c) optimal and acceptable range of source parameters (acceptable parameters correspond to source models yielding misfit values not 1% larger than the lowest misfit associated with the optimal source model), (d) misfit function evolution.	181
B.2 Uncertainties and tradeoffs as shown from ensembles produced by Neighbourhood Algorithm and plotted as pairs of source parameters for the experiment of Figure B.1. Normalized frequency plots are shown at the bottom. The black dashed lines correspond to the input model ($\phi = 281^\circ, \delta = 84^\circ, \lambda = 17^\circ, M_w = 8.1$) and red dashed lines correspond to optimal models determined from the inversions. Mean (μ) and standard deviation (σ) values are also shown.	182

B.5 Results from a point source inversion for the artificial 1998 Antarctic plate strike slip earthquake, using a combination of the amplitude and FFT misfits (97% amplitude and 3% FFT) using the GCMT location and fault geometry, assuming a total rupture duration of 90 s and rupture length of 240 km, based on the rupture model of Nettles <i>et al.</i> (1999), as the input model ($\phi = 281^\circ, \delta = 84^\circ, \lambda = 17^\circ, M_w = 8.1, T_r = 90$ s, $L = 240$ km). SAW12D 3-D model is used to build the synthetic data and PREM for the excitation kernels: (a) 480-hr optimal fit acceleration amplitude spectra of ${}_0S_2$, ${}_0S_3$ and ${}_0S_0$ multiplets, (b) optimal source mechanism, (c) optimal and acceptable range of source parameters (acceptable parameters correspond to source models yielding misfit values not 1% larger than the lowest misfit associated with the optimal source model), (d) misfit function evolution.	185
B.6 Uncertainties and tradeoffs as shown from ensembles produced by Neighbourhood Algorithm and plotted as pairs of source parameters for the experiment of Figure B.5. Normalized frequency plots are shown at the bottom. The black dashed lines correspond to the input model ($\phi = 281^\circ, \delta = 84^\circ, \lambda = 17^\circ, M_w = 8.1$) and red dashed lines correspond to optimal models determined from the inversions. Mean (μ) and standard deviation (σ) values are also shown.	186

B.7 Results from a point source inversion for the artificial 2007 Kuril normal faulting earthquake, using a combination of the amplitude and FFT misfits (97% amplitude and 3% FFT) using the GCMT location and fault geometry, assuming a total rupture duration of 60 s and rupture length of 220 km, based on the rupture model of Lay *et al.* (2009), as the input model ($\phi = 43^\circ, \delta = 59^\circ, \lambda = -115^\circ, M_w = 8.1, T_r = 60$ s, $L = 220$ km). SAW12D 3-D model is used to build the synthetic data and the excitation kernels: (a) 480-hr optimal fit acceleration amplitude spectra of ${}_0S_2$, ${}_0S_3$ and ${}_0S_0$ multiplets, (b) optimal source mechanism, (c) optimal and acceptable range of source parameters (acceptable parameters correspond to source models yielding misfit values not 1% larger than the lowest misfit associated with the optimal source model), (d) misfit function evolution. 187

B.8 Uncertainties and tradeoffs as shown from ensembles produced by Neighbourhood Algorithm and plotted as pairs of source parameters for the experiment of Figure B.7. Normalized frequency plots are shown at the bottom. The black dashed lines correspond to the input model ($\phi = 43^\circ, \delta = 59^\circ, \lambda = -115^\circ, M_w = 8.1$) and red dashed lines correspond to optimal models determined from the inversions. Mean (μ) and standard deviation (σ) values are also shown. 188

B.9 Results from a point source inversion for the artificial 2007 Kuril normal faulting earthquake, using a combination of the amplitude and FFT misfits (97% amplitude and 3% FFT) using the GCMT location and fault geometry, assuming a total rupture duration of 60 s and rupture length of 220 km, based on the rupture model of Lay <i>et al.</i> (2009), as the input model ($\phi = 43^\circ, \delta = 59^\circ, \lambda = -115^\circ, M_w = 8.1, T_r = 60$ s, $L = 220$ km). SAW12D 3-D model is used to build the synthetic data and the excitation kernels. White noise is also added to synthetic data: (a) 480-hr optimal fit acceleration amplitude spectra of ${}_0S_2$, ${}_0S_3$ and ${}_0S_0$ multiplets, (b) optimal source mechanism, (c) optimal and acceptable range of source parameters (acceptable parameters correspond to source models yielding misfit values not 1% larger than the lowest misfit associated with the optimal source model), (d) misfit function evolution.	189
B.10 Uncertainties and tradeoffs as shown from ensembles produced by Neighbourhood Algorithm and plotted as pairs of source parameters for the experiment of Figure B.9. Normalized frequency plots are shown at the bottom. The black dashed lines correspond to the input model ($\phi = 43^\circ, \delta = 59^\circ, \lambda = -115^\circ, M_w = 8.1$) and red dashed lines correspond to optimal models determined from the inversions. Mean (μ) and standard deviation (σ) values are also shown.	190

B.11 Results from a point source inversion for the artificial 2007 Kuril normal faulting earthquake, using a combination of the amplitude and FFT misfits (97% amplitude and 3% FFT) using the GCMT location and fault geometry, assuming a total rupture duration of 60 s and rupture length of 220 km, based on the rupture model of Lay <i>et al.</i> (2009), as the input model ($\phi = 43^\circ, \delta = 59^\circ, \lambda = -115^\circ, M_w = 8.1, T_r = 60$ s, $L = 220$ km). SAW12D 3-D model is used to build the synthetic data and PREM for the excitation kernels: (a) 480-hr optimal fit acceleration amplitude spectra of ${}_0S_2$, ${}_0S_3$ and ${}_0S_0$ multiplets, (b) optimal source mechanism, (c) optimal and acceptable range of source parameters (acceptable parameters correspond to source models yielding misfit values not 1% larger than the lowest misfit associated with the optimal source model), (d) misfit function evolution.	191
B.12 Uncertainties and tradeoffs as shown from ensembles produced by Neighbourhood Algorithm and plotted as pairs of source parameters for the experiment of Figure B.11. Normalized frequency plots are shown at the bottom. The black dashed lines correspond to the input model ($\phi = 43^\circ, \delta = 59^\circ, \lambda = -115^\circ, M_w = 8.1$) and red dashed lines correspond to optimal models determined from the inversions. Mean (μ) and standard deviation (σ) values are also shown.	192

B.13 Results from a point source inversion for the artificial 2010 Chile thrust earthquake, using a combination of the amplitude and FFT misfits (97% amplitude and 3% FFT) using an artificial unilateral rupture model based on the source model of Delouis *et al.* (2010) assuming a total rupture duration of 230 s and rupture length of 600 km, as the input model ($\phi = 15^\circ, \delta = 18^\circ, \lambda = 110^\circ, M_w = 8.8, T_r = 230$ s, $L = 600$ km). SAW12D 3-D model is used to build the synthetic data and the excitation kernels: (a) 480-hr optimal fit acceleration amplitude spectra of ${}_0S_2$, ${}_0S_3$ and ${}_0S_0$ multiplets, (b) optimal source mechanism, (c) optimal and acceptable range of source parameters (acceptable parameters correspond to source models yielding misfit values not 1% larger than the lowest misfit associated with the optimal source model), (d) misfit function evolution. 193

B.14 Uncertainties and tradeoffs as shown from ensembles produced by Neighbourhood Algorithm and plotted as pairs of source parameters for the experiment of Figure B.13. Normalized frequency plots are shown at the bottom. The black dashed lines correspond to the input model ($\phi = 15^\circ, \delta = 18^\circ, \lambda = 110^\circ, M_w = 8.8$) and red dashed lines correspond to optimal models determined from the inversions. Mean (μ) and standard deviation (σ) values are also shown. 194

B.17 Results from a point source inversion for the artificial 2010 Chile thrust earthquake, using a combination of the amplitude and FFT misfits (97% amplitude and 3% FFT) using an artificial unilateral rupture model based on the source model of Delouis *et al.* (2010) assuming a total rupture duration of 230 s and rupture length of 600 km, as the input model ($\phi = 15^\circ, \delta = 18^\circ, \lambda = 110^\circ, M_w = 8.8, T_r = 230$ s, $L = 600$ km). SAW12D 3-D model is used to build the synthetic data and PREM for the excitation kernels: (a) 480-hr optimal fit acceleration amplitude spectra of ${}_0S_2$, ${}_0S_3$ and ${}_0S_0$ multiplets, (b) optimal source mechanism, (c) optimal and acceptable range of source parameters (acceptable parameters correspond to source models yielding misfit values not 1% larger than the lowest misfit associated with the optimal source model), (d) misfit function evolution. 197

B.18 Uncertainties and tradeoffs as shown from ensembles produced by Neighbourhood Algorithm and plotted as pairs of source parameters for the experiment of Figure B.17. Normalized frequency plots are shown at the bottom. The black dashed lines correspond to the input model ($\phi = 15^\circ, \delta = 18^\circ, \lambda = 110^\circ, M_w = 8.8$) and red dashed lines correspond to optimal models determined from the inversions. Mean (μ) and standard deviation (σ) values are also shown. 198

C.7 Results from a finite source inversion for the artificial 2007 Kuril normal faulting earthquake, using a combination of the amplitude and FFT misfits (97% amplitude and 3% FFT) using the GCMT location and fault geometry, assuming a total rupture duration of 60 s and rupture length of 220 km, based on the rupture model of Lay <i>et al.</i> (2009), as the input model ($\phi = 43^\circ, \delta = 59^\circ, \lambda = -115^\circ, M_w = 8.1, T_r = 60$ s, $L = 220$ km). SAW12D 3-D model is used to build the synthetic data and PREM for the excitation kernels: (a) 480-hr optimal fit acceleration amplitude spectra of ${}_0S_2^{\pm 1, \pm 2}$ and ${}_0S_0^0$ singlets, (b) optimal source mechanism, (c) optimal and acceptable range of source parameters (acceptable parameters correspond to source models yielding misfit values up to 1% larger than the lowest misfit associated with the optimal source model), (d) misfit function evolution.	206
C.8 Uncertainties and tradeoffs as shown from ensembles produced by Neighbourhood Algorithm and plotted as pairs of source parameters for the experiment of Figure C.7. Normalized frequency plots are shown at the bottom. The black dashed lines correspond to the input model ($\phi = 43^\circ, \delta = 59^\circ, \lambda = -115^\circ, M_w = 8.1, T_r = 60$ s, $L = 220$ km) and red dashed lines correspond to optimal models determined from the inversions. Mean (μ) and standard deviation (σ) values are also shown.	207

C.11 Results from a finite source inversion for the artificial 2010 Chile thrust earthquake, using a combination of the amplitude and FFT misfits (97% amplitude and 3% FFT) using an artificial unilateral rupture model based on the source model of Delouis <i>et al.</i> (2010) assuming a total rupture duration of 230 s and rupture length of 600 km, as the input model ($\phi = 15^\circ, \delta = 18^\circ, \lambda = 110^\circ, M_w = 8.8, T_r = 230$ s, $L = 600$ km). SAW12D 3-D model is used to build the synthetic data and PREM for the excitation kernels: (a) 480-hr optimal fit acceleration amplitude spectra of ${}_0S_2^{\pm 1, \pm 2}$, ${}_0S_3^{\pm 1, \pm 3}$ and ${}_0S_0^0$ singlets, (b) optimal source mechanism, (c) optimal and acceptable range of source parameters (acceptable parameters correspond to source models yielding misfit values up to 1% larger than the lowest misfit associated with the optimal source model), (d) misfit function evolution.	210
C.12 Uncertainties and tradeoffs as shown from ensembles produced by Neighbourhood Algorithm and plotted as pairs of source parameters for the experiment of Figure C.11. Normalized frequency plots are shown at the bottom. The black dashed lines correspond to the input model ($\phi = 15^\circ, \delta = 18^\circ, \lambda = 110^\circ, M_w = 8.8, T_r = 230$ s, $L = 600$ km) and red dashed lines correspond to optimal models determined from the inversions. Mean (μ) and standard deviation (σ) values are also shown.	211
D.1 Results from a point source inversion for the 2005 Nias earthquake. SAW12D 3-D model is used to build the excitation kernels: (a) 240-hr optimal fit amplitude spectra of ${}_0S_2$, ${}_0S_3$, ${}_0S_4$, ${}_1S_2$, ${}_0S_0$, ${}_0S_5$, ${}_1S_{3-2}S_{2-3}S_1$ multiplets with respect to the GCMT centroid location, (b) optimal source mechanism, (c) optimal and acceptable range of source parameters (acceptable parameters correspond to source models yielding misfit values up to 1% larger than the lowest misfit associated with the optimal source model), (d) misfit function evolution.	215

D.2 Uncertainties and tradeoffs as shown from ensembles produced by Neighbourhood Algorithm and plotted as pairs of source parameters for inversion results of Figure D.1 for the 2005 Nias earthquake. Normalized frequency plots are shown at the bottom. Mean (μ) and standard deviation (σ) values are also shown on top of the normalized frequency plots. Red dashed lines show optimal source parameters obtained from point source inversion.	216
D.3 Results from a point source inversion for the 2007 Bengkulu earthquake. SAW12D 3-D model is used to build the excitation kernels: (a) 240-hr optimal fit amplitude spectra of ${}_0S_2$, ${}_0S_3$, ${}_0S_4$, ${}_1S_2$, ${}_0S_0$, ${}_0S_5$, ${}_1S_3$ - ${}_2S_2$ - ${}_3S_1$ multiplets with respect to the GCMT centroid location, (b) optimal source mechanism, (c) optimal and acceptable range of source parameters (acceptable parameters correspond to source models yielding misfit values up to 1% larger than the lowest misfit associated with the optimal source model), (d) misfit function evolution.	217
D.4 Uncertainties and tradeoffs as shown from ensembles produced by Neighbourhood Algorithm and plotted as pairs of source parameters for inversion results of Figure D.3 for the 2007 Bengkulu earthquake. Normalized frequency plots are shown at the bottom. Mean (μ) and standard deviation (σ) values are also shown on top of the normalized frequency plots. Red dashed lines show optimal source parameters obtained from point source inversion.	218

Chapter 1

Introduction

Instrumental observations of seismic motions with wave periods ranging from less than a second to 54 minutes provide useful information about earthquake source processes, the physical properties of the Earth's interior and the site effects associated with the structural complexity in the vicinity of seismic stations. Over the past decades there has been much progress in seismological research to address these issues. For example, sophisticated algorithms are now available to determine earthquake source parameters (e.g., location, magnitude, mechanism) in near real time. In addition, high-resolution images of the Earth's deep interior built using seismic tomography are increasingly available. Accurate earthquake source models are key for improved Earth's tomography studies and for a better understanding of active tectonics and of natural hazards (e.g., earthquake cycle, tsunamis). Moreover, robust kinematic characterisations of earthquakes provide useful information for further detailed studies of the physics of earthquakes, from the dynamic modelling of earthquake ruptures to understanding earthquake statistical properties, stress transfer and scaling laws. However, often there are large discrepancies between kinematic source models produced by different authors for a given earthquake, suggesting large uncertainties, and showing that there remains much scope for thorough validation tests of source models. Moreover, it is important to further explore the full spectra of seismic data, including the lowest wave frequencies, for a complete characterisation of seismic sources.

1.1 Global earthquakes

Tectonic earthquakes occur in faults, which are surfaces on the Earth where one block slides with respect to the other. The two blocks are initially locked as friction prevents the two sides from slipping. When the accumulated strain overcomes the friction that holds the two blocks together, the fault slips with the simultaneous release of elastic waves, resulting in an earthquake. This theory known as elastic rebound theory was proposed by Reid (1910) after the 1906 $M 7.8$ San Francisco earthquake on the San Andreas fault.

The global seismicity map in Figure 1.1 clearly shows that the distribution of earthquake epicentres is non-uniform and highly concentrated on plate boundaries. Most of the events occur around the Pacific margin and the Alpine-Himalayan belt (thrust earthquakes), with many others along midocean ridges and intraplate events (strike-slip, normal earthquakes). The depth distribution of subduction zone earthquakes is well established by the so-called Wadati-Benioff zones. Often, in subduction zones shallow depth thrust earthquakes occur down to depths of around 40 km with fault dip angles shallower than 30° . Intermediate-depth events occur at depths of 70–300 km and deep events can occur deeper than 300 km, down to 700 km, with dip angles becoming successively steeper as the oceanic plate sinks into the mantle (e.g. Lay and Wallace, 1995).

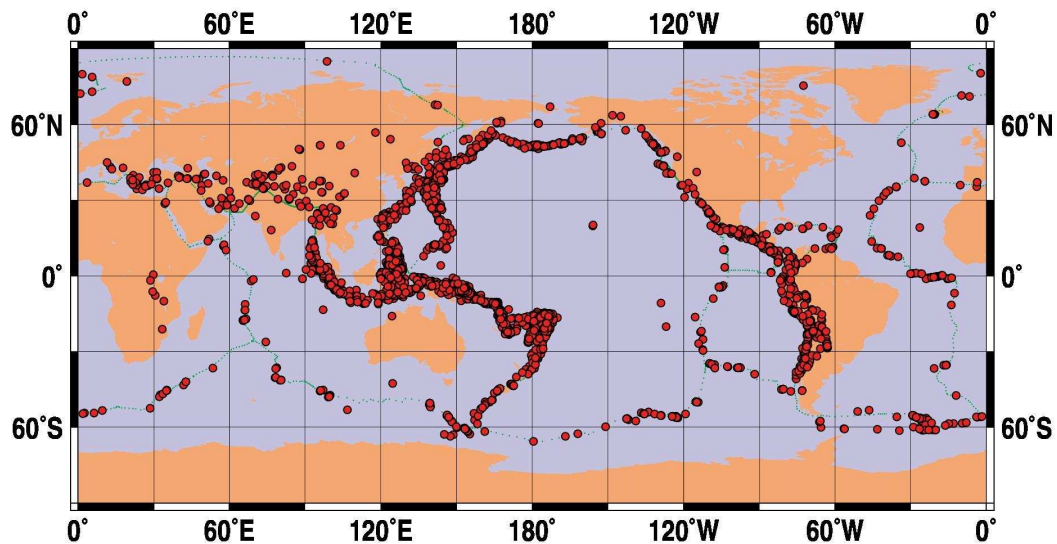


Figure 1.1: Global seismicity ($M_w \geq 6.0$) according to the Global Centroid Moment Tensor (GCMT) catalogue for the past 20 years. Red circles show GCMT epicentres and green lines show plate boundaries.

Based on the elastic rebound theory, four different periods of the so-called seismic

cycle can be defined. During the interseismic period, strain is accumulated on the fault with no slip or some aseismic creep possibly taking place. The preseismic phase immediately before the mainshock often involves foreshock activity. The mainshock defines the coseismic phase, where motion on the fault takes place, and, finally, the postseismic phase is typically characterised by the occurrence of aftershocks accompanied by deformation due to afterslip (Pollitz *et al.*, 2008) and/or viscoelastic or poroelastic relaxation (Hergert and Heidbach, 2006).

The seismic cycle can last thousands of years, with the interseismic stage being the most difficult to study for long recurrence time earthquakes because of the lack of instrumental observations prior to the 20th century. However, there are cases where it has been successfully observed, such as in the Sumatra and South America subduction zones using geodetic data (e.g. Chlieh *et al.*, 2004; Prawirodirdjo *et al.*, 2010). Indeed, recent advances in geodetic measurements, such as GPS and InSAR, have been key to study the interseismic and postseismic phases of various earthquakes, such as of the 23 June 2001 M_w 8.4 Peru earthquake (Melbourne and Webb, 2002; Hergert and Heidbach, 2006; Biggs *et al.*, 2009) and the 25 September 2003 M_w 8.3 Hokkaido earthquake (Miyazaki *et al.*, 2004). The coseismic phase of large magnitude earthquakes can involve a wide range of extreme rupture behaviours, from recently discovered silent slip events, such as the 1999 Cascadia event of aseismic slip over a 50 km by 300 km area, a rupture equivalent to an earthquake of moment magnitude 6.7 (Dragert *et al.*, 2001), to supershear rupture, where the rupture propagates with a rupture velocity higher than the shear wave speed, such as for the 17 August 1999 M_w 7.5 Izmit earthquake (Bouchon *et al.*, 2002). Moreover, some subduction zone earthquakes, such as the 2 September 1992 M_w 7.6 Nicaragua and the 2 June 1994 M_w 7.8 Java events (Polet and Kanamori, 2000; Abercrombie *et al.*, 2001) have been associated with anomalously large tsunami excitation as a consequence of a low ratio of seismic radiated energy to seismic moment. A slow slip component in the rupture of very large magnitude earthquakes ($M_w > 9.0$) has been observed for the great 22 May 1960 M_w 9.5 Chile earthquake (Kanamori and Cipar, 1974; Kanamori and Anderson, 1975a; Cifuentes and Silver, 1989) and the 26 December 2004 M_w 9.3 Sumatra-Andaman earthquake (Park *et al.*, 2005; Stein and Okal, 2005), yielding anomalously long source durations. As a consequence, it can be difficult to detect the total seismic moment released

by such earthquakes using standard source inversion techniques based on seismic data in a relatively narrow frequency range (Tsai *et al.*, 2005). In contrast, the 11 March 2011 M_w 9.1 Tohoku earthquake was characterised by a compact rupture length and duration with respect to its magnitude (Politz *et al.*, 2011b; Simons *et al.*, 2011). In addition, the latter event and the 27 February 2010 M_w 8.8 Maule, Chile earthquake have been characterised by a frequency-dependent rupture behaviour, with short-period and long-period radiation arising from different regions in the megathrust (Koper *et al.*, 2011; Kiser and Ishii, 2011, 2012).

The past decade has been marked by the occurrence of many great earthquakes ($M_w \geq 8.5$) i.e., from the 2004 M_w 9.3 Sumatra-Andaman earthquake, and two subsequent thrust and a strike slip earthquake (followed within two hours by a M_w 8.2 strike slip event) in the same area, to the 2010 M_w 8.8 Maule, Chile and the 2011 M_w 9.1 Tohoku earthquakes. Some of these earthquakes highlighted the diverse and sometimes surprising character of earthquake rupture, such as the 2004 Sumatra-Andaman which involved a slow slip component observed from low-frequency seismic data (e.g. Park *et al.*, 2005). One of the most striking examples is also the unexpected for its magnitude, 2011 M_w 9.1 Tohoku earthquake (Hayes, 2011). Body wave inversions showed radiation from up-dip (Ammon *et al.*, 2011), while back-projection studies indicated short-period radiation from down-dip (Koper *et al.*, 2011). Furthermore, geodetic studies indicated that slip was observed further off-shore but with significant slip close to the trench (Simons *et al.*, 2011). Discrepancies often observed in different studies highlight rupture complexities that need to be further investigated as they have profound consequences for our understanding of earthquake physics and seismic hazard.

1.2 Seismological observation of earthquakes: which data?

It has been over a century since the first instrumental observation of a teleseismic event occurring in Japan in 1889, by Von Rebeur-Paschwitz in Germany, which marked the beginning of a new era in observational seismology. A few years later, in 1903, the International Association of Seismology was founded at a conference in Strasburg in order to build the first database of seismic recordings. The first systematic catalogue of earthquakes was released in 1918 (ISS, International Seismological Summary) and in 1964 it

was replaced by the International Seismological Centre (ISC) bulletin (Villaseñor *et al.*, 1997).

Technological progress enabled the design and construction of several types of seismographs, with many analogue instruments being deployed globally since 1950. This motivated the community for a unified global seismograph network, which was established in 1964 (World-Wide Standard Seismograph Network). The WWSSN consisted of 120 analogue three-component seismographs which operated for approximately 20 years. In the 1980s there was an effort to replace the old analogue seismographs with new digital broadband instruments. Meanwhile, other global networks, such as the French GEOSCOPE, have been developed and included in the unified current Global Seismograph Network (GSN) shown in Figure 1.2. The importance of the GSN is highlighted by a significant amount of pioneering seismic source studies based on their recordings (e.g. Dziewonski *et al.*, 1981; Kikuchi and Kanamori, 1982; Kanamori and Rivera, 2008; Ekström *et al.*, 2012), seismic tomography studies (e.g. Dziewonski and Anderson, 1981; Ritsema *et al.*, 1999) and other seismic observations (e.g. Kanamori, 1993; Masters and Widmer, 1995).

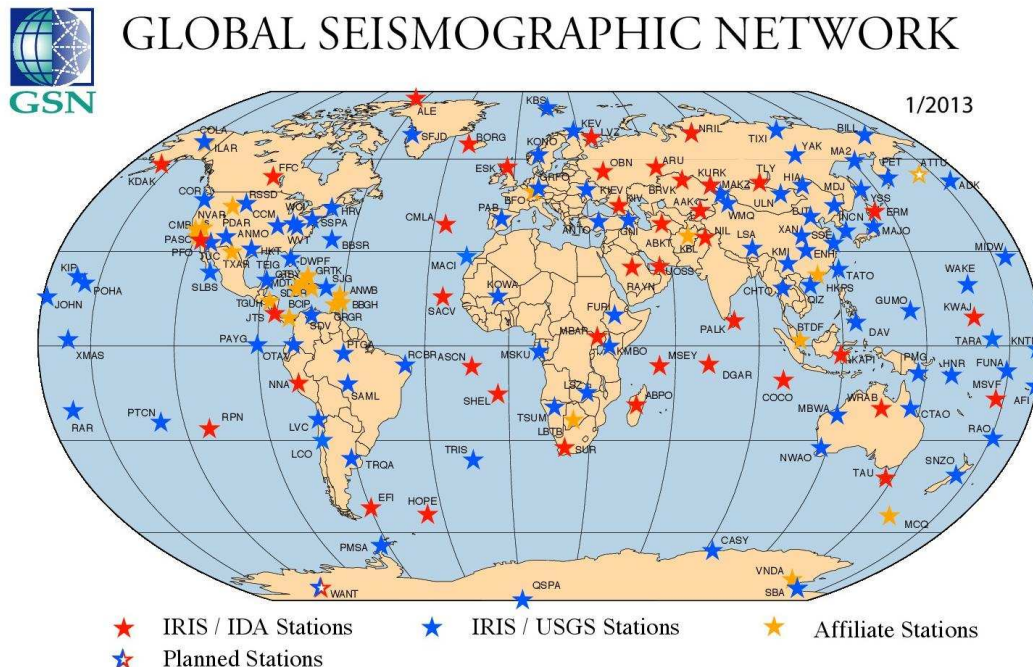


Figure 1.2: A global map showing the distribution of the current seismic stations included in the GSN network. Figure downloaded from IRIS (<http://www.iris.edu/hq/programs/gsn>).

The primary GSN data used in earthquake source studies are records from stations

at teleseismic distances from the earthquake (e.g., distances of 30–90°), where direct (P , SV , SH) and surface reflected (pP , sP , sS) body wave phases can be well observed and modelled for earthquakes of $M_w > 5.5$ (e.g. Kikuchi and Kanamori, 1982; Vallée *et al.*, 2011). Figure 1.3 shows typical three-component seismograms, with P body waves arriving first, followed by S body waves. Surface wave (Rayleigh and Love) arrivals can be easily identified in the seismograms roughly 30 minutes after the earthquake’s origin time. Rayleigh waves (R) are the result of constructive interference of P and SV waves and are observed on vertical and longitudinal component records. Love waves (L) result from the interference of SH waves, trapped close to the surface, and are observed on transverse component data.

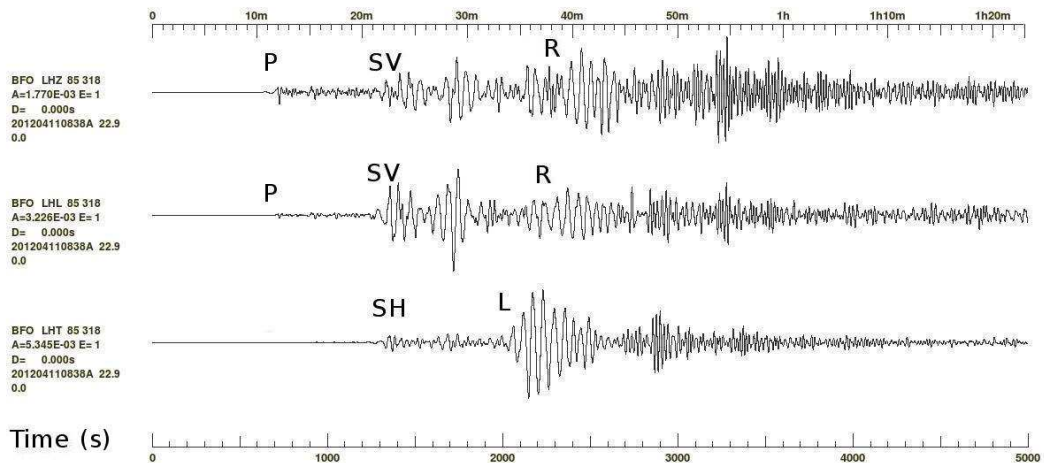


Figure 1.3: An example of three-component seismograms (LHZ: vertical, LHL: longitudinal, LHT: transverse) from the GSN showing ground displacement after the 11 April 2012 M_w 8.6 Sumatra strike-slip earthquake recorded at BFO station at an epicentral distance of 85° and azimuth of 318°. Body waves (P , SV , SH) as well as Rayleigh (R) and Love (L) surface wave arrivals are shown in the seismograms.

Another type of seismic data are the Earth’s normal modes or free oscillations, which are standing waves resulting from the constructive interference of opposite direction travelling long-period surface waves (Figure 1.4). The theoretical description of the Earth’s normal modes was presented by Poisson (1829). Lamb (1882) calculated for the first time analytically theoretical normal mode eigenfrequencies based on simple models, whereas eigenfrequencies of normal modes for more realistic Earth models have only been computed almost a century later (Pekeris and Jarosch, 1958; Takeuchi, 1959; Backus and Gilbert, 1961). Although recordings of body and surface waves were available from the early 1920s, normal mode observations have not been reported until the 1960s. The first

unambiguous observation of normal modes was reported by Benioff *et al.* (1961) after the 22 May 1960 M_w 9.5 Chile earthquake. With the subsequent development of the GSN and of very broadband seismometers (e.g., STS-1, STS-2, KS-54000), many more new observations have been possible (see, e.g., Figure 1.4), including recent observations of the Earth's hum (Webb, 2007; Kurle and Widmer-Schnidrig, 2008; Brominski and Gerstoft, 2009), which is a nearly constant signal around 10 mHz, observed in the absence of large earthquakes. At the same time, new theoretical developments and increased computational power allowed more realistic calculations of normal mode eigenfrequencies and eigenfunctions, and their observations (e.g. Woodhouse and Dahlen, 1978; Masters *et al.*, 1982, 1983; Masters and Widmer, 1995; Zürn *et al.*, 2000; Tanimoto, 2001; Rosat *et al.*, 2003; Davis *et al.*, 2005). All these efforts led to great contributions to studies of the structure of the Earth's deep interior, notably to Earth's density studies due to the unique sensitivity of normal modes to density structure (e.g. Dziewonski and Anderson, 1981; Resovsky and Ritzwoller, 1998; Ritsema *et al.*, 1999; Mégnin and Romanowicz, 2000). Normal modes have been also observed using non-seismological instruments, such as, with superconducting gravimeters and tiltmeters (e.g. Courtier *et al.*, 2000; Widmer-Schnidrig, 2003; Ferreira *et al.*, 2006; Braatenberg *et al.*, 2006), and, recently with a ring laser system that is sensitive to rotational ground motions (Igel *et al.*, 2011).

The Earth's normal modes play an important role in source studies of very large magnitude earthquakes ($M_w > 8.0$), providing useful constraints on the fault geometry, the magnitude and on source directivity (e.g. Abe, 1970; Ben-Menahem *et al.*, 1972; Kanamori and Cipar, 1974; Kedar *et al.*, 1994; Park *et al.*, 2005; Stein and Okal, 2005; Lambotte *et al.*, 2006, 2007; Tanimoto *et al.*, 2012; Okal *et al.*, 2012). However, because of very long and continuous time-series needed for their observations, their use in source studies has been somewhat limited compared to body and surface waves. Hence, the full potential of free oscillation data for earthquake source studies has not been fully examined yet. This thesis addresses this issue by investigating the use of normal mode data in independent tests of earthquake source parameters and in source inversions for simple finite source models of great earthquakes.

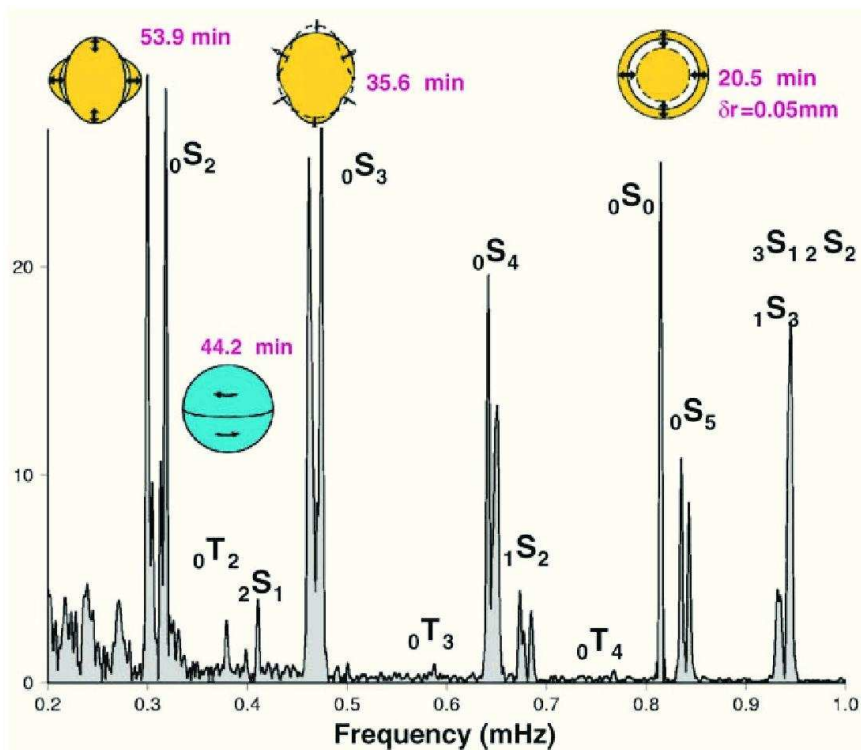


Figure 1.4: Observed vertical component spectra of 240 hours of free oscillations in the 0–1 mHz frequency band recorded at CAN (Canberra, Australia) station for the 26 December 2004 M_w 9.3 Sumatra-Andaman earthquake. Spheroidal and toroidal surface patterns are also shown for some of the gravest free oscillations in the spectra. Figure taken by Park *et al.* (2005).

1.3 Determination of earthquake source parameters

1.3.1 Early studies

Since the beginning of the observational era in seismology many different ways have been used to measure the size of an earthquake. Early studies used the body wave (m_b) and Rayleigh surface wave (M_S) magnitudes, based on short (~ 1 s) and long period (~ 20 s) observations of body and surface waves, respectively. However, Aki (1967) showed that the body wave magnitude saturates after an earthquake of $M \sim 6$ and the surface magnitude saturates after an earthquake of $M \sim 8$, underestimating the earthquakes' energy. This limitation was addressed by the introduction of the seismic moment by Aki (1966), which is directly related to the energy radiated from a double couple seismic source. Kanamori (1977) introduced the moment magnitude (M_w) as a unified earthquake magnitude measurement, compatible with other magnitude types, like the surface wave magnitude, until it saturates (M_S 8.2).

Gilbert (1970) introduced the concept of the seismic moment tensor, which is a mathematical representation of the equivalent body force of a seismic source. Its nine components are the nine force couples which involve the seismic moment and the mechanism of the source, described by the fault's strike (ϕ), dip (δ) and rake (λ). Gilbert (1970) showed that the moment tensor is linearly related to the normal mode ground motions that are generated by an earthquake, bringing a new perspective to source parameter determinations whereby normal mode data can be relatively easily inverted for earthquake source parameters (Gilbert, 1973). Langston and Helmberger (1975) extended the theory to body waves excited by shallow earthquakes, by deriving expressions for ground displacements recorded at teleseismic distances. Dziewonski *et al.* (1981) introduced the concept of the centroid moment tensor, whereby the seismic source is described by a centroid in space and time which minimises the first spatial and temporal moments of the moment rate distribution $\dot{m}(t, x)$ (stress glut rate, in Backus and Mulcahy, 1976). Hence, the centroid location represents an average point source location which, in contrast with the hypocenter which is associated with the rupture initiation point, being often derived from onset times of high-frequency body waves. The study of Dziewonski *et al.* (1981) initiated a systematic effort for the routine determination of source parameters of global and regional earthquakes with magnitudes $M_w \geq 5.5$ (Dziewonski and Woodhouse, 1983), which led to the very successful and widely used Global Centroid Moment Tensor (GCMT) project (Ekström *et al.*, 2012). Modifications of this technique have been carried by Ekström (1989) and Arvidsson and Ekström (1998) to extend the analysis to even lower magnitude earthquakes ($M_w \geq 4.5$).

1.3.2 Existing global earthquake catalogues

The systematic observation of earthquakes through the deployment of regional and global seismograph networks and the routine calculation of earthquake source parameters (spatio-temporal location and moment tensor), led to the determination of thousands of source models. Today there are several catalogues either global, such as the ISC catalogue

(<http://www.isc.ac.uk/>) which reports locations of global earthquakes, or regional catalogues such as the seismic catalogue of the European-Mediterranean Seismological Centre (EMSC, <http://www.emsc-csem.org>). In this section we shall discuss some of the major global earthquake source catalogues, which will be used in this thesis.

One of the most widely used earthquake catalogues is the Global Centroid Moment Tensor (GCMT) catalogue. From 1982 to 2006 the project was operated at Harvard University, known as the Harvard CMT Project. Since 2006 the project is operated by the Lamont-Doherty Earth Observatory at Columbia University, being now known as the Global CMT project (GCMT), with more than 25,000 moment tensor solutions for earthquakes with $M_w \geq 4.5$ since 1976 (<http://www.globalcmt.org/>). In addition, the United States Geological Survey (USGS) routinely reports PDE (Preliminary Determination of Epicenters) earthquake locations, as well as Centroid Moment Tensor source models (<http://earthquake.usgs.gov/regional/neic/>). The Earthquake Research Institute (ERI) at University of Tokyo also carries out its own CMT analysis (<http://www.eri.u-tokyo.ac.jp/eng/>), using similar techniques to those developed by the GCMT project (Kawakatsu, 1995). The data used in the CMT approach are typically three-component body waves with wave periods in the band 40–150 s for low magnitude earthquakes ($M_w \leq 5.5$), while body ($T \sim 40$ –150 s), surface ($T \sim 50$ –150 s) and long-period mantle wave data ($T \sim 125$ –350 s) are used for earthquakes with $M_w \sim 5.5$ –7.0. For large magnitude earthquakes ($M_w > 7.0$), the filtering is shifted to longer periods, thus, for example for earthquakes with $M_w > 8.0$ mantle waves with periods ~ 450 –200 s are used in the inversions (Ekström *et al.*, 2012). Normal mode summation is used in the modelling, whereby the seismic moment tensor is obtained from a linear inversion of the data using a least-squares algorithm. Once there is an initial estimate of the moment tensor, the least-squares algorithm proceeds in an iterative way allowing small perturbations with respect to the spatial-temporal location parameters and updating the moment tensor in each iteration, until a good agreement between the observed and synthetic seismograms is achieved. In its current version, the GCMT technique uses the SH8/U4L8 3-D Earth model (Dziewonski and Woodward, 1992) in the modelling.

The identification of the W seismic phase, a very long-period phase (100–1000 s) first

recognised after the 2 September 1992 M_w 7.6 Nicaragua earthquake (Kanamori, 1993), has further contributed to ongoing efforts for accurate and fast determinations of earthquake source parameters. The W phase has a fast group velocity (4.5–9.0 km/s), being observed between P and S wave arrivals, and long before seismic surface waves. Hence, it is a data type very well suited for rapid source model inversions soon after an earthquake's occurrence. Furthermore, its very long wavelength (~ 1200 km) is well adapted to source inversions of large magnitude earthquakes, in terms of far-field source spectra characteristics (corner frequency) and fault area dimensions that control the potential for significant tsunami excitation (Kanamori, 1972). The W-phase technique has some similarities to the Centroid Moment Tensor method (Dziewonski *et al.*, 1981; Dziewonski and Woodhouse, 1983), being usually referred to as the WCMT method, since the determined parameters are the six components of the moment tensor and four centroid location parameters (origin time, depth, latitude, longitude). However, significant differences include the data type, the time window and the algorithm used to determine the source models. In the first stage, a preliminary W-phase magnitude is estimated. The second stage provides a first solution based on the PDE location and, finally, during the third stage, a grid search for the final centroid moment tensor is carried out (for details, see Duputel *et al.*, 2012b,a). The 1-D Earth model PREM (Dziewonski and Anderson, 1981) is used in the modelling; however, the use of such simplified 1-D Earth structure is not a significant drawback of the method, since most of the W-phase propagation takes place in the relatively homogeneous lower mantle. The systematic determination of WCMT source models for large earthquakes ($M_w \geq 6.5$) in the 1990–2010 period, led to the recently developed W-phase global catalogue (<http://wphase.unistra.fr/>) based on the W-phase technique (Duputel *et al.*, 2012b). The technique is also routinely implemented by the USGS.

Recently, a new catalogue of source models based on long-period body waves (0.005–0.03 Hz) has been produced. It includes source parameters for significant earthquakes ($M_w > 6.5$) since 1993 and for earthquakes with $M_w \geq 5.4$ since 2011. Source models are obtained using the SCARDEC method (Vallée *et al.*, 2011), which is now an automated technique for the routine determination of earthquake source parameters (fault strike, dip, rake, M_w , depth and source time functions; see <http://geoazur.oca.eu/SCARDEC>). The SCARDEC method uses only body waves (P , P_cP , PP , SH S_cS)

including all the reflected and refracted seismic phases in the crust recorded at teleseismic distances ($30\text{--}90^\circ$). Thus, the SCARDEC method only needs approximately 30-minute time-series after the earthquake's origin, in contrast with the GCMT method, which needs much longer time-series including the slower surface waves. Hence, the SCARDEC technique could potentially be useful for applications requiring fast source models, notably for ocean-wide tsunami alert purposes. The source duration is first estimated by using the direct P wave high-frequency signal (1–2 Hz) on the vertical component at teleseismic distances (Lomax, 2005; Ni *et al.*, 2005). A deconvolution approach is then used to estimate the source parameters. A relative source time function describing the rupture's time history is obtained at each station that is used in the modelling, which is very useful to identify complexities in the earthquake source process as well as to identify slow tsunami earthquakes which have a source process anomalously long and smooth compared to that expected for their magnitude (Kanamori, 1972). A limitation of the SCARDEC method is that it relies on simplified forward modelling using ray theory and the 1-D IASP91 Earth model (Kennett and Engdahl, 1991).

It is well known that earthquakes occur on faults which have finite dimensions; hence, the earthquake point source models discussed so far may be limited. While the simplicity of the point source approximation is attractive and the modelling of small to moderate earthquakes ($M_w \sim 5$) as point sources in the far field (at distances of several wavelengths from the source) using data with wave periods much longer than the source's duration may be sufficient, for larger earthquakes the point source model is generally more limited (e.g., Tsai *et al.*, 2005; Vallée *et al.*, 2011). The SCARDEC catalogue reports point source parameters along with earthquake source time functions, which reflect finite source characteristics (e.g., rupture directivity). This goes beyond the approach followed by the GCMT which determines the source half duration using a scaling law with respect to the seismic moment, and WCMT which determines the centroid time shift as an estimate of the source duration (Duputel *et al.*, 2013).

1.4 Some current challenges

With over 30 years of high quality digital seismic recordings and rapidly growing computing power, seismology has greatly progressed in the past decades. High resolution 3-D

tomographic models (e.g. Ritsema *et al.*, 1999), purely numerical seismic waveform forward modelling tools (Komatitsch and Tromp, 2002a,b) and many advances in fast and robust source model determinations using seismic data (e.g. Kanamori and Rivera, 2008; Vallée *et al.*, 2011; Duputel *et al.*, 2012b) are just a few of the recent achievements in seismology.

Nevertheless, objective validation tests, such as earthquake source blind tests (Mai *et al.*, 2007, 2010) as well as resolution and error analyses (e.g., Ferreira and Woodhouse, 2006; Hjörleifsdóttir and Ekström, 2010; Ferreira *et al.*, 2011) of existing source model techniques are much needed. Indeed, source models for a given earthquake obtained by different authors may show large discrepancies, which need to be understood for meaningful applications of the models. In addition, existing methods use different inversion techniques, such as, least-squares inversions (e.g. Dziewonski and Anderson, 1981; Dziewonski and Woodhouse, 1983; Ekström *et al.*, 2012) which depend on the starting model, or global search techniques over a parameter space using different optimisation schemes, such as, simulated annealing (Hartzell and Liu, 1995), genetic algorithms (Zhou *et al.*, 1995) or the Neighbourhood Algorithm (Sambridge, 1999a) used for example in SCARDEC technique (Vallée *et al.*, 2011). However, despite the various methods for the determination of earthquake source parameters, realistic estimation of uncertainties is still not a routine process, apart from a few exceptions (e.g. Vallée *et al.*, 2011).

As discussed previously, while body and surface waves have been extensively used in earthquake source studies, normal mode data have received less attention. However, various studies e.g. of the 2004 Sumatra-Andaman M_w 9.3 earthquake (Park *et al.*, 2005; Stein and Okal, 2005; Tsai *et al.*, 2005) have highlighted the importance of using normal modes to study large magnitude ($M_w > 8.0$) seismic sources (Tanimoto *et al.*, 2012), notably to characterise their magnitudes. Moreover, successful determinations of bulk rupture characteristics by using the gravest free oscillations (0–1 mHz, Lambotte *et al.*, 2006, 2007) further validated results obtained using different seismic data types as well as geodetic observations (e.g. Tsai *et al.*, 2005; Ishii *et al.*, 2005; Walker *et al.*, 2005). Ultra low-frequency normal modes (0–1 mHz) being closer to the static deformation limit than to any other seismic data, have the potential to help bridging the gap between geodetic (e.g., Delouis *et al.*, 2010) and traditional seismic data (e.g., Ekström *et al.*, 2012)

estimates.

1.5 Motivation and Thesis outline

The goal of this thesis is to study the source parameters of large magnitude earthquakes ($M_w \geq 7.5$) which often occur in subduction zones, are characterised by complex rupture and can excite significant tsunamis which cause serious damage and fatalities. A specific kind of seismic data, the Earth's normal modes, which are standing waves produced by the constructive interference of long-period surface waves, was extremely well recorded by very broadband seismometers after the occurrence of the giant 26 December 2004 Sumatra-Andaman earthquake and enabled for the first time the observation that standard and routine techniques, such as the Global Centroid Moment Tensor technique (GCMT), underestimated the earthquake's magnitude as a result of slow slip (e.g., Park *et al.*, 2005; Stein and Okal, 2005). This observation motivated a number of low-frequency normal mode studies which either focused on the spatio-temporal characterisation of seismic sources (e.g., Lambotte *et al.*, 2006, 2007), or to the identification of afterslip (e.g., Tanimoto *et al.*, 2012; Okal *et al.*, 2012). However, the full potential of low-frequency normal mode data for earthquake source studies is not entirely explored yet.

In the first part of the thesis, independent and comprehensive validation tests of a new fully automated body wave technique, called SCARDEC (Vallée *et al.*, 2011), are carried out using normal mode data as a forward modelling tool in order to assess its overall robustness. The use of body wave data further enabled the assessment of the SCARDEC dip angles which are systematically found steeper in comparison with a standard and well accepted technique, such as the GCMT. Moreover, other constraints such as the global subduction zone model Slab1.0 (Hayes *et al.*, 2012) were used to validate our findings.

In the second part of the thesis, a novel normal mode inversion technique for the simultaneous determination of source parameters (strike, dip, rake, M_w) and spatio-temporal characteristics (rupture duration and length) of unilateral rupture earthquakes was developed in order to examine the resolution of ultra low-frequency (0–1 mHz) normal mode data for earthquake source characterisations. The technique uses the Neighbourhood Algorithm (Sambridge, 1999a) as an optimisation scheme, which enables the systematic

calculation of source parameter uncertainties and the identification of tradeoffs. Extensive synthetic tests were carried out showing that the technique is robust and can be used in real earthquake applications, which validated previous results on the M_w 9.3, 2004 Sumatra-Andaman earthquake (e.g., Park *et al.*, 2005; Stein and Okal, 2005; Tsai *et al.*, 2005; Lambotte *et al.*, 2006, 2007) and offered the first finite source model for the M_w 9.1, 2011 Tohoku earthquake, obtained from ultra low-frequency normal mode data, suggesting that the Earth's free oscillations are a complementary data set for robust source characterisations of large magnitude earthquakes.

Chapter 2 covers theoretical aspects of the forward modelling methods underpinning this thesis. Normal mode theory for 1-D and 3-D Earth models as well as the spectral element method are briefly presented.

In Chapter 3 a broad earthquake source model validation test is carried out using results from the SCARDEC earthquake source catalogue. Twenty-two thrust subduction zone, shallow earthquakes ($M_w \geq 7.5$) with substantial differences between SCARDEC dip angles and dip angles in existing earthquake catalogues are examined in detail.

Chapter 4 presents the theoretical basis, numerical implementation and synthetic tests of a new normal mode grid search technique for the simultaneous determination of earthquake source parameters and bulk spatio-temporal rupture characteristics of large magnitude ($M_w > 8.0$) unilateral rupture earthquakes. Four artificial earthquakes based on real earthquakes are used to extensively test the robustness of the technique.

In Chapter 5 we present new source models for six global earthquakes obtained by applying the technique presented in Chapter 4 to real data. Specifically, we study the Sumatra-Andaman earthquake (26 December 2004, M_w 9.3), the Nias, Sumatra earthquake (28 March 2005, M_w 8.6), the Bengkulu, Sumatra earthquake (12 September 2007, M_w 8.5), the Tohoku earthquake (11 March 2011, M_w 9.1), the recent Okhotsk Sea earthquake (24 May 2013, M_w 8.3) and the Maule, Chile earthquake (27 February 2010, M_w 8.8).

Finally, in Chapter 6 we discuss and summarise the main points and key findings of this thesis, and outline possible future work.

Chapter 2

Forward modelling of normal mode, body and surface waves: Theoretical background

2.1 Summary

This Chapter gives a brief presentation of the theoretical basis of the forward modelling methods used in this thesis. We start by discussing the basics of normal mode theory for a Spherical, Non-Rotating, Elastic, Isotropic (SNREI) Earth model. We discuss both classical methods for the calculation of theoretical seismograms such as normal mode summation techniques, as well as more recent purely numerical methods, notably the Spectral Element Method (SEM).

Starting from a SNREI Earth model, we then consider the case where perturbations are added due to the Earth's rotation, ellipticity and 3-D mantle structure using a Higher Order Perturbation Theory (HOPT) approach. Specifically, we use the HOPT package developed by Lognonné (1991); Clévédé and Lognonné (2003) to calculate realistic normal mode spectra and we examine by forward modelling the importance of the mode coupling scheme (self-coupling versus full-coupling) for ultra long-period normal modes in the frequency range of 0–1.3 mHz. Even though we only find minor differences between these coupling schemes for the data considered, a full coupling scheme is favoured for completeness.

Furthermore, we examine the effect of lateral heterogeneity on theoretical normal mode spectra. We calculate a set of theoretical spectra taking into account the Earth's rotation and ellipticity, for the 1-D PREM model, and a set of synthetic spectra where Earth's rotation, ellipticity and 3-D mantle structure are taken into account, notably using the mantle model SAW12D (Li and Romanowicz, 1996). As expected, we do not observe a strong effect of the lateral heterogeneity on the ultra low-frequency normal mode amplitude spectra, but the phase spectra can show some important effects.

2.2 Normal modes of the Earth

As briefly explained in Chapter 1, the normal modes of the Earth can be considered as a superposition of long-period body waves and surface waves that travel in opposite directions in the Earth. An example referring to surface waves is given in Figure 2.1. Their constructive interference generates standing waves, which correspond to the normal modes of the Earth.

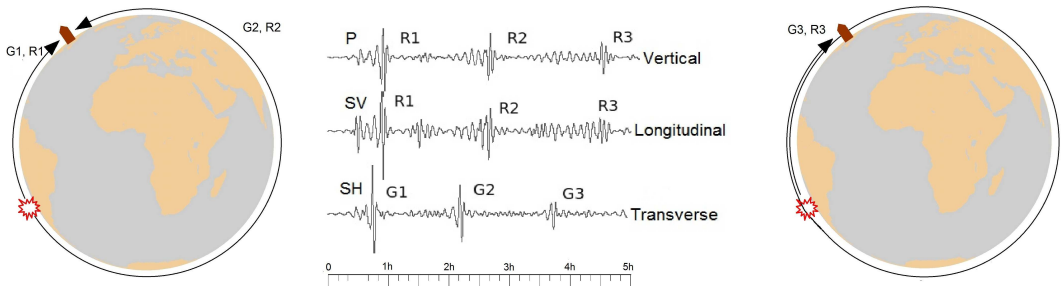


Figure 2.1: Minor and major-arc surface waves that circle the Earth and a three-component seismogram, filtered between 350 s and 150 s, with the seismic wave arrivals for the $M_w = 8.0$ Peru 2007 earthquake. The source is represented as an explosion and the station Flin Flon, Canada (FFC) as a house. R_N and G_N refer to Rayleigh and Love surface waves, respectively. $N=1$ corresponds to minor-arc path, $N=2$ corresponds to major-arc path and $N=3$ involves one great-circle path followed by a minor-arc.

Here, we give a brief introduction to normal mode theory. Full details can be found, e.g., in Woodhouse (e.g., 1996); Dahlen and Tromp (e.g., 1998); Stein and Wysession (e.g., 2003); Lay and Wallace (e.g., 1995); Aki and Richards (e.g., 2002).

In order to represent a seismic source we introduce a body force distribution F . The equation of motion can then be written:

$$(\mathcal{H} + \rho^0 \partial_t^2)u = F, \quad (2.1)$$

where ρ^o is the initial density, ∂_t denotes the partial differentiation with respect to time, \mathcal{H} is a integro-differential operator involving elastic and gravitational effects and u is the elastic displacement field. Taking the Fourier transform of the homogeneous ($F=0$) equation 2.1 ($(\mathcal{H} - \rho^o\omega^2)\bar{u} = 0$) and for a given Earth model, we represent the solution in terms of eigenfrequencies ω_k and eigenfunctions s_k , satisfying:

$$\mathcal{H}s_k = \rho^o\omega_k^2 s_k, \quad (2.2)$$

where $k = 1, 2, \dots, \infty$. The general solution of the form:

$$u(x, t) = e^{i\omega_k t} s_k(x). \quad (2.3)$$

satisfies then the homogeneous ($F=0$) equation 2.1. These are called normal modes or free oscillations of the Earth. Since the eigenfunctions that are associated to different eigenfrequencies are orthogonal (e.g., Dahlen and Tromp, 1998), the displacement field $u(x, t)$ solution of the equation 2.1 can be expressed as a superposition of eigenfunctions, where a_k is the attenuation constant of the k^{th} eigenfunction:

$$u(x, t) = \sum_k a_k(t) s_k(x). \quad (2.4)$$

In spherical coordinates (r, θ, ϕ) the displacement field of a SNREI Earth can be expressed in terms of three radial eigenfunctions ${}_n U_l$, ${}_n V_l$ and ${}_n W_l$ and a set of fully normalized spherical harmonics Y_l^m (Edmonds, 1960):

$$Y_l^m(\theta, \phi) = (-1)^m \left[\frac{(2l+1)(l-m)!}{4\pi(l+m)!} \right]^{1/2} P_l^m(\cos\theta) e^{im\phi}, \quad (2.5)$$

where $P_l^m(x)$ are the associated Legendre functions, l is the angular order and m is the azimuthal order. Following Gilbert and Dziewonski (1975) and Woodhouse and Girnius (1982) we can write the displacement field as:

$$u(r) = {}_n U_l(r) Y_l^m(\theta, \phi) \hat{r} + {}_n V_l(r) \nabla_1 Y_l^m(\theta, \phi) - {}_n W_l(r) \hat{r} \times \nabla_1 Y_l^m(\theta, \phi), \quad (2.6)$$

where ∇_1 is the tangential gradient operator on a unit sphere.

For a SNREI Earth model the eigenfrequencies and eigenfunctions are calculated by solving equation 2.2 subject to the corresponding boundary conditions. In general, we can identify four different kinds of conditions. First, we consider the free surface. This can be the outer surface of the solid Earth and the ocean floor, where the traction vanishes. Second, we consider a solid-solid interface such as the boundary between the upper and lower mantle at 670 km depth, where no slip is allowed upon the interface. Third, we can consider a fluid-solid boundary such as the inner-core boundary or the core-mantle boundary, where only tangential slip is allowed. Fourth, the gravitational potential vanishes at infinity. In a similar manner, eigenfrequencies and eigenfunctions can be calculated for a spherical, non-rotating, anelastic and isotropic Earth model (SNRAI). A detailed analysis can be found, e.g., in Dahlen and Tromp (1998).

There are two different types of normal modes, the spheroidal modes resulting from the constructive interference of Rayleigh surface waves and the coupling between P and SV body waves, and the toroidal modes including Love surface waves and SH body waves. In the case of a SNREI Earth we use a standard notation ${}_nS_l$ for the spheroidal modes and ${}_nT_l$ for the toroidal modes. Each mode is described by its radial order or overtone number n and the angular order l . The radial order $n=0$ corresponds to the fundamental mode branch, and all $n \geq 1$ are the overtones. The radial order represents the number of nodes in the radial direction, while the angular order represents the number of nodes at the Earth's surface (see Figure 2.2). In a rotating Earth each mode (or multiplet) splits into $2l + 1$ singlets, which are described by the azimuthal order m which ranges in $-l \leq m \leq l$. Hence, each singlet has its own eigenfrequency ${}_n\omega_l^m$.

Following Gilbert and Dziewonski (1975), Stein and Geller (1977) and Woodhouse and Girnius (1982), the displacement that corresponds to spheroidal modes only is described by equation 2.7 as a particular case of equation 2.6:

$$\begin{aligned}
 u^S(r, \theta, \phi) &= \sum_n \sum_l \sum_{m=-l}^l {}_nA_l^m [{}_nU_l(r)R_l^m(\theta, \phi) + {}_nV_l(r)S_l^m(\theta, \phi)] e^{i{}_n\omega_l^m t} \\
 R_l^m &= (Y_l^m, 0, 0) \\
 S_l^m &= \left(0, \frac{\partial Y_l^m(\theta, \phi)}{\partial \theta}, \frac{1}{\sin \theta} \frac{\partial Y_l^m(\theta, \phi)}{\partial \phi} \right),
 \end{aligned} \tag{2.7}$$

where ${}_nA_l^m$ is the excitation amplitude of each mode, depending on the seismic source. R_l^m and S_l^m are surface eigenfunctions in spherical coordinates. The spheroidal modes

include both radial and horizontal displacement and they can be observed in vertical, longitudinal and transverse components. In case where there is only radial displacement ($l=0$) this subgroup of spheroidal modes is called radial modes.

The toroidal modes include only horizontal displacement and they can be recorded in the transverse component. However, in a rotating Earth, toroidal modes can be observed in vertical component data too, because of spheroidal-toroidal Coriolis coupling (e.g., Resovsky and Ritzwoller, 1998; Zürn *et al.*, 2000; Dahlen and Tromp, 1998; Rogister, 2003). The splitting and coupling of normal modes will be briefly described in section 2.5.2. Similarly to equation 2.7, the toroidal modes displacement for a SNREI Earth model is expressed by:

$$u^T(r, \theta, \phi) = \sum_n \sum_l \sum_{m=-l}^l {}_n A_l^m {}_n W_l(r) T_l^m(\theta, \phi) e^{i_n \omega_l^m t} \quad (2.8)$$

$$T_l^m = \left(0, \frac{1}{\sin \theta} \frac{\partial Y_l^m(\theta, \phi)}{\partial \phi}, -\frac{\partial Y_l^m(\theta, \phi)}{\partial \theta} \right),$$

where T_l^m is the surface eigenfunction for toroidal modes.

In Figure 2.2 we illustrate some examples of normal modes. On top we show the ${}_0 S_0$ and ${}_1 S_0$ radial modes. The ${}_0 S_0$ mode is also known as the breathing mode and involves radial displacement of the whole Earth as a compression and dilatation. ${}_1 S_0$ mode has an internal surface of zero motion separating the Earth in two parts, which move inward and outward in opposite directions. In the middle we show the ${}_0 S_2$ and ${}_0 S_3$ spheroidal modes. The ${}_0 S_2$ mode is also called the football mode since it alternates between a prolate and an oblate, having two nodal points at each hemisphere, while ${}_0 S_3$ has three nodal points, and so on. At the bottom, the ${}_0 T_2$ and ${}_0 T_3$ toroidal modes are shown. The ${}_0 T_2$ mode corresponds to twisting of the Earth such that the northern hemisphere moves clockwise and the southern counterclockwise, having a nodal surface, while ${}_0 T_3$ has two nodal surfaces, and so successively.

It must be mentioned that no ${}_0 S_1$ mode exists since it would correspond to a lateral shift of the planet, which can happen only in the presence of an external force. The ${}_0 T_1$ mode does not exist either since it cannot have any nodal surfaces and it would correspond to a rigid body rotation of the inner core and mantle. In a similar way, ${}_0 T_0$ has no physical meaning as it should involve radial displacement, which does not exist for toroidal modes. Finally, the existence of the ${}_1 S_1$ mode, also called the Slichter mode (Slichter, 1961), is

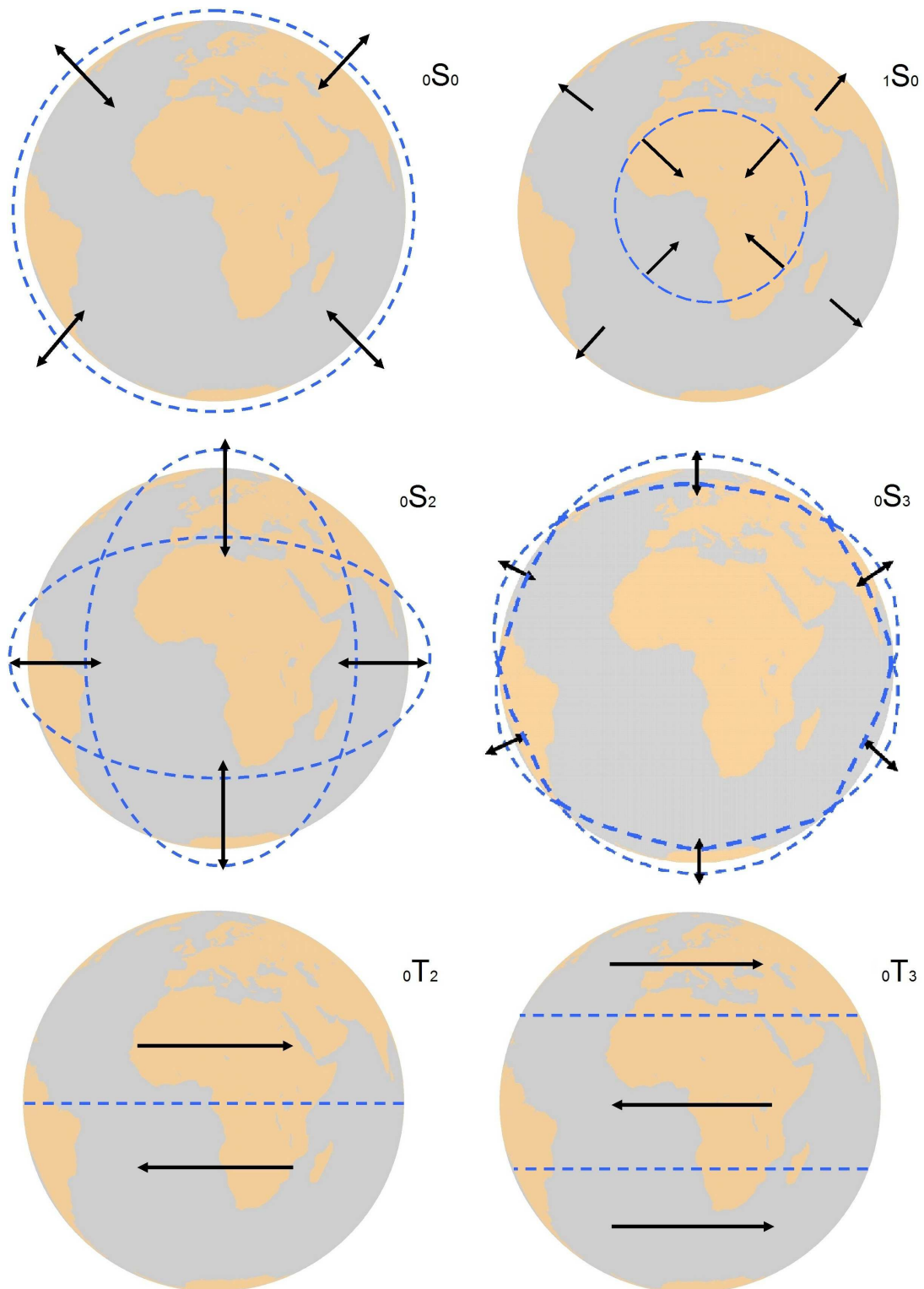


Figure 2.2: A cartoon illustrating the different types of normal modes. Radial modes (top) ${}_0S_0$ (or so-called the breathing mode) and ${}_1S_0$ involve only radial displacement. Spheroidal modes (middle) ${}_0S_2$ (or so-called the football mode) and ${}_0S_3$ involve both radial and horizontal displacement. Toroidal modes (bottom) ${}_0T_2$ and ${}_0T_3$ involve only horizontal displacement.

predicted in theory, but it has never been clearly observed. Its motion corresponds to a rigid translation of the solid inner core with respect to the fluid outer core and the mantle.

For all the existing normal modes within a frequency range, whose eigenfrequencies and eigenfunctions can be easily calculated for a given SNREI Earth model, a plot of their eigenfrequencies against their angular order lead to a dispersion diagram. For the PREM model (Dziewonski and Anderson, 1981) shown in Figure 2.3, the corresponding degenerate eigenfrequencies of the normal modes are plotted as distinct points in the dispersion diagrams in Figure 2.4. These dispersion diagrams can be very useful to relate normal modes with propagating seismic waves.

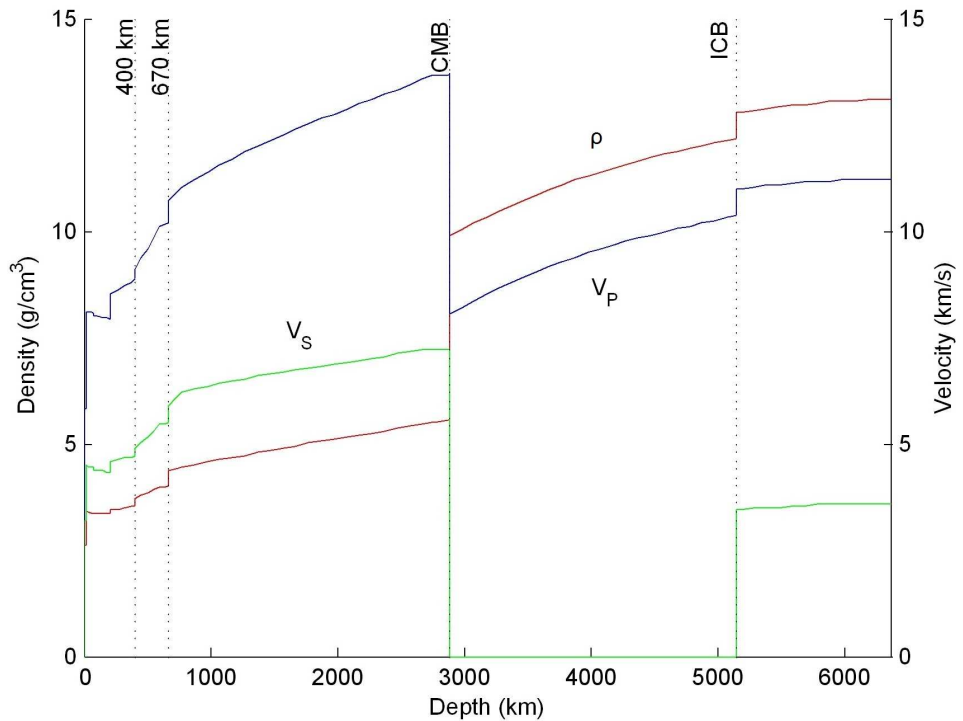


Figure 2.3: The Preliminary Reference Earth Model (PREM) of Dziewonski and Anderson (1981). Density (ρ), compressional (V_P) and shear (V_S) wave velocity variations with depth are indicated in red, black and green, respectively. Transition zone (400–670 km), core-mantle (CMB) and inner-core boundaries (ICB) are highlighted.

In the spheroidal dispersion diagram (Figure 2.4, left) the fundamental branch (labelled in green with a 0) with angular order greater than about 20 corresponds to fundamental Rayleigh surface waves. As both radial and angular order increase, the overtone branches correspond to higher Rayleigh wave overtones, referring to the upper right part of the diagram. However, the middle and the left parts of the diagram correspond to SV and P seismic waves. In particular, the modes to the left with low angular order (0–10)

correspond to P wave core phases (P_cP , PKP , $PKiKP$), while those slightly to the right are related with mantle P waves ($20 \leq l \leq 30$). These two groups are separated by the core diffracted phase (P_{diff}). Because of the lower shear velocity, the S wave phases are plotted to the centre of the diagram ($30 \leq l \leq 70$) and in particular, the core phases are plotted to the left (S_cS , SKS), while the core diffracted phase (SV_{diff}) are plotted between the latter and the SV direct waves.

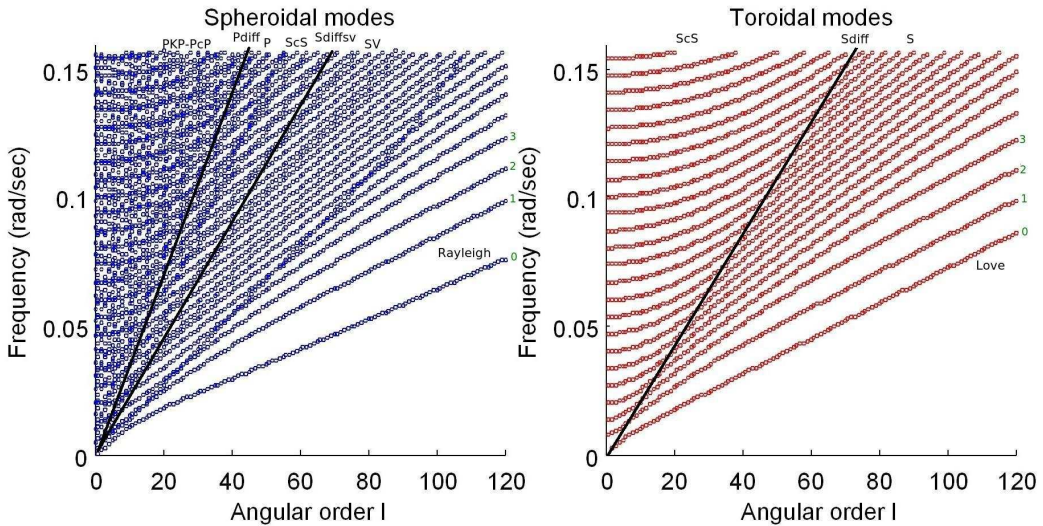


Figure 2.4: Dispersion diagrams for spheroidal (left) and toroidal (right) modes. The degenerate eigenfrequencies for the PREM model are plotted as small circles for angular order up to $l=120$. The fundamental mode, 1st, 2nd and 3rd overtone branches are indicated by the green labels on the right. The corresponding seismic travelling waves are indicated in black (see main text for more details).

In the toroidal dispersion diagram, things are slightly simpler. Similarly to the spheroidal mode dispersion diagram, the fundamental Love surface waves correspond to the fundamental mode branch (labelled with a 0) for angular order greater than about 20. The higher mode branches correspond to overtone Love waves plotted in the upper right part of the diagram. The toroidal modes involve only SH body waves. In particular, the middle part of the diagram corresponds to mantle SH phases, while the left part involves core phases separated to the right by the core diffracted phase (SH_{diff}).

The spheroidal fundamental modes include energy in the whole mantle for up to angular order $l \sim 12$. For higher angular order (i.e., for shorter wave periods), the fundamental spheroidal mode energy is concentrated towards the upper mantle and crust. Similarly, the toroidal fundamental modes include energy in the whole mantle for up to angular order $l \sim 7$. On the other hand, spheroidal modes can also sample the outer core and, in some

cases, the inner core of the Earth.

2.3 Normal mode summation for a SNREI model

Once we have calculated the eigenfrequencies and the eigenfunctions for a SNREI Earth model, it follows from equation 2.4 that we can represent the ground displacement in a simpler form as a summation of the normal modes in a representation of spherical harmonics (Woodhouse and Girnius, 1982). For all k modes, where $k=(l, n)$, the ground displacement u at the receiver x_r over time t , excited by an earthquake at location x_s and characterised by a seismic moment tensor M is given by:

$$u(x_r, t) = \sum_k M : \epsilon_k(x_s) s_k(x_r) e^{i\omega_k(1+i/2Q_k)t}, \quad (2.9)$$

where s_k are the normal mode eigenfunctions that correspond to ω_k eigenfrequencies, Q_k is the quality factor of each mode and ϵ is the symmetric strain tensor, where $\epsilon = \frac{1}{2}[\nabla u + \nabla u^T]$.

In order to calculate a theoretical seismogram, we have to account for the recording instrument too. If the latter is represented as a unit vector v , in the direction of motion sensed by the instrument (v_r, v_θ, v_ϕ) also incorporating an operator characterising the instrument's response, the theoretical seismogram can then be expressed by a summation involving two terms, the source $S_k(\theta_s, \phi_s)$ and the receiver $R_k(\theta_r, \phi_r)$ terms:

$$v \cdot u = \sum_k R_k(\theta_r, \phi_r) S_k(\theta_s, \phi_s) e^{i\omega_k(1+i/2Q_k)t}. \quad (2.10)$$

The source term in equation 2.10 involves the scalar radial eigenfunctions U, V and W evaluated at the source depth and the six elements of the moment tensor. The receiver term involves the scalar radial eigenfunctions U, V and W evaluated at the Earth's surface (at the receiver's location). In both cases, the scalar eigenfunctions are expressed using spherical harmonics evaluated at the source and the receiver, respectively. For more details, the reader is referred to Woodhouse and Girnius (1982); Woodhouse (1996); Dahlen and Tromp (1998).

2.4 Normal modes of a rotating, anelastic, elliptical laterally heterogeneous Earth

In this section we briefly present some key formulae and concepts related to the normal modes of a rotating, anelastic, laterally heterogeneous Earth, which will be used in the next section to discuss how to calculate theoretical seismograms in such media. We will use the Dirac "Bra" ($\langle \alpha |$) and "Ket" notation ($|\alpha \rangle$), originally introduced in quantum mechanics, as it is a concise representation useful for perturbation theory. The symbol $\langle \alpha | \beta \rangle$ represents a complex number which is equal to the inner product of the "Ket" $|\alpha \rangle$ with $|\beta \rangle$. According to the latter definition $\langle \alpha | \beta \rangle = \langle \beta | \alpha \rangle^*$, where $*$ denotes complex conjugate. According to Woodhouse and Dahlen (1978), the motion of a rotating, elastic Earth is described by:

$$\partial_t^2 |u(t)\rangle - iB\partial_t |u(t)\rangle + A|u(t)\rangle = |F(t)\rangle \quad (2.11)$$

where $|u(t)\rangle$ is the displacement field, B is the Coriolis operator describing Earth's rotation, A is the corresponding elasto-dynamic operator accounting the effects of lateral heterogeneity, Earth's shape and interfaces, and $F(t)$ is the equivalent body force. Taking the Fourier-Laplace transformation, where the complex frequency due to real frequency ω and attenuation rate α is:

$$\sigma = \omega + i\alpha, \quad (2.12)$$

the equation 2.11 for an anelastic, physical dispersive and rotating Earth can now be expressed as:

$$-\sigma^2 |u(\sigma)\rangle + \sigma B|u(\sigma)\rangle + A(\sigma)|u(\sigma)\rangle = |F(\sigma)\rangle. \quad (2.13)$$

Since the elasto-dynamic operator is symmetric and the Coriolis operator is anti-symmetric (Lognonné, 1991), in order to account for rotation and anelasticity we need to go beyond the elastic self-adjoint case and introduce a duality relation of the normal mode eigenproblem and that obtained by simply reversing the Earth's rotation. The eigenfunctions

s_k , their duals s'_k and the associated eigenfrequencies σ_k are given by:

$$\begin{aligned} -\sigma_k^2|s_k\rangle + \sigma_k B|s_k\rangle + A(\sigma_k)|s_k\rangle &= 0 \\ -\sigma_k^2\langle s'_k| + \sigma_k \langle s'_k|B^\dagger + \langle s'_k|A^\dagger(\sigma_k) &= 0, \end{aligned} \quad (2.14)$$

where the † symbol denotes the dual operator, defined as:

$$\begin{aligned} \langle s'|Bs\rangle &= -\langle B^\dagger s'|s\rangle \\ \langle s'|As\rangle &= \langle A^\dagger s'|s\rangle. \end{aligned} \quad (2.15)$$

The eigenfunction s'_k and the eigenfrequency σ_k describe a mode of the "anti-Earth" if and only if s_k and σ_k is a mode of the actual Earth. Hence, the second equation in 2.14 can be written as:

$$-\sigma_k^2|s'_k\rangle - \sigma_k B|s'_k\rangle + A(\sigma_k)|s'_k\rangle = 0 \quad (2.16)$$

showing that the eigenfrequencies of the Earth are independent of the direction of rotation. In order to solve equation 2.13 for a laterally heterogeneous Earth and obtain the displacement caused by an earthquake described by an equivalent body force, it is necessary to compute both the normal modes and their duals (Lognonné, 1991). This can be done using perturbation theory, as outlined in the following section.

2.5 Higher Order Perturbation Theory (HOPT)

As discussed in the previous sections, realistic normal mode modelling requires the consideration of a number of effects, such as the effect of the Earth's rotation, ellipticity, lateral heterogeneities and anelasticity. One of the first approaches used to tackle these issues was to use degenerate perturbation theory that considered only isolated multiplets (e.g. Backus and Gilbert, 1961; Madariaga, 1972; Dahlen, 1974; Woodhouse and Girnius, 1982), or quasi-degenerate perturbation theory taking into account coupling within a multiplet (e.g. Woodhouse, 1983; Dahlen, 1987). A different approach, which is considered one of the most accurate, is the use of variational or Galerkin methods (Park and Gilbert, 1986). However, their use can be very demanding in terms of computational power (Lognonné and Romanowicz, 1990). On the other hand, normal mode higher order perturbation theory has been introduced by Lognonné and Romanowicz (1990) in the case

of the elastic Earth and it has been shown that it leads to very accurate results with respect to a variational method (Morris *et al.*, 1987). The general formulation can be expressed in terms of a Hamiltonian operator as:

$$\sigma^2|s\rangle = (H_o + \delta H(\sigma_k))|s\rangle, \quad (2.17)$$

where σ is the complex eigenfrequency, s is the eigenfunction, $H_o = A_o(\sigma_o)$ is the Hamiltonian associated with a SNREI model, with A_o standing for the corresponding elasto-dynamic operator and σ_o being the eigenfrequency for the SNREI model. Taking into account the effects of rotation, 3-D mantle structure and anelasticity, it can be shown that the Hamiltonian associated with the system's perturbations is given by:

$$\delta H(\sigma_k) = -\sigma_o^2 \delta K + \sigma_o B + A(\sigma_k) - A_o(\sigma_o), \quad (2.18)$$

where δK is the perturbation in density.

Starting from a SNREI or SNRAI Earth model for which the eigenfunctions and eigenfrequencies can be computed following, e.g., Tromp and Dahlen (1990), as briefly explained previously, the problem for the actual Earth ($|s_k\rangle$) and the "anti-Earth" ($|s'_k\rangle$) can be described in terms of perturbation theory as (Woodhouse and Dahlen, 1978):

$$\begin{aligned} \sigma_k^2|s_k\rangle &= H(\sigma_k)|s_k\rangle \\ \sigma_k^2|s'_k\rangle &= \hat{H}(\sigma_k)|s'_k\rangle, \end{aligned} \quad (2.19)$$

where k denotes a singlet, and H and \hat{H} are the Hamiltonian operators of the actual Earth and the "anti-Earth", respectively. The perturbations in eigenfrequencies and eigenfunctions can be expanded in terms of series as:

$$\begin{aligned} \sigma_k &= \sigma_{ok} + \delta_1 \sigma_k + \delta_2 \sigma_k + \dots \\ |s_k\rangle &= |s_k^{(o)}\rangle + |s_k^{(1)}\rangle + |s_k^{(2)}\rangle + \dots \\ |s'_k\rangle &= |s'_k^{(o)}\rangle + |s'_k^{(1)}\rangle + |s'_k^{(2)}\rangle + \dots, \end{aligned} \quad (2.20)$$

where σ_{ok} is the spherical frequency of eigenfunction k , $\delta_n \sigma_k$ is the n^{th} -order perturbation in the eigenfrequency, $|s_k^{(n)}\rangle$ is the n^{th} -order perturbation of the eigenfunction and $|s'_k^{(n)}\rangle$ is the n^{th} -order perturbation of the dual eigenfunction.

Lognonné (1991) showed that by substituting the expansions in Equation 2.20 as well as an expansion of the δH operator into Equation 2.17, we can obtain separate equations that can be solved iteratively for the eigenfrequencies and eigenfunctions associated with each perturbation order. In order to calculate such perturbed modes, one needs to know in particular the various quantities $\langle s_q^{(0)} | \delta_n H | s_{q'}^{(0)} \rangle$ characterising the coupling between the various spherical singlets $|s_q^{(0)}\rangle$. Hence, so-called coupling matrices (also known as splitting or interaction matrices) that characterise the various effects taken into account in the modelling (e.g., Earth's rotation, ellipticity and/or lateral heterogeneity) have to be calculated using, e.g., the expressions derived by Woodhouse and Dahlen (1978). Once the perturbed modes are calculated and diagonalised, synthetic seismograms can be calculated by mode summation using an expression similar to Equation 2.10, whereby the source (N) and receiver (M) terms only need to be calculated once and for all for each earthquake. Thus, the computation of $N * M$ seismograms need only $N + M$ computational time (Clévédé and Lognonné, 1996; Millot-Langet *et al.*, 2003).

2.5.1 The HOPT package

Using the HOPT package developed by Lognonné and Clévédé (2002), we are able to calculate theoretical normal mode spectra up to the second order in amplitude and up to the third order in frequency using the procedure explained above. In practice, the HOPT package starts by calculating reference eigenfrequencies and eigenfunctions for a spherically symmetric Earth model (SNREI or SNRAI). Then, as explained previously, coupling matrices accounting for the effects of the Earth's rotation, ellipticity and/or lateral heterogeneity are built. Full coupling between different modes in a frequency range of interest is included. For enhanced computational efficiency, the Frobenius norm of each coupling matrix is calculated, which characterises the coupling strength between modes (Millot-Langet *et al.*, 2003). Only modes that show substantial coupling, with Frobenius norm values above a threshold value, are used in the calculations. Subsequently, the perturbed eigenfrequencies and eigenfunctions in Equation 2.20 can be determined, followed by their diagonalisation and, finally, by the calculation of theoretical seismograms by mode summation. The computation of all spheroidal mode perturbed eigenfrequencies

and eigenfunctions in the 0–1 mHz frequency band and their diagonalisation does not require more than one minute of CPU time on a dual processor, six core Intel X5650 2.66 GHz system with 24 GB of RAM. One typical calculation of 240-hr, vertical component synthetic seismograms, for three stations, based on the latter modelling takes less than one minute of CPU time. However, the most demanding part (computationally) is the calculation of interaction matrices which depend on the setup for each application and are built once and for all. In our case, we calculated interaction matrices up to 4 mHz which required approximately one hour of CPU time for the Earth’s rotation and ellipticity effects, and up to six hours of CPU time for the computation of interaction matrices regarding a laterally heterogeneous Earth model.

2.5.2 Normal mode splitting and coupling

In this section we briefly present two effects associated with realistic normal mode modelling, notably the splitting and coupling of the Earth’s free oscillations. We present the causes of these effects and we give their basic mathematical representation. A detailed presentation of the associated theory can be found, e.g., in Woodhouse and Girnius (1982), Ritzwoller *et al.* (1986), Smith and Masters (1989) and Dahlen and Tromp (1998).

As discussed in the previous sections, in the case of a SNREI Earth model, each spheroidal or toroidal multiplet is associated with its degenerate eigenfrequency ω_o . However, the Earth’s rotation, ellipticity and lateral heterogeneity remove this degeneracy and split the multiplets into $2l + 1$ singlets, where l is the angular order. The eigenfrequency perturbation of an isolated mode with respect to the azimuthal order m can be written as:

$$\delta\omega_m = \omega_o(a + bm + cm^2), \text{ with } -l \leq m \leq l, \quad (2.21)$$

where a and c are the ellipticity splitting coefficients and b is the rotational coefficient, accounting for the Coriolis force to first order and the centrifugal force to second order (Dahlen, 1968). Following Woodhouse and Girnius (1982), the displacement field of a rotating, elastic Earth model can be written as:

$$u(t) = \text{Re}[e^{i\omega t} R \cdot e^{iHt} \cdot S] \quad (2.22)$$

where $u(t)$ is the displacement over time t , ω is the frequency, R is the receiver vector and S is the source term. The splitting of a multiplet is described by the $(2l+1) \times (2l+1)$ splitting matrix H which contains all the information about elastic and anelastic lateral heterogeneities:

$$H_{mm'} = \omega_o[(a + bm + cm^2)\delta_{mm'} + \sum \gamma_s^{mm'} c_s^{m-m'} + i \sum \gamma_s^{mm'} d_s^{m-m'}] \quad (2.23)$$

where $-l \leq m \leq l$, $-l \leq m' \leq l$ and s is the degree of heterogeneity, which must be an even number. The $\gamma_s^{mm'}$ are integrals over three spherical harmonics (for details, see Dahlen and Tromp, 1998), $c_s^{m-m'}$ and $d_s^{m-m'}$ are structure coefficients (Ritzwoller *et al.*, 1986; Smith and Masters, 1989). The first term of equation 2.23 describes the splitting due to rotation and ellipticity, the second term accounts for the effects of elasticity and the third term for the anelasticity. The splitting due to the Earth's rotation is symmetric with respect to the degenerate eigenfrequency, similar to the Zeeman splitting which is the effect of splitting a spectral line into several components in the presence of a static magnetic field, first observed on hydrogen atoms. The effect is widely observed in well isolated multiplets, such as ${}_0S_2$ which splits uniformly into five singlets. On the other hand, the splitting due to the Earth's ellipticity is asymmetric, and the spacing of the singlets can be irregular or approximately parabolic, such as in the case of ${}_{11}S_4$ and ${}_{10}S_2$ multiplets. Splitting due to rotation dominates mainly very low-frequency multiplets (up to 1.5 mHz) as a consequence of their vicinity to the Earth's rotation frequency. At higher frequencies, ellipticity and Earth's lateral heterogeneities play a more important role on the splitting of the multiplets. Lower mantle and inner-core sensitive modes, such as ${}_0S_6$, ${}_2S_4$, ${}_3S_2$, ${}_6S_3$ and ${}_{13}S_2$, are anomalously split since their splitting width is substantially larger than that predicted by the effects of rotation and ellipticity alone (Masters and Gilbert, 1981; Ritzwoller *et al.*, 1986). The reasons behind the anomalous splitting are not fully explained, with one of the most accepted reasons being the presence of anisotropy (e.g Woodhouse *et al.*, 1986; Tromp, 1993).

In the previous paragraph we discussed the splitting of an isolated mode based on the so-called self-coupling approximation, which is based on the simplifying assumption that the effects of the Earth's rotation, ellipticity and 3-D structure are only first order effects and that the difference of a given target multiplet to its neighbours is of zeroth

order, which simply states the unperturbed eigenfrequencies and eigenfunctions of a non-rotating Earth model. The self-coupling approximation is only sensitive to even-degree structure and is only a reasonable approximation for well isolated modes, such as for some ultra low-frequency modes ($f < 1$ mHz). Normal mode coupling can be strong when the frequencies of two modes are very close together ($f > 1$ mHz) and in order to account for coupling between such pairs, they must be treated as a quasi-degenerate supermultiplet. The perturbed singlet eigenfunctions (\tilde{s}) in a narrow frequency band can be approximated by hybrid combinations of singlets eigenfunctions (s_k) associated with the multiplets whose coupling we wish to calculate:

$$\tilde{s} = \sum_k q_k s_k \quad (2.24)$$

where q_k are expansion coefficients (Woodhouse, 1980; Park and Gilbert, 1986). Examples of such pairs are the spheroidal-toroidal pairs ${}_0S_{11} - {}_0T_{12}$, ${}_0S_{19} - {}_0T_{20}$ and ${}_0S_{32} - {}_0T_{31}$.

Normal mode coupling can lead to a shift in the degenerate frequency and quality factor of a mode, or, in contrast with the isolated multiplet case, normal modes can be also sensitive to odd-degree structure. There are two main types of normal mode coupling: (i) along-branch coupling, when two modes of the same radial order n and different angular order l are coupled together; and, (ii) cross-branch coupling, in all other cases. Normal mode coupling can be described by coupling matrices, as discussed previously (also known as splitting or interaction matrices) and is controlled by several selection rules (see, e.g., Dahlen and Tromp, 1998). In particular, coupling due to the Earth's rotation and ellipticity is controlled by the following angular degree selection rules:

- Spheroidal – toroidal coupling is caused by Coriolis force effects between multiplets that differ by a single angular degree (${}_nS_l - {}_{n'}T_{l\pm 1}$ and ${}_nT_l - {}_{n'}S_{l\pm 1}$). Examples of normal mode pairs affected by this type of coupling are ${}_0S_{11} - {}_0T_{12}$, ${}_0S_{19} - {}_0T_{20}$ and ${}_0S_{32} - {}_0T_{31}$ (see the example in Figure 2.5);
- Spheroidal – spheroidal and toroidal – toroidal coupling is caused by the Earth's ellipticity, and affects multiplets that differ by two angular degrees (${}_nS_l - {}_{n'}S_{l\pm 2}$ and ${}_nT_l - {}_{n'}T_{l\pm 2}$);

- Coupling between toroidal multiplets of the same angular order is caused by the Earth's ellipticity (${}_nT_l - {}_{n'}T_l$);
- Coupling between spheroidal multiplets of the same angular order is caused by the Earth's rotation and ellipticity (${}_nS_l - {}_{n'}S_l$).

Elastic or anelastic lateral heterogeneities control the coupling between spheroidal and toroidal multiplets, spheroidal – spheroidal or toroidal – toroidal multiplets:

- A multiplet ${}_nS_l$ or ${}_nT_l$ is coupled with a multiplet ${}_{n'}S_{l'}$ or ${}_{n'}T_{l'}$ by lateral heterogeneity of degree s if $|l - l'| \leq s \leq l + l'|$;
- Two spheroidal multiplets ${}_nS_l$ and ${}_{n'}S_{l'}$, or two toroidal multiplets ${}_nT_l$ and ${}_{n'}T_{l'}$ are coupled by lateral heterogeneity of degree s if $l + l' + s$ is even;
- A spheroidal multiplets ${}_nS_l$ is coupled with a toroidal multiplet ${}_{n'}T_{l'}$ by lateral heterogeneity of degree s if $l + l' + s$ is odd.

The first observations of normal mode coupling were reported by Masters *et al.* (1983). They showed that the most dominant reason for spheroidal – toroidal normal mode coupling in the frequency band 1–3 mHz is Coriolis coupling. For frequencies higher than 3 mHz, the effects of lateral heterogeneity become more important. Park (1986) studied Rayleigh – Love surface wave coupling in the time domain and showed that 3-D structure is dominant for frequencies higher than 4.2 mHz. Zürn *et al.* (2000) studied the spheroidal – toroidal coupling in the frequency band of 0–1 mHz and found that Coriolis force strongly controls coupling in this frequency range, leading to toroidal mode signals on the vertical component. Resovsky and Ritzwoller (1998) identified 25 pairs of coupled multiplets in the 0–3 mHz frequency range and showed the importance of cross-coupling in normal mode spectra calculations in the 1.5–3 mHz frequency band. Deuss and Woodhouse (2001) proposed a full-coupling scheme in comparison with self-coupling and group-coupling in the frequency band 0–3 mHz by identifying 33 key pairs of coupled multiplets.

Figures 2.6 and 2.7 show examples of HOPT theoretical normal mode spectra calculations for the 2011 M_w 9.1 Tohoku earthquake based on the GCMT source model for the ${}_1S_3 - {}_3S_1 - {}_2S_2 - {}_0T_5$ and ${}_0S_7 - {}_2S_3 - {}_0T_7 - {}_1T_1$ supermultiplets, respectively. Earth's

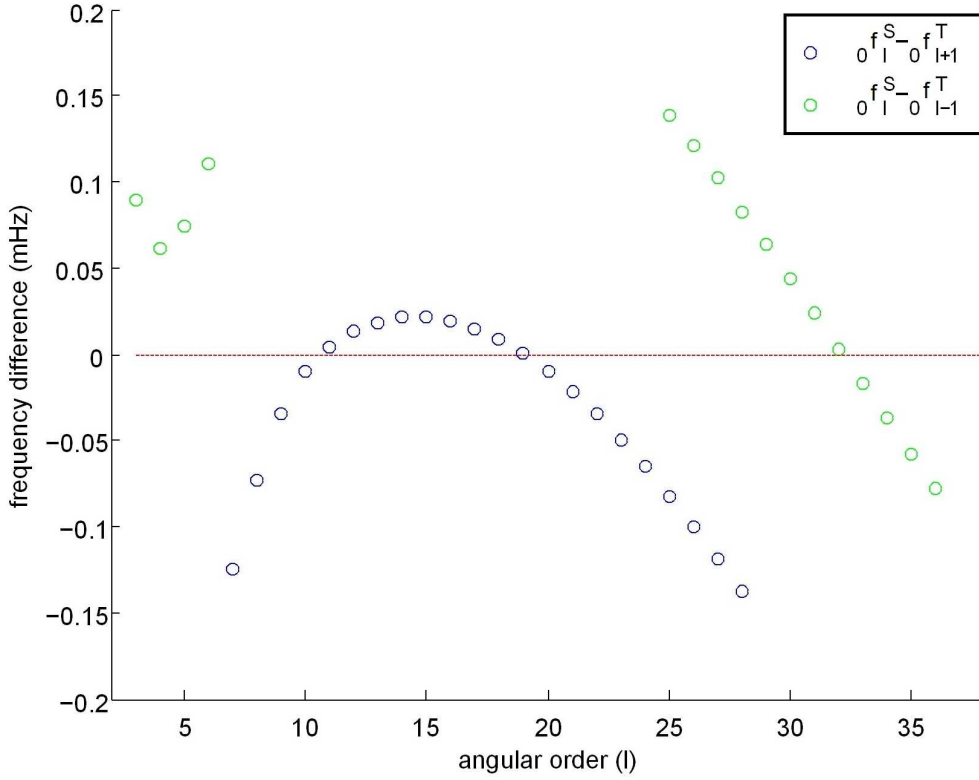


Figure 2.5: PREM degenerate eigenfrequency differences for fundamental spheroidal and toroidal modes. $0f_l^S - 0f_{l+1}^T$ differences are plotted using blue circles, in the range $l = 7 - 28$ and $0f_l^S - 0f_{l-1}^T$ differences are plotted using green circles, in the range $l = 3 - 6$ and $l = 25 - 36$. The strongest coupling is observed for the quasi-degenerate pairs $0S_{11} - 0T_{12}$, $0S_{19} - 0T_{20}$ and $0T_{31} - 0S_{32}$. The main coupling factor is the Coriolis force, due to the Earth's rotation.

rotation, ellipticity and 3-D structure using the SAW12D mantle model are taken into account in the calculations, using a self-coupling scheme and a full-coupling scheme in the frequency band 0–1.3 mHz. Full-coupling involves all modes in this frequency range. As explained in section 2.5.1. for each coupling matrix, its Frobenius norm is calculated, which characterises the coupling strength between modes. In order to speed up our calculations, we only use modes that are significantly coupled, using the Frobenius norm as criterion by setting a Frobenius cut-off equal to 10^{-2} . Observed spectra is also plotted in Figures 2.6 and 2.7 for reference. The two different coupling schemes do not show any substantial differences in the spectra fit, however, the full-coupling scheme is favoured for completeness and will be used in the normal mode forward modelling carried out in Chapters 4 and 5.

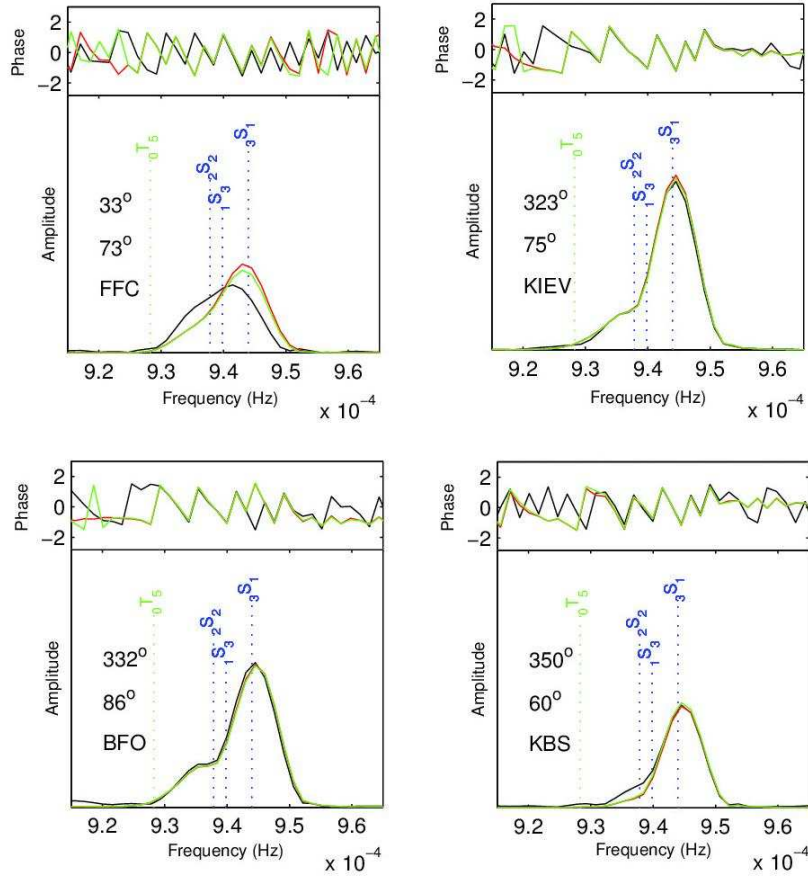


Figure 2.6: Vertical component acceleration data amplitude and phase spectra (black) for the multiplet $1S_3 - 3S_1 - 2S_2$ compared to GCMT synthetic amplitude and phase spectra calculated using a self-coupling scheme (red) and a full-coupling scheme (green) for the 2011 Tohoku earthquake. Earth's rotation, ellipticity and 3-D structure (SAW12D) are taken into account in the theoretical spectra calculations. The time window of the time series used is 12–90 hr after the earthquake's occurrence time. Station azimuths, epicentral distances and station names are shown in the left hand side of each diagram.

2.5.3 The effect of 3-D Earth structure

Normal modes below 1.5 mHz are very sensitive to lower-mantle structure where shear velocity lateral heterogeneities are not very strong compared to upper-mantle structure (Figure 2.8). For higher frequency fundamental modes and overtones, excitation kernels can show a strong sensitivity to upper-mantle structure (see, e.g. Dahlen and Tromp, 1998).

Figure 2.9 compares HOPT theoretical normal mode spectra in the frequency range of 0–1 mHz for the 2011 M_w 9.1 Tohoku earthquake calculated using both PREM (red) and the mantle model SAW12D (green). Observed spectra (black) is also shown for reference. There are only some very slight differences in amplitude between the spectra calculated

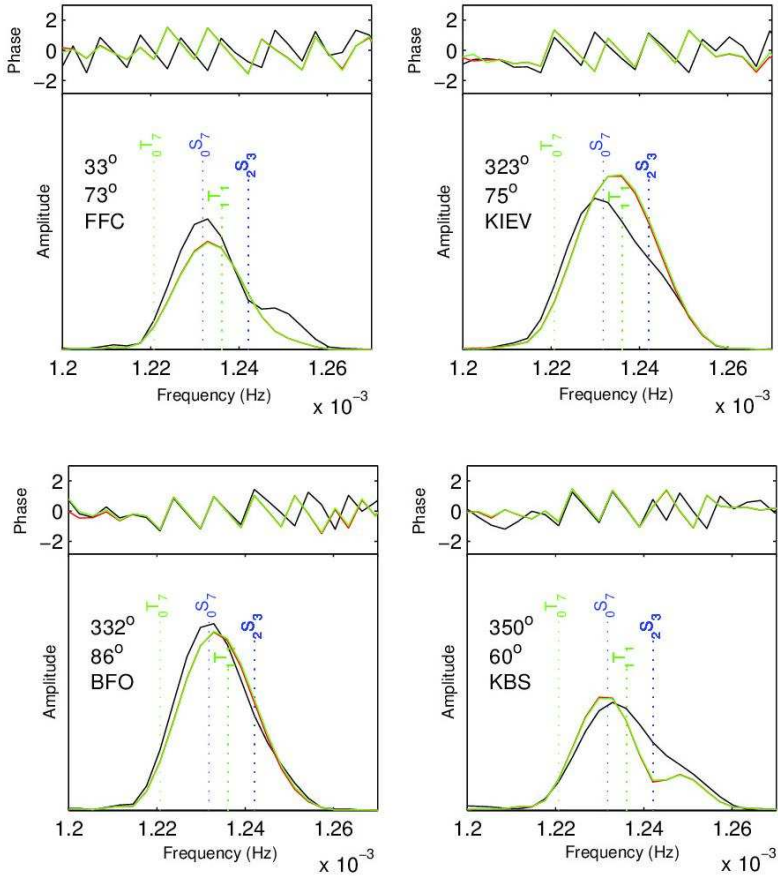


Figure 2.7: Vertical component acceleration data amplitude spectra and phase in radians (black) for the multiplet ${}_0S_7 - {}_2S_3$ compared to GCMT synthetic amplitude spectra and phase calculated using a self-coupling scheme (red) and a full-coupling scheme (green) for the 2011 Tohoku earthquake. Earth's rotation, ellipticity and 3-D structure (SAW12D) are taken into account in the theoretical spectra calculations. The time window of the time series used is 5–45 hr after the earthquake's occurrence time. Station azimuths, epicentral distances and station names are shown in the left hand side of each diagram.

using PREM and SAW12D, with both theoretical spectra showing an excellent agreement with the observed amplitude spectra. The most substantial differences occur only for higher frequency modes such as for the ${}_1S_3 - {}_3S_1$ supermultiplet, with PREM synthetics showing systematically larger amplitudes. On the other hand, discrepancies in phase spectra between synthetics built using 1-D and 3-D Earth structure are more significant, even for the lower frequency modes.

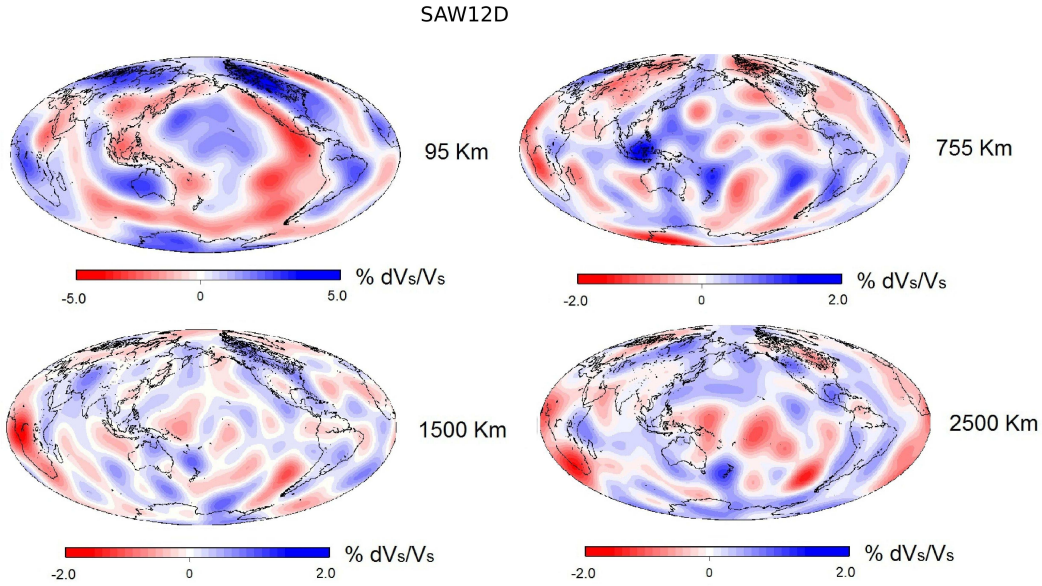


Figure 2.8: 3-D SH mantle model SAW12D for four different depth slices (95 km, 755 km, 1500 km, 2500 km). The blue colour indicates areas where the shear wave velocity is higher than the average, while the red colour indicates areas where the shear wave velocity is lower, expressed as a percentage of perturbation from PREM.

2.6 Spectral element method

While normal mode forward modelling techniques have now been used in seismology for over 30 years, accurate purely numerical methods have only been used in global seismology since relatively recently. One example of such purely numerical technique is the Spectral Element Method (SEM), which was first used in the 80's in fluid dynamics simulations (Patera, 1984). However, it was in the 90's that the method was introduced in 2-D (Seriani *et al.*, 1992; Cohen *et al.*, 1993; Priolo *et al.*, 1994) and in 3-D earthquake simulations (Faccioli *et al.*, 1997; Komatitsch and Vilotte, 1998; Seriani, 1998; Komatitsch *et al.*, 1999; Paolucci *et al.*, 1999). Komatitsch and Tromp (1999) implemented an efficient parallel version of the SEM for global 3-D seismic wave propagation simulations, which resulted in the open-source, freely-distributed SPECFEM3D-GLOBE algorithm and package (<http://www.geodynamics.org/cig/software/specfem3d>).

As a high order version of the Finite Element Method (FEM), the SEM solves the weak form of the equation of motion. This form is obtained by taking the dot product of the momentum equation with an arbitrary test vector w and integrating by parts over the

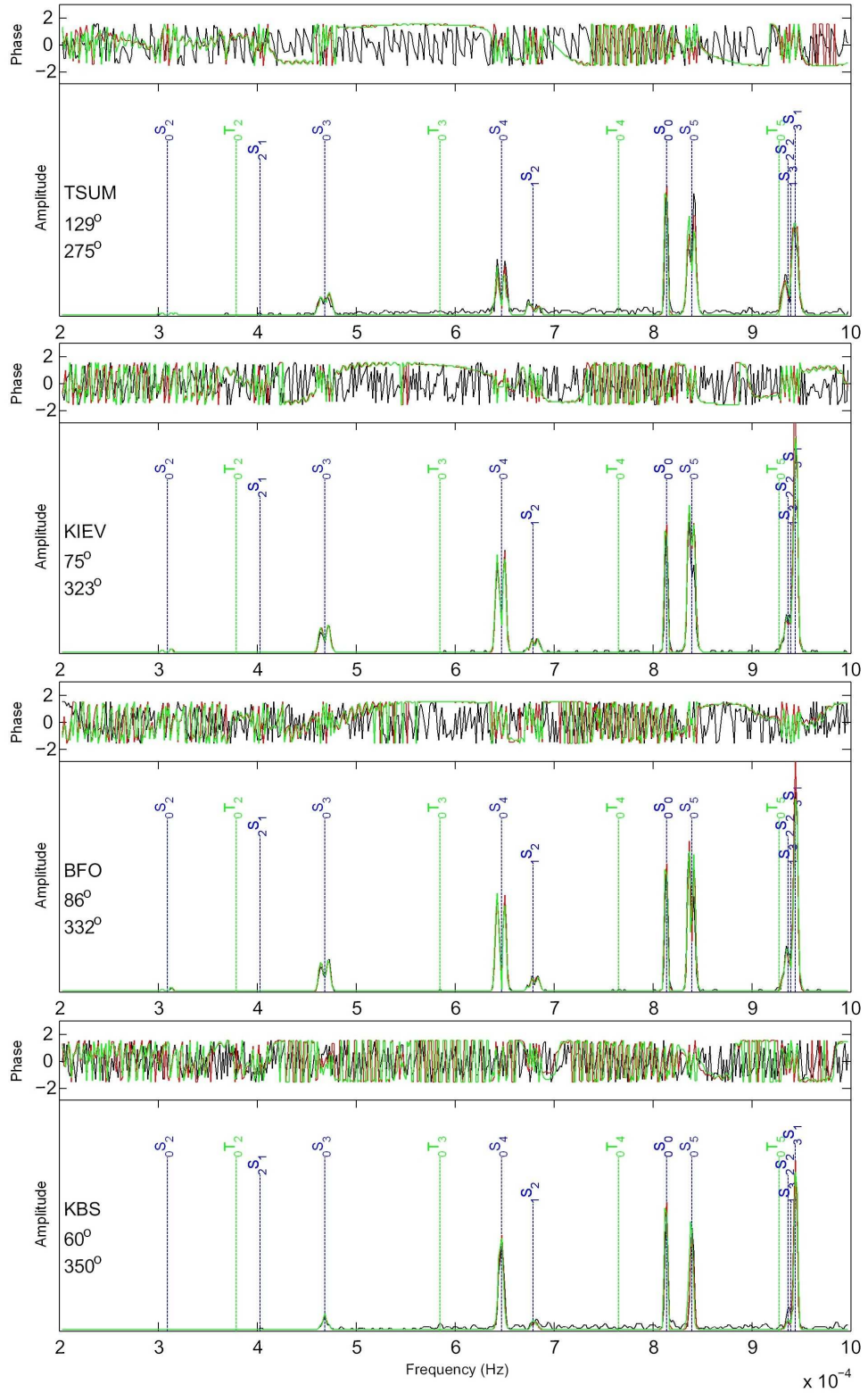


Figure 2.9: Observed vertical component acceleration data amplitude and phase spectra (black) compared to GCMT synthetic amplitude spectra and phase calculated taking into account Earth's rotation and ellipticity using PREM (red) and 3-D SAW12D mantle model (green), for the 2011 Tohoku earthquake for various seismic stations from the Global Seismic Network. A full-coupling scheme is used from 0.2 mHz up to 1.3 mHz. The time window of the time series used is 144h. Station names, epicentral distances and station azimuths are shown in the left hand side.

Earth's volume Ω :

$$\int_{\Omega} \rho w \cdot \partial_t^2 s(x, t) d^3 x = - \int_{\Omega} \nabla w : T d^3 x + M : \nabla w(x_s) S(t) \quad (2.25)$$

where T is the stress tensor, s is the displacement, x_s is the point source location, M is the moment tensor, ρ is the density, M is the seismic moment tensor and $S(t)$ is the source time function. The term in the left hand side of equation 2.25 is related to the mass matrix and the first term in the right hand side is related to the stiffness matrix, while the second term is the source term.

First, a mesh representing the Earth has to be defined. In the SPECFEM3D-GLOBE algorithm, the model volume Ω is divided into a number of non-overlapping hexahedral elements Ω_e . The shape of these elements can be defined typically in terms of Lagrange polynomials of degree four to ten with a numerical quadrature of Gauss-Lobatto-Legendre integration points. As a result, the mass matrix is always diagonal. In addition, since high order Lagrange polynomials are used for the interpolation, the obtained resolution will be higher compared to FEM methods, where only low degree polynomials are used for the representation of functions on the hexahedral elements. The resulting mesh is an unstructured globe representation between the cube and the sphere, called the cubed-sphere. Any typical 3-D Earth model can then be superimposed on it, while the surface topography, bathymetry and the Earth's ellipticity can also be taken into account.

Next, the weak form of the equation of motion is solved at each element. First, the displacement field and the test vector are expressed in terms of Lagrange polynomials. These expressions are then substituted in the term on the left hand side of equation 2.25 and the ground acceleration can be obtained at each grid point. Next, the stiffness matrix is evaluated by calculating the displacement gradient. Finally, the source term is expressed using the test vector. The displacement vectors of the global mesh at all grid points can now be obtained. The displacement vector over time can finally be expressed in the symbolic form of the differential equation:

$$M \ddot{U} + KU = F \quad (2.26)$$

where M is the global mass matrix, K is the global stiffness matrix and F represents the

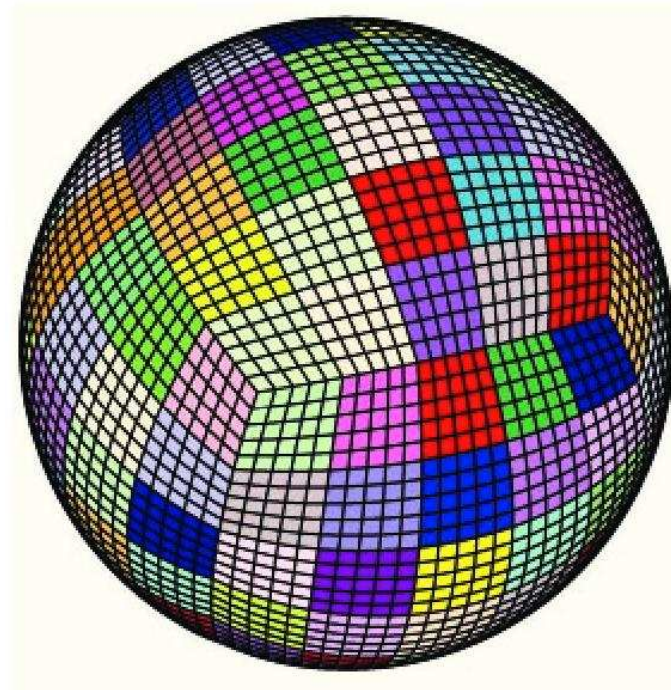


Figure 2.10: A visual example of the Earth represented by the cubed sphere, divided in six chunks. In the implementation of SPECFEM3D-GLOBE used in this study, each chunk is subdivided into 5^2 slices of elements, resulting in 150 slices (which corresponds to the number of processors used in the calculations), as shown by different colours. The figure is taken from Komatitsch and Tromp (2002a).

source term. A complete description of the method can be found, e.g., in Komatitsch and Tromp (1999); Komatitsch *et al.* (2002); Tromp *et al.* (2008).

SPECFEM is a purely numerical technique for the accurate, realistic calculation of synthetic seismograms in a 3-D Earth model. It is well benchmarked against a normal mode summation technique for SNREI Earth models (Komatitsch and Tromp, 2002a,b), however it is computationally heavier. In particular, it only runs on high performance computer clusters in parallel.

In this thesis, we carry out simulations using the SPECFEM3D-GLOBE package (version 5.1.3) in earthquake source validations in Chapter 3. The algorithm runs at the UEA high performance computer cluster using 150 processors with 25 slices of elements in total (Figure 2.10) and at HECToR, the UK's national supercomputing service, using 600 processors with 100 slices of elements in total. With these configurations, our synthetic seismograms are accurate down to wave periods of 17 s. The *mesh*er needs approximately 50 minutes of CPU time at UEA's cluster and 30 minutes of CPU time in HECToR. The *solver* takes approximately 17 hours of CPU time at UEA's computer cluster and six hours

at HECToR to simulate 1.5-hr long synthetic seismograms for one earthquake.

Chapter 3

Testing earthquake source models using forward modelling

3.1 Summary

In this Chapter, we assess the quality of source parameters of large magnitude ($M_w \geq 7.5$) shallow subduction earthquakes of the past 20 years determined using SCARDEC, a recent fully-automated broadband body wave source inversion technique for the fast estimation of the moment magnitude, depth, focal mechanism and source time functions of global events, as briefly discussed in Chapter 1. We find that SCARDEC source parameters agree well with those reported in the Global CMT (GCMT) catalogue, with only the fault dip angle showing a tendency for steeper SCARDEC dip values than GCMT. We investigate this discrepancy through independent validation tests of the source models by: (i) testing how well they explain data not used in their construction, notably low-frequency normal mode data; and, (ii) assessing the data fit using 3-D forward modelling tools more sophisticated than those used to build the source models; specifically, we use a spectral element method (SEM) for a 3-D Earth model. We find that SCARDEC source parameters explain normal mode data reasonably well compared to GCMT solutions. In addition, for the 3-D Earth model used in our experiments, SCARDEC dip angles explain body wave data similarly or slightly better than GCMT. Moreover, SCARDEC dip angles agree well with results from individual earthquake studies in the literature and with geophysical constraints for different subduction zones. Our results show that SCARDEC is

a reliable technique for rapid determinations of source parameters of large ($M_w \geq 7.5$) subduction earthquakes. Since the SCARDEC method provides realistic source time functions allowing the fast identification of classical tsunami earthquakes, it is complementary to existing methods routinely used for earthquake monitoring and suitable for ocean-wide tsunami warning purposes.

3.2 Introduction

As explained in Chapter 1, earthquake source parameters are routinely determined and reported in global catalogues, such as the Global Centroid Moment Tensor (GCMT) catalogue (<http://www.globalcmt.org/CMTsearch.html>), and the U.S. Geological Survey - National Earthquake Information Center (USGS - NEIC, <http://earthquake.usgs.gov/earthquakes/recenteqsw/>). For large magnitude ($M_w \geq 7.5$) earthquakes, the GCMT method (e.g., Dziewonski *et al.*, 1981; Ekström *et al.*, 2012) often uses only long-period mantle waves ($T \sim 125 - 350$ s), and in some cases employs long-period body waves ($T \sim 40 - 150$ s) as well as mantle and surface wave ($T \sim 50 - 150$ s) data. On the other hand, the USGS catalogue reports, amongst others, source models obtained using W-phase data (Kanamori and Rivera, 2008). While surface waves are not ideal for rapid source parameter estimations, as they travel slower than body waves, the W-phase travels faster than shear waves, thus being more suitable for real time applications, notably for tsunami alert purposes (Kanamori and Rivera, 2008). However, for shallow dip-slip earthquakes, which often occur in subduction zones, both W-phase and GCMT methods suffer from a tradeoff between the seismic moment and the dip angle (Kanamori and Given, 1981; Tsai *et al.*, 2011) when Rayleigh waves are used. For these earthquakes, the excitation of long-period surface waves is proportional to both the seismic moment and the sine of the dip angle ($M_0 \sin 2\delta$), but the two parameters are not well constrained separately.

Body wave techniques can help address these issues, as broadband body waves used in earthquake source inversions, typically with wave periods smaller than those of surface waves, are little sensitive to the moment-dip tradeoff, which only becomes significant for earthquakes very close to the surface (see, e.g., the radiation pattern terms for the $P-pP-sP$ wavetrain in Bouchon, 1976). As explained in Chapter 1, an example of such

body wave technique is the recently developed SCARDEC method (Vallée *et al.*, 2011), which is now fully automated and used in rapid routine analyses of large ($M_w \geq 5.5$ –6.0) global earthquakes available online (<http://geoazur.oca.eu/SCARDEC>) about 45 minutes after an event. The method uses a deconvolution approach to determine the optimal set of source parameters. Ray theory is used to calculate double couple point-source body-wave signals in the 1-D IASP91 Earth model (Kennett and Engdahl, 1991), for a given source depth, fault geometry and mechanism (strike, dip and rake). By deconvolving these point source signals from real data, and taking into account some physical constraints on the resulting relative source time functions (see Vallée *et al.*, 2011, for details), the SCARDEC method retrieves the optimal set of source parameters. SCARDEC thus determines simultaneously relative source time functions at each station, along with the focal mechanism, depth and moment magnitude. The determination of relative source time functions, which are allowed to be different at each station, makes SCARDEC particularly well adapted to the analysis of large earthquakes, setting it apart from classical body wave approaches (e.g., Nabelek, 1984). Moreover, unlike many other routine earthquake source analysis techniques and studies in the literature, the SCARDEC method reports uncertainties in earthquake magnitude, dip angle and depth. As explained in Vallée *et al.* (2011), a heuristic approach is used to estimate uncertainties, whereby fixing the fault's strike and rake to their optimal values, misfit values are computed for a range of 30 km around the optimal source depth and for a range of $\pm 15^\circ$ around the optimal dip angle. The analysis of the misfit functions obtained following this procedure for a large number of earthquakes showed that the misfit function has a typical bell-shape, with a flat misfit area surrounded by a zone of rapidly increasing misfit. The limit of the flat misfit area was found to be controlled by a 10% misfit deterioration criterion, which corresponds to the extreme acceptable models. While these uncertainty estimates do not arise from a rigorous statistical analysis, they reflect the resolution of the SCARDEC method, being more realistic than, e.g., the standard errors reported in the GCMT catalogue, which assume that uncorrelated noise is the only source of error, leading to very low uncertainty values, particularly for large events (see, e.g., the discussion in Hjörleifsdóttir and Ekström, 2010).

As mentioned above, the SCARDEC method is now a fully automated technique

which analyses earthquakes with $M_w \geq 5.5$ in the NEIC catalogue. It uses only up to a 32 min interval of data after the event's origin, and the inversions take 5-12 minutes, so that SCARDEC solutions are obtained within 45 minutes after the earthquake. Vallée *et al.* (2011) give a full description of the method and they show results obtained from 17 large ($M_w \geq 7.8$) subduction earthquakes of the past 20 years. The limited magnitude range in their study is related with the frequency range of the data used in those inversions. In the newer, refined version of the method which we assess in this Chapter, the highpass period depends on the earthquake magnitude and duration, and ranges from 80 s for a $M_w \sim 6$ earthquake to 333 s for a very large and long source duration earthquake ($M_w \sim 9$). Specifically, the choice of the optimal High-Pass Filter (HPF) represents a balance between three factors: (i) the corner frequency of the earthquake, which is related to its source duration (SD); (ii) the signal-to-noise ratio; and, (iii) the validity of the body wave formalism used in the SCARDEC method. For the large earthquakes analysed in this Chapter, using a high-pass filter of 0.005 Hz always respects condition (ii). However, when the earthquakes have very long source durations, their corner frequency (which is roughly close to the inverse of the source duration) may be too close to 0.005 Hz, which lead us to lower the high-pass filter to a value equal to $1/(2.5 \text{ SD})$. It must be noted that this can be done because the first step of the SCARDEC technique is to determine the SD by a high-frequency analysis of the P-waves. Finally, condition (iii) imposes a lower bound to the HPF, as very low frequency waves, such as the W-phase (Kanamori and Rivera, 2008), are not considered in the SCARDEC formalism. This explains why the HPF is not chosen to be lower than 0.003 Hz. This implementation leads to slightly different results to those presented by Vallée *et al.* (2011). Updated source parameters and their acceptable intervals are shown in Table A.1 in Appendix A, which shows that for the 17 earthquakes common to the two studies, there are some slight differences. For example, the updated moment magnitude values in this Chapter are slightly larger than those reported by Vallée *et al.* (2011) (with a median difference in M_w of about 0.05). This slight increase in moment magnitude naturally results from lowering the HPF as explained above for earthquakes with a source duration longer than 80 s. Details on the updated results, stations used and optimal source model - data fit plots can be found at <http://geoazur.oca.eu/SCARDEC>. Hereinafter, we will refer to Vallée

et al. (2011) as the source for the SCARDEC technique, but we will refer to Table A.1 for the SCARDEC source parameters used in this Chapter. Even if varying little from the SCARDEC solutions reported by Vallée *et al.* (2011), given the refinement of the technique to account for the effect of the earthquake's corner frequency in a more rigorous way, the latest SCARDEC solutions should be the most reliable.

In this Chapter, we carry out independent validation tests to objectively assess the quality and robustness of the updated SCARDEC source models. We focus on 34 subduction earthquakes with $M_w \geq 7.5$, occurring at shallow depths, which can potentially excite tsunamis with significant heights, depending also on the fault dip angles. The choice of our moment magnitude criterion is motivated by existing tsunami alert systems, such as the Pacific Tsunami Warning Centre (PTWC), which issues tsunami messages for earthquakes of the same or higher moment magnitudes (http://ptwc.weather.gov/ptwc/about_messages.php). We analyse large shallow earthquakes that occurred in the past 20 years and we carry out comparisons with solutions in the GCMT catalogue, as it is the most widely used and complete global moment tensor catalogue for that period. We start by testing how well SCARDEC source parameters explain data not used to constrain them; specifically, we use low-frequency normal mode data. As the source parameters are based on simplifying approaches such as 1-D Earth ray theory for the SCARDEC method (Vallée *et al.*, 2011), and the great-circle approximation for the GCMT method (Dziewonski *et al.*, 1981), we then assess the impact of such simplifications by using a more sophisticated technique - the spectral element method on a 3-D Earth model (Komatitsch and Tromp, 1999) - to verify how well the source models explain body wave data. Finally, we compare the various dip angle estimates with those from previous individual earthquake studies and with geophysical constraints on subduction zones, and discuss the implications of this work in terms of the reliability of the SCARDEC method for routine subduction earthquake characterisations and ocean-wide tsunami warning purposes.

More broadly, this Chapter contributes to ongoing efforts in earthquake source model validation (e.g., the Source Inversion Validation (SIV) project, <http://eqsource.webfactional.com/wiki/>). Finding objective strategies to benchmark, compare and independently test the quality of earthquake source models, as done in this Chapter, is a crucial step for the rigorous quantification of seismic source processes and associated

uncertainties in future earthquake studies.

3.3 Subduction earthquakes studied

We first consider all the large ($M_w \geq 7.5$), shallow (depth ≤ 50 km), interplate subduction (thrust mechanism with a dip angle smaller than 40°) earthquakes that occurred in the past 20 years. We exclude the 2004 great Sumatra earthquake whose exceptionally long source duration causes poor results when using the SCARDEC method. Moreover, we exclude large events occurring minutes to a day after a major earthquake (e.g., the 17th November 2000 New Britain earthquake and the large early aftershock of the 2011 Tohoku-Oki earthquake), whose interference causes noisy waveforms. This leads to a selection of the 34 earthquakes shown in Figure 3.1 and Table 3.1. Their SCARDEC source parameters, including uncertainties in dip angle, depth and magnitude can be found in Table A.1 of the Appendix A.

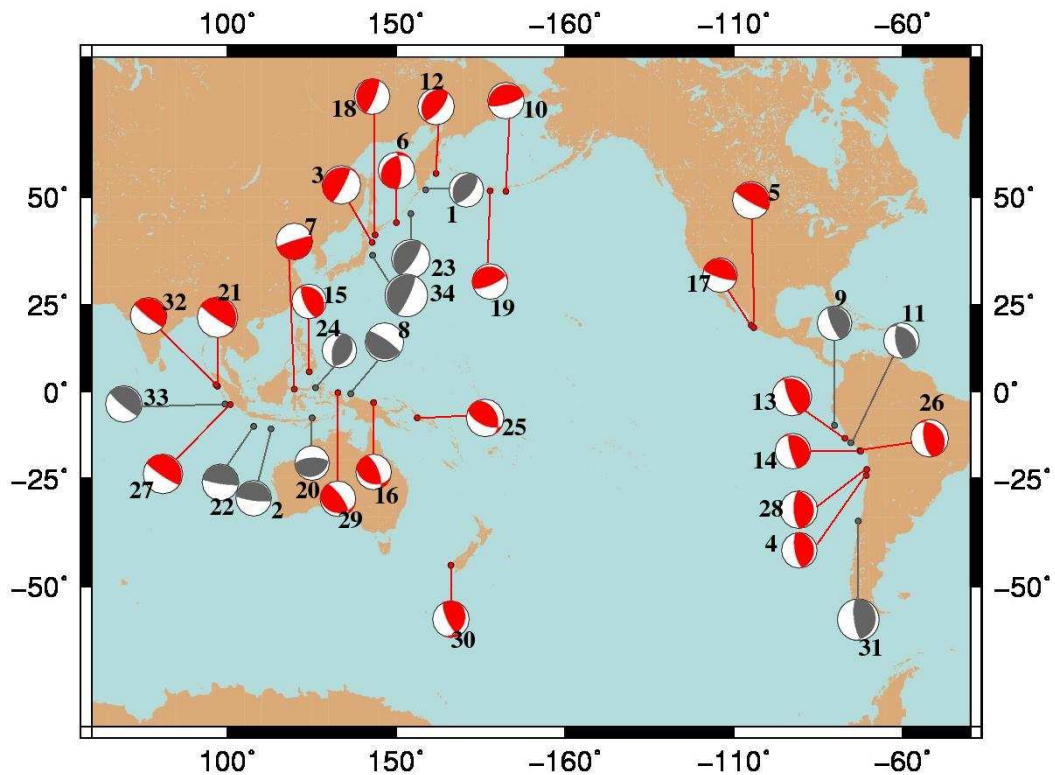


Figure 3.1: Global map showing the locations and GCMT source mechanisms of the major subduction earthquakes considered in this Chapter. Earthquakes where GCMT dip angles lay outside of SCARDEC dip angle intervals are plotted in red. All the remaining earthquakes are plotted in grey. A detailed list of the earthquakes can be found in Table 3.1 and in Table A.1 of the Appendix A.

Table 3.1: List and index codes of the large magnitude ($M_w \geq 7.5$) shallow subduction earthquakes of the past 20 years used in this Chapter. Their GCMT and SCARDEC fault geometries are shown by their beach balls. Earthquakes where GCMT dip angles lay outside of SCARDEC dip angle intervals are shown in bold (earthquakes in red in Figures 3.1–3.3).

Index	Event name	GCMT	SCARDEC
1	060893D - Kamchatka 1993	●	●
2	060294A - Java 1994	●	●
3	122894C - Honshu 1994	●	●
4	073095A - Chile 1995	●	●
5	100995C - Jalisco 1995	●	●
6	120395E - Kuril 1995	●	●
7	010196C - Minahassa 1996	●	●
8	021796B - Irian Jaya 1996	●	●
9	022196B - N. Peru 1996	●	●
10	061096B - Andreanof 1996	●	●
11	111296D - Peru 1996	●	●
12	120597C - Kamchatka 1997	●	●
13	062301E - Peru 2001a	●	●
14	070701F - Peru 2001b	●	●
15	030502H - Mindanao 2002	●	●
16	090802H - New Guinea 2002	●	●
17	012203A - Jalisco 2003	●	●
18	092503C - Hokkaido 2003	●	●
19	111703B - Rat Islands 2003	●	●
20	111104M - Timor 2004	●	●
21	200503281609A - Sumatra 2005	●	●
22	200607170819A - Java 2006	●	●
23	200611151114A - Kuril 2006	●	●
24	200701211127A - Molucca 2007	●	●
25	200704012039A - Solomon Islands 2007	●	●
26	200708152340A - Peru 2007	●	●
27	200709121110A - Sumatra 2007	●	●
28	200711141540A - Chile 2007	●	●
29	200901031943A - Irian Jaya 2009	●	●
30	200907150922A - New Zealand 2009	●	●
31	201002270634A - Chile 2010	●	●
32	201004062215A - N. Sumatra 2010	●	●
33	201010251442A - S. Sumatra 2010	●	●
34	201103110546A - Honshu 2011	●	●

Figure 3.2 compares GCMT and SCARDEC earthquake source parameters for the studied earthquakes. There is generally a good agreement between SCARDEC and GCMT for fault strike, rake, depth and M_w , especially when taking SCARDEC uncertainties into account (i.e., often the range of acceptable SCARDEC source parameters comprises the GCMT solution), with no obvious trends in the scatter plots for these parameters. In contrast, SCARDEC dip angles are generally steeper than those in the GCMT catalogue, showing a clear systematic trend of larger SCARDEC dip angles, except for six events (Peru 1996, Kamchatka 1997, Timor 2004, Kuril 2006, Solomon Islands 2007, Peru 2007; see Tables 3.1 and A.1 for further details about these earthquakes and corresponding source parameters). The average difference in dip angles between SCARDEC and GCMT ($\Delta\delta = \delta^{GCMT} - \delta^{SCARDEC}$) is $\bar{\Delta}\delta = -3.9^0$, with Jalisco 2003 having the largest dip angle difference ($\Delta\delta = -12.5^0$), and with 19 earthquakes showing dip angle differences larger than the average of differences. This systematic bias of steeper SCARDEC dip angles can be possibly explained due to the fixed PDE location used by SCARDEC, and/or differences in depth and source durations in comparison with GCMT. For the remaining earthquakes, while the trend in the differences between SCARDEC and GCMT dip angles generally persists, the differences are smaller, especially when taking into account the SCARDEC uncertainties.

Vallée *et al.* (2011) found that for half of the earthquakes in their study, steeper SCARDEC dip angle estimates were associated with a smaller moment magnitude than GCMT, with an average difference in M_w over all the earthquakes of 0.095. They showed that the discrepancies between GCMT and SCARDEC are consistent with the $M_w - \delta$ tradeoff, by using a corrected moment magnitude for GCMT, which lead to a lower average difference. In this Chapter we find a substantially lower average difference in magnitude between GCMT and the updated SCARDEC source parameters for the new set of earthquakes (0.00 for the whole set of earthquakes and 0.01 for the $M_w \geq 7.8$ earthquakes studied by Vallée *et al.* (2011)). The reasons and implications of these differences are discussed below in section 3.8.

Figure 3.3 compares SCARDEC and GCMT moment tensor components for the 34 earthquakes considered. Given that the dip angles show the largest discrepancies of all parameters in Figure 3.2, this leads to the dip-slip components of the moment tensor ($M_{r\theta}$,

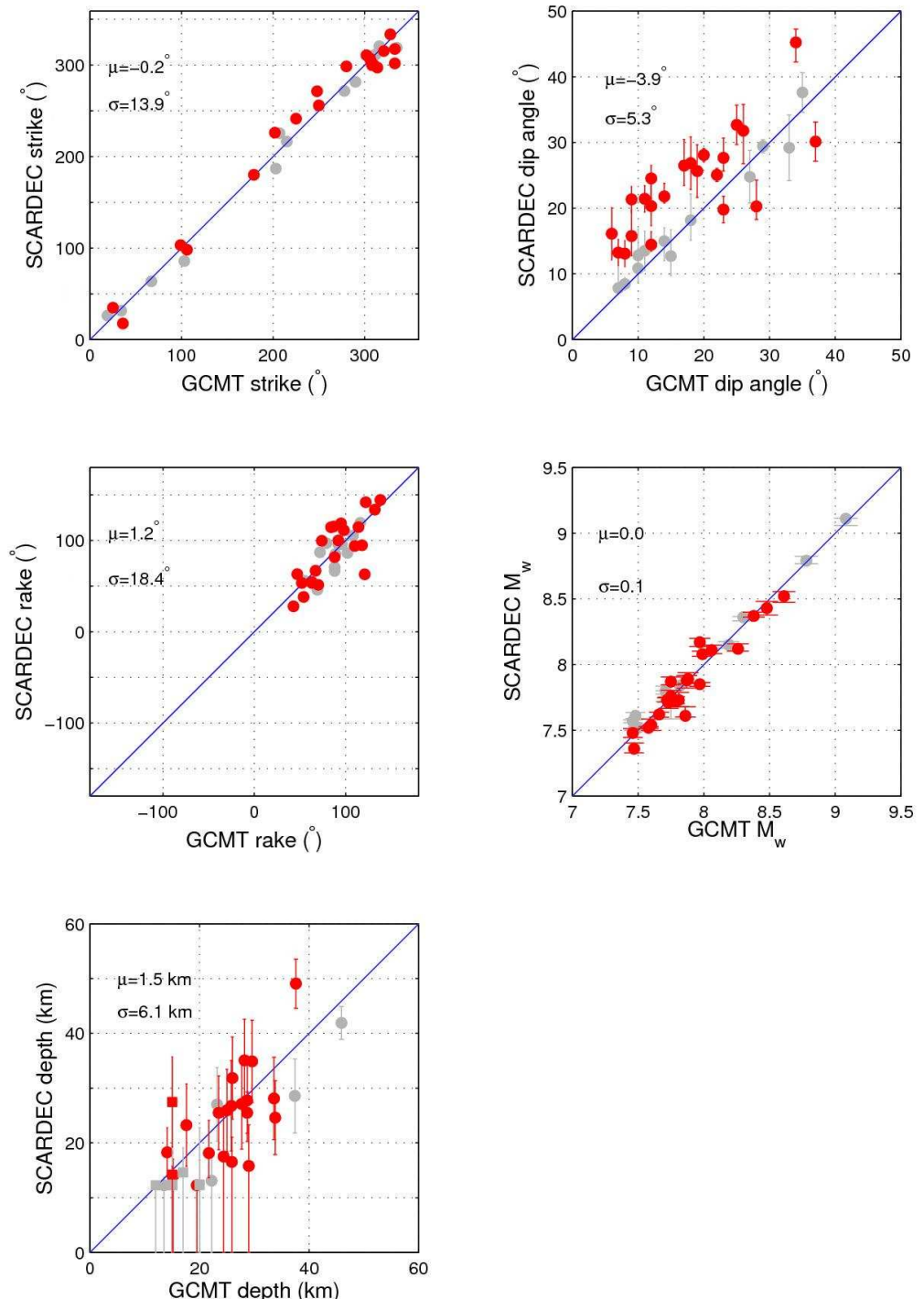


Figure 3.2: Scatter plots of GCMT source parameters versus SCARDEC (strike, dip, rake angles, depth, moment magnitude). Error bars correspond to SCARDEC uncertainties. Red circles correspond to the earthquakes studied, for which GCMT dip angles lay outside of SCARDEC dip angle intervals. Square symbols in the diagram with depth comparisons correspond to earthquakes where the GCMT depth is fixed. All the remaining earthquakes are plotted in grey. A detailed list of the earthquakes can be found in Table 3.1. Mean value (μ) and standard deviation (σ) of the differences between GCMT and SCARDEC parameters are plotted in the top left corner of each diagram.

$M_{r\phi}$) having the largest average differences between SCARDEC and GCMT amongst all the moment tensor component estimates.

In the remainder of this Chapter, we shall carry out independent tests of SCARDEC source models. Since the main differences between SCARDEC and GCMT source parameters are found for fault dip angles, we focus on the set of 22 earthquakes for which GCMT dip angles lay outside of SCARDEC dip angle intervals (see the red symbols in Figures 3.1–3.3 and the earthquakes in bold in Table 3.1).

3.4 Normal mode data tests

Normal mode data illuminate overall, bulk earthquake source characteristics and are a useful tool to test the SCARDEC method independently, as they are not used in the construction of SCARDEC source models. Moreover, the frequency range (0.1 – 4 mHz) of the very long time-series (48-hr) used in this test is much lower than that used in the shorter duration (25 min) surface wave comparisons (150 – 200 s) presented in Vallée *et al.* (2011). In order to study the Earth’s normal modes, we use three-component broad-band data from the Global Seismographic Network (GSN) for the earthquakes in this Chapter.

In this section, we focus only on earthquakes with $M_w \geq 7.8$, of the 22 earthquakes where GCMT dip angles lay outside of SCARDEC dip angle intervals. This magnitude threshold is used because only such large earthquakes can excite relatively well ultra-long period normal modes (0.1–1.0 mHz), providing a high signal to noise ratio in this frequency range. The amplitude spectra of lower magnitude earthquakes is generally dominated by noise in this frequency range. This leads to a set of 14 earthquakes (Chile 1995, Jalisco 1995, Kuril 1995, Minahassa 1996, Andreanof 1996, Kamchatka 1997, Peru 2001, Hokkaido 2003, Sumatra 2005, Solomon Islands 2007, Peru 2007, Sumatra 2007, New Zealand 2009 and Sumatra 2010; see Tables 3.1 and A.1 for details). We apply a Fast Fourier Transform (FFT) to 48 hours of continuous displacement data, after multiplication by a Hanning window, to obtain amplitude data spectra between 0.1 and 4.0 mHz. We visually examine all the amplitude spectra and only consider data in frequency intervals with high quality, similar to that shown in Figure 3.4. We then calculate theoretical seismograms using a mode summation technique (e.g., Gilbert and Dziewonski, 1975), for both the SCARDEC and GCMT source parameters. We sum over all the spheroidal and

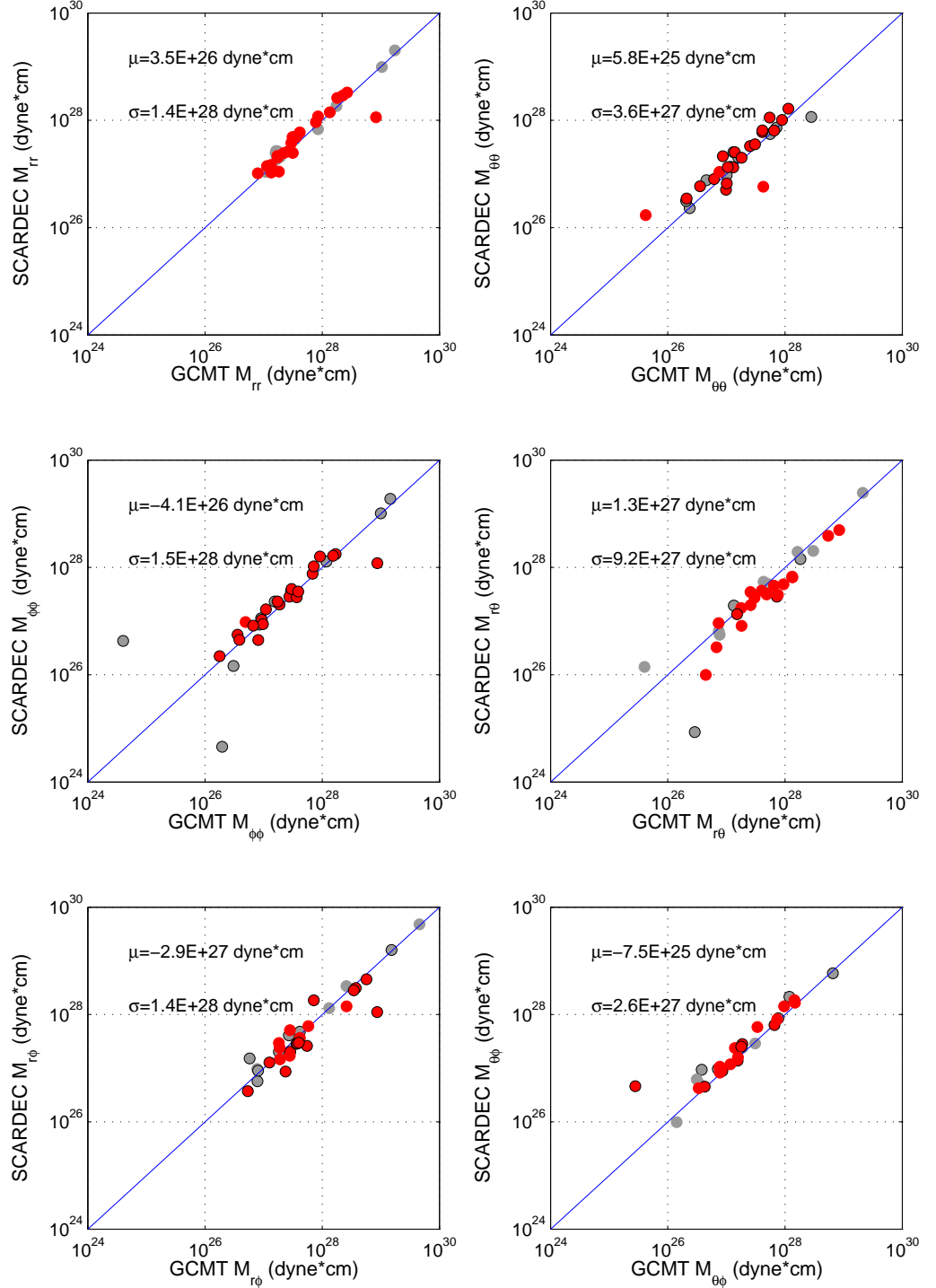


Figure 3.3: Scatter plots of GCMT moment tensor components versus SCARDEC. Red circles correspond to the earthquakes studied for which the GCMT and SCARDEC dip angles lay outside of SCARDEC dip angle intervals. All the remaining earthquakes are plotted in grey. Black circle contours indicate negative moment tensor components (all SCARDEC and GCMT moment tensor components compared here have the same signs). Mean value (μ) and standard deviation (σ) of the differences between GCMT and SCARDEC are plotted in the top left corner of each diagram.

toroidal fundamental modes and overtones from 3233 s (${}_0S_2$) down to 30 s for completeness, for a spherically symmetric, non-rotating, elastic, isotropic (SNREI) Earth model, using the 1-D PREM (Dziewonski and Anderson, 1981) model. Since we use only 48 hours of data, the splitting of the low frequency modes is not very strong, and hence, for the purpose of comparing how well the two sets of source parameters fit the data, we do not take into account the effects of ellipticity and rotation in our calculations. The same processing as for the real data is then applied to the synthetics to obtain synthetic amplitude spectra. Despite calculating theoretical seismograms with periods down to 30 s, we compute amplitude spectra between 0.1 and 4.0 mHz (as for the real data).

We quantify the fit between synthetic and real data spectra by calculating L_2 -norm amplitude misfits (equation 3.1) and L_2 -norm Fast Fourier Transform (FFT) real and imaginary part misfits (equation 3.2):

$$m_{Amp.}^2 = \frac{\sum_i \sum_n (d_i^A(f_n) - s_i^A(f_n))^2}{\sum_i \sum_n (d_i^A(f_n))^2} \quad (3.1)$$

$$m_{Re/Im}^2 = \frac{\sum_i \sum_n ((d_i^{Re}(f_n) - s_i^{Re}(f_n))^2 + (d_i^{Im}(f_n) - s_i^{Im}(f_n))^2)}{\sum_i \sum_n ((d_i^{Re}(f_n))^2 + (d_i^{Im}(f_n))^2)} \quad (3.2)$$

where f_n is the n^{th} frequency in the spectral domain, and d_i^A and s_i^A are the data and synthetic amplitude spectra at the i^{th} station, respectively. d_i^{Re} and s_i^{Re} , and d_i^{Im} and s_i^{Im} are the real and imaginary parts of the data and synthetics in the frequency domain, respectively. The amplitude misfit evaluates the discrepancy in the amplitude spectra between the data and the synthetics, while the real and imaginary FFT part misfit provides information about the discrepancies in both the amplitude and phase of the signal. Noisy parts of the observed spectra are discarded from the misfit calculations.

An illustrative example of normal mode amplitude spectra comparisons can be found in Figure 3.4 for the M_w 8.4 Sumatra 2007 earthquake. The earthquake occurred about 130 km SW of Bengkulu, with a rupture extending 350 km to the NW from the hypocentre and a duration of about 100 s (Konca *et al.*, 2008). The main shock was followed by a moderate tsunami with respect to its magnitude, with run-up heights up to 4 m (Lorito *et al.*, 2008; Borrero *et al.*, 2009). Figure 3.4 shows that GCMT and SCARDEC synthetics fit the observed normal mode amplitude spectra equally well, for both vertical and

transverse component data. We calculated amplitude misfits over 20 vertical and 13 transverse component traces and found the same results. Amplitude and real and imaginary part FFT misfits for GCMT are $m_{ampl.Z}^2 = 0.38$, $m_{Re/ImZ}^2 = 0.90$, $m_{ampl.T}^2 = 0.52$ and $m_{Re/ImT}^2 = 1.03$ for the vertical and transverse components, respectively. Misfit values for SCARDEC are $m_{ampl.Z}^2 = 0.38$, $m_{Re/ImZ}^2 = 0.93$, $m_{ampl.T}^2 = 0.53$ and $m_{Re/ImT}^2 = 1.06$, respectively.

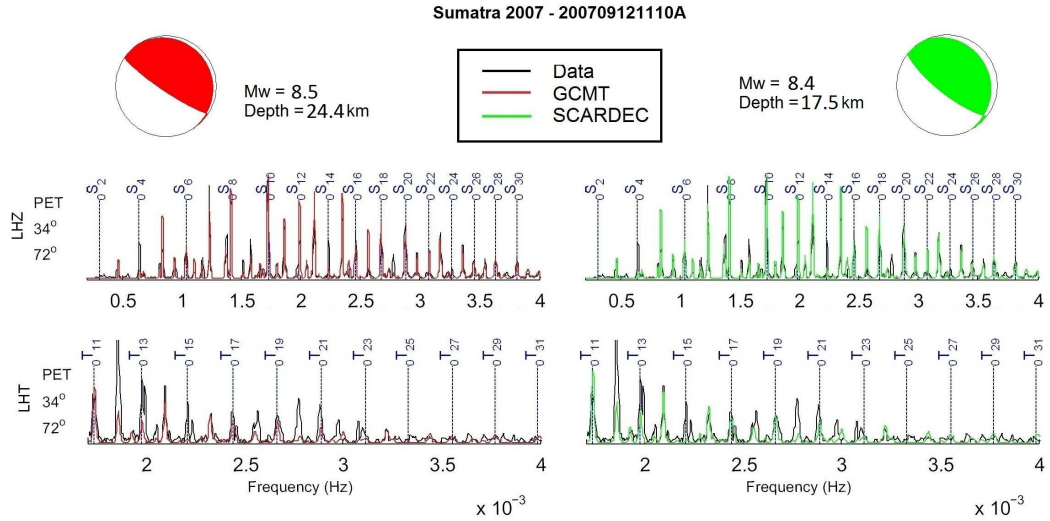


Figure 3.4: An illustrative example of vertical and transverse component normal mode spectra up to 4 mHz, calculated for the M_w 8.5 Sumatra 2007 earthquake with GCMT code 200709121110A, for GSN station PET. 48-hour data spectra are in black, GCMT synthetics in red and SCARDEC synthetics in green. PREM mode eigenfrequencies are shown in blue every two modes for clarity. All the noisy parts of the spectra are discarded from the plots and the misfit calculations. Station name, azimuth and epicentral distance are shown in the left hand side from the top to the bottom. Amplitude misfits for vertical and transverse components over the total number of stations used (20 for the vertical and 13 for the transverse component) are: $m_{ampl.Z}^2 = 0.38$ and $m_{ampl.T}^2 = 0.52$ for GCMT, and $m_{ampl.Z}^2 = 0.38$ and $m_{ampl.T}^2 = 0.53$ for SCARDEC, respectively. Real and imaginary part FFT misfits are: $m_{Re/ImZ}^2 = 0.90$, $m_{Re/ImT}^2 = 1.03$ for GCMT and $m_{Re/ImZ}^2 = 0.93$, $m_{Re/ImT}^2 = 1.06$, for SCARDEC. Focal mechanisms of the two different source models are shown as beach balls on top.

Figure 3.5 shows amplitude and Re/Im normal mode data misfits for the 14 earthquakes considered in this section. The differences between GCMT and SCARDEC misfit values are relatively small, with only the 1995 Jalisco earthquake showing a larger SCARDEC Re/Im misfit due to the combination of considerable differences in fault strike (8°), dip (12°) and M_w (0.13) between SCARDEC and GCMT source parameters. In most other cases, the GCMT misfit values are slightly lower than for SCARDEC, probably because the GCMT method uses hours of long-period mantle waves, which are closer to the normal mode data used here, than the body wave data used by SCARDEC. Overall, it is

encouraging that SCARDEC source parameters explain long-period 48-hour data spectra relatively well, despite being based only on the first 32 min of body wave data after the earthquake, in comparison with GCMT, which uses much longer data time windows.

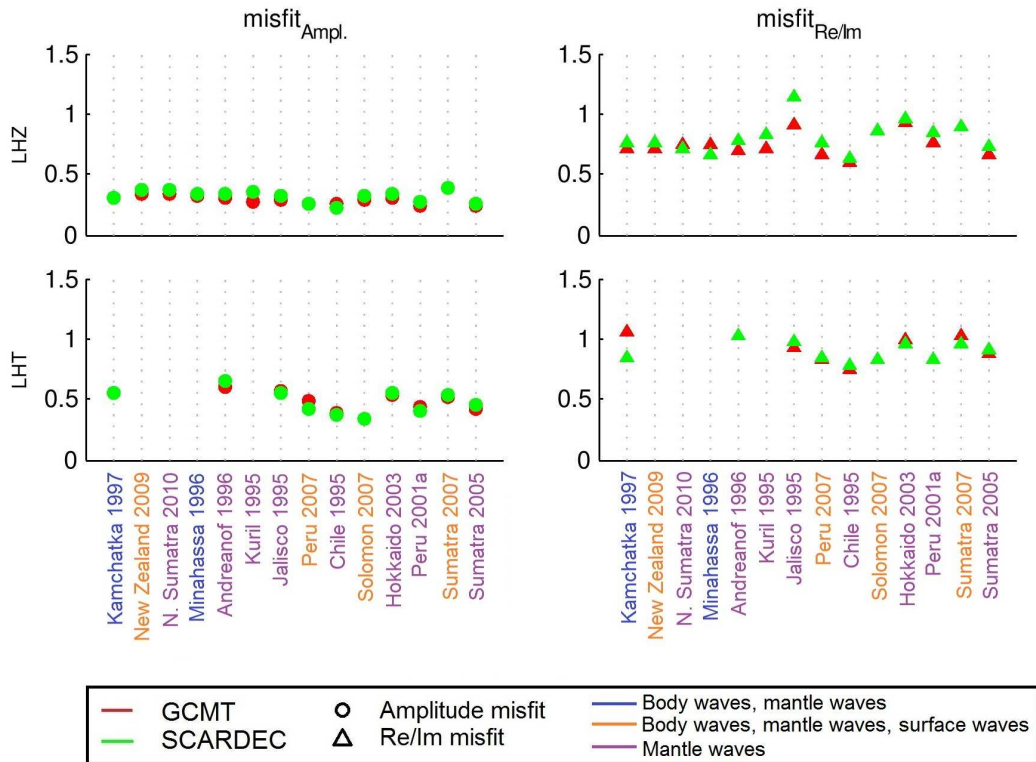


Figure 3.5: Amplitude (left) and Re/Im (right) misfit plots between data and GCMT synthetics (red), and data and SCARDEC synthetics (green) for the earthquakes ($M_w \geq 7.8$) where GCMT dip angles lay outside of SCARDEC dip angle intervals. In cases where not enough data were available (fewer than ten stations) no misfits were calculated (i.e., for the transverse component of the Kuril 1995, Minahassa 1996, New Zealand 2009 and N. Sumatra 2010 earthquakes). The SCARDEC amplitude and Re/Im misfits are on average 6–9% larger than GCMT for vertical (LHZ) component data. For transverse (LHT) component data, SCARDEC and GCMT misfits are very similar. Earthquakes are plotted in ascending M_w order and their names are written in different colours according to the data used in the GCMT catalogue (blue for body and mantle waves, orange for body, mantle and surface waves, purple for mantle waves).

Figure 3.5 shows larger differences between SCARDEC and GCMT misfits for spheroidal modes (vertical component) than for toroidal modes (transverse component). Specifically, the SCARDEC misfits for both the amplitude and the real and imaginary part of the FFT, are on average about 6–9% larger than GCMT for vertical component data (mean misfit values are presented in Table 3.2 and detailed misfit values in Table A.2 in Appendix A). For toroidal modes, on average SCARDEC and GCMT source parameters explain the normal mode data equally well. This is probably related to the distinct characteristics of toroidal and spheroidal modes along with data noise issues. Love waves (and thus toroidal

Table 3.2: Mean misfit values (amplitude misfits and real and imaginary FFT misfits, see equations 3.1–3.2) obtained over all the earthquakes studied in section 3.4 from normal mode comparisons between GCMT and SCARDEC synthetics and real data, for both vertical and transverse components.

	Vertical component	Transverse component
$m_{\text{Ampl.}-\text{GCMT}}^2$	0.30	0.48
$m_{\text{Ampl.}-\text{SCARDEC}}^2$	0.32	0.48
$m_{\text{Re/Im}-\text{GCMT}}^2$	0.76	0.92
$m_{\text{Re/Im}-\text{SCARDEC}}^2$	0.81	0.90

modes) are generally not as well excited by thrust earthquakes as Rayleigh waves. This, together with the fact that horizontal components are usually noisier than vertical components, may make it more difficult to distinguish slight differences in thrust earthquake source parameters when analysing Love waves/toroidal modes.

3.5 Body-wave 3-D forward modelling tests

Shallow earthquake source inversions using broadband body waves in the 0.003–0.03 Hz frequency range for earthquakes deeper than 5–10 km are relatively insensitive to the moment-dip tradeoff so the SCARDEC method is expected to be able to resolve the two parameters independently. In order to test the quality of SCARDEC subduction earthquake dip angles and assess the impact of using simplified theories and Earth structure in the modelling (notably, ray theory on the 1-D IASP91 Earth model, Kennett and Engdahl, 1991), we use a more sophisticated seismic wave propagation tool to calculate body wave data misfits. We use the spectral element method – SEM – (Komatitsch and Tromp, 1999) for the 3-D Earth crust CRUST2.0 (Bassin *et al.*, 2000) and S20RTS (Ritsema *et al.*, 1999) mantle models to calculate synthetic seismograms with high accuracy down to wave periods of $T \sim 17$ s. Although computationally expensive, the spectral element method is very accurate, in contrast with ray theory, which works under the assumption that the wavelength of the seismic waves is much smaller than the scale length of heterogeneity.

In order to examine the impact of the differences between SCARDEC and GCMT dip angles on the data fit, we consider all the 22 earthquakes selected in section 3.3 for which GCMT dip angles lay outside of SCARDEC dip angle intervals. Given of the $M_o - \delta$ tradeoff and bearing in mind that the GCMT dip angle is associated with the M_o^{GCMT}

estimate and the rest of the GCMT parameters, plus the centroid, the use of the GCMT dip angle alone in combination with the rest of the SCARDEC parameters may not be necessarily a conclusive test. However, our goal is to focus on the effect of different dip angle estimates and how they affect the body-wave data fit.

We calculate SEM theoretical seismograms for: (i) the SCARDEC source parameters; and, (ii) all source parameters as in SCARDEC, except for the fault dip angle, which is taken from the GCMT catalogue. We band-pass filter synthetic displacement seismograms between 20 s and 250 s and rotate the horizontal components into longitudinal and transverse components. Since the dominant period in the seismograms is shorter than the rupture time of the earthquakes studied, we convolve the synthetic seismograms with the average SCARDEC source time functions, smoothed at 1 s. We then filter and rotate the corresponding real displacement data in the same way as with the synthetics and calculate L_2 -norm waveform data misfits for the two sets of synthetics:

$$m_X^2 = \frac{\sum_i (d_i - s_i)^2}{\sum_i d_i^2}, \quad (3.3)$$

where d_i is the time-domain body-wave data at the i^{th} station and s_i is the corresponding synthetic seismogram. X denotes the station component (Z for the vertical and T for the transverse component, respectively).

Figure 3.6 shows examples of body wave comparisons for the M_w 8.4 Peru 2001 earthquake, which occurred in the southern part of the Peru subduction zone. The main shock generated a relatively destructive tsunami and was followed by several large aftershocks. The rupture was unilateral and propagated to the SE for 320–400 km (Bilek and Ruff, 2002; Melbourne and Webb, 2002; Giovanni *et al.*, 2002; Robinson *et al.*, 2006). Only a few illustrative stations are shown in Figure 3.6, but a larger number of stations for both the vertical (16) and the transverse components (15) are used to calculate waveform data misfits for the two sets of synthetics. The use of the GCMT dip angle yields a relatively poorer fit to the data ($m_Z^2 = 0.30$ and $m_T^2 = 0.23$ for vertical and transverse components, respectively) than SCARDEC ($m_Z^2 = 0.22$ and $m_T^2 = 0.16$), mainly in the amplitude and in a few cases in the phase of the signal. The largest differences are observed at SBA station on the vertical component and TAM station on the transverse

component, where the SCARDEC dip angle leads to an improved body-wave data fit.

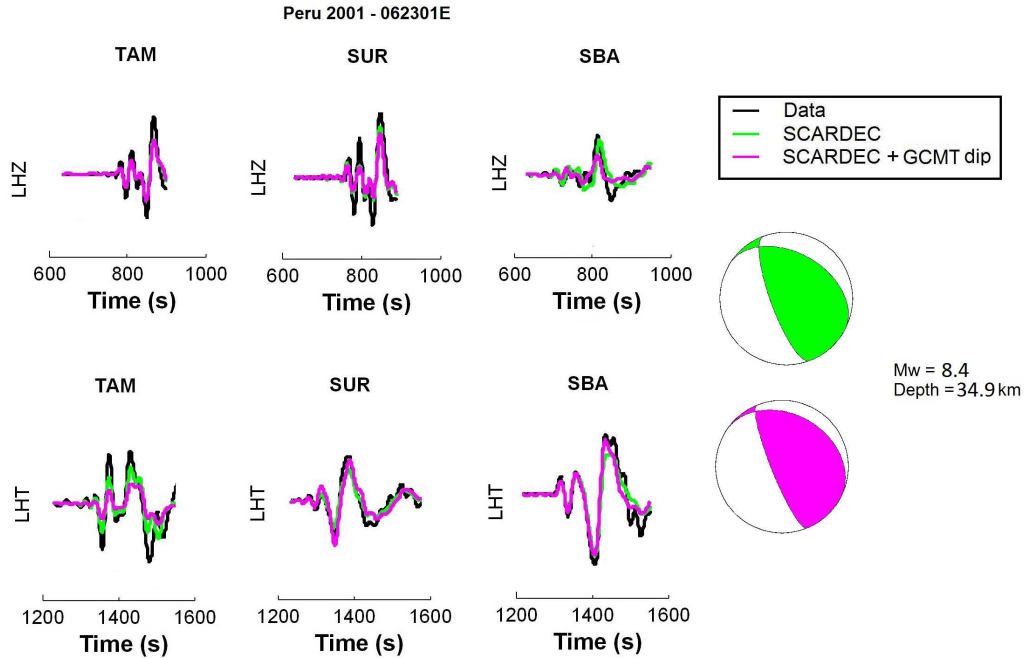


Figure 3.6: Illustrative examples of body wave displacement comparisons for the M_w 8.4 Peru 2001 (GCMT code: 062301E) earthquake in vertical (top, P-waves) and transverse (bottom, SH-waves) components. Data are shown in black, SCARDEC synthetics in green and SCARDEC synthetics with the GCMT dip angle, in magenta. SCARDEC waveform misfits for vertical and transverse components over the total number of stations used (16 for the vertical and 15 for the transverse component) are: $m_Z^2 = 0.22$ and $m_T^2 = 0.16$ for SCARDEC dip angle, and $m_Z^2 = 0.30$ and $m_T^2 = 0.23$ for GCMT dip angle, respectively. Focal mechanisms of the two different source models are shown as beach balls on the right hand side.

Figure 3.7 shows the overall body wave waveform misfit values calculated after modelling all the 22 earthquakes used in our study. The SCARDEC dip angles lead to similar or slightly better data fits in almost all cases for the vertical component, and for some earthquakes for the transverse component data. Despite being small, one needs to bear in mind that these variations in body-wave misfit are obtained by changing just one single earthquake source parameter - the dip angle, not accounting for other types of tradeoffs (e.g., moment-depth). Overall, the use of GCMT dip angles leads to an increase in the average body wave misfit of about 5% for both vertical and transverse components, showing that both GCMT and SCARDEC dip angles explain the data relatively well, with the SCARDEC dip angles leading to an apparent slightly improved data fit (see Table 3.3 for average misfit values over all the earthquakes). Nevertheless, it is worth pointing out that these dip angle comparisons are potentially affected by complications arising from the finite character of the rupture (subduction earthquakes typically rupture an interface with

variable dip angle, along fault's strike and depth) and by the fact that whereas the GCMT method is based on estimations of the centroid in space and time, the SCARDEC method estimates source parameters for the PDE location. In addition, our misfit comparisons may also be influenced by possible tradeoffs between the source parameters and the 3-D Earth models used in the calculation of the synthetic seismograms. Hence, the significance of the apparent improvements in body wave misfits using SCARDEC dip angles is not entirely clear.

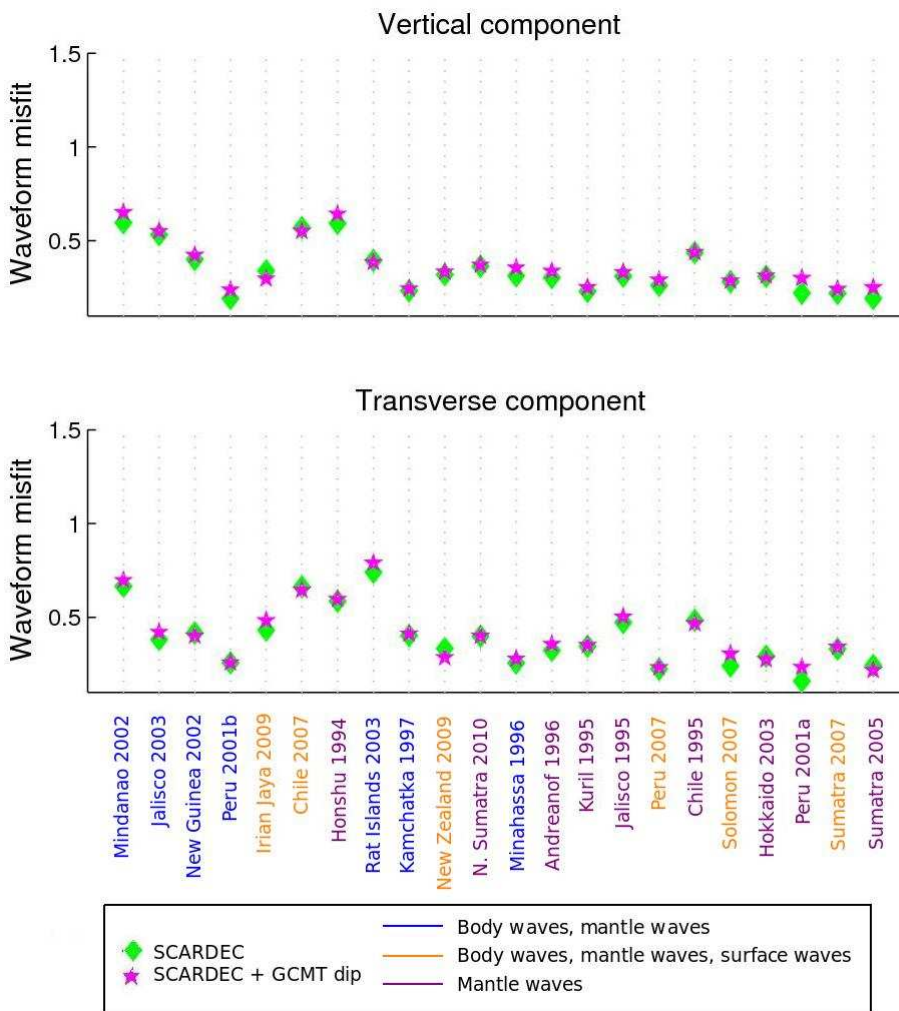


Figure 3.7: Waveform misfits between body wave data and SCARDEC synthetics (green diamonds), and between data and SCARDEC synthetics with the GCMT dip (magenta stars) for all the earthquakes studied. The use of GCMT dip angles yields mean misfit values about 5% larger than SCARDEC for vertical and transverse component data. Earthquakes are plotted in ascending M_w order and their names are written in different colours according to the data used in the GCMT inversions (blue for body and mantle waves, orange for body, mantle and surface waves, purple for mantle waves).

Table 3.3: Mean waveform misfit values obtained over all the earthquakes studied in section 4 from body wave comparisons between real data and 3-D SEM synthetics using either SCARDEC or GCMT ($m_{SCARDEC(\delta_{GCMT})}^2$) dip angles for both vertical and transverse components (see main text for details).

	Vertical component	Transverse component
$m_{SCARDEC}^2$	0.35	0.39
$m_{SCARDEC(\delta_{GCMT})}^2$	0.37	0.41

3.6 Comparisons with other studies and with geophysical constraints

Our independent tests of SCARDEC source parameters are further supported by comparisons with fault dip angles reported in individual earthquake studies published in the literature, using a wide range of data sets, like body waves (Sato *et al.*, 1996; Zobin, 1997; Kisslinger and Kikuchi, 1997; Escobedo *et al.*, 1998; Mendoza and Hartzell, 1999; Gómez *et al.*, 2000; Bilek and Ruff, 2002; Giovanni *et al.*, 2002; Yamanaka and Kikuchi, 2003; Ito *et al.*, 2004; Yagi, 2004; Ji, 2007; Tavera *et al.*, 2006; Delouis *et al.*, 2009; Furlong *et al.*, 2009; Peyrat *et al.*, 2010), surface waves (Tanioka *et al.*, 1996; Robinson *et al.*, 2006; Hébert *et al.*, 2009), W-phase data (Kanamori and Rivera, 2008), strong motion data (Koketsu *et al.*, 2003; Honda *et al.*, 2004), tsunami data (Ortiz *et al.*, 1998; Lorito *et al.*, 2008), geological and geodetic data, such as InSAR and GPS (Jordan *et al.*, 1983; Melbourne *et al.*, 1997; Miura *et al.*, 2004; Miyazaki *et al.*, 2004; Tanioka *et al.*, 2007; Konca *et al.*, 2008; Biggs *et al.*, 2009; Chen *et al.*, 2009; Béjar-Pizarro *et al.*, 2010), summarised in Figure 3.8 (for details, see Table A.3 in Appendix A). Moreover, we include comparisons with recent results from W-phase inversions (Duputel *et al.*, 2012b) and from the Slab1.0 three-dimensional subduction zone model (Hayes *et al.*, 2012). To our knowledge, the Slab1.0 model is the most complete subduction zone compilation built so far by combining active source seismic data from geophysical surveys with information from the global EHB (Engdahl *et al.*, 1998), NEIC PDE and GCMT earthquake catalogues, and with bathymetry data and sediment thickness maps. While ideally dip values averaged over the rupture area should be used, we use local Slab1.0 dip angle values at the GCMT source location, as the rupture areas are generally not known accurately for all the earthquakes considered. Nevertheless, we verified that Slab1.0 dip angles do not vary

substantially within a circle with a 0.5° radius around the locations of the earthquakes (we found an average dip angle variability of 5°).

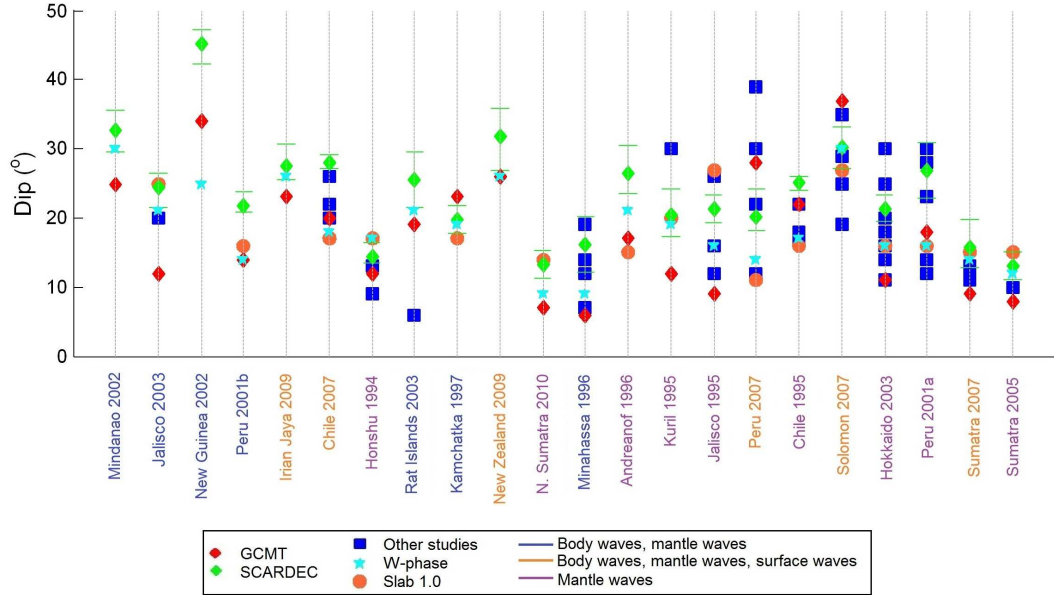


Figure 3.8: Dip angle comparisons between GCMT (red diamonds) and SCARDEC (green diamonds, including uncertainties) for earthquakes where GCMT dip angles lay outside of the SCARDEC dip angle intervals. Dip angles obtained from individual earthquake studies published in the literature (blue squares), W-phase inversions (cyan stars) and the Slab1.0 subduction zone model (Hayes *et al.*, 2012, orange circles) are also shown, where available. Slab1.0 dip angles correspond to the GCMT locations (latitude and longitude). Slab1.0 depths may differ compared to GCMT depths, with Peru 2007 earthquake having the largest difference (20.8 km). The mean absolute difference is 6.6 km and the median is 5.0 km. Earthquakes are plotted in ascending M_w order and their names are written in different colour according to the data used by GCMT (blue for body and mantle waves, orange for body, mantle and surface waves, purple for mantle waves).

Figure 3.8 shows that there is large scatter in published earthquake fault dip angle values, often spreading over a range of 20° or more (e.g., for New Guinea 2002, Rat Islands 2003, Peru 2007), with the Peru 2007 earthquake showing the largest variability (28°). The mean intra-event dip angle variability over all the earthquakes studied is 14° . In some cases the GCMT dip angles are the lowest end-members and the SCARDEC dip angles are the highest end-members, especially for earthquakes where there are not many dip angle values available from other studies (e.g., for Mindanao 2002, Irian Jaya 2009, New Zealand 2009).

GCMT dip angles determined using only long-period mantle waves (see earthquakes in purple font in Figure 3.8) are always shallower than SCARDEC, and in most cases shallower than Slab1.0 or W-phase dip angles (e.g., Sumatra 2005, Hokkaido 2003, Jalisco 1995, Kuril 1995, N. Sumatra 2010, Honshu 1994). When body-waves are also included

in the GCMT inversions (earthquakes in blue and orange font in Figure 3.8), for a few earthquakes GCMT dip angles are steeper than SCARDEC (Kamchatka 1997, Peru 2007, Solomon 2007).

Comparing SCARDEC and GCMT fault dip angles with those determined using the W-phase method and in the Slab1.0 model, we find that on average W-phase values are slightly closer to GCMT (with an average of absolute differences in dip angles between W-phase and GCMT of $|\overline{\delta^{GCMT} - \delta^{Wphase}}| = 4.7^\circ$) than to SCARDEC ($|\overline{\delta^{SCARDEC} - \delta^{Wphase}}| = 5.3^\circ$). In contrast, Slab1.0 fault dip angles show an overall better agreement with SCARDEC ($|\overline{\delta^{SCARDEC} - \delta^{Slab1.0}}| = 5.1^\circ$) than with GCMT ($|\overline{\delta^{GCMT} - \delta^{Slab1.0}}| = 7.3^\circ$). Nevertheless, these differences are relatively small and possibly not significant, thus rather highlighting that overall there is a reasonable agreement between SCARDEC and both Wphase and Slab1.0 dip angles, and better than with GCMT ($|\overline{\delta^{GCMT} - \delta^{SCARDEC}}| = 7.8^\circ$ for the 22 earthquakes considered in this section).

3.7 Frequency dependency of the comparisons

Since our earthquake data set consists of very large earthquakes with long and complex rupture processes we have to account for the details of the source time function when we model relatively short period seismic waves. Here we present a simple example highlighting these frequency effects.

Figure 3.9 shows an example of body and surface waves for the $M_w=8.3$ Hokkaido 2003 earthquake recorded on the vertical component of ANTO station. The body wave and surface wave displacement data (black traces) and the SCARDEC synthetics, convolved with both a triangular source time function (red traces) and with the SCARDEC relative source time function (green traces), are filtered around five different dominant wave periods. The SCARDEC source duration of this earthquake is 72 s.

The body wave comparisons (Figure 3.9, left) show the direct P wave, the pP free surface reflection, the reflection at the core-mantle boundary P_cP and the sP free surface reflection, all observed in the first 20 s of the seismogram. About 170 s later the surface reflection PP is observed. In the end of the seismogram the large amplitude seismic phase corresponds to the direct S wave. On the other hand, the surface wave comparisons (Figure 3.9, right) show the fundamental Rayleigh wave R_1 . By modelling the body wave

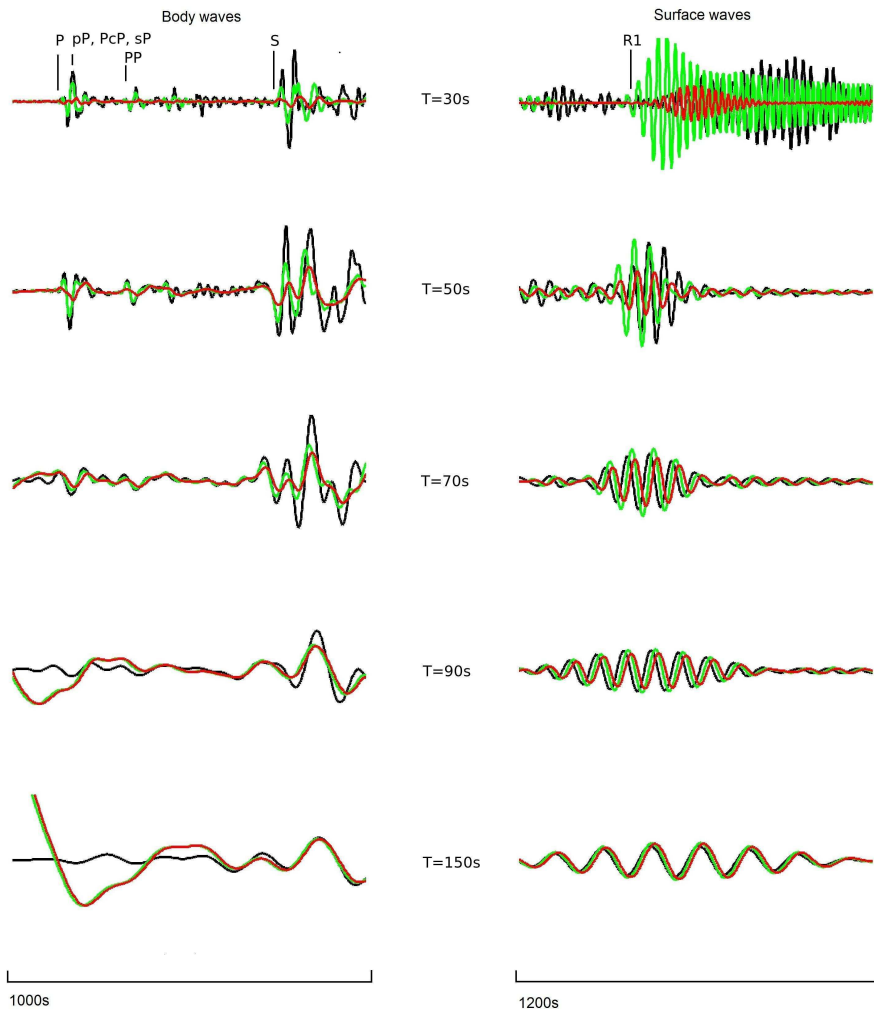


Figure 3.9: Body-wave (left) and surface-wave (right) comparisons for the $M_w=8.3$ Hokkaido 2003 earthquake for the vertical component of ANTO station. Data (black) and: (i) SCARDEC synthetics convolved with a triangular source time function (red) and (ii) SCARDEC synthetics convolved with the station's relative source time function obtained from SCARDEC (green). The SCARDEC source duration is 72 s. The dominant periods of the waveforms plotted from the top to the bottom are 30 s, 50 s, 70 s, 90 s and 150 s, respectively.

data we observe that the synthetics convolved with the triangular source time function do not explain the data for periods shorter than the source duration of the earthquake, in contrast with the synthetics convolved with the SCARDEC relative source time function. As the body wave dominant period increases this effect weakens and when the body wave dominant period ($T \sim 70$ s) is almost equal to the source duration ($T_d=72$ s) the two types of synthetics are almost identical. For body wave periods longer than 70 s the P wave reflections are no longer observable, however the S wave data are explained very well by both types of synthetics. Similar results are found for the surface waves (Figure 3.9, right). However, the fit to the data is also affected by our knowledge of the Earth's structure,

particularly for the shorter period surface waves, which are very sensitive to the shallower structure. As the surface wave dominant period increases the fit gets better for both types of synthetics.

To summarize, for seismic waves with periods longer than the source duration, the source dimensions become invisible. For periods shorter than the source duration, the seismic waves carry all the information we need to accurately determine the fine details of the source time function.

3.8 Discussion

As discussed in Chapter 1, despite tremendous advances in earthquake source imaging in the past decades, results produced by different agencies and/or research groups for the same earthquake often disagree (e.g., Weston *et al.*, 2011, 2012), suggesting large uncertainties in the models. The problem is further compounded by the fact that earthquake model uncertainties are, if at all, only rarely quantified, and by the general lack of groundtruth solutions. Thus, new source imaging benchmarking exercises and validation strategies are much needed for meaningful applications of earthquake source models (e.g., Mai *et al.*, 2007, 2010; Hjörleifsdóttir and Ekström, 2010). In order to objectively assess the quality of seismic source models and thus advance uncertainty quantification, it is important to go beyond classical resolution and/or misfit analyses. In particular, it is desirable to apply sophisticated modelling techniques to assess uncertainties due to simplified theoretical formulations and/or Earth structure employed to build the source models. Moreover, it is important to verify how well the models explain data not used in their construction for a full quantitative assessment of the robustness of the earthquake source models. This study addresses these issues and is thus well aligned with ongoing source validation efforts by carrying out new independent tests of large subduction zone earthquake source parameters estimated using SCARDEC, which is a recent fully-automated body-wave technique for the fast determination of the seismic moment, focal mechanism, depth and source time functions. Despite only using the first 32 min of body-wave data after an earthquake, we find that SCARDEC source parameters (strike, rake, M_w and depth) for the subduction earthquakes studied agree generally well with those determined using longer data time windows, signals sensitive to lower frequencies and different inversion

approaches (e.g., GCMT). Indeed, the GCMT and SCARDEC methods solve different mathematical problems (e.g., while the GCMT method determines moment tensor components, the SCARDEC technique solves directly for seismic moment, fault strike, dip and rake), with a different number of free parameters. Hence, the general agreement between SCARDEC and GCMT source parameters is encouraging, with the only clear systematic discrepancy occurring for fault dip angle estimates, where SCARDEC dip angles tend to be larger than GCMT. Our tests of these discrepancies show that SCARDEC source parameters explain independent 48-hr long, ultra-low frequency normal mode data relatively well. Vallée *et al.* (2011) found similar results when testing how well SCARDEC source parameters explain shorter time-series (25 min) of long-period surface waves (150 – 200 s) for a smaller illustrative set of subduction earthquakes (17). By using longer time-series (48-hr), lower frequency normal mode data (0.1 – 4.0 mHz) and for a larger number of earthquakes (34), this study goes beyond the work of Vallée *et al.* (2011), providing a clearer and more general demonstration of the reliability of SCARDEC source parameters at explaining completely independent datasets. Indeed, several studies have shown that free oscillation data provide useful, independent information about earthquake sources (e.g., Park *et al.*, 2005; Lambotte *et al.*, 2006, 2007); however, the full potential of these data for earthquake studies has not been studied yet, an issue that deserves to be further investigated in future work.

When using complete 3-D Earth synthetic seismograms computed using the highly accurate spectral element method, we find that SCARDEC fault dip angles explain real body-wave data as well or slightly better than GCMT dip angles, for the 3-D Earth model considered. The slight deterioration in data fit when using GCMT dip angles might be due to the surface wave moment-dip tradeoff affecting the GCMT source inversions for the earthquakes studied. Nevertheless, one needs to bear in mind that these dip angle comparisons are potentially affected by a number of complications, notably the fact that large subduction earthquakes tend to rupture an interface with a variable dip angle and possibly by tradeoffs between source and Earth structure.

At first glance it may seem surprising that the trend of steeper SCARDEC dip angles than GCMT is not associated with an overall tendency for lower SCARDEC moment magnitudes than GCMT (see Figure 3.2), for consistency with the GCMT moment-dip

tradeoff, as was reported by Vallée *et al.* (2011) for about half of the earthquakes in their study. As explained in section 3.2, the updated SCARDEC magnitudes are slightly larger than those reported by Vallée *et al.* (2011), as a result of the improved high-pass filtering introduced in the automated version of the technique. In addition, there is a number of compounding factors, such as discrepancies in earthquake depth and source duration. Indeed, for earthquakes with both similar SCARDEC and GCMT depth and source duration, we do find that steeper SCARDEC dip angles are associated with lower moment magnitudes than GCMT, reflecting the GCMT surface wave dip-moment tradeoff for shallow events (e.g., for the 2003 Hokkaido, or the 2005 and 2007 Sumatra earthquakes). However, long-duration or shallow earthquakes require a larger moment magnitude to generate long-period body waves of the same amplitude than impulsive, shorter-duration and deeper earthquakes. As some earthquakes are found shallower or longer duration by SCARDEC than GCMT, this partly explains why SCARDEC magnitudes are not systematically smaller than GCMT. Moreover, the presence of long-duration tsunami earthquakes or complex events, which will be discussed later in the Chapter, also tends to increase the SCARDEC magnitudes.

Comparisons of SCARDEC dip angles with those reported in other earthquake catalogues (GCMT and W-phase), in the Slab1.0 model and from individual earthquake studies in the literature show a large scatter in values reported for a given earthquake. This intraevent dip angle variability ranges from 6° to 28° , underlining the difficulties in constraining earthquake fault dip angles. The observed spread in dip estimates is consistent with previous findings. For example, Weston *et al.* (2011) report differences between 73 GCMT and InSAR-determined dip angles with a standard deviation of about 15° . Moreover, Ferreira *et al.* (2011) found an average intraevent variability of about 32° in fault dip estimates associated with the use of different Earth models and theories in long-period CMT surface wave inversions. In addition, Hjörleifsdóttir and Ekström (2010) quantified the resolution and errors in GCMT source determinations due to unmodelled 3-D Earth structure and data noise using SEM synthetic data. They found that the fault dip angle can be underestimated by about 5° and that the seismic moment is overestimated by about 20% for shallow subduction zone earthquakes when body wave, surface wave and mantle wave data are used in the inversions. For earthquakes with $M_w \geq 7.5$, as in this

Chapter, additional errors are expected because of the point source approximation used by GCMT. Our work, as well as these previous studies, highlight the need for quantitative uncertainty estimates to be reported along with the source parameters, particularly for subduction earthquake fault dip angles, which can strongly control tsunami run-up heights. Nevertheless, SCARDEC dip angle estimates are found to be broadly consistent with other reported values in the literature and slightly closer to those in the Slab1.0 model than GCMT.

Overall, the independent assessment of the SCARDEC method carried out in this Chapter revealed its reliability in source parameter determinations of large subduction earthquakes. The fast and fully automated version currently operating routinely has a strong potential for tsunami alert purposes, with the plus of providing realistic source time functions compared to other fast methods such as the W-phase (Kanamori and Rivera, 2008; Duputel *et al.*, 2012b). This allows the rapid identification of classical tsunami earthquakes, which have a source process anomalously long and smooth compared to that expected for their magnitude (e.g. Nicaragua 1992, N. Peru 1996, Java 2006, S. Sumatra 2010). In contrast, e.g., since 2004 the GCMT method assumes a triangular source time function (and before that a boxcar function) with half-duration determined by a constant stress drop scaling relation to the seismic moment.

Figure 3.10 compares the average SCARDEC source time functions (green) with rupture duration estimates from various individual earthquake studies. Blue vertical lines in Figure 3.10 correspond to source duration estimates obtained mainly by body-waves, and in a few cases by body and surface waves (Abercrombie *et al.*, 2001; Ammon *et al.*, 2006, 2008; Biggs *et al.*, 2009; Bilek and Engdahl, 2007; Bilek and Ruff, 2002; Bukchin and Mostinskii, 2007; Carlo *et al.*, 1999; Delouis *et al.*, 1997; Giovanni *et al.*, 2002; Gómez *et al.*, 2000; Henry and Das, 2002; Ihmlé and Ruegg, 1997; Johnson *et al.*, 1995; Kisslinger and Kikuchi, 1997; Konca *et al.*, 2008; Lay *et al.*, 2010, 2011; Lee *et al.*, 2011; Mendoza and Hartzell, 1999; Nakano *et al.*, 2008; Peyrat *et al.*, 2010; Poiata *et al.*, 2010; Robinson *et al.*, 2006; Sato *et al.*, 1996; Swenson and Beck, 1999; Tanioka *et al.*, 1996; Tanioka and Ruff, 1997; Tavera *et al.*, 2006; Yamanaka and Kikuchi, 2003; Yagi, 2004; Zobin, 1997; Zobin and Levina, 2001; Zhang *et al.*, 2012). For reference, we also show triangular/boxcar source time functions with source duration calculated using the same

scaling relation as used by the GCMT (red) for the 34 subduction earthquakes considered in section 3.3. Interplate thrust earthquakes shallower than 50 km such as those studied here are usually characterized by lower stress drops and longer source durations than other kinds of earthquakes such as, e.g., normal and/or thrust intraplate earthquakes (Allmann and Shearer, 2009). The shape and duration of their source time functions are likely related to the rheology of different subduction zones, amongst other factors (Houston, 2001). Figure 3.10 shows that overall there is a good agreement between the rupture durations obtained using SCARDEC and the majority of the values reported in individual studies. The only exception is for the M_w 7.5 Molucca Sea event, where the study by Nakano *et al.* (2008) reports a rupture duration of 16 s for this event based on a new frequency-domain waveform technique. Nevertheless, the authors do acknowledge that the value that they obtain is shorter than that expected for a M_w 7.5 event (26 s for the constant stress drop scaling relation used by the GCMT, which agrees well with the SCARDEC estimate). Although for some $M_w \leq 7.8$ events there is indeed a good agreement between SCARDEC and the triangular/boxcar source time functions used by the GCMT (e.g., for the Peru 2001b, New Guinea 2002, Irian Jaya 2009 and New Zealand 2009 earthquakes), SCARDEC generally leads to longer source durations (except for Minahassa 1996 and Jalisco 2003). Importantly, SCARDEC source time functions allow the clear identification of classical tsunami earthquakes (e.g., N. Peru 1996, Java 2006, S. Sumatra 2010), as well as of complex events (Peru 2007). The M_w 7.5 N. Peru 1996 event (022196B) is a typical tsunami earthquake, having generated a larger tsunami than expected from its surface wave magnitude, $M_s = 6.6$ (Heinrich *et al.*, 1998). Moreover, its body-wave magnitude is significantly lower ($m_b = 5.8$) than the moment magnitude, and the associated tsunami was characterised by run-up heights of 1 to 5 m along a coastline of 400 km (Bourgeois *et al.*, 1999). Similarly, the M_w 7.7 Java 2006 earthquake (200607170819A) caused a deadly tsunami with run-up heights up to 8 m to the south coast of Java. The main shock is a classical tsunami earthquake with a significant discrepancy between its surface magnitude ($M_s = 7.7$) and body-wave magnitude ($m_b = 6.1$), characterised by an unusually low rupture velocity (1.0 – 1.5 km/s). The rupture included five to six episodes of moment release on a smooth and long source time function of 185 s (Ammon *et al.*, 2006). Finally, the M_w 7.8 S. Sumatra 2010 earthquake (201010251442A)

caused a tsunami with run-up heights up to 9 m along the southwestern coasts of Pagai islands, significantly higher than expected, given its magnitude. The rupture time which was found by independent studies (Lay *et al.*, 2011; Newman *et al.*, 2011), 90 – 125 s, much longer than the duration used by the GCMT, is in good agreement with SCARDEC. Moreover, the main shock was characterised as a slow event with a rupture velocity of 1.5 km/s and with a typical tsunamigenic earthquake difference between surface magnitude ($M_s = 7.8$) and body-wave magnitude ($m_b = 6.5$).

The SCARDEC source time functions also enable us to identify some complex features in the rupture history of the earthquakes in our data set, with the M_w 8.0 Peru 2007 earthquake (200708152340A) being one of the most prominent cases. The main shock caused strong damage to the city of Pisco and was followed by a significant local tsunami with run-up heights up to 10 m at the Paracas peninsula (Sladen *et al.*, 2010). While the earthquake has a GCMT source half-duration of 23.5 s, its SCARDEC source time function highlights the complex character of this rupture with two different episodes and a total source duration of 121 s. Indeed, other studies reported a slip history of the main shock being characterised by the presence of two distinct patches, rupturing a total fault area of about 300 km by 160 km. The first patch was located close to the hypocentre and the second, which was larger, ruptured to the south around 60 s later (Motagh *et al.*, 2008; Sladen *et al.*, 2010), in good agreement with SCARDEC's source time function.

All these examples clearly show the power of the SCARDEC method for the rapid discrimination of typical tsunami events and of complex rupture patterns, underlining its strong potential for seismic monitoring and tsunami warning efforts. In practice, SCARDEC's source time functions could be used in an automated way to identify tsunami subduction earthquakes using criteria such as: (i) earthquake depth being shallower than around 25 km; (ii) the source time function having a duration at least 1.5–2 times longer than the values used by the GCMT; and, (iii) the source time function peak moment rate being at least 1.5–2 times lower than that in the triangular source time function used by the GCMT.

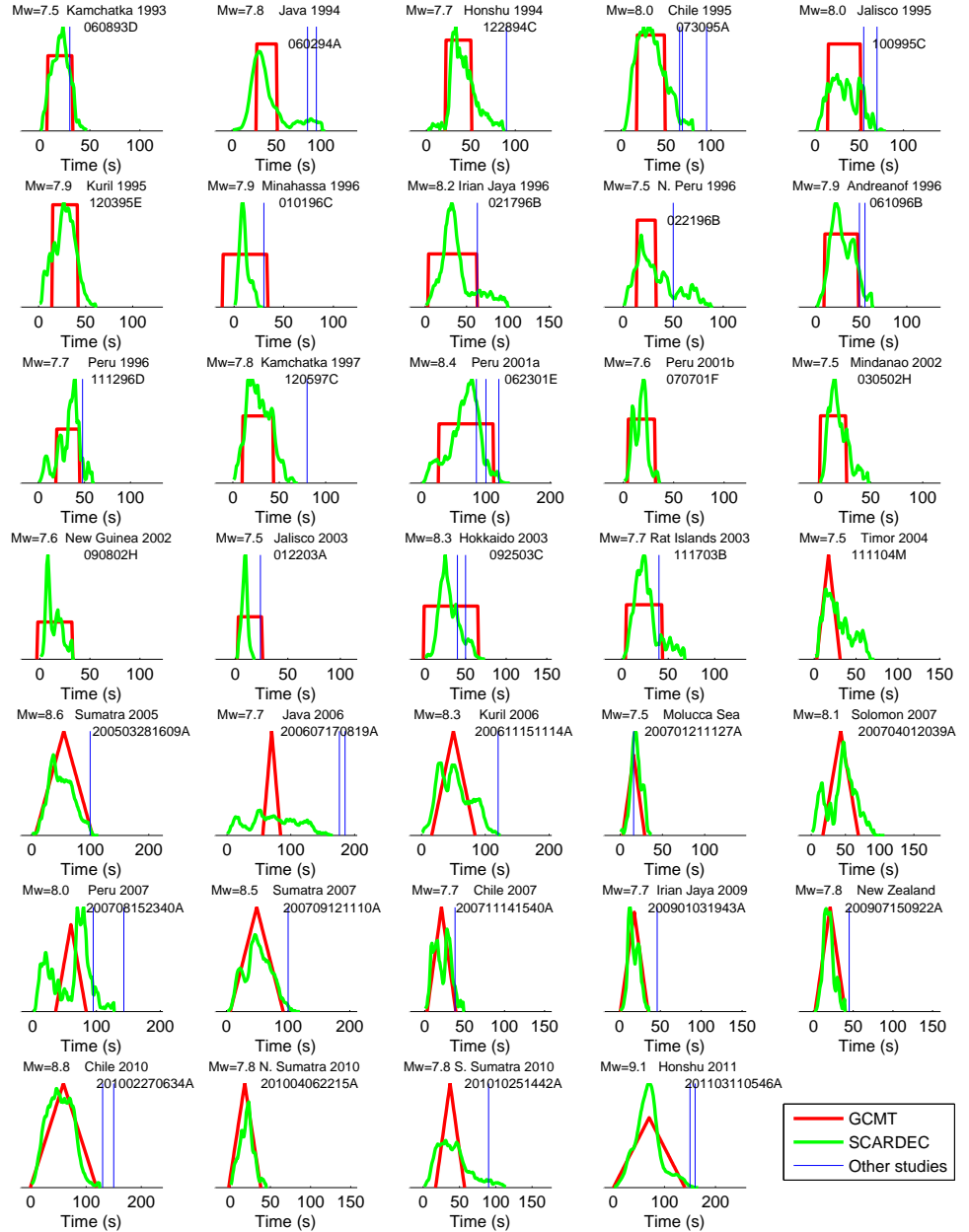


Figure 3.10: Comparison between SCARDEC average source time functions (green) with rupture durations estimated from individual earthquake studies (blue vertical lines; see main text). For reference, we also show triangular/boxcar source time functions with rupture duration estimated from a constant stress drop scaling relation, as used by the GCMT catalogue (red), for the 34 subduction earthquakes considered in this Chapter. GCMT source time functions are represented as boxcar functions for earthquakes that occurred before 2004. After the 1st of January 2004 the GCMT source time function is assumed to be triangular (Ekström *et al.*, 2012). Zero time corresponds to the PDE time of each earthquake. Earthquake names, GCMT magnitudes and codes are shown on top of each plot. Three cases of classical tsunami earthquakes are identified (M_w 7.5 N. Peru 1996 – 022196B, M_w 7.7 Java 2006 – 200607170819A, M_w 7.8 S. Sumatra 2010 – 201010251442A) by SCARDEC, having smoother and longer source time functions than expected from their moment magnitude.

3.9 Conclusions

We have tested the robustness and reliability of SCARDEC source parameters for major ($M_w \geq 7.5$) shallow subduction earthquakes of the past 20 years. We found an overall good agreement between SCARDEC and GCMT source parameters except for the fault dip angle, for which the SCARDEC values were found on average steeper than GCMT solutions. We examined these discrepancies and validated the method by showing that overall SCARDEC source parameters explain independent long-period, 48-hour normal mode data spectra reasonably well, despite using only the first 32 min of body wave data following the earthquake. Using accurate purely numerical forward modelling of body wave data on a 3D Earth model, we found that the SCARDEC dip angles explain body wave data as well or slightly better than the GCMT method. SCARDEC dip angles showed also a good agreement with values from other individual earthquake studies and with subduction slab geophysical constraints. In addition, unlike some other routine source inversion methods, SCARDEC estimates realistic source time functions, enabling the rapid identification of classical tsunami earthquakes with anomalously large source durations compared to their magnitudes and the modelling of the associated complex seismic waveforms. Thus, the SCARDEC method complements existing routine seismic monitoring techniques and offers a strong potential for applications in ocean-wide tsunami warning.

Chapter 4

A normal mode earthquake source inversion technique for the determination of spatio-temporal characteristics of large earthquakes

4.1 Summary

As briefly discussed in previous Chapters, low-frequency normal mode data provide an independent way of characterising the overall kinematic source process of large magnitude earthquakes ($M_w > 8.0$). We present a new earthquake source inversion method based on normal mode data for the simultaneous determination of the rupture duration, length and moment tensor of large earthquakes with unilateral rupture. We use ultra-low-frequency ($f < 1$ mHz) normal mode spheroidal multiplets and the phases of split free oscillations, which are modelled using Higher Order Perturbation Theory (HOPT), taking into account the Earth's rotation and ellipticity, self-gravitational forces and lateral heterogeneity. A Monte Carlo exploration of the model space is carried out, enabling the assessment of source parameter tradeoffs and uncertainties. We carry out synthetic tests for four different realistic artificial earthquakes with different faulting mechanisms and magnitudes M_w 8.1–9.3 to investigate errors in the source inversions due to: (i) unmodelled 3-D Earth structure; (ii) noise in the data; (iii) uncertainties in spatio-temporal earthquake location;

and, (iv) neglecting the source finiteness in point source moment tensor inversions. We find that rupture duration determinations are relatively insensitive to the presence of noise in the data and to errors in earthquake location. However, they are strongly affected by errors in 3-D Earth structure, notably for the lowest magnitude (M_w 8.1) events considered, for which the rupture duration cannot be determined if lateral heterogeneity is not properly taken into account in the modelling. On the other hand, noisy data, uncertainties in location and unmodelled lateral heterogeneity can all lead to substantial errors in rupture length estimates, up to 50-60% errors for the M_w 8.1 events. We find that the errors in moment magnitude, fault strike and dip angles from the finite source inversion tests are generally small, with the rake angle showing slightly larger errors (up to 14°). In addition, when studying the effect of ignoring the source finiteness on multiplet point source inversions, the rake angle also shows the largest errors (up to 20°). Nevertheless, all the errors in point source parameters found in this study are comparable or smaller to those reported in previous earthquake source studies. This suggests that the new technique presented is useful for robust characterisations of bulk kinematic source parameters of large earthquakes.

4.2 Introduction

Since the great 1960 Chile earthquake, the Earth's low-frequency normal modes have been observed and used to investigate deep Earth structure (e.g., Dziewonski and Anderson, 1981; Masters *et al.*, 1982; Ritsema *et al.*, 1999; Mégnin and Romanowicz, 2000), and, to some extent, to study earthquake sources (Abe, 1970; Ben-Menahem *et al.*, 1972; Gilbert, 1973; Kedar *et al.*, 1994; Park *et al.*, 2005; Lambotte *et al.*, 2006, 2007). Normal mode data are useful to characterise the overall source kinematics of very large earthquakes ($M_w > 8.0$), notably to estimate their seismic moment. However, compared to other data types (e.g., body and surface waves), the Earth's free oscillations have been less used in source studies, because they typically require very long continuous high-quality recordings of several days, which restricts their use in fast and routine source studies.

Early source studies using normal mode data were limited to seismic moment determinations (e.g., Abe, 1970; Kedar *et al.*, 1994) or to fault geometry and mechanism estimates (e.g., Ben-Menahem *et al.*, 1972). For example, Kedar *et al.* (1994) took into

account the finiteness of the source when modelling long-period free oscillations excited by the 1989 Macquarie ridge earthquake and found that the Global Centroid Moment Tensor (GCMT) catalogue (Dziewonski *et al.*, 1981; Ekström *et al.*, 2012) underestimated the moment magnitude of this earthquake. More recently, the giant 2004 Sumatra earthquake was extremely well recorded by the global seismic network, which offered a unique opportunity to observe and study high-quality free oscillations in the ultra low-frequency band (0–1 mHz), prompting several normal mode source studies of this earthquake. For example, Park *et al.* (2005), Stein and Okal (2005) and Okal and Stein (2009) used normal mode data to show that the magnitude of the 2004 Sumatra earthquake was much larger ($M_w \sim 9.3$) than initially inferred from mantle waves in the GCMT catalogue ($M_w \sim 9.0$). Specifically, they showed that the GCMT source model poorly explains normal mode amplitude spectra in the 0–1 mHz frequency band, with an additional seismic moment of roughly 7.16×10^{29} dyne*cm being required. Lambotte *et al.* (2006, 2007) used the phase of normal mode singlets to determine the rupture duration and length of the 2004 Sumatra event and to investigate the rupture history of the 28 March 2005 $M_w 8.6$ Nias earthquake, offering the first estimates of rupture duration and length ever obtained from normal mode data. Moreover, Konca *et al.* (2007) used normal mode data to test source models of the 2005 Nias earthquake. Nevertheless, and despite this recent progress, the potential of normal mode data for source studies has not been fully investigated yet. In particular, issues such as the influence of 3-D Earth structure, noisy data and of non-uniqueness in normal mode source inversions deserve further attention.

Previous studies have shown that various sources of error can affect earthquake source inversions based on body and surface waves, such as station coverage, noise in the data and unmodelled 3-D Earth structure (Helffrich, 1997; Ferreira and Woodhouse, 2006; Ferreira *et al.*, 2011; Hjörleifsdóttir and Ekström, 2010; Mai *et al.*, 2007, 2010). Moreover, some past studies have investigated the issue of non-uniqueness in strong motion, body and surface wave earthquake source inversions (e.g., Pavlov, 1994; Mai *et al.*, 2010; Kane *et al.*, 2011; Wen and Chen, 2011). In addition, various attempts have been carried out to assess earthquake source parameter uncertainties (e.g., Valentine and Trampert, 2012), which are still not routinely fully quantified and reported. Probabilistic inversion schemes searching the model space (e.g., Sambridge, 1999a; Marson-Pidgeon *et al.*, 2000; Vallée

et al., 2011) are particularly attractive, as they enable error estimations and parameter tradeoff analyses by generating an ensemble of models with acceptable data fit, rather than just the determination of an optimal model.

This study addresses these issues in the context of low-frequency normal mode earthquake source inversions. We present a source inversion technique for the simultaneous determination of fault mechanism, moment magnitude and the length and duration of unilateral rupture earthquakes using normal mode data. We assess the robustness of the technique by carrying out realistic systematic synthetic tests to quantify errors in the source parameters due to noise in the data, incomplete knowledge of the earthquake's spatio-temporal location and unmodelled 3-D Earth structure. We focus on earthquakes in four different representative tectonic settings and use a direct search inversion scheme to explore the parameter space and investigate tradeoffs and uncertainties in the source parameters. In addition, issues such as the choice of misfit function used in the source inversions and the effect of neglecting the source's finiteness in normal mode multiplet point source inversions are also addressed.

4.3 Methodology

4.3.1 Theoretical background

As explained in Chapter 2, normal mode multiplets are characterized by spectral peaks of degenerate eigenfrequencies in a spherically symmetric, non-rotating perfectly elastic and isotropic (SNREI) Earth model. The Earth's rotation, ellipticity and heterogeneity remove this degeneracy and split the multiplets into $2l + 1$ singlets each characterised by an azimuthal order m , where l is the angular order. When studying very large magnitude earthquakes with rupture lengths exceeding several hundreds of kilometers, the finite character of the source cannot be neglected when modelling low-frequency Earth's free oscillations. Thus, a finiteness term F_m must be taken into account in order to represent correctly the amplitudes and phases of the normal mode singlets. The Fourier transform of the finite source acceleration response α_m^{fs} of an isolated singlet with azimuthal order m and with angular eigenfrequency ω_k can be expressed as (Ben-Menahem and Singh, 1980):

$$\alpha_m^{fs}(x, \omega) = \alpha_m^{ps}(x, \omega) F_m \quad (4.1)$$

where F_m is the source finiteness term and $\alpha_m^{ps}(x, \omega)$ is the point source acceleration response:

$$\alpha_m^{ps}(x, \omega) = \sum_{i=1}^6 \psi_i^m(x, \omega) M_i \quad (4.2)$$

M_i are the six elements of the seismic moment tensor and $\psi_i^k(x, \omega)$ are the excitation kernels, i.e., the partial derivatives of the synthetic spectra of a point source with respect to the moment tensor elements:

$$\psi_i^m = \frac{\partial \alpha_m^{ps}}{\partial M_i}. \quad (4.3)$$

Assuming a simple unilateral rupture with constant dislocation and step time dependence, the source finiteness term can be represented as a function of the so-called initial phase X_m of a singlet with azimuthal order $\pm m$ (Ben-Menahem and Singh, 1980):

$$F_m = \frac{\sin(X_m)}{X_m} e^{-iX_m} \quad (4.4)$$

with the initial phase being linearly related to the rupture duration (T_r) and length (L):

$$X_m = \frac{\pi T_r}{T_m} + \frac{L m \sin(\phi)}{2 r_o \sin(\theta)} \quad (4.5)$$

where r_o is the Earth's radius, T_m is the singlet's period, ϕ is the fault's azimuth and θ is the epicentral colatitude. The first term of equation 4.5 carries information about the rupture duration, while the second term is associated with the fault's length.

Equation 4.5 is an approximate description of the phase of normal mode singlets (Dziewonski and Romanowicz, 1977; Ben-Menahem and Singh, 1980). It is exact only when the second term is close to zero, thus only for singlets with $m=0$ and radial modes, or for E-W oriented faults lying on the equator (Lambotte *et al.*, 2006). In section 4.4 we carry out some numerical experiments to test the domain of validity of equation 4.5.

4.3.2 Forward modelling

In order to obtain realistic theoretical low-frequency ($f < 1.0$ mHz) normal mode seismograms and point source excitation kernels $\psi_i^k(x, \omega)$ (see equation 4.2), we use the Higher Order Perturbation Theory (HOPT) approach developed by Lognonné and Romanowicz (1990), Lognonné (1991) and Lognonné and Clévédé (2002). We follow the approach explained in Chapter 2, whereby the equation of motion is solved in the frequency domain starting from a spherical, non-rotating, elastic or anelastic Earth using the 1-D PREM model (Dziewonski and Anderson, 1981). Perturbations are then added to the operators taking into account the Earth's rotation and ellipticity as described by Dahlen and Tromp (1998) and three-dimensional structure using the mantle model SAW12D, (Li and Romanowicz, 1996). Perturbations are obtained up to the 3rd order in frequency and 2nd order in amplitude.

Interaction matrices are built according to Woodhouse and Dahlen (1978) and lateral variations in density are taken into account by a renormalization of the elasto-dynamic operator (Lognonné and Romanowicz, 1990). For a given mode, a Frobenius norm quantifying the coupling strength between the mode and all other modes is computed, so that all the free oscillations with significant coupling strength are used in the calculations. Finally, source and receiver modulation functions are calculated (Clévédé and Lognonné, 1996) and the seismograms are then obtained by means of mode summation.

4.3.3 Source inversion algorithm

We have implemented a grid search technique for the determination of earthquake source parameters using ultra-low frequency spheroidal normal mode data (0–1 mHz). Our source inversion technique is designed to carry out inversions in two different ways: (a) a simple normal mode multiplets inversion, assuming a point source, for the determination of four source parameters – strike, dip, rake and moment magnitude ($\phi, \delta, \lambda, M_w$, respectively); (b) a normal mode singlets inversion, taking into account the finite rupture of a unilateral seismic source for the determination of six source parameters – strike, dip, rake, moment magnitude, rupture duration and rupture length ($\phi, \delta, \lambda, M_w, T_r, L$, respectively).

A flowchart summarising our algorithm is shown in Figure 4.1.

The technique consists of two major parts. In the first part, data and excitation kernels

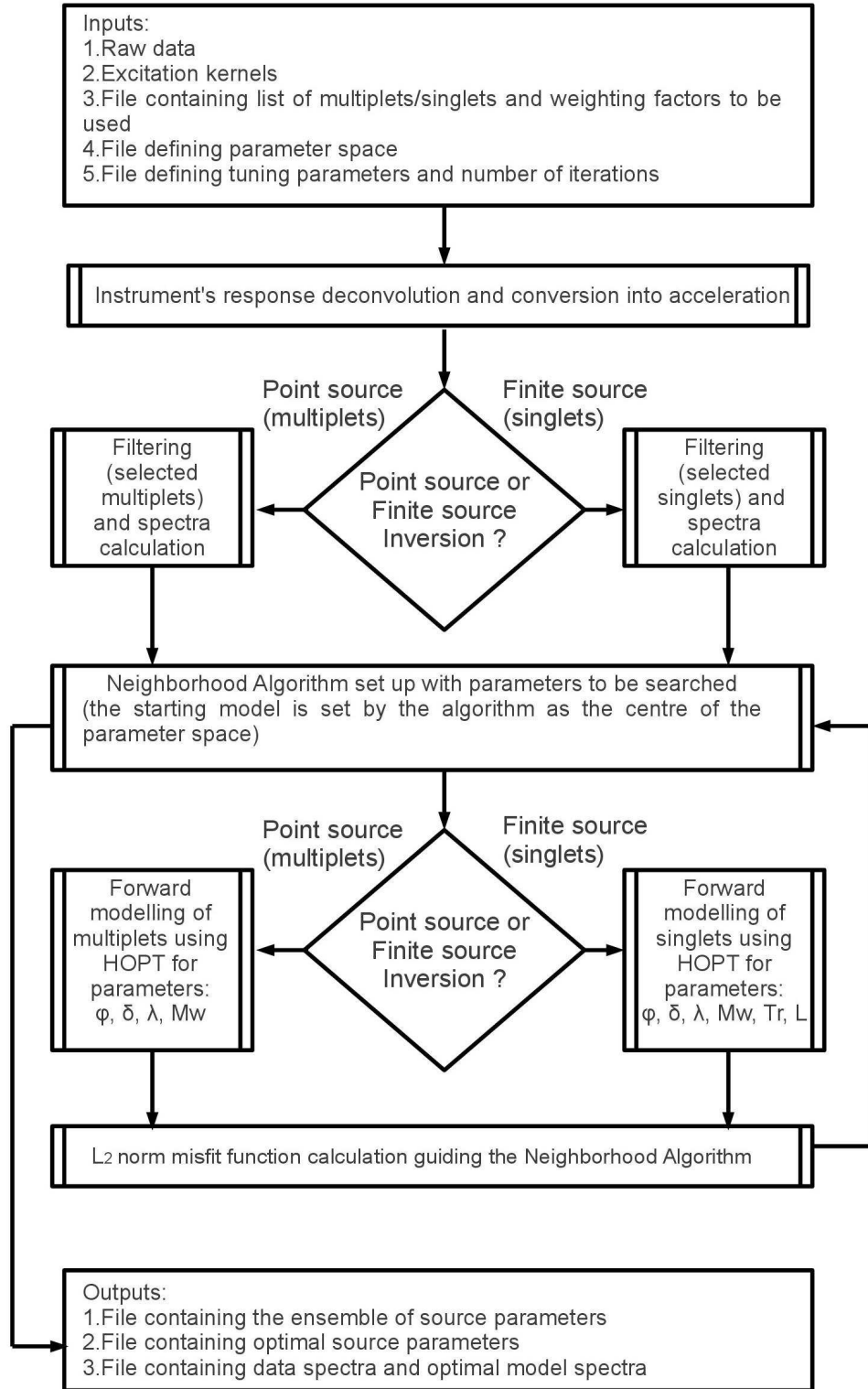


Figure 4.1: Simple flowchart showing the structure of the new algorithm developed in this Chapter for normal mode earthquake source inversions. The first part of the algorithm carries out all the necessary processing, while the second part is doing the grid search and determines the optimal model. The filtering of and spectra calculations of singlets is followed by the calculation of the phases of the singlets as explained in section 4.4.

are read by the algorithm and all the necessary input parameters are defined (parameter space, multiplets/singlets to be used and their weighting factors and tuning parameters for the grid search). Realistic excitation kernel seismograms are built using HOPT for a given spatio-temporal earthquake location, as described in the previous subsection. According to the inversion type used (point source or finite source inversion), different parameter space and tuning parameters are used; these details will be discussed in subsection 4.3.3.1. The instrument response is deconvolved from the data and they are converted into acceleration. Again according to the inversion type, data and excitation kernel seismograms are filtered multiplet by multiplet, or singlet by singlet, proper time windows are selected (see section 4.3.3.2 for details), a Hanning taper is applied, the seismograms are padded with zeros and their spectra are finally obtained. In the second part of the algorithm, the grid search is carried out using the Neighbourhood Algorithm (Sambridge, 1999a). The Neighbourhood Algorithm (NA) is a well adapted algorithm to solve different geophysical problems like tomographic problems, earthquake location and source inversion problems (i.e., Sambridge, 1999a; Marson-Pidgeon *et al.*, 2000; Sambridge and Kennett, 2001; Vallée *et al.*, 2011). It is a directed search method that falls in the same category of genetic and simulated annealing algorithms and, in a similar manner, it has a number of control parameters. Specifically, the NA requires two tuning parameters: (i) n_s , the number of models generated at each iteration; and, (ii) n_r , the number of Voronoi cells in which the n_s models are randomly selected. The tuning parameters strongly depend on the misfit function used and on the dimensions of the parameter space. Therefore, each geophysical problem should be treated with caution as the tuning parameters are very likely to differ from one application to the other (Sambridge, 1999a; Marson-Pidgeon *et al.*, 2000). For our point source inversions (four-dimensional parameter space) we carried out many experiments and found that the optimal tuning parameters are $n_s=36$ and $n_r=9$, and for our finite source inversions (six-dimensional parameter space) the optimal tuning parameters are $n_s=80$ and $n_r=10$.

The grid search involves forward modelling and the calculation of a data misfit function, which drives the search over the multi-dimensional parameter space. According to the inversion type selected in the first part, forward modelling is carried out based on equation 4.1 if a six-dimensional finite source inversion is selected, or equation 4.2

if a four-dimensional point source inversion is selected instead. The theoretical spectra ($\alpha^s(\omega)$) is then compared to the data spectra ($\alpha^d(\omega)$) through a L_2 – norm misfit function (m_{L_2}), which is sent back to the Neighbourhood Algorithm and drives the grid search:

$$m_{L_2} = \sum_{i=1}^{N_k} \sum_{j=1}^{N_{st}} \int_{\omega_1}^{\omega_2} w_{i,j} \left[\frac{(\alpha_{i,j}^d(\omega) - \alpha_{i,j}^s(\omega))^T (\alpha_{i,j}^d(\omega) - \alpha_{i,j}^s(\omega))}{\alpha_{i,j}^d(\omega)^T \alpha_{i,j}^d(\omega)} \right] d\omega \quad (4.6)$$

where T denotes the transpose matrix, N_k is the number of multiplets or singlets, N_{st} is the number of stations and w is a weighting factor, ranging from zero to one. ω_1 and ω_2 define the frequency interval of the multiplet/singlet considered in the inversion. For our synthetic tests we used the same weighting factor ($w=1$) for all multiplets/singlets. We carried out many inversions using a variety of observables, from amplitude spectra to real and imaginary spectra (which we denote as FFT spectra), as well as combinations of the two. In sections 4.5.3 and 4.5.4 we present results based on a misfit function where a combination of amplitude and FFT spectra are used, giving a weight of 0.97 to the amplitude part and a weight of 0.03 to the FFT part of the function. In section 4.5.5 we shall discuss various tests carried out for a variety of misfit functions. Once the NA converges, the ensemble of the source models, optimal source model, data spectra and optimal source model spectra are then written into output files.

Following an approach similar to Vallée *et al.* (2011), a heuristic misfit deterioration criterion is used (acceptable parameters correspond to source models yielding misfit values 1% larger than the lowest misfit associated with the optimal source model). Furthermore, standard deviations of distributions of parameters from the Neighbourhood Algorithm are also useful to assess uncertainties.

We successfully implemented both the serial and parallel versions of the NA. Point source inversions using the serial version take up to six minutes of CPU time, while the parallel version (using 36 processors) is roughly a couple of minutes faster in a Intel Xeon 2.6GHz 8-core processors computer cluster. Most of our finite source singlets inversions take up to 30 minutes in the serial version, and about eight to ten minutes less in the parallel version (using 80 processors). However, the time spent for the inversions to be carried out depends on the number of iterations and the number of multiplets/singlets to be processed.

4.3.3.1 Parameter space definition

Given a guess start source model $\phi_o, \delta_o, \lambda_o, M_{w_o}$, a parameter space over the fault geometry and the moment magnitude is chosen as $\phi_o \pm 20^\circ, \delta_o \pm 15^\circ, \lambda_o \pm 20^\circ, M_{w_o} \pm 0.3$. In the case where the spatio-temporal characteristics of a unilateral rupture earthquake are also included in the inversion, a start guess value for the rupture duration T_{r_o} is obtained from the earthquake's seismic moment according to the scalar equation $\tau_h = h \cdot M_o^{1/3}$, where $T_{r_o} = 2\tau_h$. τ_h is the half-duration in s, M_o is the seismic moment in Nm and $h = 2.4 \times 10^{-6}$ s/(Nm)³ is a coefficient. The latter is similar to the scaling law used in the GCMT catalogue for half-duration determinations as discussed in Dahlen and Tromp (1998). The start guess value for rupture length (L_o) is then estimated from T_{r_o} , assuming that an average rupture velocity of 2.4 km/s is representative for large magnitude earthquakes ($M_w > 8.0$) (e.g., Vallée, 2007; Lorito *et al.*, 2008). We then carry out the grid search using a range of 100 s and of 240 km around L_o and T_{r_o} , respectively. The use of these large intervals of source parameters ensure a good sampling of the parameter space by the NA; indeed, these parameter ranges are much larger than differences in source parameters reported by various existing catalogues such as the GCMT, W-phase (Kanamori and Rivera, 2008; Duputel *et al.*, 2012b) and SCARDEC (Vallée *et al.*, 2011). For an explicit reference to typical ranges of model parameters from various studies, the reader is referred to comparisons in Chapter 3.

4.3.3.2 Time window selection

For the finite source inversion a good separation of a multiplet's singlets is essential in order to account for the finiteness effect. The time window needed to separate a multiplet's singlets is at least one Q-cycle (Dahlen, 1982). The Q-cycle is simply the time needed for the signal amplitude to decay by $\exp(-\pi)$. If $N_m = \pi/\gamma_m$ is the Q-cycle of a normal mode singlet of azimuthal order m , where γ_m is the attenuation rate ($\gamma_m = \omega_m/2Q_m$, ω_m and Q_m are the angular eigenfrequency and the quality factor of the singlet), the Q-cycle can be simply expressed as a product of the eigenperiod T_m and the quality factor Q_m of the singlet:

$$N_m = \frac{2\pi Q_m}{\omega_m} = T_m Q_m \quad (4.7)$$

High quality factor fundamental spheroidal multiplets in the 0–1 mHz frequency range, like ${}_0S_2$ and ${}_0S_3$, have Q-cycles of 19 and 10 days, respectively. The ${}_0S_0$ radial mode has a Q-cycle of about 75 days. Phase estimates of this mode are stable after 15 days, as found by Lambotte *et al.* (2007). For this reason in the case of the singlets' inversion, we restrict our time window to 20 days for all three multiplets. On the other hand, ${}_0S_4$ and ${}_0S_5$ multiplets have much lower quality factors, meaning that their signal decays much faster before their singlets are being separated adequately because of the broader spectral peaks. Therefore, they are not used in the singlet inversions, same as in Lambotte *et al.* (2006). Use of more sophisticated techniques, such as the singlet stripping technique, would allow a better singlet separation of these multiplets (Lambotte *et al.*, 2007).

For the point source multiplet inversions, any time window can be potentially used, as long as a high signal to noise ratio is achieved as a function of the earthquake's magnitude. However, for consistency, all the point source (multiplets) synthetic tests presented in this Chapter are carried out using the same 20-day time window same as in the finite source (singlets) inversions. Singlets or multiplets spectra are finally extracted after narrow-filtering the time-series within the frequency range of each target spectral peak. Specifically, low-pass and high-pass cosine filters are used by setting pass-band and pass-stop frequencies according to the target frequency of the spectral peak and the frequency range of the associated multiplet or singlet.

4.4 Validity of the initial phase modelling

As explained in the previous section, equation 4.5 describing the relationship between rupture length and duration and the initial phase of normal mode singlets is approximate, being only exact for radial modes, or for E-W oriented faults lying on the equator (Lambotte *et al.*, 2006). We started by carrying out various experiments to test its validity for different fault orientations and different earthquake latitude locations.

We assume an artificial unilateral rupture thrust earthquake, with a rupture duration $T_r=100$ s, over a line fault with total length $L=240$ km. Finite rupture seismograms, which are used as input synthetic data, are represented as a superposition of three point source seismograms with the same fault geometry and mechanism, evenly distributed along the line fault, each one with the same moment magnitude (Figure 4.2). We then calculate

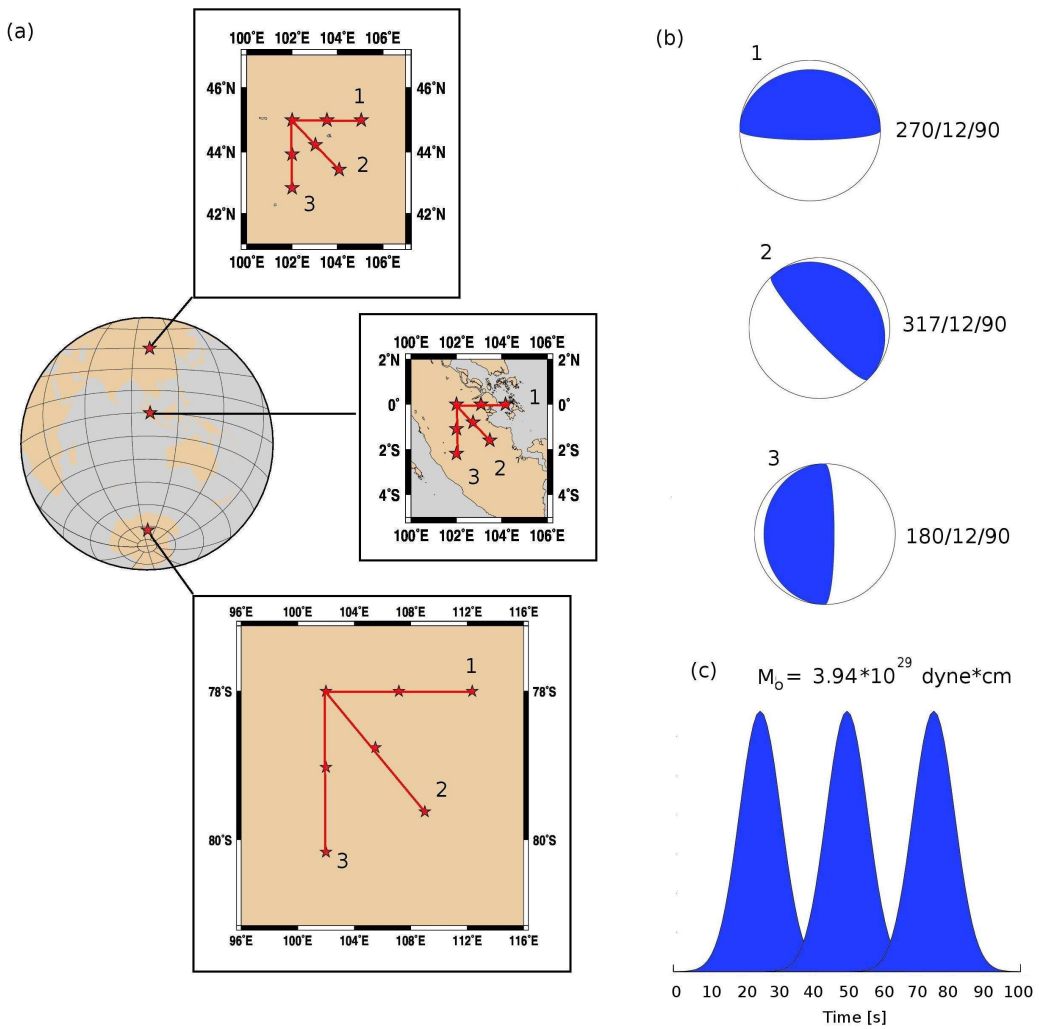


Figure 4.2: (a): A global map showing locations of three sites in different latitudes (north hemisphere, equator, south hemisphere) where line faults with three different orientations are used to generate finite source synthetic data for the experiments presented in section 4.4. Stars in zoom-in maps show locations of three point sources superimposed to build finite source synthetic data with the rupture propagating over 240 km in length towards east (1), southeast (2) and south (3). (b): Earthquake mechanisms of point sources that are used to build synthetic data. (c): Moment rate function of finite synthetic data with a total duration of 100 s. Each of the three point sources is represented as a Gaussian function of 50 s in duration, rupturing every 25 s.

point source seismograms at the rupture initiation location with seismic moment equal to the total seismic moment used to build the finite rupture seismograms, and with the same fault geometry and mechanism. All synthetic seismograms are built using HOPT taking into account Earth's rotation, ellipticity and 3-D mantle heterogeneity, notably SAW12D mantle model (Li and Romanowicz, 1996), for different combinations of earthquake latitude locations and fault orientations (see Table 4.1).

Equation 4.1 is a simple linear problem which can be represented in matrix notation for n data points recorded at the j^{th} station as:

$$\begin{bmatrix} d_{a_1}^j \\ d_{b_1}^j \\ d_{a_2}^j \\ d_{b_2}^j \\ \cdot \\ \cdot \\ d_{a_n}^j \\ d_{b_n}^j \end{bmatrix} = \begin{bmatrix} G_{a_1}^j & -G_{b_1}^j \\ G_{b_1}^j & G_{a_1}^j \\ G_{a_2}^j & -G_{b_2}^j \\ G_{b_2}^j & G_{a_2}^j \\ \cdot & \cdot \\ \cdot & \cdot \\ G_{a_n}^j & -G_{b_n}^j \\ G_{b_n}^j & G_{a_n}^j \end{bmatrix} \times \begin{bmatrix} F_m^{Re} \\ F_m^{Im} \end{bmatrix} \quad (4.8)$$

where d is the data vector and G stands for the point source theoretical spectra. The subscripts a and b are the real and imaginary parts of the Fourier transform. The phase of the complex number F_m is the initial phase of a singlet (X_m) which can estimate the rupture duration and length of a simple rupture model.

The real and imaginary parts of the complex finiteness term can be determined by using a least-squares approach (e.g. Tarantola, 1987):

$$F_m = (G^T C_d^{-1} G)^{-1} G^T C_d^{-1} d \quad (4.9)$$

where T stands for the transpose matrix and C_d is the covariance matrix which includes *a priori* data uncertainties. In our case, we use this approach to carry out synthetic tests without noise added to the synthetic data (finite source seismograms) and using the same Earth model to build both the finite and point source seismograms. Therefore, in these tests we can simply replace the covariance matrix with the identity matrix.

We first linearly invert equation 4.1 for the real and imaginary parts of the finiteness

terms of a set of different singlets. Their initial phases ($X_m = \text{atan}^{-1}(F_m^{Im}/F_m^{Re})$) are then calculated and they are used to build a new data vector. If n singlets have been used in the previous step ($n > 2$), equation 4.5 can be written in matrix notation as an overdetermined linear problem with only two variables to be determined, the rupture duration and length:

$$\begin{bmatrix} X_{m_1} \\ X_{m_2} \\ \cdot \\ \cdot \\ X_{m_n} \end{bmatrix} = \begin{bmatrix} \frac{\pi}{T_{m_1}} & \frac{m_1 \sin(\phi)}{2r_o \sin(\theta)} \\ \frac{\pi}{T_{m_2}} & \frac{m_2 \sin(\phi)}{2r_o \sin(\theta)} \\ \cdot & \cdot \\ \cdot & \cdot \\ \frac{\pi}{T_{m_n}} & \frac{m_n \sin(\phi)}{2r_o \sin(\theta)} \end{bmatrix} \times \begin{bmatrix} T_r \\ L \end{bmatrix} \quad (4.10)$$

The linear system described by equation 4.10 can be similarly solved in a second step linear inversion, yielding single rupture duration and length estimates.

For the purpose of our synthetic tests we extract all the ${}_0S_2$ singlets and ${}_0S_0$ radial modes from the point and finite source synthetic data. These singlets are then used in linear inversions based on equation 4.1, to determine singlets finiteness terms F_m , which are in turn used to calculate the corresponding initial phases, as described above. Finally, we perform linear inversions of the initial phases to determine rupture duration and length using equation 4.5. Our main results are summarised in Table 4.1, which shows that the rupture duration is very well retrieved even for earthquake latitudes quite far from the equator (e.g., for $\text{lat} = -78^\circ$) and for fault orientations deviating $\sim 45^\circ$ from an E-W orientation. Rupture length estimates are more sensitive to deviations in earthquake latitude location and to fault strike, but are still overall well determined, with errors not exceeding about 5% for the cases considered. For a N-S fault orientation, the second term of equation 4.5 vanishes, thus, only a rupture duration determination is feasible.

4.5 Synthetic tests

In this section we carry out synthetic tests to investigate the full potential of low-frequency normal mode data for earthquake source characterizations in the presence of data noise, errors in Earth's structure and uncertainties in spatio-temporal earthquake location.

Table 4.1: Results of rupture duration (T_r) and length (L) obtained from linear inversion synthetic tests, with respect to earthquake's latitude and orientation. A simple finite source which is considered as a superposition of three subevents, ruptures unilaterally a line fault of 240 km in 100 s. Rupture duration is always well determined, no matter the latitude of the earthquake or the orientation of the source.

Strike ($^{\circ}$)	Latitude ($^{\circ}$)	T_r (s)	L (km)
180.0	0.0	99.9	—
180.0	45.0	99.9	—
180.0	-78.0	99.9	—
270.0	0.0	99.9	239.9
270.0	45.0	100.1	239.5
270.0	-78.0	100.0	229.0
317.0	0.0	99.9	243.1
317.0	45.0	99.9	240.1
317.0	-78.0	99.9	228.8

4.5.1 Selected earthquakes

We built a synthetic data set for four artificial earthquakes with different faulting mechanisms (thrust, strike-slip, normal) occurring in different tectonic settings (Figure 4.3). In order to ensure that our tests are realistic, the events used are based on real earthquakes reported in the GCMT catalogue. We select two thrust earthquakes based on the M_w 8.8 27 February 2010 Chile and on the M_w 9.2–9.3, 26 December 2004 Sumatra earthquakes. We also include the 13 January 2007 M_w 8.1 Kuril islands normal earthquake and the 25 March 1998 M_w 8.1 Antarctic plate strike-slip earthquake.

The 2004 Sumatra earthquake is one of the largest thrust earthquakes that occurred in the past 20 years, characterized by unilateral rupture (Tsai *et al.*, 2005; Ammon *et al.*, 2005; Ishii *et al.*, 2005) and followed by a devastating tsunami. For the purpose of our synthetic test we use the composite model of Tsai *et al.* (2005), assuming that the rupture initiated at latitude 3.27° , longitude 94.6° and a depth of 25 km, and propagated towards the North with a total rupture duration of 545 s, rupturing segments of total length of 1140 km. The Chile 2010 thrust earthquake is characterized by bilateral rupture. In the first 30 s the source propagated southwards and then slip took place in both directions, with the largest slip observed to the North (Delouis *et al.*, 2010; Kiser and Ishii, 2011). For our synthetic test we use an artificial unilateral rupture model based on the source model of Delouis *et al.* (2010). Specifically, we consider that the rupture started at 36.21° S,

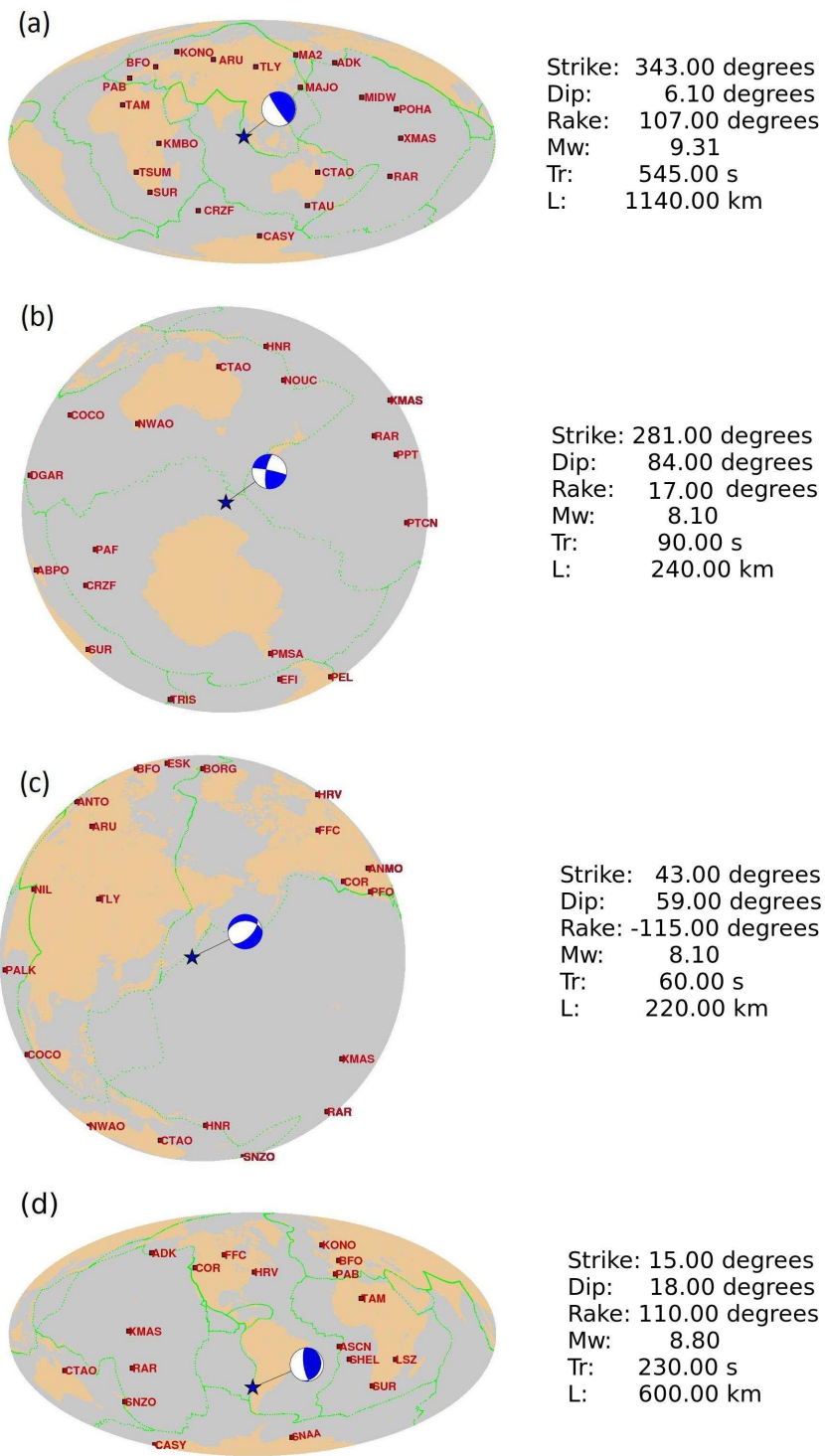


Figure 4.3: Maps showing centroid locations (blue stars), fault mechanisms, stations' distribution used in the synthetic tests (left), source models and spatio-temporal characteristics (right) used to build the synthetic data for the point and finite source inversion tests. Four earthquakes in different tectonic settings are tested: (a) a thrust earthquake based on the model of Tsai *et al.* (2005) for the M_w 9.3, 2004 Sumatra earthquake, (b) a strike-slip earthquake for the M_w 8.1, 1998 Antarctic plate earthquake, based on the GCMT source model (rupture model by Nettles *et al.* (1999)), (c) a normal earthquake based on the GCMT source model of the M_w 8.1, 2007 Kuril earthquake (rupture model based on the model of Lay *et al.* (2009)), (d) a thrust earthquake based on the model of Delouis *et al.* (2010) for the M_w 8.8 2010 Chile earthquake.

72.96°W and a depth of 32 km and that propagated 600 km northward for a duration of 230 s yielding an average rupture velocity of 2.6 km/s, in consistency with the average rupture velocity reported by Delouis *et al.* (2010). The 1998 Antarctic plate strike-slip earthquake is one of the largest oceanic intraplate strike-slip earthquakes ever recorded. The mainshock occurred on a fault with E-W orientation and was characterized by a unilateral rupture (Nettles *et al.*, 1999; Kuge *et al.*, 1999; Anatolik *et al.*, 2000; Henry *et al.*, 2000; Toda and Stein, 2000; Hjörleifsdóttir *et al.*, 2009), which propagated mainly from the East towards the West. Our synthetic data are built using the GCMT location and fault geometry, assuming a total rupture duration of 90 s and rupture length of 240 km, based on the rupture model of Nettles *et al.* (1999). The 2007 Kuril islands earthquake was one of the largest extensional earthquakes that ever occurred. It was located in the upper portion of the Pacific plate and caused a relatively small tsunami (Ammon *et al.*, 2008; Lay *et al.*, 2009; Ogata and Toda, 2010). Although its rupture was bilateral, for the purpose of our study, we treat our artificial earthquake as having a unilateral rupture starting at the GCMT location and propagating towards North-East. We use the fault geometry reported in the GCMT and consider a total rupture duration of 60 s and a rupture length of 220 km, based on the rupture history obtained from teleseismic P and SH wave inversion by Lay *et al.* (2009).

4.5.2 Synthetic data

The station distribution and input source models used in the synthetic tests for the four artificial earthquakes considered are summarized in Figure 4.3. We build a corresponding dataset of synthetic seismograms using HOPT, following the procedure explained in section 4.3.2, summing over all spheroidal fundamental modes in the frequency range 0–1 mHz. The synthetic data are convolved singlet by singlet with the associated finiteness terms in order to introduce the appropriate initial phases. Figure 4.4 compares amplitude spectra of ${}_0S_2$ and ${}_0S_0$ singlets calculated using PREM and using the mantle model SAW12D for station CTAO, for the four events studied. There are some clear peak shifts due to 3-D Earth structure, notably for the ${}_0S_2^{-1}$, ${}_0S_2^0$ and ${}_0S_2^1$ singlets. Figure 4.5 shows the amplitude and phase spectra of excitation kernels for ${}_0S_2$, ${}_0S_3$ and ${}_0S_0$ multiplets for the 2004 Sumatra event using both SAW12D and PREM Earth models. It is worth

noting that $M_{r\theta}$ and $M_{r\phi}$ components cannot be constrained for such a shallow (25 km) earthquake with ultra-long period normal mode data (Kanamori and Given, 1981) as the excitation of their amplitudes is proportional to the seismic moment and the dip angle ($M_o \sin(2\delta)$), so the shallower the dip angle, the largest the required moment. As the excitation amplitude of normal modes depends on the seismic moment and hence on the rigidity on the seismic fault, systematic errors by the use of 1-D Earth structure can bias the results. Specifically, modelling of shallow earthquakes using PREM model produces larger seismic moments, yielding large values of dip-slip components ($M_{r\theta}$, $M_{r\phi}$) which lead to near vertical dip-slip mechanisms (Ferreira and Woodhouse, 2006; Konca *et al.*, 2007). Moreover, although only small differences in amplitude spectra are observed among kernels for the two Earth models used, the phase spectra show larger discrepancies. In some synthetic tests white noise is added to the time-series, using a relatively good signal-to-noise ratio (SNR) (SNR > 4). An illustrative example of the effect of the white noise on the amplitude spectra of ${}_0S_2$ singlets and on ${}_0S_0$ radial mode is shown in Figure 4.6 for the various earthquakes considered. While some modes are quite affected by the white noise (e.g., the ${}_0S_2^0$ singlets for the strike-slip earthquake), other modes show a smaller effect, notably the ${}_0S_0$ mode, which has a much higher quality factor, as discussed previously in subsection 4.3.3.2.

4.5.3 Normal mode multiplet point source inversions

In this section we present results of synthetic tests obtained by normal mode multiplets inversions over a four-dimensional parameter space ($\phi, \delta, \lambda, M_w$). We use finite source artificial spectra as synthetic input data and we invert for fault geometry and moment magnitude by assuming a point source. The first four rows in Table B.1 of the Appendix B shows the parameter space used in the inversions. Table 4.2 summarises the deviations between the actual solution and the results of various source inversions for the four events considered, whereby the effects of source finiteness, noise in data and of incomplete knowledge of the Earth's structure are investigated. In all cases we used ${}_0S_2$, ${}_0S_3$ and ${}_0S_0$ multiplets.

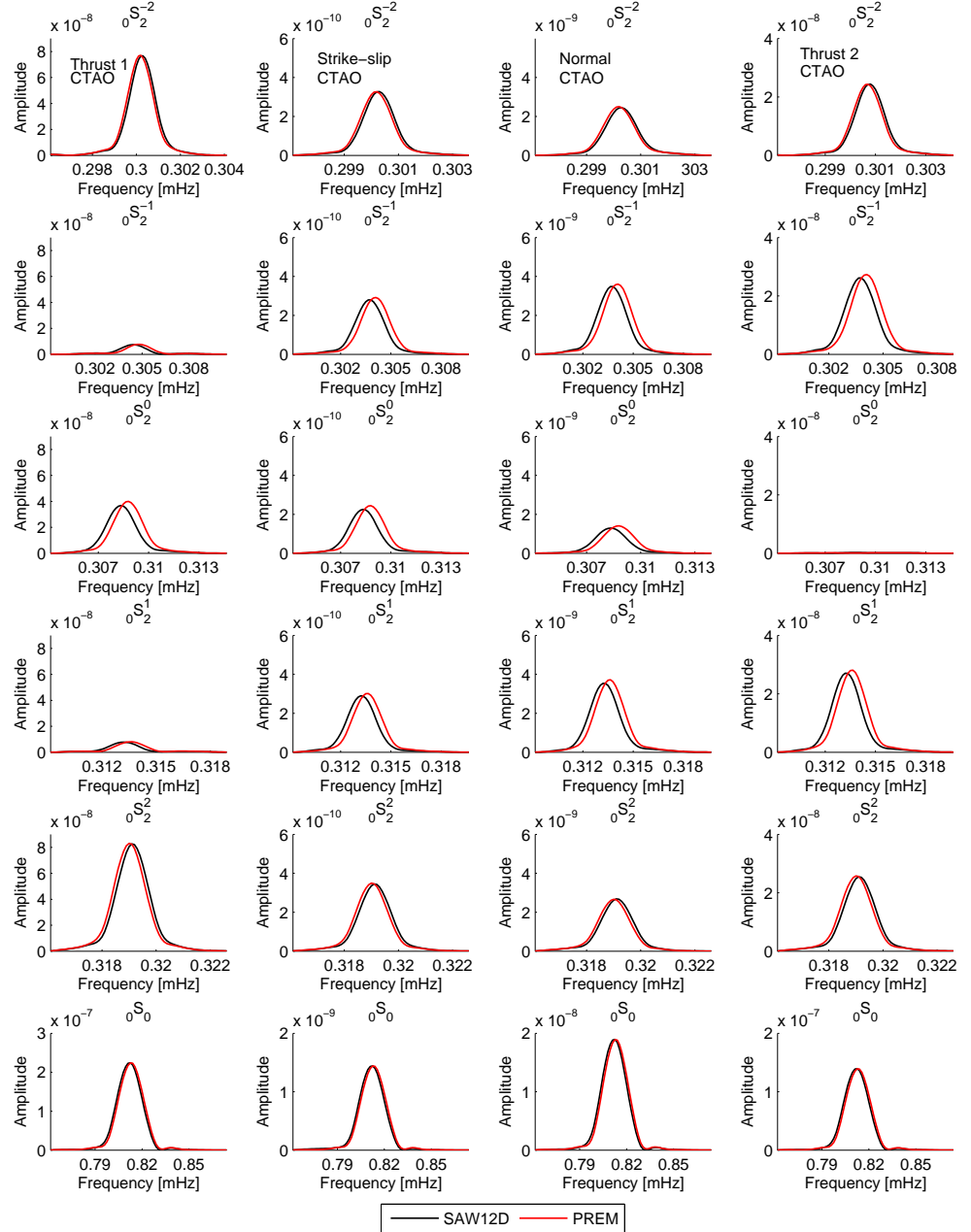


Figure 4.4: The effect of uncertainties in the Earth's model as observed on acceleration amplitude spectra of ${}_0S_2$ spheroidal mode singlets and ${}_0S_0$ radial mode. Synthetic data built using SAW12D model (black) are shown in comparison with input model synthetics using PREM (red) for the four earthquakes tested (thrust 1: Sumatra 2004, strike-slip: Antarctic plate 1998, normal: Kuril 2007, thrust 2: Chile 2010). Different earthquakes are plotted column by column. Note the frequency shift observed, especially at ${}_0S_2^0$ and ${}_0S_2^{\pm 1}$ singlets.

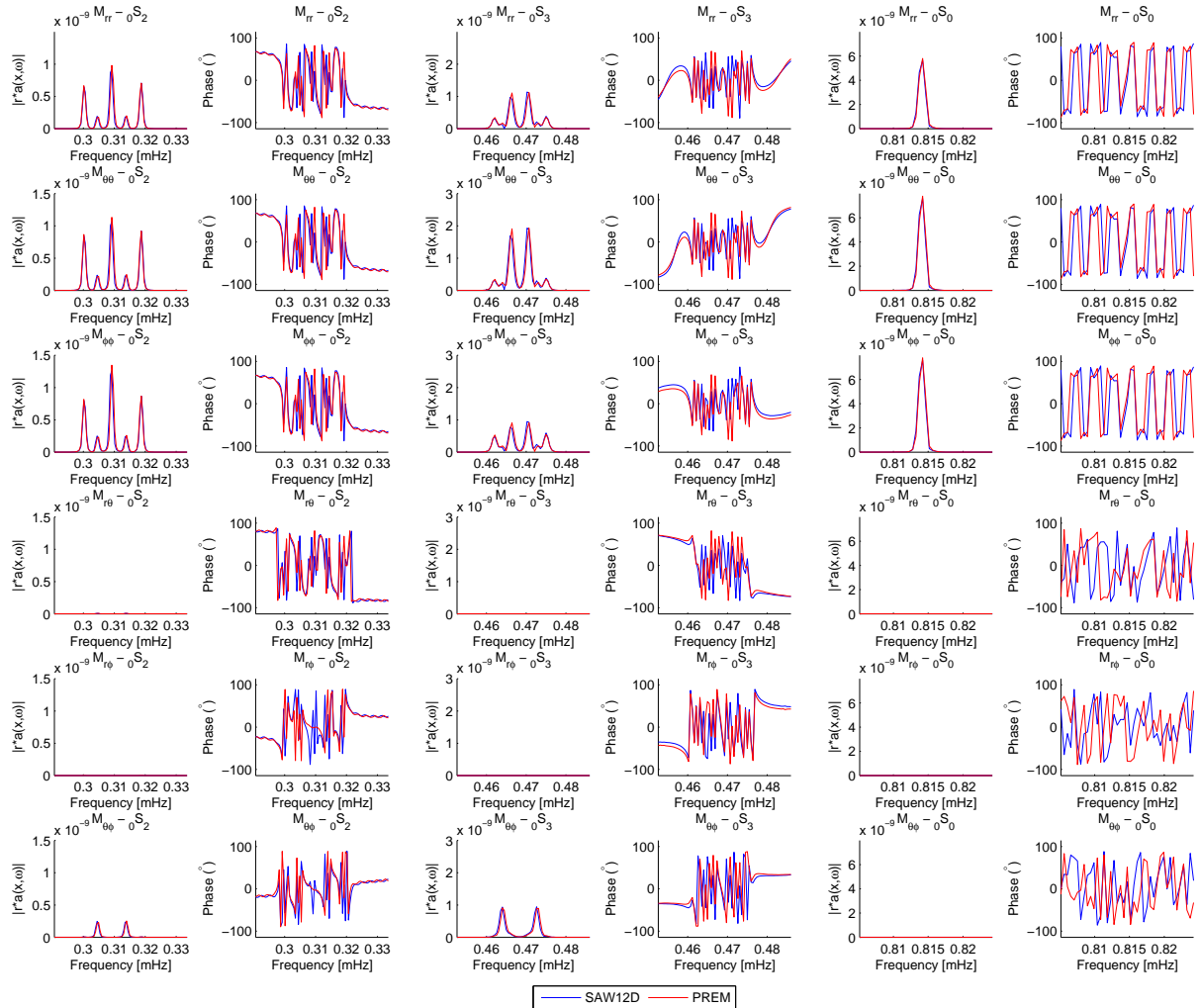


Figure 4.5: 480-hr acceleration amplitude spectra and phase of selected spheroidal multiplets excitation kernels (${}_0S_2$, ${}_0S_3$, ${}_0S_0$) for the artificial 2004 Sumatra earthquake, based on the model of Tsai *et al.* (2005), observed at TLY station at epicentral distance of 45.8° and azimuth of 9.2° . Kernels are presented for the SAW12D Earth model (blue) and PREM (red). All calculations are carried out using HOPT. Rotation, ellipticity and gravity corrections are taken into account in the calculations.

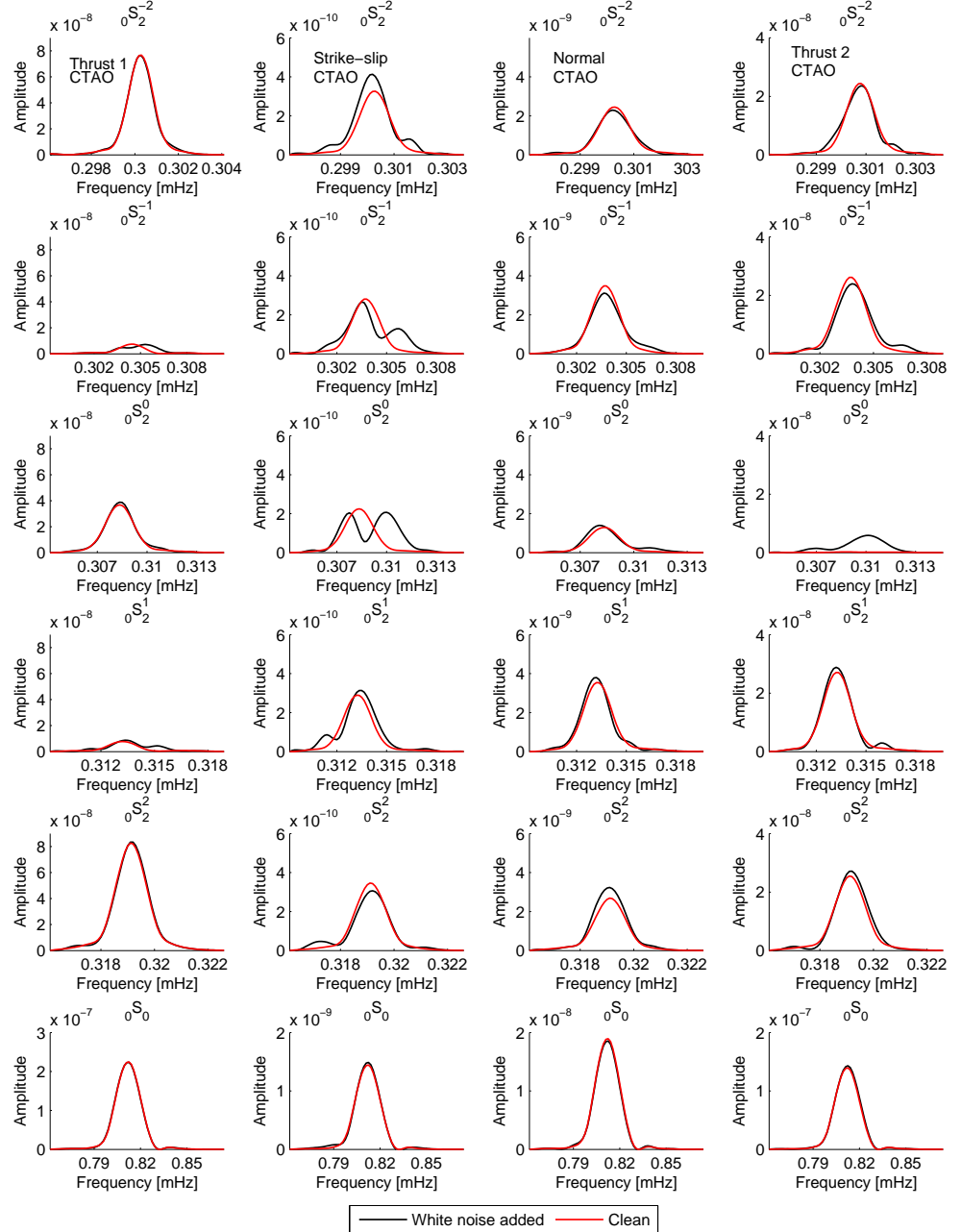


Figure 4.6: The effect of adding white noise in synthetic data to theoretical acceleration amplitude spectra of ${}_0S_2$ spheroidal mode singlets and ${}_0S_0$ radial mode at station CTAO for the four earthquakes tested (thrust 1: Sumatra 2004, strike-slip: Antarctic plate 1998, normal: Kuril 2007, thrust 2: Chile 2010). Different earthquakes are plotted column by column. Synthetic data with white noise added (black), are shown in comparison with synthetic data without noise added (red). The Earth's model used in both cases is SAW12D.

Table 4.2: Differences between input models and results of source inversions for strike ϕ , dip δ , rake λ , moment magnitude M_w , obtained from point source inversions using a misfit function involving a combination of the amplitude spectra and FFT observables (97% amplitude – 3% FFT). The top part of the Table shows the effect of the finite source when using point source kernels built with the same Earth model (SAW12D) as the input synthetic data. The bottom part of the Table shows results for the four different artificial earthquakes tested, in three different cases. SAW12D-WN: Synthetic data and excitation kernels are built using SAW12D Earth's model, but white noise is added to the synthetic data, PREM: synthetic data are built using SAW12D Earth's model while excitation kernels are built using PREM model, PREM-WN: synthetic data are built using SAW12D Earth's model while excitation kernels are built using PREM model and white noise is added to the synthetic data. Input models and beachballs are shown on top, and optimal model beachballs and misfits are shown at the bottom.

INPUT MODELS																				
$\phi = 343^\circ$ $\delta = 6.1^\circ$ $\lambda = 107^\circ$ $M_w = 9.3$ $T_r = 545$ s $L = 1140$ km			$\phi = 281^\circ$ $\delta = 84^\circ$ $\lambda = 17^\circ$ $M_w = 8.1$ $T_r = 90$ s $L = 240$ km			$\phi = 43^\circ$ $\delta = 59^\circ$ $\lambda = -115^\circ$ $M_w = 8.1$ $T_r = 60$ s $L = 220$ km			$\phi = 15^\circ$ $\delta = 18^\circ$ $\lambda = 110^\circ$ $M_w = 8.8$ $T_r = 230$ s $L = 600$ km											
																				
OUTPUT MODELS																				
SAW12D			SAW12D			SAW12D			SAW12D											
$\Delta\phi^{(0)}$	-5.18			-0.36			0.33			-9.06										
$\Delta\delta^{(0)}$	-0.26			2.46			-0.15			1.07										
$\Delta\lambda^{(0)}$	-20.30			4.83			0.18			-9.28										
ΔM_w	0.05			0.01			0.00			-0.02										
																				
misfit	0.05398			0.00065			0.00060			0.00876										
SAW12D WN			PREM WN			SAW12D WN			PREM WN											
$\Delta\phi^{(0)}$	-7.94	-4.46	-8.11	-0.54	0.23	0.03	2.60	-3.30	0.62	-1.38	-7.35									
$\Delta\delta^{(0)}$	-0.15	0.49	-4.86	1.79	3.25	5.19	9.58	1.13	12.67	4.71	2.02									
$\Delta\lambda^{(0)}$	-25.78	-15.82	-23.06	3.89	5.56	7.54	7.83	-1.57	8.11	-3.05	-11.15									
ΔM_w	0.02	0.03	0.19	0.00	0.02	0.01	0.01	0.01	0.02	-0.07	-0.04									
																				
misfit	0.05416			0.02183			0.00669			0.00974										
0.05591			0.05126			0.07130			0.02814											
0.05609			0.03401			0.02604			0.02702											

4.5.3.1 Impact of source finiteness

Figure 4.7 shows the results obtained from a multiplets point source inversion of the artificial thrust earthquake based on the 2004 Sumatra earthquake (the corresponding results are summarised in the first top column in Table 4.2). For this test we use excitation kernels built with the same Earth's model as our synthetic data (SAW12D) without adding any white noise to the latter in order to isolate the effect of neglecting the finiteness term. Figure 4.7a clearly shows that neglecting the rupture's length and duration of this event yields a poor amplitude fit of all the multiplets, notably for ${}_0S_2$ and ${}_0S_3$. This leads to an underestimation of the event's moment magnitude by 0.05, to an error in fault strike of about 5° and to a large error in rake angle of 20° . Nevertheless, when considering the range of source parameters with misfit values not deviating more than 1% from the optimal misfit value (Figure 4.7c), these ranges are relatively close to the input source parameters. Figure 4.7d shows that the inversion converges to the optimal model within 500 iterations.

Considering the results of source inversions for the other events shown in the second-fourth columns of the upper part of Table 4.2 (Figures B.1, B.2, B.7, B.8, B.13, B.14), as expected, the effect of neglecting the finite rupture is gradually stronger as the dimensions of the source increase. Hence, overall the thrust event in Sumatra shows the largest discrepancies in retrieved source parameters, followed by the 2010 Chile ($L = 600$ km, $T_r = 230$ s) event, by the 1998 Antarctic plate ($L = 240$ km, $T_r = 90$ s) and finally by the 2007 Kuril ($L = 220$ km, $T_r = 60$ s) event. Amongst all source parameters, in these examples, the rake angle is the parameter which is affected the most by neglecting the finiteness of the source.

4.5.3.2 Effect of data noise

Figure 4.8 shows results obtained from a multiplets point source inversion of the thrust event based on the 2004 Sumatra earthquake when white noise is also added to the input synthetic data, keeping the SNR >4 (Figure 4.6). The first column entitled SAW12D-WN of the lower part of Table 4.2 summarises the results obtained. As expected, the data fit is slightly poorer compared to the previous example (see the misfit values in Table 4.2 and Figure 4.8a). However, similar features are found, with the rake angle having the largest

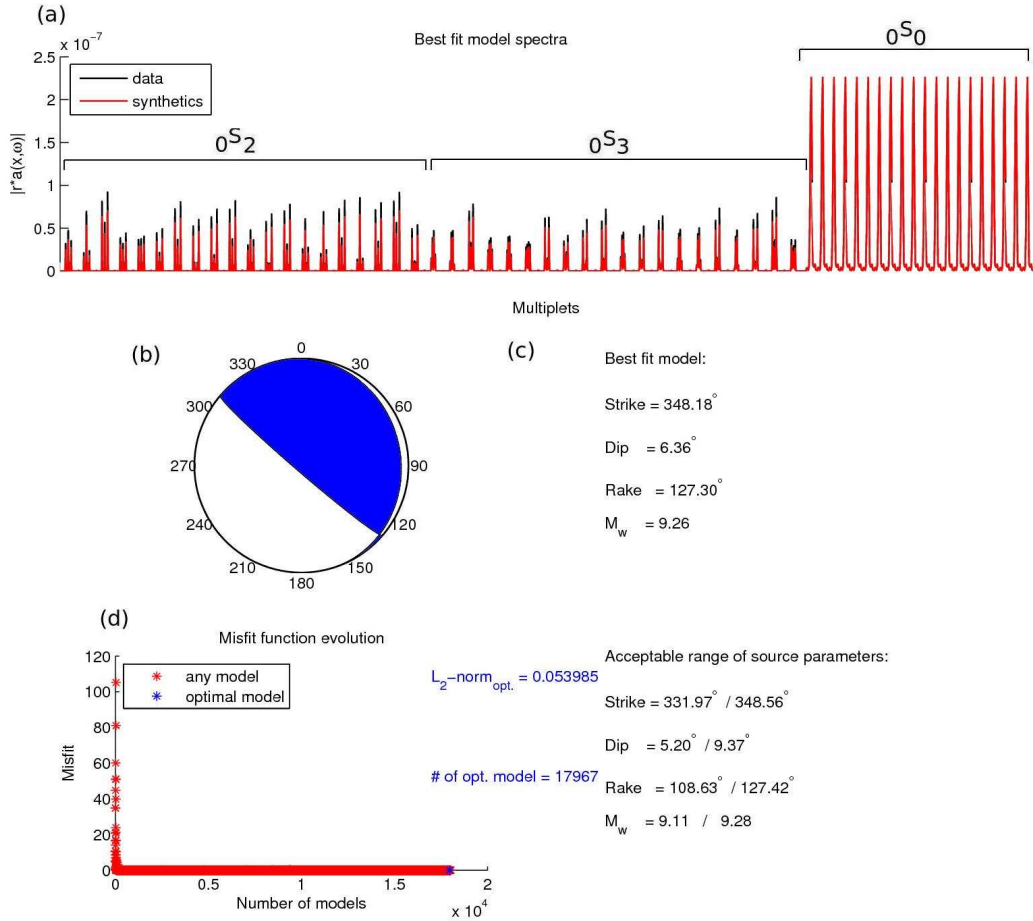


Figure 4.7: Results from a point source inversion for the artificial 2004 Sumatra earthquake, using a combination of the amplitude and FFT misfits (97% amplitude and 3% FFT) for the finite source model of Tsai *et al.* (2005) as the input model ($\phi = 343^\circ$, $\delta = 6.1^\circ$, $\lambda = 107^\circ$, $M_w = 9.31$, $T_r = 545$ s, $L = 1140$ km). SAW12D 3-D model is used to build the synthetic data and the excitation kernels: (a) 480-hr optimal fit amplitude spectra of $0S_2$, $0S_3$, $0S_0$ multiplets, (b) optimal source mechanism, (c) optimal and acceptable range of source parameters (acceptable parameters correspond to source models yielding misfit values not 1% larger than the lowest misfit associated with the optimal source model), (d) misfit function evolution.

deviation to the actual solution, showing a $\sim 25^\circ$ difference. Overall, adding white noise to the data leads to a deterioration in the retrieval of the fault strike of about $\sim 3^\circ$ and in the retrieval of the rake of about $\sim 5^\circ$, which is smaller than the effect of neglecting the source finiteness.

The rest of the earthquakes examined (Figures B.3, B.4, B.9, B.10, B.15, B.16 in Appendix B), also show poorer fit to the synthetic data spectra when adding white noise to the synthetic data (compare misfit values between upper and second-bottom parts in Table 4.2). Columns entitled SAW12D-WN in Table 4.2 summarise those results, showing that earthquake mechanism errors do not exceed $\sim 10^\circ$, with the rake angle being the

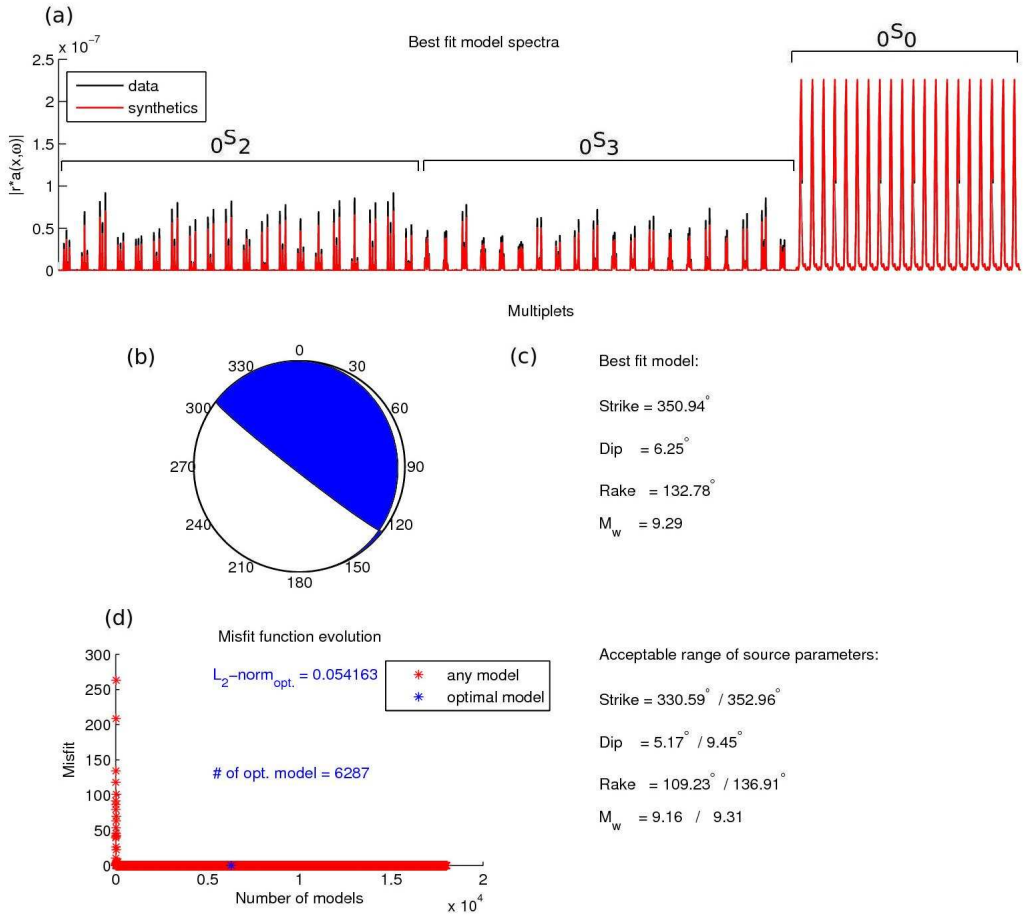


Figure 4.8: Same as in Figure 4.7, but white noise is added to the synthetic data.

parameter with the overall largest discrepancy.

4.5.3.3 Importance of 3-D Earth structure

We investigate the effect of 3-D Earth structure on the point source inversions by carrying out multiplets inversions using 1-D PREM excitation kernels, which have been illustrated, e.g., in Figure 4.4. We do not add noise to the synthetic data in order to isolate the effects of 3-D Earth structure. Figure 4.9 and the second-bottom column entitled PREM in Table 4.2 show the results obtained.

We find similar results to the previous cases, where the fault rake angle shows the largest errors. Indeed, in this case the results are very similar to those found in section 4.5.3.1, suggesting that for this event the effect of neglecting the source finiteness for the Sumatra event is larger than the effect of 3-D Earth structure. Interestingly, for this event, the error in rake angle due to the combined effect of neglecting both 3-D Earth

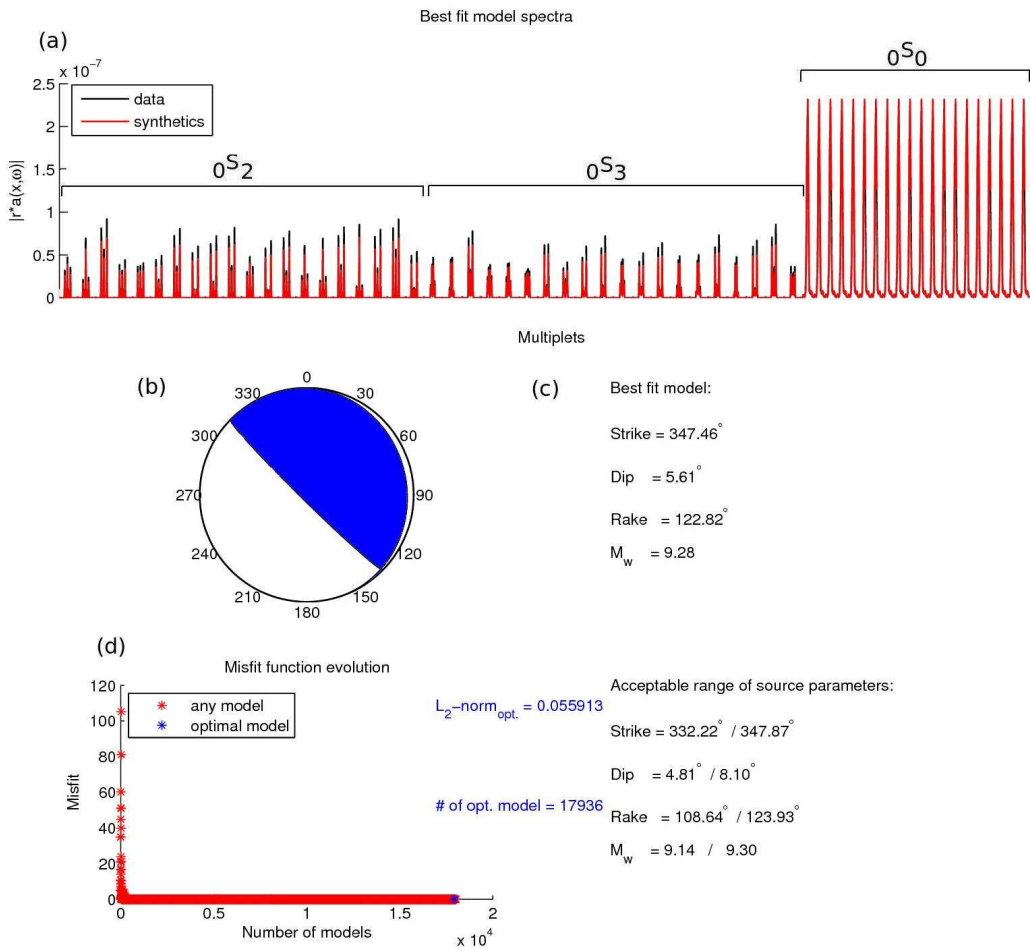


Figure 4.9: Same as in Figure 4.7, but PREM excitation kernels are used in the inversion.

structure and the finiteness of the source is about $\sim 5^\circ$ smaller than that due to the source finiteness alone, suggesting some tradeoffs between source and Earth structure. For the remaining events (Figures B.5, B.6, B.11, B.12, B.17, B.18 in Appendix B), we find that the combined effect of neglecting both 3-D Earth structure and the source finiteness is similar to the effect of the latter alone, with only the errors in moment magnitude slightly increasing (Table 4.2). This suggests that ignoring the source finiteness affects the point source inversions considered in this study much more than 3-D Earth structure.

Figure 4.10 shows tradeoff plots between the various source parameters retrieved in the inversions presented in sections 4.5.3.1-4.5.3.3 for the event based on the 2004 Sumatra earthquake. In all cases there are clear tradeoffs between rake and strike, and, as expected, between M_w and fault dip angle (Kanamori and Given, 1981). In addition, while for some source parameters the distributions are relatively similar (e.g., for the fault dip angle), for other parameters there are some clear differences (e.g., for the rake angle).

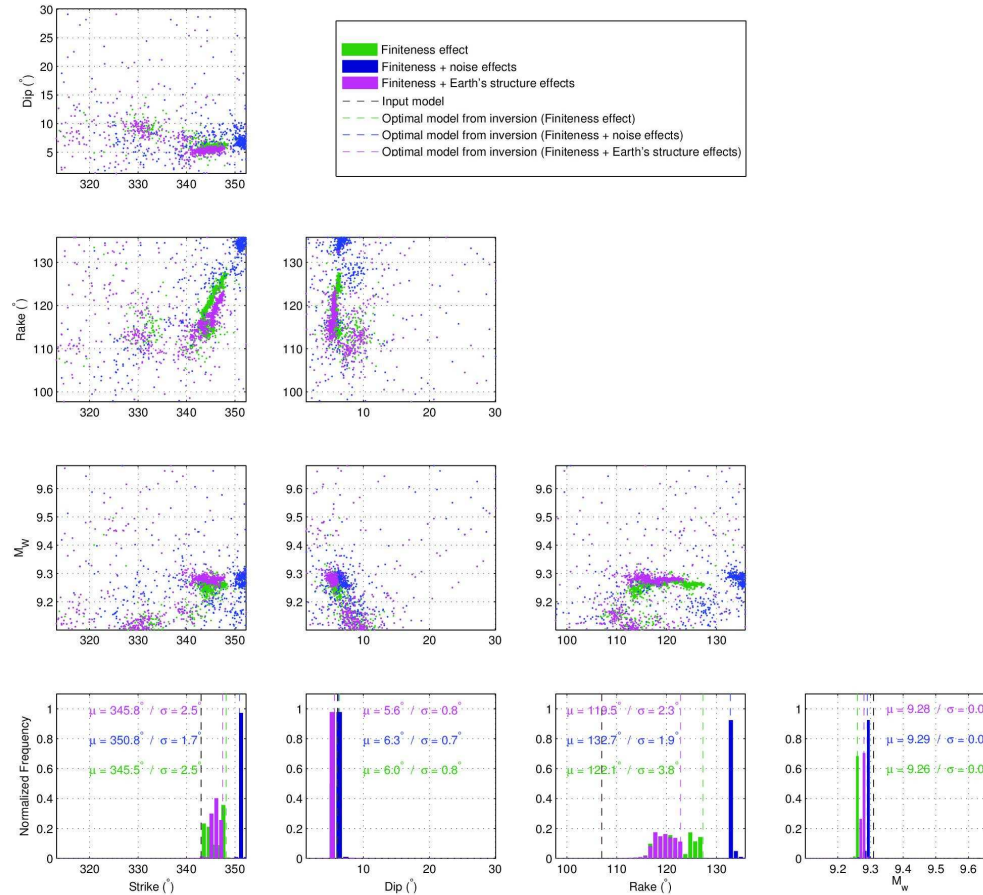


Figure 4.10: Uncertainties and tradeoffs as shown from ensembles produced by Neighbourhood Algorithm and plotted as pairs of source parameters for the experiments of Figure 4.7 (green), Figure 4.8 (blue) and Figure 4.9 (magenta). Normalized frequency plots are shown at the bottom. The black dashed lines correspond to the input model ($\phi = 343^\circ, \delta = 6.1^\circ, \lambda = 107^\circ, M_w = 9.31$). Green, blue and magenta dashed lines correspond to optimal models determined from the inversions. Mean (μ) and standard deviation (σ) values are also shown.

4.5.3.4 Combined effect of data noise and 3-D Earth structure

In our final multiplets synthetic tests we carried out inversions combining all sources of errors (see columns named PREM-WN in Table 4.2). We used finite rupture theoretical seismograms with white noise added as input synthetic data and PREM excitation kernels in the inversions. Again, there are large discrepancies in rake angle for the artificial earthquake with the largest source dimensions (Sumatra 2004). Moreover, in this case the moment magnitude is underestimated, with a difference of 0.19 to the actual input value. For the remainder earthquakes, the errors are overall smaller than for Sumatra, and in the same range as those found in sections 4.5.3.1-4.5.3.3.

In summary, overall the main findings from our multiplet point source inversions are that rake angle determinations are strongly affected by finite rupture effects, particularly for the events with largest rupture dimensions (i.e., for the two thrust events). On the other hand, noise in the input synthetic data does not have a very strong impact on the inversions and uncertainties in Earth structure yield relatively small errors in source parameters. Strong dip- M_w tradeoff due to poor constraint of dip-slip moment tensor components and strike-rake tradeoff are found in all cases. The latter is rather a geometric tradeoff as the strike and rake are mutually correlated in a manner that their difference is kept constant (Han *et al.*, 2011, 2013).

4.5.4 Normal mode singlet finite source inversions

In this section we present results of synthetic tests obtained by normal mode singlets inversions over a six-dimensional parameter space $(\phi, \delta, \lambda, M_w, T_r, L)$. We use the same input synthetic data as in section 4.5.3 but we now invert for fault geometry, moment magnitude and source spatio-temporal dimensions (rupture duration and length). Table B.1 in the Appendix B shows the parameter space used in the inversions.

We first test the effect of adding noise to the input synthetic data. Figure 4.11 shows detailed results of the corresponding synthetic test for the thrust event based on the 2004 Sumatra earthquake. These results are also summarised in the first column of Table 4.3. The data fit of the optimal solution (see Figure 4.11a) is excellent and the errors in the source parameters due to the presence of noise in the synthetic data are overall small, being up to 2° in fault geometry, 0.07 error in magnitude, almost no error in rupture

duration and a small discrepancy in rupture length (~ 20 km). For the other earthquakes (see SAW12D-WN columns in Table 4.3), we observe that rupture duration values are in excellent agreement with input models and that there are relatively small errors in fault geometry (up to 8°). However, rupture length estimates can be strongly affected by data noise, notably for the strike-slip event, where the error in rupture length is of about 50%.

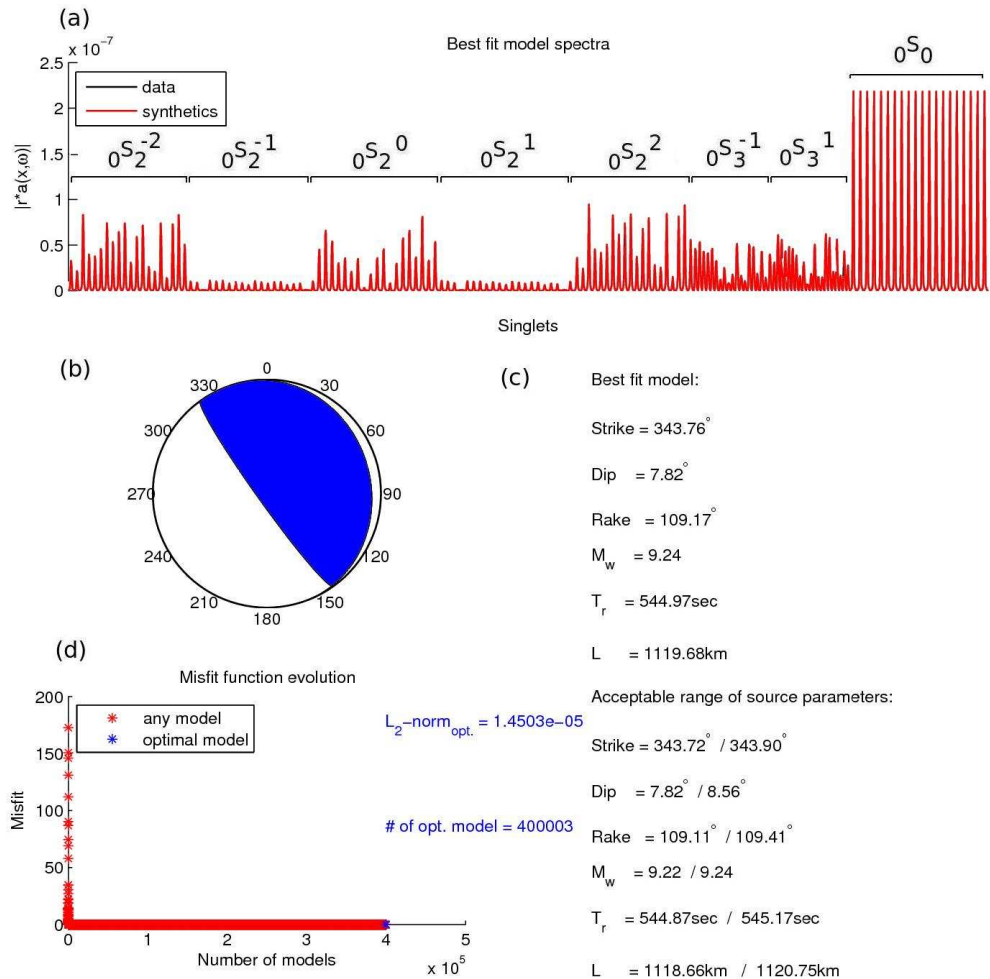


Figure 4.11: Results from a finite source inversion for the artificial 2004 Sumatra earthquake, using a combination of the amplitude and FFT misfits (97% amplitude and 3% FFT) for the finite source model of Tsai *et al.* (2005) as the input model ($\phi = 343^\circ$, $\delta = 6.1^\circ$, $\lambda = 107^\circ$, $M_w = 9.31$, $T_r = 545$ s, $L = 1140$ km). SAW12D 3-D model is used to build the synthetic data and the excitation kernels. White noise is added to synthetic data: (a) 480-hr optimal fit amplitude spectra of ${}_0S_2^{-2}$, ${}_0S_2^{-1}$, ${}_0S_2^0$, ${}_0S_2^1$, ${}_0S_2^2$, ${}_0S_3^{-1}$, ${}_0S_3^1$, ${}_0S_0^0$ singlets, (b) optimal source mechanism, (c) optimal and acceptable range of source parameters (acceptable parameters correspond to source models yielding misfit values not 1% larger than the lowest misfit associated with the optimal source model), (d) misfit function evolution.

Table 4.3: Same as in Table 4.2, but now for finite source inversions, for the determination of six source parameters (strike ϕ , dip δ , rake λ , moment magnitude M_w , rupture duration T_r , length L).

INPUT MODELS											
$\phi = 343^\circ$ $M_w = 9.3$			$\phi = 281^\circ$ $M_w = 8.1$			$\phi = 43^\circ$ $M_w = 8.1$			$\phi = 15^\circ$ $M_w = 8.8$		
$\delta = 6.1^\circ$ $T_r = 545$ s	$\delta = 84^\circ$ $T_r = 90$ s	$\lambda = 107^\circ$ $L = 1140$ km	$\delta = 84^\circ$ $T_r = 90$ s	$\lambda = 17^\circ$ $L = 240$ km	$\delta = 59^\circ$ $T_r = 60$ s	$\lambda = -115^\circ$ $L = 220$ km	$\delta = 18^\circ$ $T_r = 230$ s	$\lambda = 110^\circ$ $L = 600$ km	$\delta = 18^\circ$ $T_r = 230$ s	$\lambda = 110^\circ$ $L = 600$ km	
OUTPUT MODELS											
SAW12D WN	PREM WN	PREM WN	SAW12D WN	PREM WN	PREM WN	SAW12D WN	PREM WN	PREM WN	SAW12D WN	PREM WN	PREM WN
$\Delta\phi(^{\circ})$ -0.76	-4.20	-8.81	-0.70	2.16	1.47	2.86	-5.38	-14.33	-0.07	-1.64	-1.44
$\Delta\delta(^{\circ})$ -1.72	-4.29	-4.45	5.73	-0.89	4.26	-0.64	-0.86	-13.08	5.19	7.76	-10.88
$\Delta\lambda(^{\circ})$ -2.17	6.83	-8.02	7.98	-3.19	6.49	-6.97	0.11	6.50	1.29	-8.10	-3.10
ΔM_w 0.07	0.19	0.17	0.00	0.01	0.02	0.01	-0.00	-0.13	-0.09	-0.15	0.12
$\Delta T_r(s)$ 0.03	84.59	84.69	-1.91	90.00	90.00	-1.44	60.00	60.00	-0.31	153.91	154.22
$\Delta L(km)$ 20.32	-21.13	16.90	121.76	30.71	149.96	93.22	141.88	45.41	131.40	137.25	26.66
misfit 0.00002	0.01775	0.01777	0.00343	0.02256	0.02438	0.00071	0.01582	0.01990	0.00010	0.02093	0.02098

Next we test the effect of 3-D Earth's structure on finite source singlets inversions. We use the same input synthetic data as in section 4.5.3, but carry out source inversions using 1-D PREM excitation kernels. Figure 4.12 and the second column of Table 4.3 show results for the event based on the 2004 Sumatra earthquake. Figure 4.12a shows that the fit to the synthetic data is still good, but poorer compared to the data noise test. Errors in fault geometry are up to 7° , but the most striking observation is the large error in rupture duration, which shows great sensitivity to Earth's structure. The other events show similar results regarding errors in fault geometry, which are up to 8° (see columns entitled PREM in Table 4.3). On the other hand, rupture duration and length show very large discrepancies compared to the input models. For short rupture dimension earthquakes (e.g., 1998 Antarctic plate earthquake, 2007 Kuril earthquake), the errors are of the order of their true values, thus in these cases we cannot constrain their source dimensions. Figure 4.13 shows the tradeoffs between the source parameters from the various singlets finite source synthetic inversions. A tradeoff between M_w and fault dip angle is clearly observed. Corresponding results for the other artificial events studied are shown in Figures C.1 – C.12 of the Appendix C. Tests based on the combination of noise in synthetic data and uncertainties in Earth's structure show similar features as in the case of the Earth's structure effect alone (see columns entitled PREM-WN in Table 4.3).

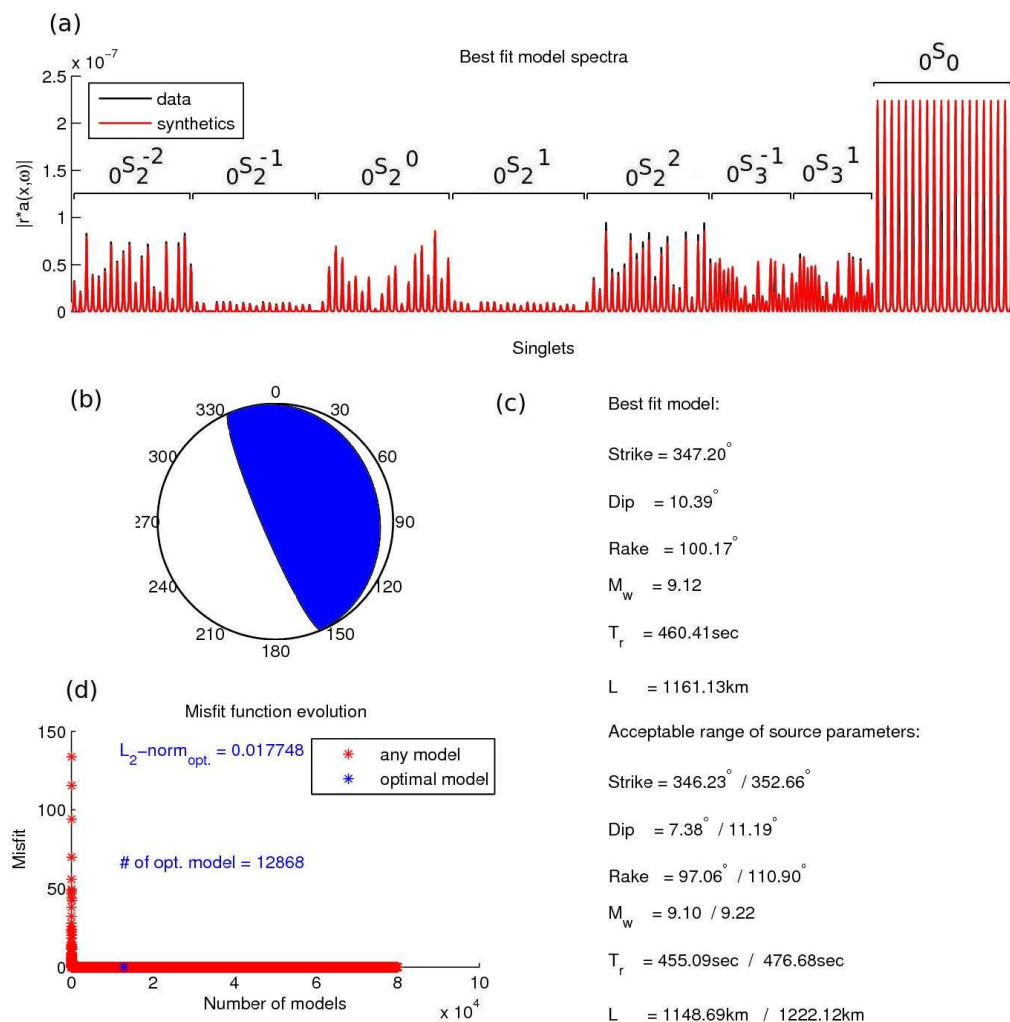


Figure 4.12: Same as in Figure 4.11, but without white noise added to synthetic data, while PREM excitation kernels are used in the inversion.

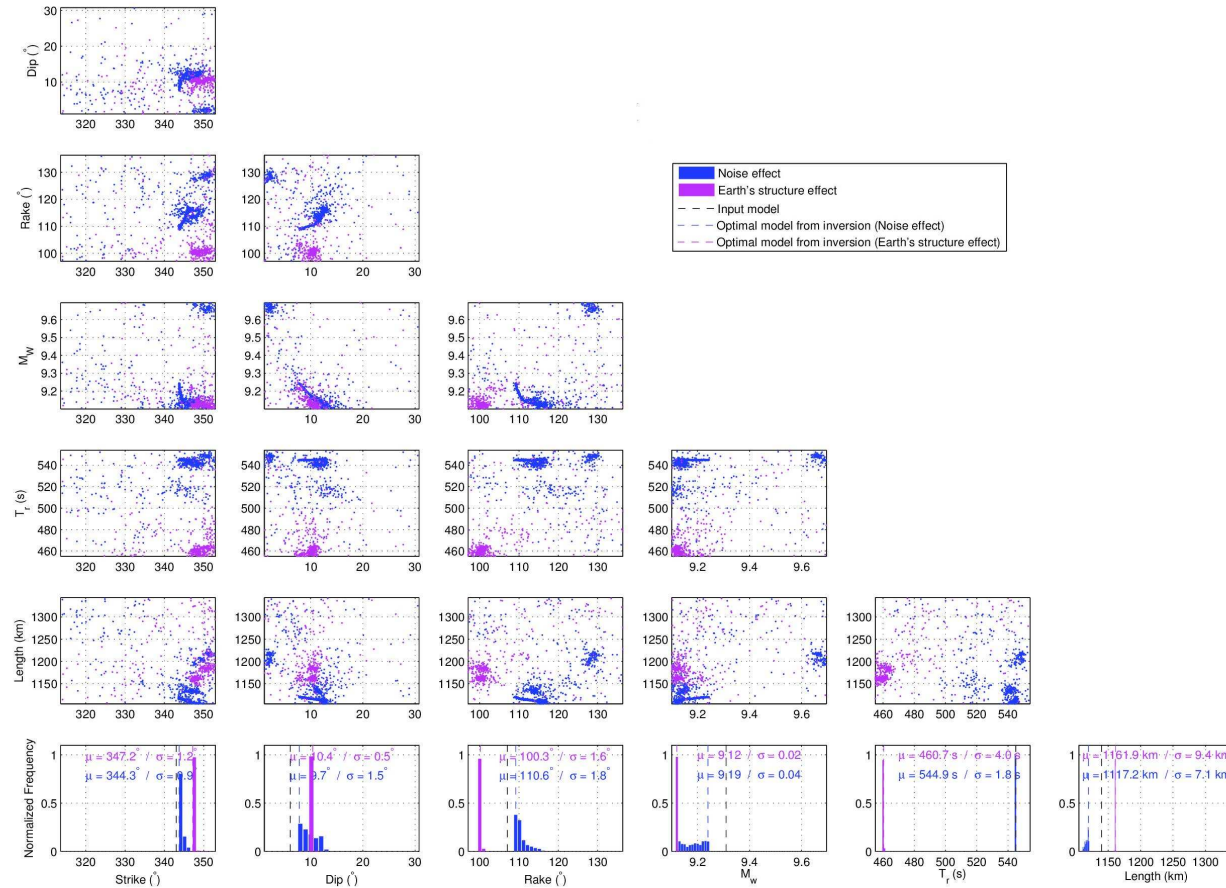


Figure 4.13: Uncertainties and tradeoffs as shown from ensembles produced by Neighbourhood Algorithm and plotted as pairs of source parameters for the experiments of Figure 4.11 (blue) and Figure 4.12 (magenta). Normalized frequency plots are shown at the bottom. The black dashed lines correspond to the input model ($\phi = 343^\circ$, $\delta = 6.1^\circ$, $\lambda = 107^\circ$, $M_w = 9.31$, $T_r = 545$ s, $L = 1140$ km). Blue and magenta dashed lines correspond to optimal models determined from the inversions. Mean (μ) and standard deviation (σ) values are also shown.

4.5.4.1 Influence of errors in spatio-temporal location

In the previous sections we have carried out inversions using the correct earthquake spatio-temporal locations. In this section, we carry out tests to study the sensitivity of singlets inversions to errors in earthquake location and origin time. Table 4.4 shows the results from these experiments for the thrust event based on the 2004 Sumatra earthquake using the same input synthetic data as in section 4.5.3. We started by carrying out inversions using SAW12D excitation kernels delayed by 10 s with respect to the assumed origin time (see first column in Table 4.4). Next, we built new sets of SAW12D excitation kernels shifting the assumed location by 1° in four directions (N, S, E, W; see columns 2–5 in Table 4.4). Finally, we carried out a test where we applied many possible errors together. Specifically, we added white noise to the input synthetic data and we performed inversions using PREM excitation kernels with 10 s error in origin time, and slightly wrong location, shifted about 50 km to NW (see column 6 of Table 4.4).

Table 4.4 shows that errors in origin time do not strongly affect fault geometry and magnitude determinations, but they have a strong impact on the estimated rupture duration and length. On the other hand, uncertainties in location cause significant errors in fault geometry, especially in rake angle and in M_w , and in some cases in rupture length. Rupture duration is not sensitive to uncertainties in source location. Finally, the combination of errors in location and in origin time, in the presence of noise in the input synthetic data and with the use of 1-D simplified Earth's structure in the inversions yields errors up to 10° in fault geometry and up to 15% and 17% in rupture duration and length, respectively.

4.5.5 Misfit function choice

Numerous tests have been carried out to study the effect of the misfit function type used in our inversions. Specifically, we test misfit functions involving: (i) the amplitude spectra alone; (ii) the phase spectra alone; (iii) the complex (real and imaginary parts) Fast Fourier Transform of the signal; or (iv) different combinations of (i)–(iii). The aim of these tests is to examine the robustness of the different features of the spectra, and to build a misfit function which is not very sensitive to noise in the data and to the Earth's structure.

Results from the tests are summarized in Figure 4.14 for point source inversions and in Figure 4.15 for finite source inversions. Amplitude and FFT misfit functions are more

Table 4.4: Differences in optimal source parameters obtained from finite source inversions compared with the input model of Tsai *et al.* (2005) for the artificial 2004 Sumatra earthquake, with respect to errors in origin time and location that have been introduced to the excitation kernels. Results for an experiment using PREM excitation kernels and adding white noise to the input synthetic data are also shown (PREM-WN). Misfit values and beachballs of the obtained source models are shown at the bottom.

Error in origin time	+10 s	+0 s	+0 s	+0 s	+0 s	+10 s
Error in latitude	+0°W	+0°W	+1°W	+0°W	+1°E	+0.60°W
Error in longitude	+0°S	+1°S	+0°S	+1°N	+0°S	+0.23°N
	SAW12D	SAW12D	SAW12D	SAW12D	SAW12D	PREM WN
$\Delta\phi(^{\circ})$	-1.83	-5.52	3.45	5.80	-0.88	9.46
$\Delta\delta(^{\circ})$	0.05	4.34	1.4	-6.30	-3.18	-2.71
$\Delta\lambda(^{\circ})$	-2.47	-14.00	7.74	-10.58	-2.02	-4.54
ΔM_w	-0.01	-0.39	-0.07	0.21	0.12	0.12
$\Delta T_r(s)$	-7.96	0.12	0.23	0.62	-0.18	70.91
$\Delta L(km)$	-190.01	-196.32	6.20	-21.90	29.21	-192.97
misfit						
	0.00884	0.00016	0.00349	0.00030	0.00011	0.02209

stable as they lead to obtained parameters closer to the input models when noise in the data and uncertainties in the Earth's model are taken into account. However, as expected, a purely amplitude spectra misfit cannot constrain well the rupture length in a finite source inversion. The phase misfit is very sensitive to fault geometry but it cannot constrain the moment magnitude. Moreover, it is very sensitive to the presence of noise and Earth's structure uncertainties and the rupture duration and length show very large discrepancies when PREM is used to build the excitation kernels. Using a combination of amplitude, FFT and phase misfit functions the algorithm converges faster to the input model, but because of the phase misfit being affected strongly by noise and/or the Earth's structure, large errors are often observed. The overall best results in the presence of noise in the data and uncertainties in the Earth's model were obtained with a combination of the amplitude and the FFT misfit (97% amplitude – 3% FFT).

4.6 Discussion

In this study we present a new normal mode source inversion technique to determine overall kinematic earthquake source parameters of large magnitude events. We use ultra-long-period normal mode multiplets and the phases of split singlets, which are accurately

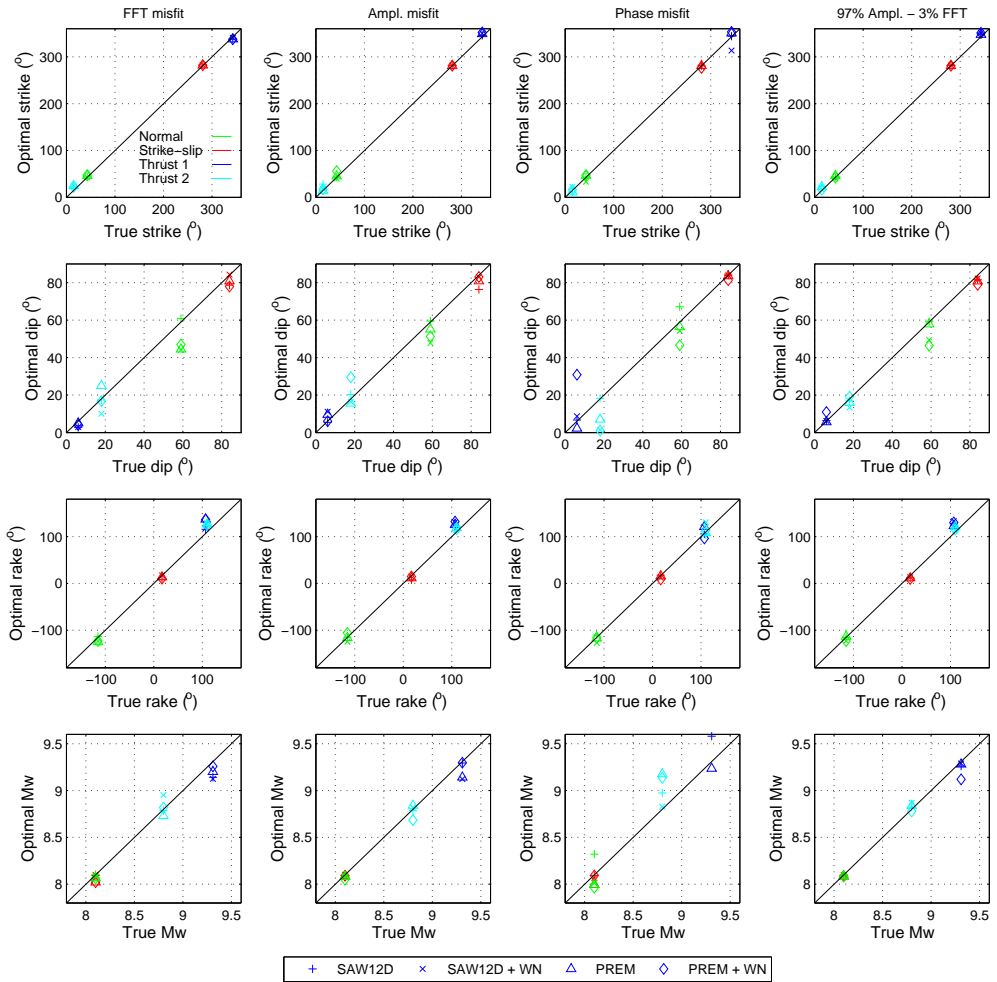


Figure 4.14: Optimal source parameters obtained from point source inversions versus true source parameters for the four artificial earthquakes tested (thrust 1: Sumatra 2004, strike-slip: Antarctic plate 1998, normal: Kuril 2007, thrust 2: Chile 2010) using the FFT misfit function (1st column), the amplitude misfit (2nd column), the phase misfit (3rd column) and a combination of the amplitude and FFT (97% amplitude, 3%FFT) misfit functions (4th column). Synthetic data are built using SAW12D Earth model. Different symbols are associated to different scenarios. Plus signs correspond to excitation kernels built using SAW12D, crosses correspond to synthetic data with white noise added and excitation kernels built using SAW12D, triangles correspond to excitation kernels built using PREM and diamonds correspond to synthetic data with white noise added and excitation kernels built using PREM.

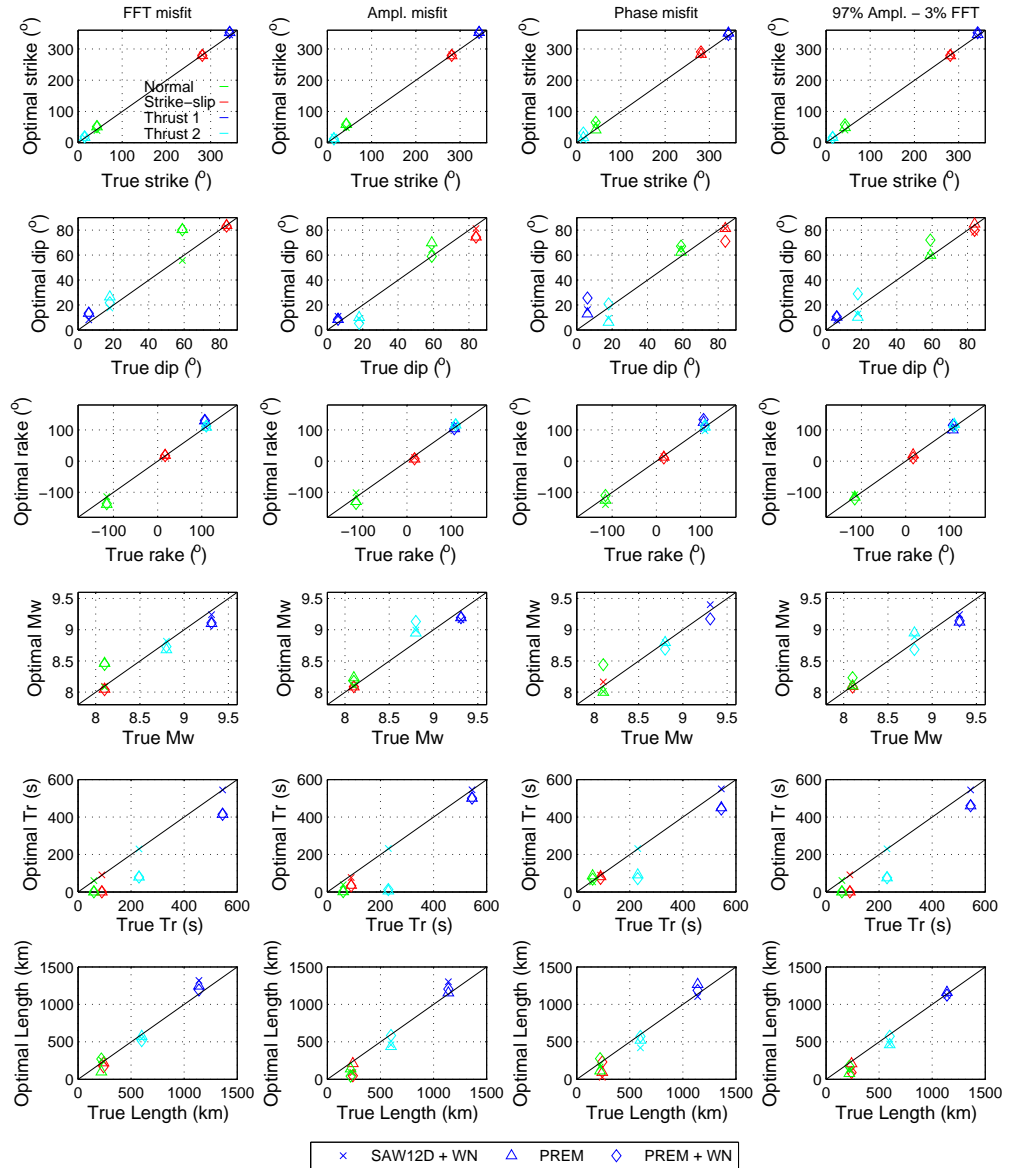


Figure 4.15: Same as in Figure 4.14, but for finite source inversions. Results are shown for FFT (1st column), amplitude (2nd column), phase (3rd column) and a combination of the amplitude and FFT (97% amplitude, 3%FFT) misfit functions (4th column).

modelled taking into account the effects of Earth's rotation, ellipticity and 3-D structure. The optimisation scheme is based on the Neighbourhood Algorithm, which allows us to extensively explore the parameter space and to characterise errors and parameter trade-offs. Park *et al.* (2005) and Lambotte *et al.* (2006, 2007) have used the phases of normal mode singlets to obtain constraints on the source duration and length of the 2004 Sumatra and 2005 Nias earthquakes. Our method generalises this work by enabling comprehensive simultaneous determinations of moment magnitude, strike, dip, rake, rupture length and duration. The method is modular, so that, e.g., if when applied to real earthquakes the data are too noisy to extract the phases of singlets, point source inversions of normal mode multiplets for magnitude, strike, dip and rake are still possible. While low-frequency normal mode data do not provide information about the fine details of the rupture history that can be illuminated using short-period body and surface waves (e.g., Yagi, 2004; Ammon *et al.*, 2005; Yagi and Fukahata, 2011b; Kiser and Ishii, 2012), they are useful to determine in an alternative and independent way the bulk rupture properties of large magnitude earthquakes. For example, independent estimates of rupture duration and length (and hence of rupture velocity) are useful for a range of applications, from tsunami modelling (Poisson *et al.*, 2011), to earthquake scaling (Wells and Coppersmith, 1994) and dynamic rupture studies (Aochi and Ide, 2011).

We conduct synthetic inversion tests to investigate the errors in the source parameters retrieved using our technique due to data noise, unmodelled 3-D Earth structure, uncertainties in spatio-temporal centroid location and neglecting the finiteness of the source. We consider four different artificial large magnitude earthquakes occurring in different tectonic settings, based on real earthquakes reported in previous studies. In addition, the noisy synthetic data used in the tests have similar characteristics to real earthquake normal mode data (see, e.g., Figure 4.6). The 3-D Earth model used in this study (SAW12D) is very smooth; e.g., it does not incorporate sharp lateral discontinuities between different tectonic blocks. However, the SAW12D mantle model is probably a good approximation for the fairly long period seismic wavefield used in this study. Hence, we consider that the errors estimated in this study are realistic and representative.

When determining rupture duration and length from the phases of free oscillation singlets, we find that the rupture duration is relatively insensitive to data noise and to errors

in the earthquake location and origin time, but that it is strongly affected by unaccounted 3-D Earth structure. Indeed, using the 1-D Earth model PREM in the source inversions leads to an underestimation of the rupture duration ranging from 16% for the M_w 9.3 thrust earthquake, to about 60% for the M_w 8.8 event, and going up to 100% for the two M_w 8.1 events considered. On the other hand, rupture length determinations are strongly affected by all these factors, notably for the two M_w 8.1 events (the smallest magnitude events in our study), for which data noise and unmodelled Earth structure lead to errors as large as $\sim 50\%$ and $\sim 60\%$, respectively. This shows that overall rupture length estimates based on our technique can be difficult, requiring not only a good knowledge of Earth structure, but also very high-quality, low-noise data. In practice, our tests indicate that this may only be achieved for very large magnitude earthquakes such as with $M_w \geq 8.8$. These results are consistent with the fact that Lambotte *et al.* (2007) could only constrain the rupture duration history of the M_w 8.6 Nias earthquake and not its spatial extent (with the additional complication that this earthquake had a bilateral rupture).

For our shallow thrust event tests, tradeoffs are expected between the seismic moment (and hence M_w) and the fault dip angle. Indeed, these appear very clearly in our tradeoff plots, with the errors in moment magnitude and dip angles of the optimal models for the two thrust earthquakes having opposite signs, as expected. We find that for these earthquakes, neglecting the 3-D Earth structure leads to larger errors in dip and M_w (of up to 8° and 0.19, respectively) than when adding noise to the data. In addition, uncertainties in the source location can also produce errors in fault dip angle of up to about 6° and of 0.39 in M_w , which is quite large. Nevertheless, such large error in M_w occurs in only one of the examples when assuming an uncertainty in earthquake location of over 100 km, which is unlikely in real cases. In most cases, we find errors in dip angle of up to 8° and of up to 0.2 in M_w , which are comparable or smaller to uncertainties in these parameters reported in other studies based on different techniques and datasets. For example, Hjörleifsdóttir and Ekström (2010) quantified the errors in GCMT source determinations due to unmodelled 3-D Earth structure and data noise using Spectral Element Method synthetic data. They found that the fault dip angle can be underestimated by about 5° and that the seismic moment is overestimated by about 20% for shallow subduction zone earthquakes when body wave, surface wave and mantle wave data are used in the inversions. For earthquakes

with $M_w \geq 7.5$, additional errors are expected because of the point source approximation used in the GCMT method. Ferreira *et al.* (2011) found an average intraevent variability of about 32° in fault dip estimates and of 0.09 in moment magnitude obtained using different Earth models and theories in long-period CMT surface wave inversions. Moreover, Weston *et al.* (2011) report differences between GCMT and InSAR-determined dip angles with a standard deviation of about 15° . When neglecting the effect of the source finiteness in multiplet point source inversions, we obtain errors in dip of about 3° and in M_w up to 0.05. This is smaller than the findings of Kedar *et al.* (1994), who argue that for a large magnitude ($M_w \sim 8$) earthquake the neglect of the finiteness term in normal mode modelling can introduce up to 50% error in seismic moment.

In our examples, fault strike, and importantly rake, are more affected by finite rupture effects than the fault dip angle, notably for the two large thrust earthquakes, which show errors in strike up to 9° and in rake of 20° when the source finiteness is ignored in point source inversions. While the errors in strike are relatively small in all the finite source inversions, and similar to those in dip angle, rake angle estimates are overall more strongly affected by data noise, 3-D Earth structure and by location uncertainties in finite source inversions, which lead to errors up to 14° . In the case of the two thrust earthquakes studied, we find a tradeoff between strike and rake, and for the strike-slip earthquake we found a clear tradeoff between dip and rake angles. For shallow dip fault mechanisms the strike and dip are not very stable parameters. In such cases, the strike and rake are mutually correlated in a manner that their difference is constant, with the strike-rake tradeoff characterised as a geometric tradeoff (Han *et al.*, 2011, 2013). Synthetic tests by Ferreira and Woodhouse (2006) showed that for a strike-slip earthquake, errors in rake due to the incorrect Earth structure can be up to 70° in long-period surface wave inversions. In this study we obtain smaller errors, probably because the ultra-low-frequency normal data used in our inversions are less sensitive to 3-D Earth structure effects than long-period surface waves. Indeed, the errors in fault strike and rake found in this study (up to 9° in strike and 25° in rake) are comparable to those determined in previous studies, such as Hjörleifsdóttir and Ekström (2010) who found errors about 7° in strike and up to 10° in rake, and Ferreira *et al.* (2011) who found an average variability of about 14° in strike and 30° in rake.

Overall, when comparing the various examples of earthquakes considered, the largest errors in source parameters occur for a finite source inversion in the presence of data noise and using the PREM model for the normal earthquake tested, which is very shallow with a depth of 12 km and difficult to constrain given the very long wavelength of the data used compared to its depth (Bukchin *et al.*, 2010).

One current limitation of our work is that we only consider unilateral earthquake ruptures. Indeed, bilateral rupture modelling could be implemented in future work. However, this would lead to a larger inverse problem requiring five parameters for the spatio-temporal characterisation of the rupture (two different rupture durations and lengths and a time delay parameter in case the rupture did not propagate simultaneously in both directions). For example Lambotte *et al.* (2007) tried to determine the spatio-temporal characteristics of the bilateral, 28 March 2005 M_w 8.6 Nias earthquake using normal mode singlet stripping, but they state that the data quality for this earthquake is not high enough to resolve all parameters.

4.7 Conclusions

In this Chapter we have developed a new earthquake normal mode source inversion technique for the simultaneous determination of the rupture duration, length and seismic moment tensor of large magnitude earthquakes ($M_w > 8.0$) with unilateral rupture. We use low-frequency ($f < 1$ mHz) normal mode spheroidal multiplets and split singlets, which are modelled using Higher Order Perturbation Theory (HOPT), taking into account the Earth's rotation and ellipticity, self-gravitational forces and lateral heterogeneity. The inversions are carried out using the Neighbourhood Algorithm, which explores the model space and allows us to investigate source parameter tradeoffs and uncertainties. We started by testing the validity of our initial phase modelling approximation. We found that the rupture duration is always well retrieved and the length determination is robust for a wide range of earthquake latitude locations and fault orientations deviating from a E-W equatorial fault. We then carried out synthetic experiments to investigate the effects of finite rupture, noise in the data, uncertainties in Earth's structure and spatio-temporal location errors in the source inversions. As expected, the effect of neglecting the finite rupture in a point source inversion increases gradually with the source dimensions and it affects

strongly rake determinations. We showed that noise in data is not a significant source of errors as long as a high signal-to-noise ratio is achieved (>4). Even for the ultra-long period normal mode data used in this study, the use of simplified 1-D Earth model can lead to important errors in fault geometry and large errors in rupture duration (up to 60%) and length (up to 30%), therefore its use is not recommended in real earthquake applications. Likewise, large spatio-temporal location uncertainties (up to 1° in epicentre and 10 s in origin time) yield important errors in rake angle determinations (up to 15%) and large errors in rupture length (up to 25%). Apart from rake, all strike, dip and moment magnitude errors are relatively small, and all source parameter errors are comparable or smaller than uncertainties reported in the literature. Thus, the technique seems appropriate for real data inversions.

Chapter 5

Earthquake source models obtained from ultra low-frequency normal mode data

5.1 Summary

We present new earthquake source models obtained using the ultra low-frequency ($f \leq 1$ mHz) normal mode source inversion technique presented in the previous Chapter. The technique is applied to five giant earthquakes ($M_w \geq 8.5$) that have occurred in the past decade: (i) the 26 December 2004 Sumatra-Andaman earthquake; (ii) the 28 March 2005 Nias, Sumatra earthquake; (iii) the 12 September 2007 Bengkulu earthquake; (iv) the Tohoku, Japan earthquake of 11 March 2011; (v) the Maule, Chile earthquake of 27 February 2010; and (vi) the recent 24 May 2013 M_w 8.3 Okhotsk Sea, Russia, deep ($h = 607$ km) earthquake. While finite source inversions for rupture length, duration, magnitude, strike, dip and rake are possible for the Sumatra-Andaman and Tohoku events, for all the other events their lower magnitudes do not allow stable inversions of mode singlets. Hence only point source inversions using normal mode multiplets are carried out for these four earthquakes. Realistic normal mode spectra are calculated using Higher Order Perturbation Theory (HOPT), taking into account the Earth's rotation, ellipticity and lateral heterogeneities in the Earth's mantle. A Monte Carlo algorithm is used to search the model parameter space and estimate model uncertainties based on a heuristic misfit deterioration

11 Earthquake source models obtained from ultra low-frequency normal mode data

criterion. We start by validating our technique by applying it to the great 2004 Sumatra-Andaman earthquake, which has been extensively studied using a wide range of data and methods, so that its source characteristics are now relatively well understood. We find a rupture length of about 1,277 km and a duration of 521 s for this event, corresponding to an average rupture velocity of 2.45 km/s, which agree well with previous estimates. In addition, our estimates of magnitude, fault strike, dip and rake for this event also show a good agreement with results from previous work. We obtain the first normal mode source model for the 2011 Tohoku earthquake, which yields a fault length of about 461 km, a rupture duration of 151 s, and hence an average rupture velocity of 3.05 km/s, giving an independent confirmation of the compact nature of this event. Moreover, our estimates of moment magnitude, fault strike, dip and rake agree well with existing results, notably with the Global Centroid Moment Tensor (GCMT) solution. For all the other earthquakes studied, our new point source models are compared with those in the literature, showing average differences of 7.5° in strike, 10.3° in rake, 2.5° in dip and 0.1 in M_w , which are comparable or smaller to reported errors in these parameters from other studies. We do not find any unexplained systematic differences between our results and those in the literature, suggesting that, for the wave frequencies considered, the moment magnitude, fault geometry and mechanism of the earthquakes studied do not show a strong frequency dependence.

5.2 Introduction

In the previous Chapter we presented in detail a new earthquake source inversion technique using the Earth's ultra low-frequency normal modes ($f \leq 1$ mHz). The technique operates in two modes, either as an inversion for point source determinations using normal mode multiplets, or as a finite source inversion of unilateral rupture earthquakes, using the splitting of the gravest spheroidal multiplets.

As explained in the previous Chapter, a main advantage of studying seismic sources using ultra low-frequency normal mode data is their ability to characterise the overall source process, e.g., revealing slow-slip components in the rupture process of very large magnitude earthquakes (Okal *et al.*, 2012). Examples of such earthquakes are the great

22 May 1960 M_w 9.5 Chile earthquake (Kanamori and Cipar, 1974; Kanamori and Anderson, 1975a; Cifuentes and Silver, 1989) and the 26 December 2004 M_w 9.3 Sumatra-Andaman earthquake (Park *et al.*, 2005; Tsai *et al.*, 2005; Stein and Okal, 2005). Very large magnitude earthquakes with very long source duration (> 250 s), like the 2004 Sumatra-Andaman earthquake, can be difficult to study using routine techniques. For example, the GCMT method (Dziewonski *et al.*, 1981; Ekström *et al.*, 2012) did not detect the total energy radiated from the source of the 2004 Sumatra earthquake as a result of slow slip (Park *et al.*, 2005; Tsai *et al.*, 2005; Stein and Okal, 2005). Even though long-period mantle waves are used in the inversion, the earthquake's moment magnitude was underestimated in the GCMT catalogue. In addition, long duration earthquakes (> 250 s), like the 2004 Sumatra earthquake, cannot be studied using for example the recently developed SCARDEC body wave technique (Vallée *et al.*, 2011) as a result of mixing of the seismic phases (P , PcP , PP and SH , ScS) used by the technique in the $60\text{--}90^\circ$ distance range.

One important issue in earthquake source inversions is that simplifying assumptions about the Earth's structure can lead to errors in earthquake source parameters (e.g. Dziewonski and Woodhouse, 1983; Ferreira and Woodhouse, 2006; Hjörleifsdóttir and Ekström, 2010; Patton and Randall, 2002; Ferreira *et al.*, 2011). As shown in Chapter 4, the use of 1-D simplified Earth structure in normal mode source inversions can yield substantial errors in the determined source parameters, especially in estimates of rupture length and duration. Therefore, lateral heterogeneities in the Earth need to be accounted for in normal mode source inversions.

Another key issue in earthquake source studies is the estimation of model uncertainties. As explained in Chapter 3, the GCMT method only reports standard uncertainties, assuming that uncorrelated data noise is the only source of error, which leads to very low uncertainty values. The SCARDEC technique reports source parameter uncertainties in a systematic way using a misfit deterioration criterion (Vallée *et al.*, 2011), while the W-phase technique recently developed a scheme to map posterior uncertainties on the obtained source models (Duputel *et al.*, 2012a). The new normal mode source inversion technique presented in Chapter 4 addresses these issues, as it takes into account

11 Earthquake source models obtained from ultra low-frequency normal mode data

the Earth's 3-D structure in the modelling and uses a probabilistic inversion scheme enabling the estimation of source parameter uncertainties. Uncertainties are estimated similar to SCARDEC in an heuristic way by setting an acceptable range of source parameters which lead to misfit values not exceeding 1% of the misfit value that corresponds to the optimal source model. This is indicative of the method's resolution and especially of the magnitude's sensitivity to the dip angle.

In this Chapter we apply this technique to real global earthquakes of $M_w \geq 8.5$ which occurred during the last decade. This includes the following shallow subduction earthquakes:

- 26 December 2004 M_w 9.3 Sumatra-Andaman
- 28 March 2005 M_w 8.6 Nias
- 12 September 2007 M_w 8.5 Bengkulu
- 27 February 2010 M_w 8.8 Maule, Chile
- 11 March 2011 M_w 9.1 Tohoku, Japan

We discard the 11 April 2012 M_w 8.6 Sumatra strike-slip earthquake as it was followed by a M_w 8.2 event within two hours; hence, it would be difficult for our technique to resolve the two seismic sources separately by fitting low-frequency normal mode data. Finally, we also include the recent 24 May 2013 M_w 8.3 Okhotsk Sea, Russia, deep earthquake in our analysis (see Figure 5.1 for illustrative data examples).

Four of the earthquakes studied in this Chapter, such as the 2004 Sumatra-Andaman, the 2005 Nias, the 2010 Maule and the 2011 Tohoku events have been previously examined using normal mode data (Park *et al.*, 2005; Stein and Okal, 2005; Lambotte *et al.*, 2006, 2007; Konca *et al.*, 2007; Okal and Stein, 2009; Tanimoto and Ji, 2010; Tanimoto *et al.*, 2012; Okal *et al.*, 2012). The most widely studied event is the 2004 Sumatra-Andaman earthquake. Results from normal mode studies (Park *et al.*, 2005; Stein and Okal, 2005) were the first to suggest that the GCMT catalogue underestimated its seismic moment and source duration. Lambotte *et al.* (2006) determined spatio-temporal characteristics of the rupture of the 2004 Sumatra earthquake using the splitting of ultra low-frequency spheroidal modes and highlighted its very long rupture duration and

length. Lambotte *et al.* (2007) applied a singlets' stripping technique to constrain rupture kinematics of the 2004 Sumatra and 2005 Nias earthquakes. They verified their previous findings for the 2004 Sumatra earthquake and the bilateral rupture of the 2005 Nias earthquake by normal mode initial phase modelling, suggesting a 40 s delay between the north and south fault segments. Konca *et al.* (2007) studied the low-frequency normal mode spectra of the 2005 Nias earthquake in combination with geodetic data, in order to better constrain the earthquake's seismic moment and dip angle which was found to range $8\text{--}10^\circ$. Motivated by the 2004 Sumatra earthquake, Tanimoto and Ji (2010) examined low-frequency normal mode data for the 2010 Chile earthquake and Tanimoto *et al.* (2012) studied low-frequency normal modes of the 2004 Sumatra, 2007 Solomon, 2010 Chile and 2011 Tohoku earthquakes. In fact, Tanimoto and Ji (2010) claimed that found evidence of afterslip for the 2010 Chile earthquake, but Tanimoto *et al.* (2012) revised the latter findings and proposed the moment - dip tradeoff as a source of uncertainty in dip angle determination which can explain the discrepancy between the observed and the GCMT theoretical normal mode spectra. Okal *et al.* (2012) also stated that they did not find any evidence about afterslip regarding the 2010 Chile earthquake.

In contrast with the latter earthquakes mentioned above, the recent 2013 Okhotsk Sea earthquake is a nearly horizontal fault event that occurred at a depth greater than 600 km. This kind of earthquakes is quite distinct from shallow thrust earthquakes regarding the normal mode spectra observations. A relatively well studied example is the 9 June 1994 M_w 8.2 Bolivia earthquake which is one of the deepest earthquakes ever recorded. Because of its great depth the contributions to the surface displacement field from modes of low radial and angular orders is predominant compared to high radial and angular order modes (Ekström, 1995). Dahlen and Tromp (1998) also show theoretical normal mode spectra comparisons for the 1994 Bolivia deep earthquake with an artificial shallow thrust earthquake. They show that after attenuation filtering both events, many more high-quality factor $PKIKP$ equivalent spheroidal modes remain visible in the observed spectra for the deep event compared to the shallow earthquake. Moreover, deep earthquakes also differ in their rupture process as imaged by the associated source time function, suggesting shorter duration with respect to their magnitude (Houston, 2001) compared to estimates using a scalar equation (e.g. Kanamori and Anderson,

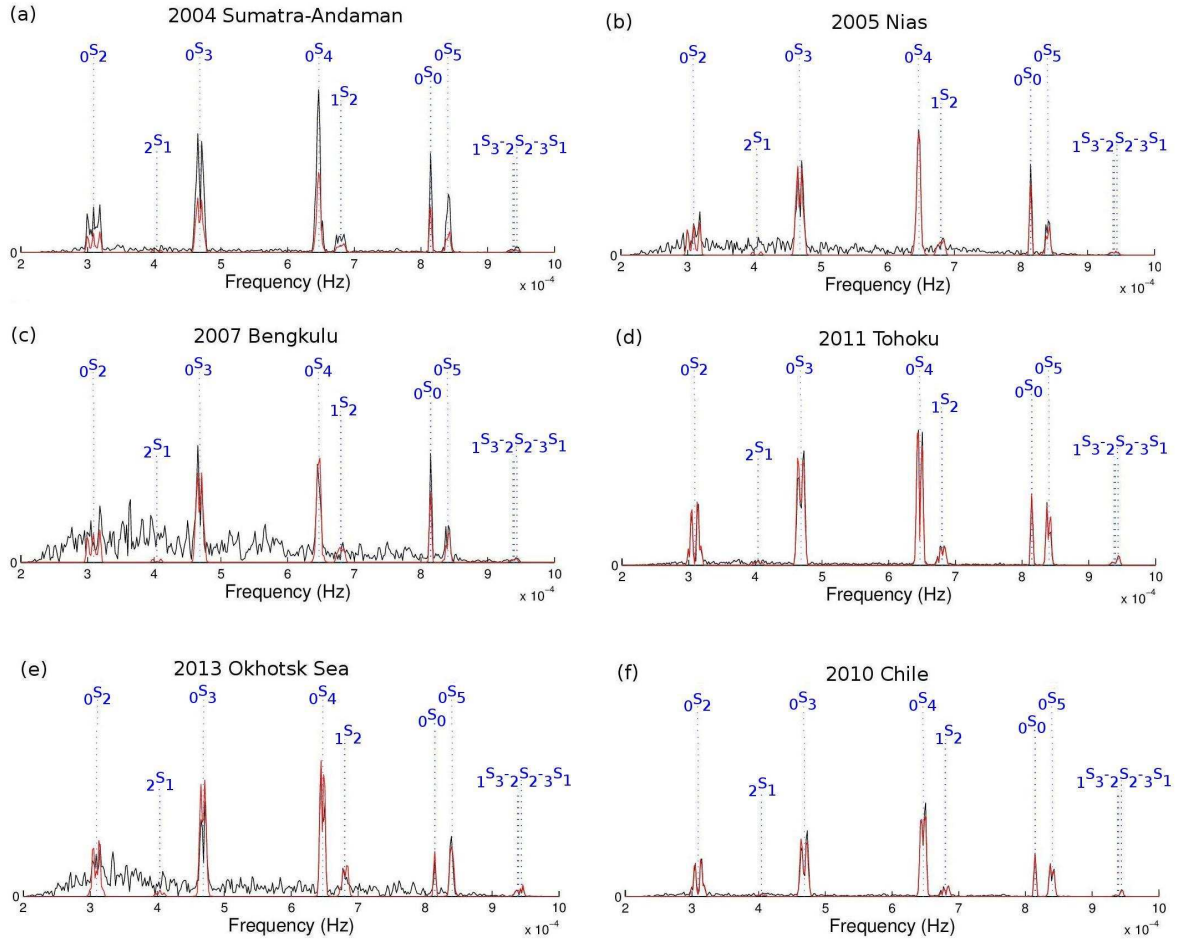


Figure 5.1: 144-hr acceleration amplitude data (black) and GCMT (red) spectra observed at BFO station for the six earthquakes analysed in this Chapter: (a) 2004 Sumatra-Andaman, (b) 2005 Nias, (c) 2007 Bengkulu, (d) 2011 Tohoku, (e) 2013 Okhotsk Sea, (f) 2010 Chile. Degenerate spheroidal mode eigenfrequencies are plotted in blue for reference.

1975b). The latter is also highlighted in SCARDEC source model of the 2013 Okhotsk Sea earthquake (http://www.geoazur.net/scardec/Results/Previous_events_of_year_2013/20130524_054449_SEA_OF_OKHOTSK/carte.jpg) suggesting a source time function of approximately 40 s of total duration.

Most previous normal mode earthquake source studies have focused on the earthquake's magnitude (Park *et al.*, 2005; Stein and Okal, 2005; Okal and Stein, 2009; Tanimoto *et al.*, 2012), or rupture duration and length determinations (Lambotte *et al.*, 2006, 2007). The new technique used here simultaneously determines the fault geometry and moment magnitude for all six earthquakes, and fault geometry, moment magnitude and rupture spatio-temporal characteristics of the 2004 Sumatra and 2011 Tohoku earthquakes.

5.3 Method and data

As explained in Chapter 4, we have implemented a new grid search technique using ultra low-frequency normal mode data (0–1 mHz) for the determination of point source models (strike ϕ , dip δ , rake λ , M_w) and/or finite source models (strike ϕ , dip δ , rake λ , M_w , rupture duration T_r , rupture length L) of great unilateral rupture earthquakes. The details of the methodology have been discussed in detail in Chapter 4, but will be briefly summarised here. Higher Order Perturbation Theory (Lognonné, 1991) is used to calculate realistic normal mode excitation kernels spectra, taking into account the Earth’s rotation, ellipticity and 3-D structure, using the mantle model SAW12D (Li and Romanowicz, 1996). Self-gravitational force corrections are also applied to the low-frequency spectra. Multiplet point source inversions are carried out using earthquake centroid locations from previous studies or catalogues (e.g., from the GCMT catalogue). On the other hand, finite source inversions are carried out using the PDE location (Preliminary Determination of Epicentres), which should be associated with the rupture’s initiation. The optimization is carried out using the Neighbourhood Algorithm developed by Sambridge (1999a) which is guided by the L_2 – norm misfit function (see equation 4.6 and other further details in Chapter 4). The parameter space is built as explained in the previous Chapter, using the GCMT source model as start model and ranges 40° in strike and rake, 30° in dip, 0.6 in moment magnitude, 100 s in rupture duration and 240 km in length. The tuning parameters used in the Neighbourhood Algorithm are the same as those used in the synthetic tests of Chapter 4.

We use very broadband time-series from the Global Seismographic Network (GSN). Except for the 2013 Okhotsk Sea event, only vertical component recordings are used as they are less noisy than horizontal component data, which are very sensitive to tilts and atmospheric perturbations. For the singlets’ inversions we use 480 hours of continuous recordings with respect to ${}_0S_2$ and ${}_0S_3$ Q-cycle (Dahlen, 1982). For details see section 4.3.3.2 in Chapter 4 and the next subsection.

For the multiplets’ point source inversions, where the finite rupture is neglected (point source approximation) there are no constraints on time window lengths and the length of the seismograms can vary according to the earthquake’s magnitude. For very large magnitude earthquakes ($M_w \geq 8.8$), we use a time window of 240 hours, and for smaller

12 Earthquake source models obtained from ultra low-frequency normal mode data

magnitude earthquakes the time window ranges between 48–240 hours in order to achieve a high signal-to-noise ratio, which is assessed by visual, manual inspection of all the data available. Gaps in the recordings are filled with zeros and glitches are removed where possible. Stations with gaps longer than five minutes or stations with multiple gaps and those reported as having questionable instrumental responses or timing errors (Davis *et al.*, 2005) are discarded. The requirement of very long, continuous (up to 20 days) and low noise level time-series, in combination with poorer ocean coverage compared to land based stations can lead to gaps in station distribution. However, for each earthquake, high quality data can be obtained for over 15 stations on average.

Finally, a visual inspection of the quality of the normal mode acceleration data was carried out prior to the inversion. The data was filtered multiplet by multiplet, or singlet by singlet depending on the inversion type to be carried out. Spectral peaks with a low signal-to-noise ratio $\sim \leq 2$ were given a weighting factor equal to zero and high quality spectral peaks (signal-to-noise ratio $\sim \geq 4$) were rewarded with a high weighting factor (up to 1). A weighting factor ranging 0.1–0.9 was used for spectral peaks with moderate signal-to-noise ratio (2–4). A weighting factor equal to zero means that the spectral peak is not taken into account in the inversion, while a weighting factor equal to one accounts strongly for the information carried by the particular signal.

5.3.1 Normal mode singlet separation

The separation of low-frequency normal mode singlets can be very challenging and is only possible due to the enhancement of data quality in the past decades. A lot of effort has been also made towards efficient normal mode spectra observations regarding the development of new techniques. The identification of spectral leakage and mode-mode interference by Dahlen (1982) as serious drawbacks in low-frequency normal mode spectra observations were well resolved by standard signal processing of data windowing and optimum record length selection. Moreover, a multitaper technique proposed by Park *et al.* (1987) yielded good spectral leakage resistance, for example in comparison with a Hanning taper, which discards 5/8 of statistical information in a time-series and weights unequally the signal by emphasising the central portion of the record. Using the variance

as a good measure, the multitaper technique shows even lower values without overemphasising the central part of the time-series.

The singlet stripping technique which was developed by Buland *et al.* (1979) has been widely applied in normal mode studies (e.g Ritzwoller *et al.*, 1986; Widmer *et al.*, 1992b,a) and has lead to the identification of anomalously splitting modes (e.g. Ritzwoller *et al.*, 1986). More recently, Lambotte *et al.* (2007) applied successfully this technique to determine the spatio-temporal kinematics of the 2004 Sumatra earthquake. Moreover, a stacking technique known as the multi-station experiment developed by Courtier *et al.* (2000) for the identification of the Slichter mode (${}_1S_1$) or any other degree one mode, was applied by Rosat *et al.* (2003) to resolve the splitting of the ${}_2S_1$ multiplet by calculating their eigenfrequencies.

We apply a Hanning taper prior to Fourier transform in order to eliminate spectral leakage and we separate the ultra-low frequency, high quality factor ${}_0S_2$ and ${}_0S_3$ singlets by using a 20-days time window according to their Q-cycle (Dahlen, 1982). We then narrow filter the signal around each target singlet in a similar way as in Lambotte *et al.* (2006). This window length provides enough resolution to separate their singlets. Figure 5.2 shows an example of ${}_0S_2$ and ${}_0S_3$ splitting after 20 days of continuous recordings. All ${}_0S_2^m$ and ${}_0S_3^m$ singlets are well resolved, except maybe ${}_0S_3^{\pm 2}$ singlets. The ${}_0S_0$ radial mode which has a Q-cycle of about 75 days does not split into singlets but it is coupled with its neighbour ${}_0S_5$ multiplet (Deuss and Woodhouse, 2001). Our goal is to separate them and eliminate their interference. Lambotte *et al.* (2007) stated that even a 15-days time window can provide stable phase estimates of this very high quality factor (5327) radial mode compared to its low quality factor (356) neighbour. ${}_0S_4$ and ${}_0S_5$ singlets are hard to separate, as for these multiplets their spectral peaks become broader because of attenuation; consequently, they are not included in the singlets' inversions.

5.4 Analysis of large magnitude earthquakes

As explained in section 5.2, we carry out source inversions for five large magnitude ($M_w \geq 8.5$ in GCMT catalogue), shallow depth (< 30 km) thrust earthquakes, as well as for the recent 2013 M_w 8.3 Okhotsk Sea, deep ($h = 607$ km), nearly horizontal fault, earthquake (see Figure 5.3). In the following subsections we present in detail the obtained

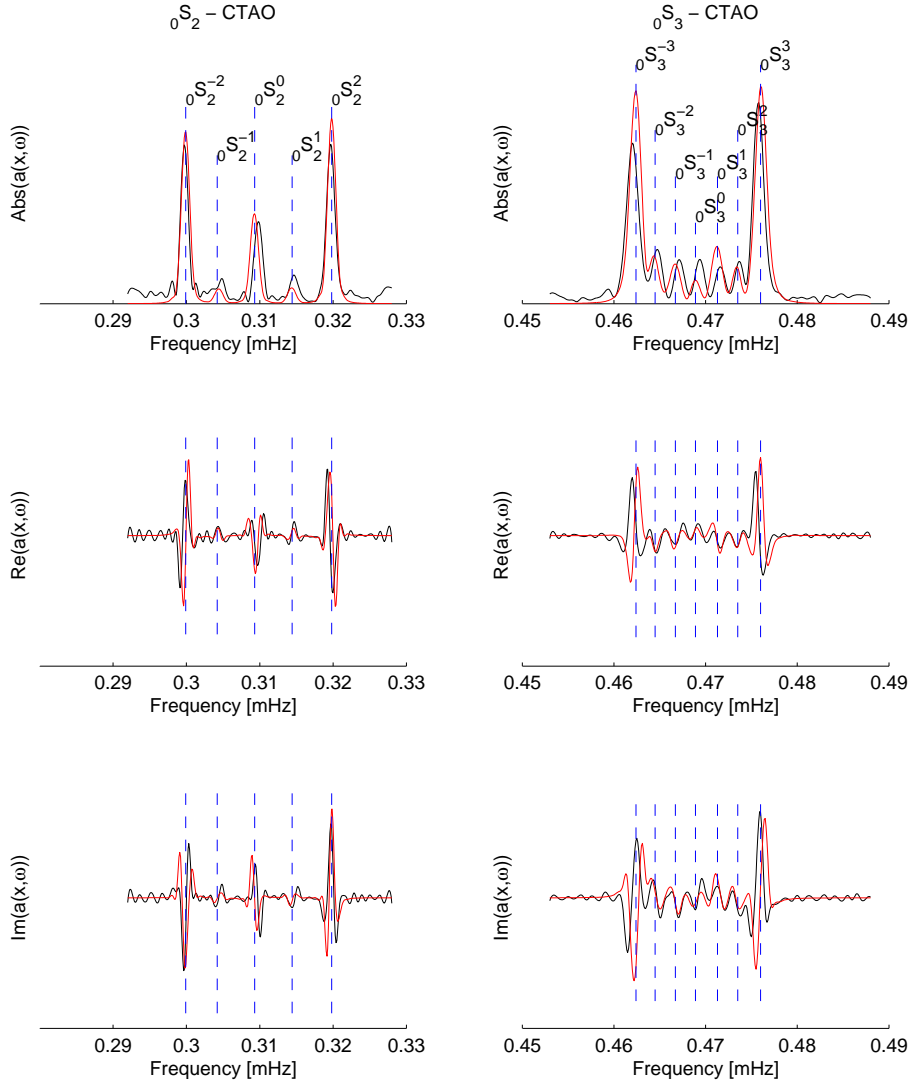


Figure 5.2: Singlets separation for ${}_0S_2$ and ${}_0S_3$ multiplets obtained from 480-hr acceleration spectra for the 26 December 2004 M_w 9.3 Sumatra-Andaman earthquake, recorded at CTAO station (black). Finite source model synthetics obtained from the singlets inversion described in subsection 5.4.1.1 are also shown (red) for reference. Top panel shows acceleration amplitude spectra, middle and bottom panels show real and imaginary FFT parts, respectively. Blue dashed lines indicate singlets' eigenfrequencies with respect to Earth's rotation, ellipticity and SAW12D Earth model.

source models.

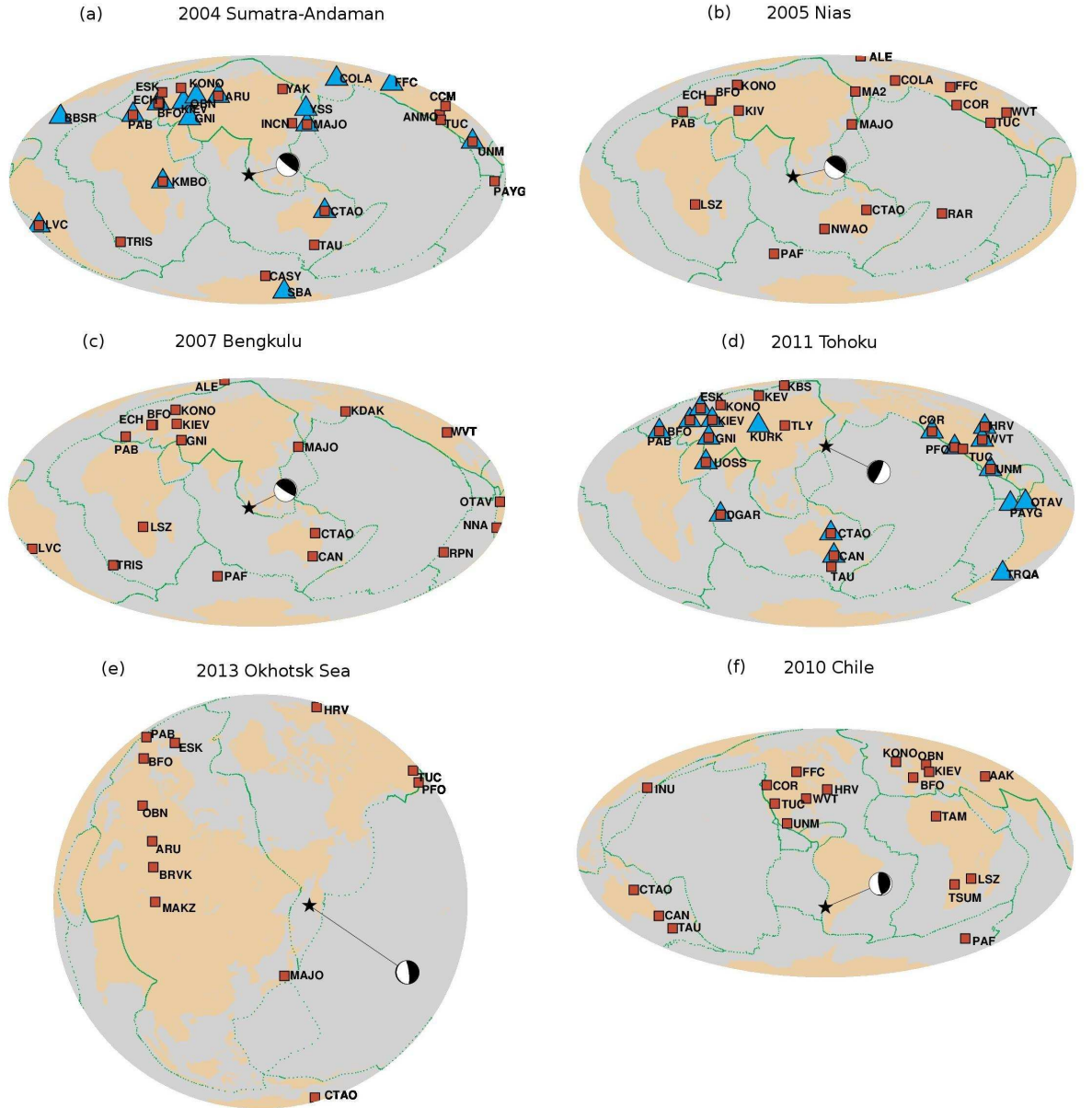


Figure 5.3: Global maps showing the GCMT locations (stars) and beachballs of the six earthquakes analysed in this Chapter: (a) 2004 Sumatra-Andaman, (b) 2005 Nias, (c) 2007 Bengkulu, (d) 2011 Tohoku, (e) 2013 Okhotsk Sea, (f) 2010 Chile. Stations used in the point source inversions are plotted as red squares and those used in the finite source inversions are plotted as cyan triangles.

5.4.1 The 2004 M_w 9.3, 2005 M_w 8.6 and 2007 M_w 8.5 Sumatra earthquakes

The Andaman-Sumatra trench where the Indo-Australian tectonic plate subducts underneath the Eurasian plate is one of the most seismically active areas on Earth. In the

12 Earthquake source models obtained from ultra low-frequency normal mode data

south-west portion, the Australian plate subducts at approximately 60 mm/yr, and towards the north-west the convergence direction becomes oblique and the rate decreases to 45 mm/yr (Figure 5.4). Along Sumatra, thrust motion takes place perpendicular to the trench and, slightly to the east, right-lateral slip over the Sumatra fault is observed (Fitch, 1972; Prawirodirdjo *et al.*, 2000; McCaffrey *et al.*, 2000). Many significant historic earthquakes are reported in the area, such as, the 1881 $M \sim 7.9$ and the 1941 $M \sim 7.7$ earthquake in the north, and the 1797 $M \sim 8.4$, the 1833 $M \sim 9.0$ and the 1861 $M \sim 8.5$ earthquake in the south (Newcomb and McCann, 1987; Zachariasen *et al.*, 1999; Rivera *et al.*, 2002; Bilham *et al.*, 2005).

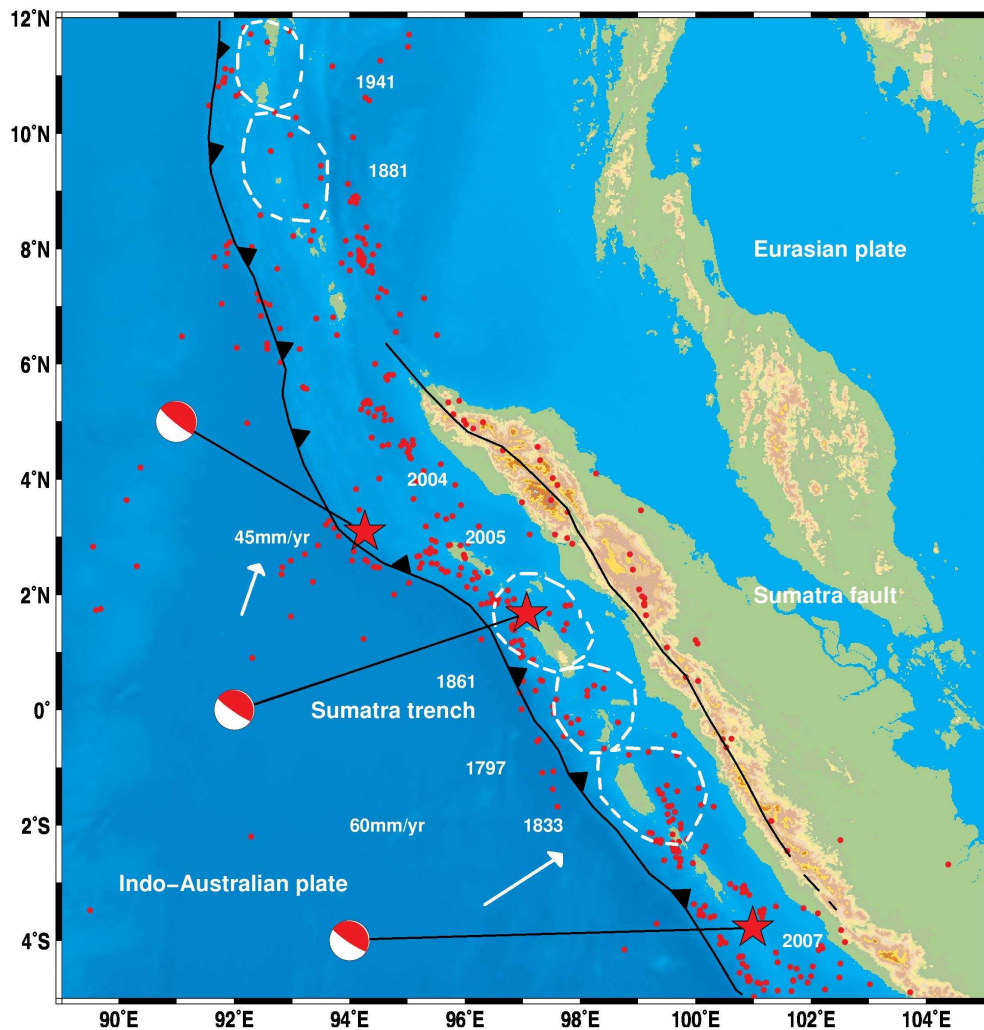


Figure 5.4: Map showing the tectonic setting of the 2004, 2005 and 2007 Sumatra earthquakes. Red stars indicate the centroid locations of the mainshocks. Red beachballs correspond to their GCMT source models. Red circles show the seismicity ($M_w \geq 5.5$ in entire GCMT catalogue) of the study area. White dashed lines indicate approximately the rupture areas of historic earthquakes.

Three great thrust earthquakes which ruptured the megathrust fault along the Sumatra

subduction zone are studied in this section. These include the 26 December 2004 M_w 9.3 Sumatra-Andaman earthquake, the 25 March 2005 M_w 8.6 Nias earthquake and the 12 September 2007 M_w 8.5 Bengkulu earthquake. The 2005 Nias earthquake ruptured the same area as the historic 1861 $M \sim 8.5$ earthquake and it may have been a consequence of Coulomb stress transfer because of the 2004 Sumatra earthquake (McCloskey *et al.*, 2005). All three generated significant tsunamis, with the most disastrous being the one associated with the 2004 Sumatra-Andaman earthquake. Runup heights up to 30 m observed along the coast of the Aceh Province and in Banda Aceh (Synolakis and Kong, 2006; Piatanesi and Lorito, 2007), resulting in over 250,000 fatalities. A small size tsunami was generated by the 2005 Nias earthquake in comparison with 2004 tsunami. Possible reasons are the much smaller rupture length of the 2005 Nias earthquake compared to the 2004 Sumatra earthquake, the maximum uplift of the 2005 event (~ 2.9 m) was much smaller compared to 2004 event (~ 5.4 m) and the greatest vertical displacement occurred along shallow water and land and not in deep water as in the case of the 2004 earthquake (Briggs *et al.*, 2006). Most of the causalities ($\sim 2,000$) associated with the 2005 Nias earthquake are due to building collapses as the tsunami occurred away from a highly populated area (Walker *et al.*, 2005). On the other hand, the 2007 Bengkulu earthquake caused a moderate tsunami with runup heights up to 4 m (Lorito *et al.*, 2008; Borrero *et al.*, 2009) and approximately 25 fatalities.

5.4.1.1 The 26 December 2004 M_w 9.3 earthquake

The 2004 Sumatra-Andaman earthquake involved a slow slip component which was not detected by the GCMT inversion, resulting in its magnitude underestimation (Park *et al.*, 2005; Tsai *et al.*, 2005; Stein and Okal, 2005). The mainshock is characterised by a unilateral rupture towards the north rupturing a total length of ~ 1200 km which lasted more than 8 minutes (e.g., Ishii *et al.*, 2005; Tsai *et al.*, 2005; Guilbert *et al.*, 2005; Ni *et al.*, 2005; Krüger and Ohrnberger, 2005; Lambotte *et al.*, 2006, 2007; Vallée, 2007). Relatively large slip (10 m) has been observed close to the hypocentre and maximum slip of 20–30 m was located close to Nicobar islands (Ammon *et al.*, 2005; Lay *et al.*, 2005; Piatanesi and Lorito, 2007; Chileh *et al.*, 2007).

We first carried out a point source inversion using 240 hours of continuous data including all spheroidal multiplets in the 0–1 mHz frequency range, except ${}_2S_1$, which is not well excited. In total, spectra of six multiplets (${}_0S_{2,0} S_{3,0} S_{4,0} S_{5,0} S_{0,1} S_2$) and the ${}_3S_1 - {}_1S_3$ supermultiplet recorded at 20 stations from the GSN used in the inversion (Figure 5.5a). The origin time and centroid location were fixed to the GCMT solution and the parameter space used in the inversions is also based on this solution (Table D.1). Our results are summarised in Table 5.1. In addition to presenting the results obtained for strike ϕ , dip δ , rake λ , M_w , we also show the corresponding uncertainties, which are estimated by considering as acceptable solutions those that correspond to data misfit values that are 1% larger than the optimal data misfit. The resulting point source model has a very steep dip angle, ($\delta=19.3^\circ$) and a lower moment magnitude ($M_w = 9.0$) in comparison with the revised GCMT model of Tsai *et al.* (2005) and the W-phase source model. Therefore, further inversions were carried out using: (i) a source depth of 10 km, as reported in the PDE catalogue; and, (ii) the centroid location of Tsai *et al.* (2005). The shallower PDE depth did not change substantially the results and the fit to the data did not improve. However, the use of the centroid location of Tsai *et al.* (2005) in our inversions resulted in a better fit to the data (see Table 5.1 and Figure 5.5a). Some spectral peaks show poorer fit compared to others due to their higher noise level (Figure 5.5a). The corresponding optimal point source model (Figure 5.5b–c) obtained after 160 iterations and the generation of 5822 models (see Figure 5.5d) is in better agreement with the W-phase solution and with the composite source model of Tsai *et al.* (2005).

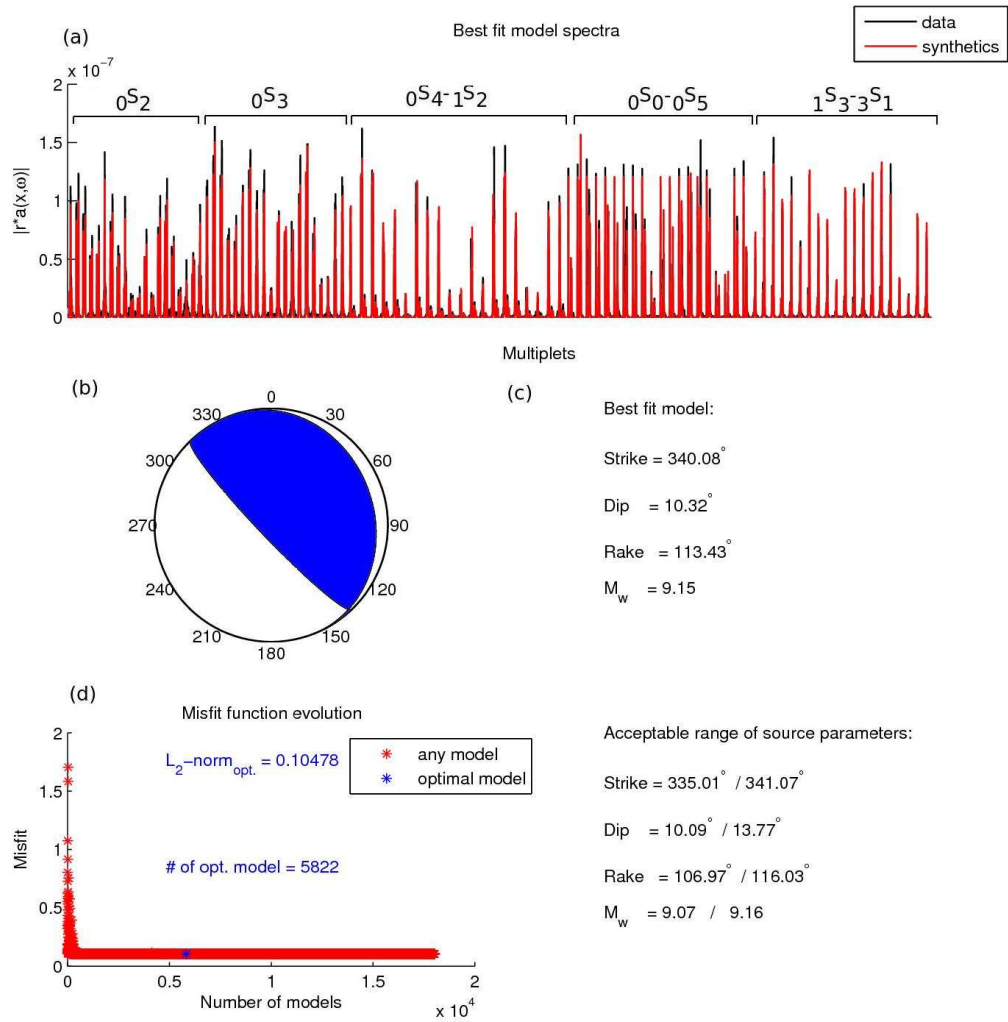


Figure 5.5: Results from a point source inversion for the 2004 Sumatra-Andaman earthquake. The SAW12D 3-D mantle model is used to build excitation kernels for the centroid location of Tsai *et al.* (2005): (a) 240-hr optimal fit amplitude spectra of $0S_2$, $0S_3$, $0S_4$, $1S_2$, $0S_0$, $0S_5$, $1S_3-2S_2-3S_1$ multiplets; (b) optimal source mechanism; (c) optimal and acceptable range of source parameters (acceptable parameters correspond to source models yielding misfit values not exceeding the minimum misfit value by more than 1%); (d) misfit function evolution as a function of the number of models generated in the parameter search.

Table 5.1: Comparison of the GCMT, W-phase and Tsai *et al.* (2005) source models for the 2004 Sumatra-Andaman earthquake with point source models obtained from our multiplet point source inversions using: (i) the GCMT location and GCMT depth of $h=28.6\text{km}$ (4th row); (ii) the GCMT location and PDE depth of $h = 10 \text{ km}$ (5th row); and, (iii) the centroid location determined by Tsai *et al.* (2005) (6th row). Reported uncertainties correspond to solutions with a data misfit not exceeding the minimum misfit value by more than 1%.

		$\phi(^{\circ})$	$\Delta\phi(^{\circ})$	$\delta(^{\circ})$	$\Delta\delta(^{\circ})$	$\lambda(^{\circ})$	$\Delta\lambda(^{\circ})$	M_w	ΔM_w	misfit	beachball
GCMT		329.0	–	8.0	–	110.0	–	9.0	–	–	
W-phase		335.6	–	7.2	–	113.7	–	9.2	–	–	
Tsai <i>et al.</i> (2005)		343.0	–	6.1	–	107.0	–	9.3	–	–	
This study	GCMT location, ($h=28.6\text{km}$)	343.7	336.5–348.8	19.3	12.8–21.8	121.2	109.2–129.4	9.0	9.0–9.1	0.114	
This study	GCMT location, ($h=10.0\text{km}$)	342.5	332.8–345.6	17.0	16.6–28.5	119.3	101.7–120.3	9.0	8.9–9.0	0.115	
This study	Tsai <i>et al.</i> (2005) Centroid location	340.1	335.0–341.1	10.3	10.1–13.8	113.4	107.0–116.0	9.2	9.1–9.2	0.105	

Table 5.2: Initial phase (X_m) estimates for the singlets included in the finite source inversion carried out for the 26 December 2004 Sumatra-Andaman earthquake. Initial phases correspond to the optimal source model determined from the inversion ($\phi = 340.9^\circ$, $T_r = 521.0$ s, $L = 1276.8$ km) with respect to the PDE location. Singlets' periods (T_m) are also shown for reference.

Singlet	T_m (s)	X_m ($^\circ$)
${}_0S_2^{-2}$	3334	-31.9
${}_0S_2^0$	3233	-29.0
${}_0S_2^2$	3140	-26.1
${}_0S_3^{-3}$	2166	-48.9
${}_0S_3^3$	2107	-38.9
${}_0S_0^0$	1228	-76.4

A finite source inversion was also carried out using 480 hours of continuous recordings including well excited normal mode spheroidal singlets in the frequency range 0–1 mHz (see Figure 5.6a). Some ${}_0S_2$ and ${}_0S_3$ singlets recorded by higher noise level stations were discarded from the inversion by penalising them with a weighting factor equal to zero (gaps in spectra of Figure 5.6a). In addition to point source parameters, the rupture duration and length were also searched in our inversion. Table 5.2 shows the associated initial phases for the singlets used in the inversion, while Table 5.3 summarises our optimal model; various source models reported in the literature (including the GCMT and W-phase solutions) are also shown for comparison. Our source model is in very good agreement with the composite model of Tsai *et al.* (2005), although our dip angle is slightly steeper. Large differences of approximately 10° are observed compared to the W-pahse strike and rake angles, however, our dip angle differs only 1° with W-pahse. Our moment magnitude from both the point and finite source inversions are in good agreement with other studies (see Table 5.3 for details), all suggesting a larger magnitude to that initially inferred from GCMT. Total rupture duration (521 s) and length (1276.8 km) determined from the singlets' inversion are also in excellent agreement with other studies presented in Table 5.3. Figure 5.6a shows the data fit of the optimal model obtained from the inversion (Figures 5.6b and 5.6c) after 269 iterations and the corresponding exploration of 21620 models (Figure 5.6d).

The tradeoff plots in Figure 5.7 show clearly the moment magnitude – dip tradeoff in both point and finite source inversions. We also observe a tradeoff between strike and rupture length in the finite source inversion, which is not unexpected considering

13 Earthquake source models obtained from ultra low-frequency normal mode data

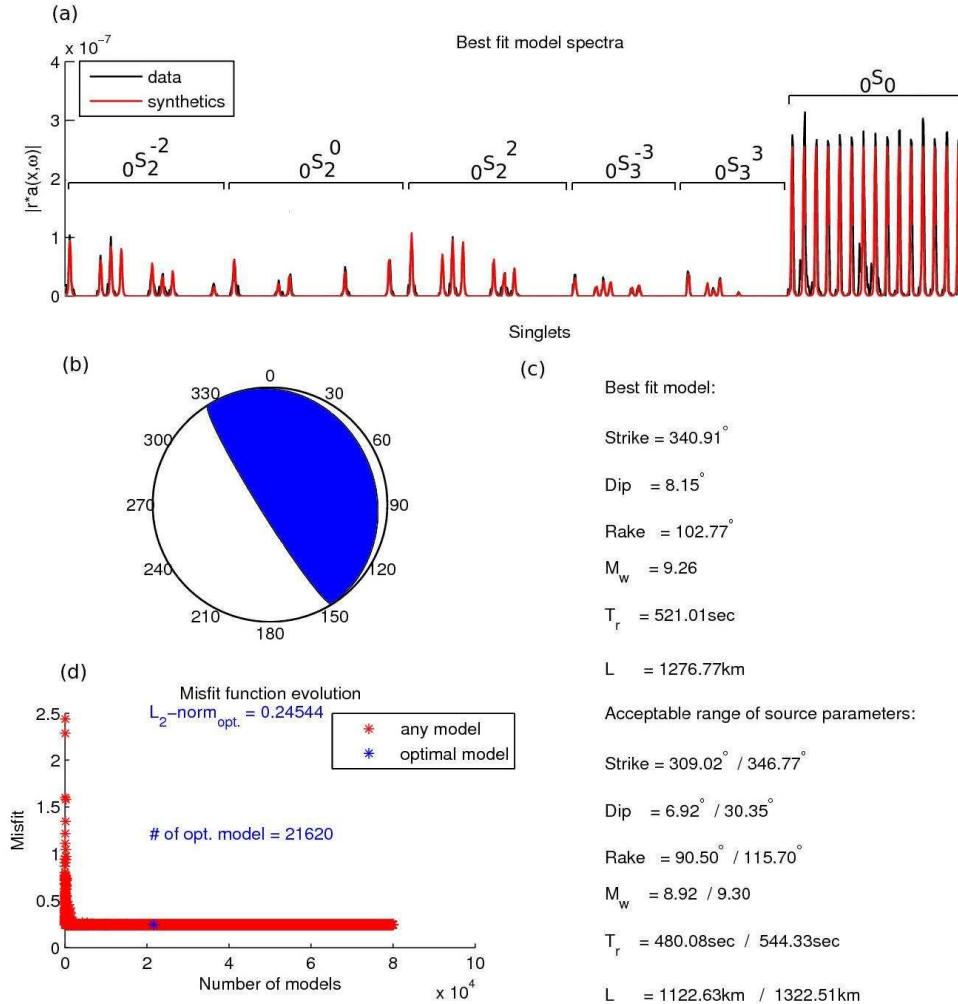


Figure 5.6: Results from a finite source inversion for the 2004 Sumatra earthquake. SAW12D 3-D model is used to build the excitation kernels: (a) 480-hr optimal fit amplitude spectra of $0S_2^{\pm 2}$, $0S_2^0$, $0S_3^{\pm 3}$, $0S_0$ singlets with respect to the PDE location, (b) optimal source mechanism, (c) optimal and acceptable range of source parameters (acceptable parameters correspond to source models yielding misfit values up to 1% larger than the lowest misfit associated with the optimal source model), (d) misfit function evolution.

equation 4.5 in Chapter 4. Since the location of the rupture initiation is fixed in the inversion, the second term of equation 4.5 varies only because of the length and the source orientation, leading to the tradeoff observed in Figure 5.7. A similar tradeoff has also been observed in synthetic tests presented in Chapter 4 (e.g. Figure 4.13).

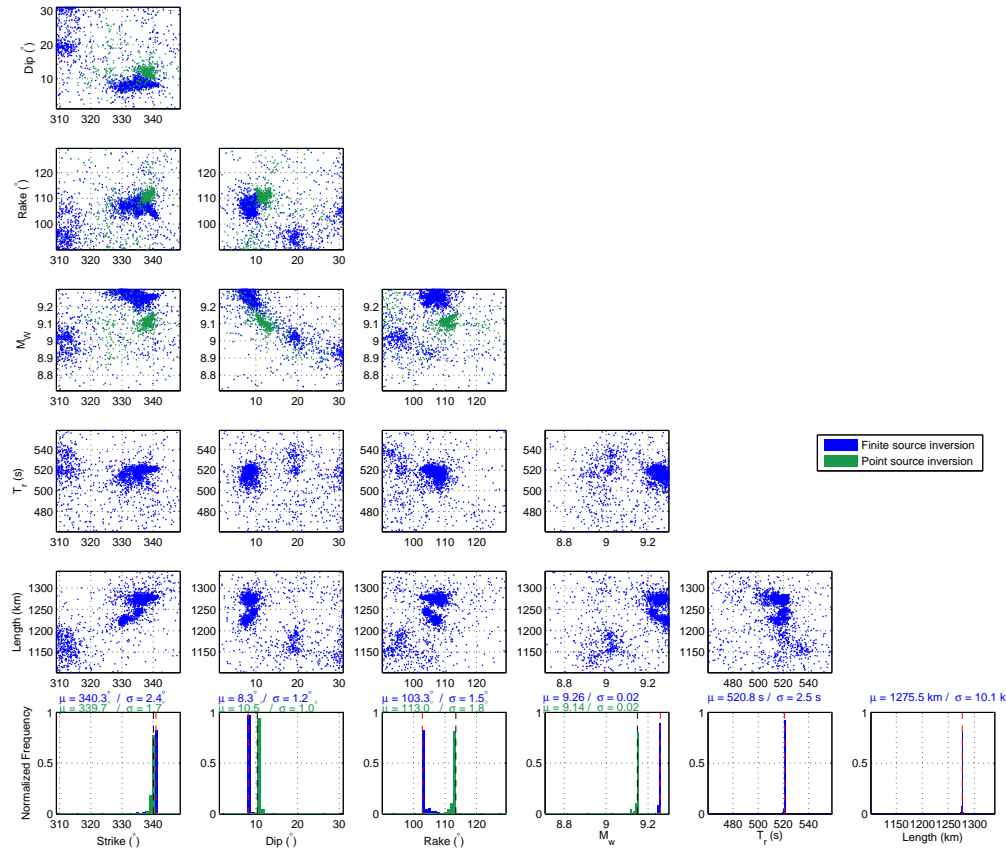


Figure 5.7: Tradeoff scatterplots from the ensemble of models produced by the Neighbourhood Algorithm for inversion results of Figure 5.5 (point source inversion; green dots) and Figure 5.6 (finite source inversion; blue dots) for the great 2004 Sumatra-Andaman earthquake. The normalised histograms in the bottom row show the distribution of the inversion results (their mean μ and standard deviation σ values are also shown). Black and red dashed vertical lines correspond to the optimal source parameters obtained from point and finite source inversions, respectively.

Table 5.3: Comparison of point $(\phi, \delta, \lambda, M_w)$ and finite $(\phi, \delta, \lambda, M_w, T_r, L)$ source models determined in this study with GCMT, W-phase, SCARDEC and other studies for the 2004 Sumatra-Andaman earthquake. Uncertainties shown correspond to models with misfit values within a 1% tolerance with respect to the optimal misfit.

	$\phi(^{\circ})$	$\Delta\phi(^{\circ})$	$\delta(^{\circ})$	$\Delta\delta(^{\circ})$	$\lambda(^{\circ})$	$\Delta\lambda(^{\circ})$	M_w	ΔM_w	$T_r(s)$	$\Delta T_r(s)$	$L(km)$	$\Delta L(km)$
GCMT	329.0	–	8.0	–	110.0	–	9.0	–	–	–	–	–
W-phase	335.6	–	7.2	–	113.7	–	9.2	–	–	–	–	–
SCARDEC	–	–	–	–	–	–	–	–	–	–	–	–
Tsai <i>et al.</i> (2005)	343.0	–	6.1	–	107.0	–	9.3	–	540.0	–	1150.0	–
Lambotte <i>et al.</i> (2006)	–	–	–	–	–	–	–	–	500.0	–	1220.0	–
Lambotte <i>et al.</i> (2007)	–	–	–	–	–	–	–	–	550.0	–	1250.0	–
Park <i>et al.</i> (2005)	–	–	–	–	–	–	9.2	–	600.0	–	1250.0	–
Ammon <i>et al.</i> (2005)	–	–	–	–	–	–	–	–	500.0	–	1250.0	–
Stein and Okal (2005)	–	–	–	–	–	–	9.3	–	–	–	1250.0	–
Ni <i>et al.</i> (2005)	–	–	–	–	–	–	–	–	500.0	–	1200.0	–
Vallée (2007)	–	–	–	–	–	–	9.1	–	580.0	–	1175.0	–
Chileh <i>et al.</i> (2007)	–	–	–	–	–	–	9.2	–	–	–	1500.0	–
Guilbert <i>et al.</i> (2005)	–	–	–	–	–	–	–	–	515.0	–	1235.0	–
Ishii <i>et al.</i> (2005)	–	–	–	–	–	–	9.3	–	–	–	1300.0	–
Krüger and Ohrnberger (2005)	–	–	–	–	–	–	–	–	490.0	–	1150.0	–
This study	340.1	335.0–341.1	10.3	10.1–13.8	113.4	107.0–116.0	9.2	9.1–9.2	–	–	–	–
This study	340.9	309.0–346.8	8.2	6.9–30.4	102.8	90.5–115.7	9.3	8.9–9.3	521.0	480.1–544.3	1276.8	1122.6–1322.5

5.4.1.2 The 28 March 2005 M_w 8.6 earthquake

The 2005 Nias earthquake involved a bilateral rupture over a total area of 400 km by 100 km, with a total duration of approximately 120 s and an average slip of 6 m (Walker *et al.*, 2005). Several studies suggest a rupture propagation towards the north, followed by southward propagation after a delay of about 40 s (Walker *et al.*, 2005; Briggs *et al.*, 2006; Lambotte *et al.*, 2007). On the other hand, Konca *et al.* (2007) argued that the rupture propagated simultaneously towards the north and the south. The mainshock was followed by a relatively small tsunami. As a result, most of the fatalities were due to collapsed buildings (Walker *et al.*, 2005).

The results of our inversions are summarised in Table 5.4 and illustrated in Figure D.1 in Appendix D. We carried out point and finite source inversions, but our finite source inversion results were unstable as far as rupture duration and length are concerned. Indeed, the modelling of the initial phase we carry out is designed to fit unilateral rupture earthquakes, in contrast with the 2005 Nias earthquake which is characterised by bilateral rupture. Therefore, we limit our results to a point source inversion, which uses 240 hours of continuous recordings including all spheroidal multiplets in the 0–1 mHz frequency range. In total, we used seven multiplets recorded at 18 stations (see Figure D.1 in Appendix D). The ${}_2S_1$ multiplet was discarded due to its low signal-to-noise ratio. ${}_2S_1$ mode is the first overtone of the so-called Slichter mode, and involves motion in the Earth's core (Rosat *et al.*, 2003). Table 5.4 shows that our optimal point source model is similar to results from other studies. The fault strike and, importantly, rake angle are larger than those found in other studies by about 8° for strike and by 15° for rake. In addition, the moment magnitude is slightly larger than in previous studies and the fault dip angle is relatively shallow compared to W-phase and SCARDEC, but steeper than GCMT. These discrepancies are consistent with clear moment magnitude – dip and strike – rake tradeoffs observed in the tradeoff plots for this earthquake (see Figure D.2 in Appendix D).

5.4.1.3 The 12 September 2007 M_w 8.5 earthquake

The 12 September 2007 M_w 8.5 Bengkulu earthquake is the smallest in our set of events in Sumatra, characterised by a unilateral rupture towards the northwest (e.g., Konca *et al.*, 2008; Lorito *et al.*, 2008). Its magnitude is not large enough to allow us to use very long

13 Earthquake source models obtained from ultra low-frequency normal mode data

Table 5.4: Comparison of point $(\phi, \delta, \lambda, M_w)$ source model determined in this study with GCMT, W-phase, SCARDEC and other studies for the 2005 Nias earthquake. Uncertainties shown correspond to models with misfit values within a 1% tolerance with respect to the optimal misfit.

	$\phi(^{\circ})$	$\Delta\phi(^{\circ})$	$\delta(^{\circ})$	$\Delta\delta(^{\circ})$	$\lambda(^{\circ})$	$\Delta\lambda(^{\circ})$	M_w	ΔM_w
GCMT	333.0	–	8.0	–	118.0	–	8.6	–
W-phase	333.2	–	12.3	–	114.5	–	8.5	–
SCARDEC	320.0	–	13.0	–	99.0	–	8.5	–
Bukchin and Mostinskii (2007)	315.0	–	10.0	–	90.0	–	8.6	–
Konca <i>et al.</i> (2007)	–	–	10.0	–	–	–	8.6	–
This study	341.0	334.7–341.8	9.4	6.2–13.8	132.8	122.8–133.2	8.7	8.5–8.7

Table 5.5: Comparison of point $(\phi, \delta, \lambda, M_w)$ source model determined in this study with GCMT, W-phase, SCARDEC and other studies for the 2007 Bengkulu earthquake. Uncertainties shown correspond to models with misfit values within a 1% tolerance with respect to the optimal misfit.

	$\phi(^{\circ})$	$\Delta\phi(^{\circ})$	$\delta(^{\circ})$	$\Delta\delta(^{\circ})$	$\lambda(^{\circ})$	$\Delta\lambda(^{\circ})$	M_w	ΔM_w
GCMT	328.0	–	9.0	–	114.0	–	8.5	–
W-phase	317.1	–	13.6	–	95.0	–	8.3	–
SCARDEC	329.0	–	17.0	–	110.0	–	8.4	–
Lorito <i>et al.</i> (2008)	–	–	–	–	–	–	8.4	–
Konca <i>et al.</i> (2008)	–	–	–	–	–	–	8.4	–
This study	329.6	321.1–333.8	8.1	7.7–19.3	111.7	97.6–116.7	8.6	8.3–8.6

time series (20 days), which are needed to separate ultra low-frequency singlets required for a finite source inversion, as the spectra of such long time series is dominated by noise for this earthquake (Figure 5.1c). Therefore, only a point source inversion was carried out, using 216 hours of continuous data, including all spheroidal multiplets in the 0–1 mHz frequency range, except again the ${}_2S_1$ multiplet, as it is poorly excited. A total of seven multiplets recorded at 18 stations is used (see Figure D.3 in Appendix D). Table 5.5 summarises our optimal point source parameters and compares them with GCMT, W-phase, SCARDEC and other source models reported in the literature. Overall, our point source model is in good agreement with the results from other studies, notably from the GCMT catalogue. However, some discrepancies in fault dip angle and in moment magnitude are observed, with our dip angle being about 1° – 9° shallower than in previous studies and our moment magnitude being about 0.1–0.2 larger than it was found in previous work. These differences are again due to the moment – dip angle tradeoff affecting our inversions, which is clearly seen in the tradeoff plot in Figure D.4 in the Appendix D.

5.4.2 The 2011 M_w 9.1 Tohoku and 2013 M_w 8.3 Okhotsk Sea earthquakes

In this section we examine the 2011 M_w 9.1 Tohoku earthquake and the recent deep (~ 607 km) 2013 M_w 8.3 Okhotsk Sea earthquake. The Tohoku earthquake occurred in the Japan trench where the Pacific plate subducts beneath the Okhotsk plate, a part of the larger North America plate, at a rate of about 92 mm/yr (DeMets *et al.*, 1990). Further to the northeast of the Japan trench, the Kuril-Kamchatka trench lies where the rate decreases to 75 mm/yr (Figure 5.8). The entire area is one of the most tectonically active regions on the Earth with many $M \sim 7$ earthquakes having occurred in the past (Yamanaka and Kikuchi, 2004). Large magnitude earthquakes mainly occur on the megathrust fault at shallow depths, however, normal faulting aftershocks occur on intraplate faults at a depth down to 100 km depth in different orientations compared to the trench strike (Nettles *et al.*, 2011; Hayes, 2011).

5.4.2.1 The 11 March 2011 M_w 9.1 Tohoku earthquake

The Japan trench is known for being the locus of large magnitude historic earthquakes, with the largest being the 1896 $M \sim 8.5$ tsunami earthquake (Kanamori, 1972) and the 1933 M_w 8.6 normal faulting earthquake (Kanamori, 1971). However, the 2011 earthquake, which ruptured the Japan megathrust fault directly south of the 1896 and 1933 earthquakes (see Figure 5.8) exceeded any expectations and generated a large tsunami responsible for the accident in Fukushima nuclear power plant. The 2011 earthquake differs from the 1896 earthquake not only in size but also because it produced strong ground shaking along the coastline, in contrast with tsunami earthquakes with weak near source short-period shaking (Koper *et al.*, 2011). Earthquake source images obtained from the back-projection of seismic waveforms recorded by large arrays show a frequency dependent rupture process with down-dip propagation of short-period energy and up-dip propagation of low-frequency energy (Koper *et al.*, 2011; Kiser and Ishii, 2012). The main features of the earthquake's rupture process, which mainly propagated towards the south, are found to be consistent among many studies which used a variety of data, such as GPS, strong motion, body and surface waves (e.g., Ammon *et al.*, 2011; Politz *et al.*, 2011b; Yagi and Fukahata, 2011b; Kiser and Ishii, 2012). Initially, the rupture propagated to the northeast for about 40 s at a relatively low velocity (1.0–1.5 km/s). During 40–90 s the

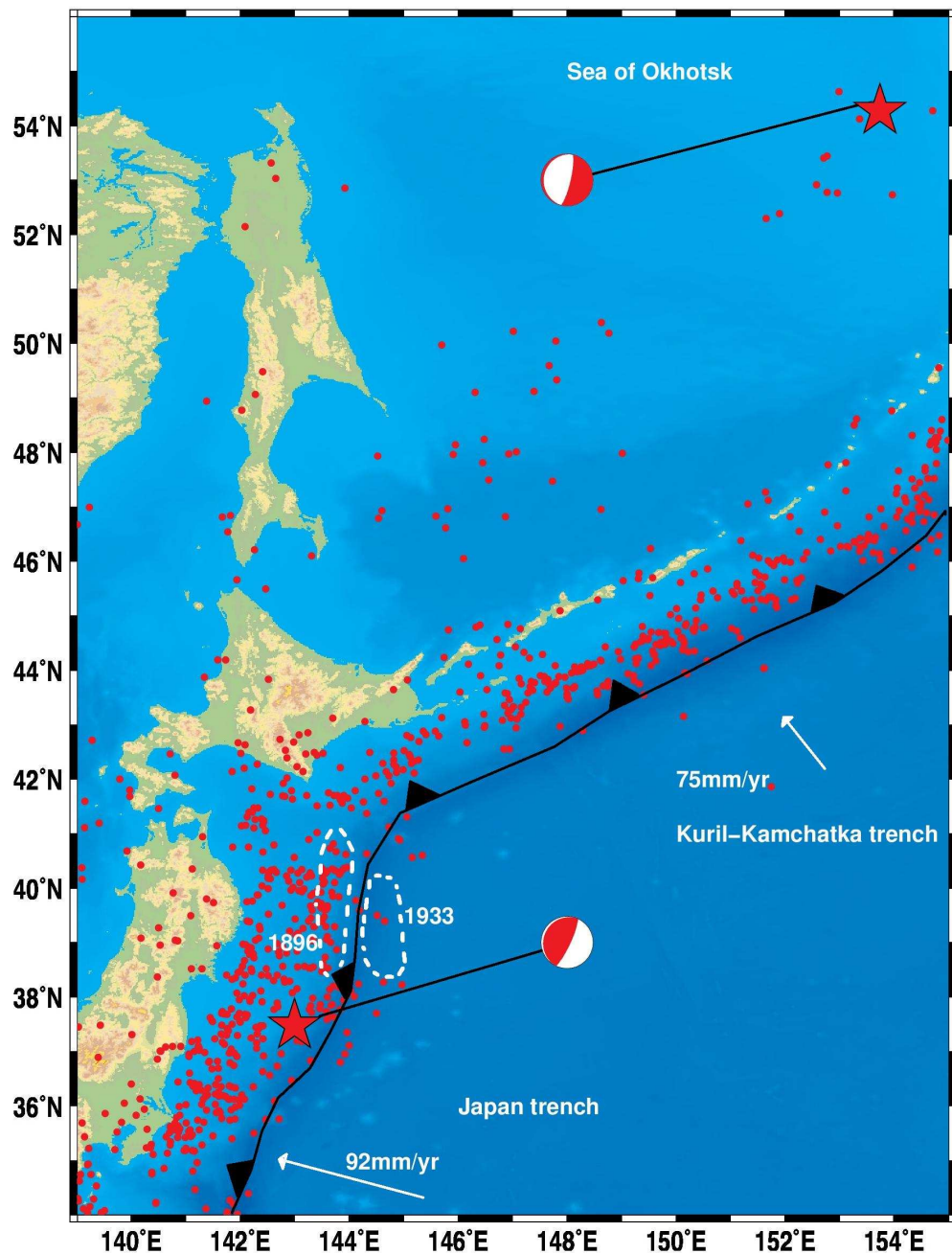


Figure 5.8: Map showing the tectonic setting of the 2011 Tohoku and the 2013 Okhotsk Sea earthquakes. Red stars indicate the centroid locations of the mainshocks. Red beachballs correspond to their GCMT source models. Red circles show the seismicity ($M_w \geq 5.5$ in entire the GCMT catalogue) of the study area. White dotted lines indicate approximately the rupture areas of historic earthquakes.

rupture propagated to the deeper parts of the subduction zone and continued towards the south with an average rupture velocity of 3.4 km/s.

For the 2011 Tohoku earthquake we carried out both a point and a finite source inversion using 240 and 480 hours of continuous recordings, respectively. We used the GCMT origin time and centroid location for the point source inversion and the PDE origin time and location for the finite source inversion. Table 5.6 shows the initial phases associated with the singlets used in the finite source inversion. The results from this and from other previous studies are summarised in Table 5.7. Figure 5.9a compares observed multiplets with theoretical calculations using our optimal point source model. Some observed spectral peaks show poorer fit due to larger amplitudes associated with higher noise level. A total of seven multiplets recorded by 20 stations are used (see Figure 5.3d). Figures 5.9b and 5.9c show our optimal earthquake source parameters and associated uncertainties from the point source inversion, and Figure 5.9d shows the misfit function evolution, with the optimal model being obtained after 61 iterations during which 4,964 models were explored. Overall there is a good agreement between our point source parameters and those reported in previous studies. Our fault strike estimate agrees well with GCMT and W-phase estimates, with the largest difference being observed in comparison with SCARDEC ($\sim 19^\circ$ difference). Rake angle is the parameter with the largest variation compared to other source models (with differences ranging from 8° to 31°). The moment magnitude M_w and fault dip angle agree well with previous studies, despite the clear moment-dip tradeoff affecting these inversions (see Figure 5.11).

Figure 5.10 shows the results from a singlets finite source inversion using a total of 11 singlets recorded by 18 stations (see Figure 5.3d). Some high noise level ${}_0S_2$ and ${}_0S_3$ singlets were given a zero weighting factor and many ${}_0S_0$ singlets had to be penalised with low weighting factors (~ 0.1) due to their noise level. Strike, moment magnitude and dip are close to GCMT and W-phase source parameters (see Table 5.7), with SCARDEC estimates showing larger discrepancies to our solutions (14° difference in strike, 3° in dip and 12° in rake). Moreover, when compared with results from other studies, our fault dip angles from both point and finite source inversions fall on the lowest end of the dip angle range. On the other hand, the rake angle estimate obtained from our finite source inversion is larger than values reported in other studies, but with differences not

Table 5.6: Initial phase (X_m) estimates for the singlets included in the finite source inversion carried out for the 11 March 2011 Tohoku earthquake. Initial phases correspond to the optimal source model determined from the inversion ($\phi = 197.3^\circ$, $T_r = 151.0$ s, $L = 461.0$ km) with respect to the PDE location. Singlets' periods (T_m) are also shown for reference.

Singlet	T_m (s)	X_m ($^\circ$)
${}_0S_2^{-2}$	3334	-9.7
${}_0S_2^{-1}$	3282	-9.1
${}_0S_2^1$	3186	-7.8
${}_0S_2^2$	3140	-7.1
${}_0S_3^{-3}$	2166	-14.9
${}_0S_3^{-2}$	2155	-14.2
${}_0S_3^{-1}$	2144	-13.5
${}_0S_3^1$	2124	-12.0
${}_0S_3^2$	2115	-11.3
${}_0S_3^3$	2107	-10.5
${}_0S_0^0$	1228	-22.1

exceeding 12° , which is smaller than for the rake value obtained from the point source inversion. Our estimates of rupture duration and length are in good agreement with those reported in the literature (Ammon *et al.*, 2011; Honda *et al.*, 2011; Koper *et al.*, 2011; Kurahashi and Irikura, 2011; Lay *et al.*, 2011; Lee *et al.*, 2011; Politz *et al.*, 2011b; Wang and Mori, 2011; Yamazaki *et al.*, 2011; Yagi and Fukahata, 2011b; Yoshida *et al.*, 2011; Zhang *et al.*, 2011; Kiser and Ishii, 2012). Figure 5.11 shows clearly moment magnitude – dip and strike – rake tradeoffs for both point and finite source inversions. As expected, a rupture length – strike tradeoff is also observed in the case of the finite source inversion, similar to the case of the 2004 Sumatra-Andaman earthquake.

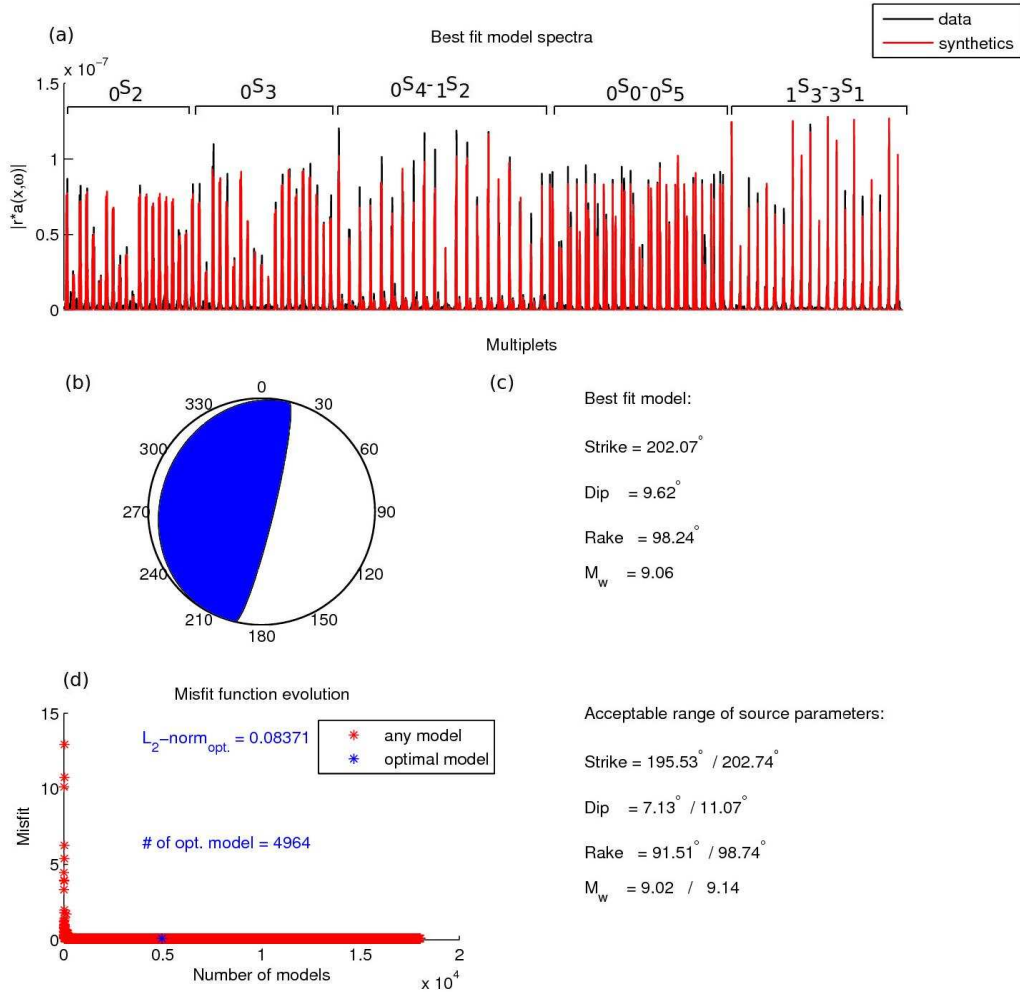


Figure 5.9: Results from a point source inversion for the 2011 Tohoku earthquake. The SAW12D 3-D mantle model is used to build the excitation kernels for the GCMT centroid location: (a) 240-hr optimal fit amplitude spectra of $0S_2$, $0S_3$, $0S_4$, $1S_2$, $0S_0$, $0S_5$, $1S_3-3S_1$ multiplets; (b) optimal source mechanism; (c) optimal and acceptable range of source parameters (acceptable parameters correspond to source models yielding misfit values not exceeding the lowest misfit value by more than 1%); (d) misfit function evolution as a function of the number of models generated in the parameter search.

14 Earthquake source models obtained from ultra low-frequency normal mode data

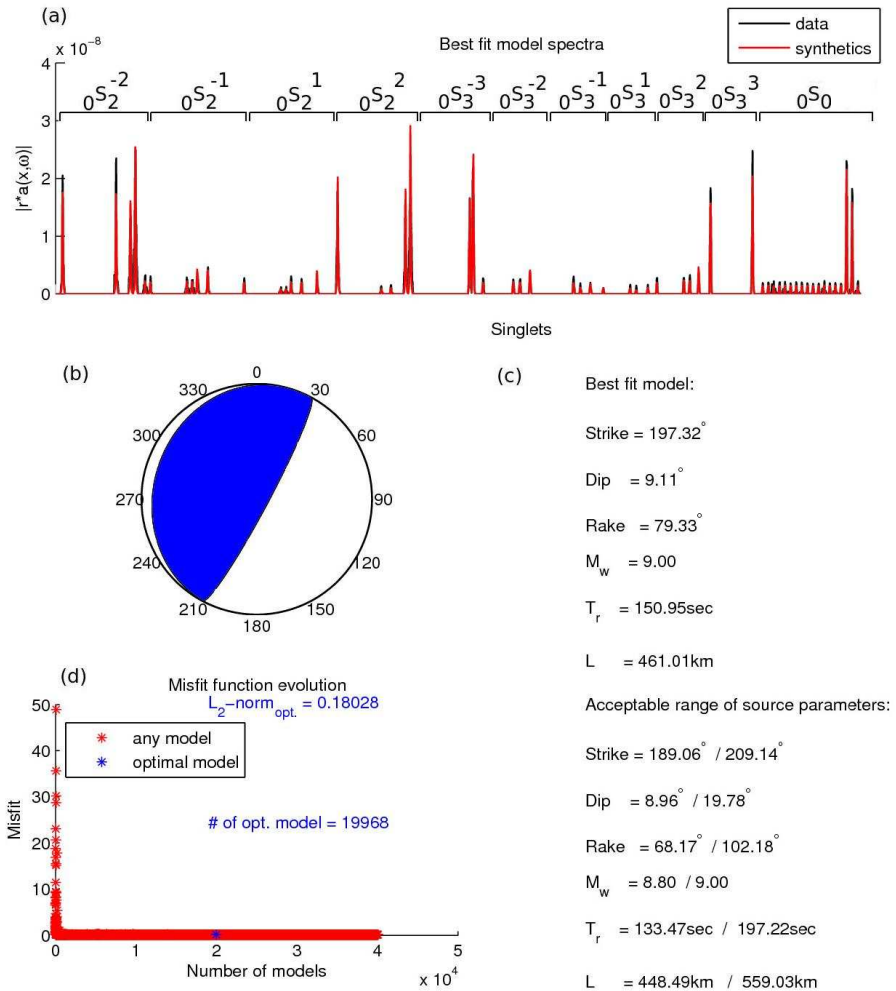


Figure 5.10: Results from a finite source inversion for the 2011 Tohoku earthquake. The SAW12D 3-D mantle model is used to build the excitation kernels for the PDE location: (a) 480-hr optimal fit amplitude spectra of $0S_2^{\pm 1}, 0S_2^{\pm 2}, 0S_3^{\pm 1}, 0S_3^{\pm 2}, 0S_3^{\pm 3}, 0S_0$ singlets; (b) optimal source mechanism; (c) optimal and acceptable range of source parameters (acceptable parameters correspond to source models yielding misfit values not exceeding the lowest misfit value by more than 1%); (d) misfit function evolution as a function of the number of models generated in the parameter search.

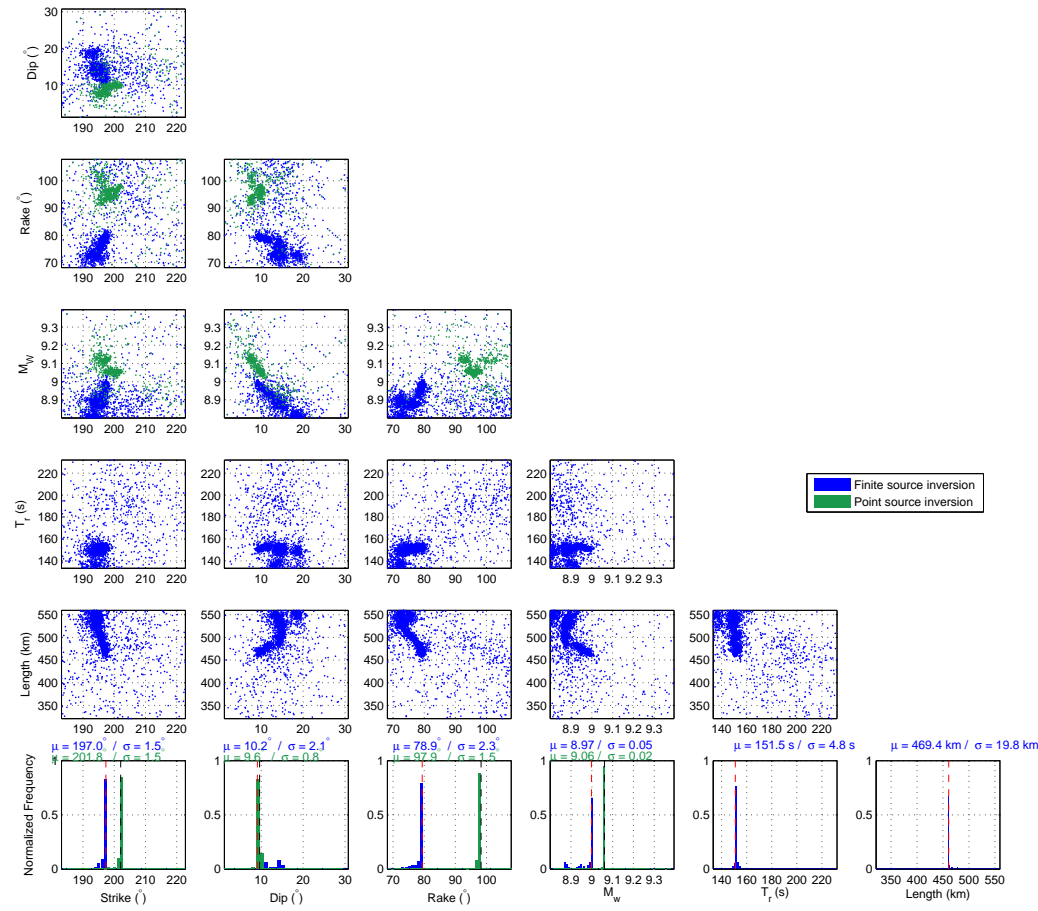


Figure 5.11: Tradeoff scatterplots from the ensemble of models produced by the Neighbourhood Algorithm for inversion results of Figure 5.9 (point source inversion; green dots) and Figure 5.10 (finite source inversion; blue dots) for the 2011 Tohoku earthquake. The normalised histograms in the bottom row show the distribution of the inversion results (their mean μ and standard deviation σ values are also shown). Black and red dashed vertical lines correspond to the optimal source parameters obtained from point and finite source inversions, respectively.

Table 5.7: Comparison of point $(\phi, \delta, \lambda, M_w)$ and finite $(\phi, \delta, \lambda, M_w, T_r, L)$ source models determined in this study with GCMT, W-phase, SCARDEC and other studies for the 2011 Tohoku earthquake. Uncertainties shown correspond to models with misfit values within a 1% tolerance with respect to the optimal misfit.

	$\phi(^{\circ})$	$\Delta\phi(^{\circ})$	$\delta(^{\circ})$	$\Delta\delta(^{\circ})$	$\lambda(^{\circ})$	$\Delta\lambda(^{\circ})$	M_w	ΔM_w	$T_r(s)$	$\Delta T_r(s)$	$L(km)$	$\Delta L(km)$
GCMT	203.0	–	10.0	–	88.0	–	9.1	–	–	–	–	–
W-phase	196.0	–	12.0	–	85.0	–	9.0	–	–	–	–	–
SCARDEC	183.0	–	12.0	–	67.0	–	9.1	–	–	–	–	–
Fujii <i>et al.</i> (2011)	–	–	–	–	–	–	9.0	–	–	–	–	–
Ammon <i>et al.</i> (2011)	–	–	–	–	–	–	–	–	–	–	300.0	–
Honda <i>et al.</i> (2011)	–	–	–	–	–	–	–	150.0	–	–	–	–
Chu <i>et al.</i> (2011)	191.0	–	23.0	–	90.0	–	–	–	–	–	–	–
Wang and Mori (2011)	–	–	–	–	–	–	–	150.0	–	–	450.0	–
Yoshida <i>et al.</i> (2011)	–	–	–	–	–	–	9.0	150.0	–	–	450.0	–
Kurahashi and Irikura (2011)	193.0	–	10.0	–	–	–	8.4	–	–	–	450.0	–
Yagi and Fukahata (2011b)	–	–	–	–	–	–	9.1	–	–	–	440.0	–
Lay <i>et al.</i> (2011)	–	–	–	–	–	–	–	150.0	–	–	–	–
Lee <i>et al.</i> (2011)	–	–	–	–	–	–	–	160.0	–	–	–	–
Politz <i>et al.</i> (2011b)	–	–	–	–	–	–	9.0	–	–	–	–	–
This study	202.1	195.5–202.7	9.6	7.1–11.1	98.2	91.5–98.7	9.1	9.0–9.1	–	–	–	–
This study	197.3	189.1–209.1	9.1	9.0–19.8	79.3	68.2–102.2	9.0	8.8–9.0	151.0	133.5–197.2	461.0	448.5–559.0

5.4.2.2 The 24 May 2013 M_w 8.3 Okhotsk Sea earthquake

The 2013 Okhotsk Sea earthquake was a nearly horizontal fault event, which occurred at a depth of approximately 607 km and ruptured a deep section of the Pacific lithosphere and stands out from the rest of our data set as one of the largest deep earthquakes ever recorded. The source region is situated at the Kuril back-arc basin where crust beneath most of the Sea of Okhotsk is 19–25 km thick, indicating a submerged continental margin (Zheng and Lay, 2006). This kind of deep earthquake is not unusual in this region. A search in the GCMT catalogue reveals several large magnitude deep nearly horizontal fault earthquakes such as the 5 July 2008 M_w 7.7 at depth of about 611 km, the 17 November 2002 M_w 7.3 at depth of \sim 480 km and many more $M_w < 7.0$ deep (> 300 km) earthquakes, however, these deep focus earthquakes do not cause any damage despite their large magnitudes.

In the case of the 24 May 2013 M_w 8.3 Okhotsk Sea earthquake, we only carry out a point source inversion as its magnitude does not allow the use of a very long time-series (~ 20 days) needed for a finite source singlets inversion (Figure 5.1e). In order to achieve a high signal-to-noise ratio we restrict our analysis to 48 hours of continuous recordings. We also include horizontal component data from the low-noise BFO seismic station, which are rotated into longitudinal and transverse components. In total, nine multiplets recorded by 12 stations (see Figure 5.3e) are used. Figures 5.12–5.13 show our results and Table 5.8 compares our point source parameters with GCMT and SCARDEC estimates. Because of the earthquake’s low magnitude the ultra low-frequency band is dominated by noise. Therefore, some very low-frequency fundamental spheroidal and toroidal multiplets recorded in high noise level stations were discarded (Figure 5.12a). The fit of the remaining spectral peaks is good, although poorer fit is observed for the lowermost frequency multiplets (e.g. ${}_0S_3$, ${}_0S_4$, ${}_0T_3$, ${}_0T_4$) which are given weighting factors ranging 0.1–0.8. Table 5.8 shows that our point source model is in very good agreement with the GCMT solution. However, we observe some differences of about 10° in strike and rake angles compared to the SCARDEC and W-phase (USGS) model for this earthquake. Figure 5.13 shows a clear strike – rake tradeoff but not a moment magnitude – dip tradeoff; indeed, given the great depth of this earthquake, the moment-dip tradeoff does not affect this source inversion. For such shallow dipping focal mechanisms (dip

14 Earthquake source models obtained from ultra low-frequency normal mode data

$\sim < 10^\circ$), the strike and rake angles are poorly constrained and mutually correlated in a manner that their difference is constant, with the strike – rake tradeoff characterised as a geometric tradeoff (Han *et al.*, 2011, 2013).

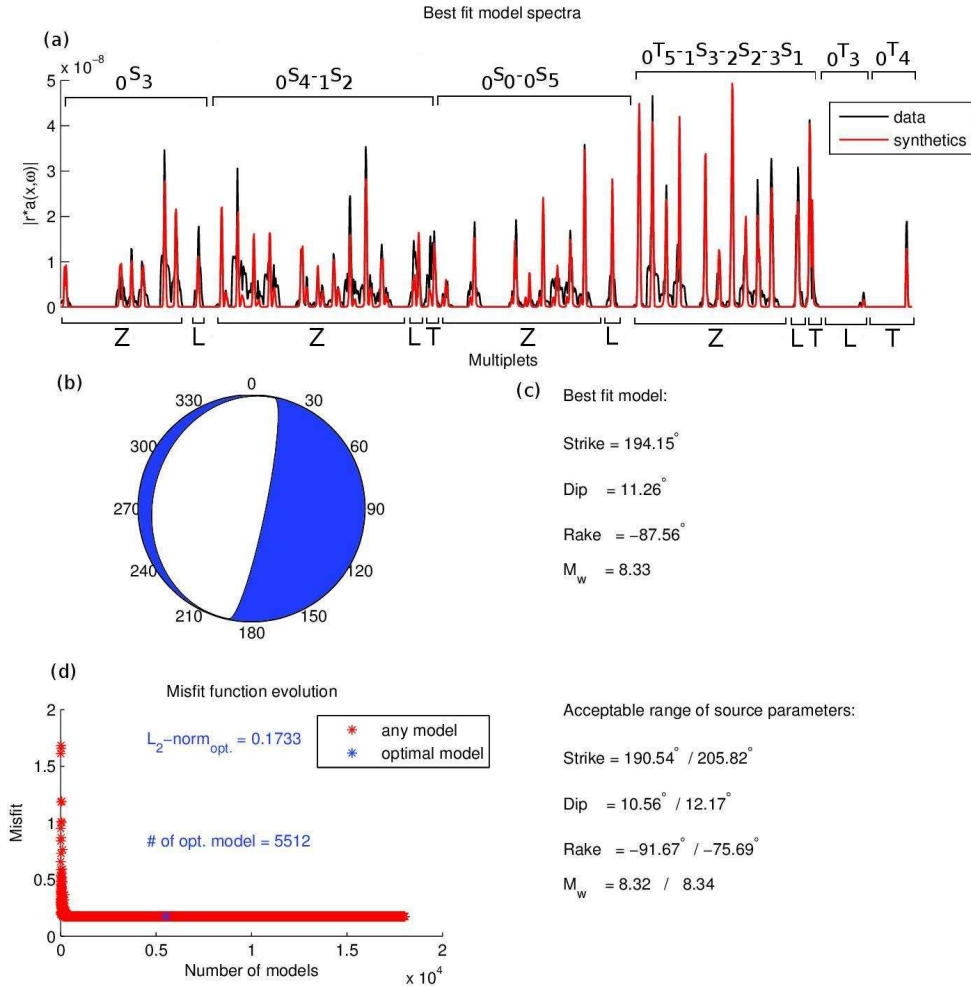


Figure 5.12: Results from a point source inversion for the 2013 Okhotsk Sea earthquake. The SAW12D 3-D mantle model is used to build the excitation kernels for the GCMT centroid location: (a) 48-hr optimal fit amplitude spectra of $0S_3$, $0S_4$, $1S_2$, $0S_0$, $0S_5$, $0T_5-1S_3-2S_2-3S_1$, $0T_3$, $0T_4$ multiplets; (b) optimal source mechanism; (c) optimal and acceptable range of source parameters (acceptable parameters correspond to source models yielding misfit values not exceeding the lowest misfit value by more than 1%); (d) misfit function evolution as a function of the number of models generated in the parameter search.

5.4.3 The 27 February 2010 M_w 8.8 Maule, Chile earthquake

The 2010 Maule earthquake occurred on a megathrust fault (Figure 5.14) where the South-American plate subducts beneath Nazca plate at a rate of approximately 65 mm/yr (Ruegg *et al.*, 2009). The earthquake ruptured a part of the known Darwin seismic gap, an area

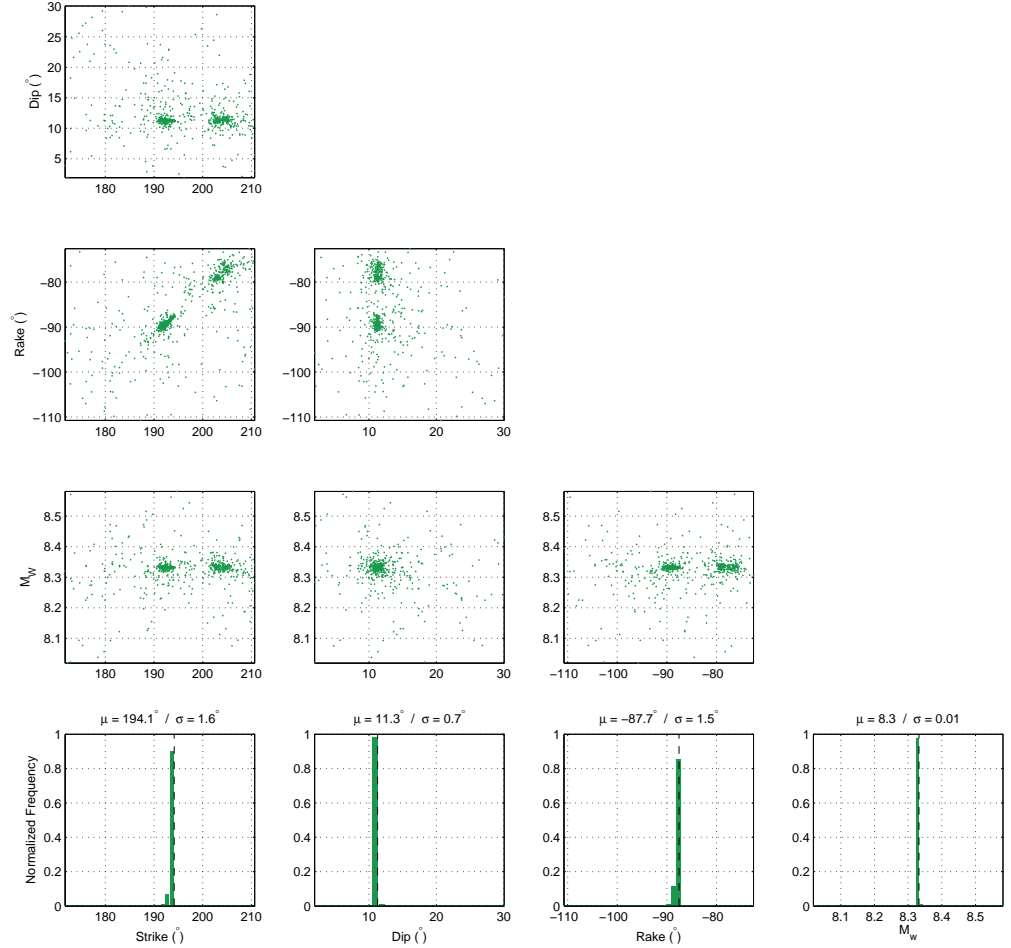


Figure 5.13: Tradeoff scatterplots from the ensemble of models produced by the Neighbourhood Algorithm for inversion results of Figure 5.12 for the 2013 Okhotsk Sea earthquake. The normalised histograms in the bottom row show the distribution of the inversion results (their mean μ and standard deviation σ values are also shown). Black dashed vertical lines correspond to the optimal source parameters obtained from the point source inversion.

Table 5.8: Comparison of point $(\phi, \delta, \lambda, M_w)$ source model determined in this study with GCMT, W-phase and SCARDEC for the 2013 Okhotsk Sea earthquake. Uncertainties shown correspond to models with misfit values within a 1% tolerance with respect to the optimal misfit.

	$\phi(^{\circ})$	$\Delta\phi(^{\circ})$	$\delta(^{\circ})$	$\Delta\delta(^{\circ})$	$\lambda(^{\circ})$	$\Delta\lambda(^{\circ})$	M_w	ΔM_w
GCMT	191.1	—	11.0	—	-91.0	—	8.3	—
W-phase (USGS)	184.0	—	10.0	—	-98.0	—	8.3	—
SCARDEC	184.0	—	10.0	—	-100.0	—	8.4	—
This study	194.2	190.5–205.8	11.3	10.6–12.2	-87.6	-91.7–-75.7	8.3	8.3–8.3

148 Earthquake source models obtained from ultra low-frequency normal mode data

between the 1960 M_w 9.5 earthquake and the 1928 M_w 8.0 earthquake. In fact, the most recent 1939 M_w 7.9 event was an intraplate earthquake (Lorito *et al.*, 2011). The earthquake was characterised by a bilateral rupture, which initially propagated southwards for the first 30 s, and then propagated bilaterally. The total rupture length of both fault segments spanned 450–550 km along the fault strike with total source duration 120–140 s. The maximum slip observed to the northeast of the hypocentre and was approximately 20 m (Delouis *et al.*, 2010; Kiser and Ishii, 2011; Koper *et al.*, 2012). The mainshock was followed by a tsunami which was moderate in size with respect to its magnitude, as the largest slip did not occur in the uppermost part of the plate interface (Delouis *et al.*, 2010). Tsunami runup heights up to 10 m reported at Constitución and caused roughly 500 fatalities (Lorito *et al.*, 2011).

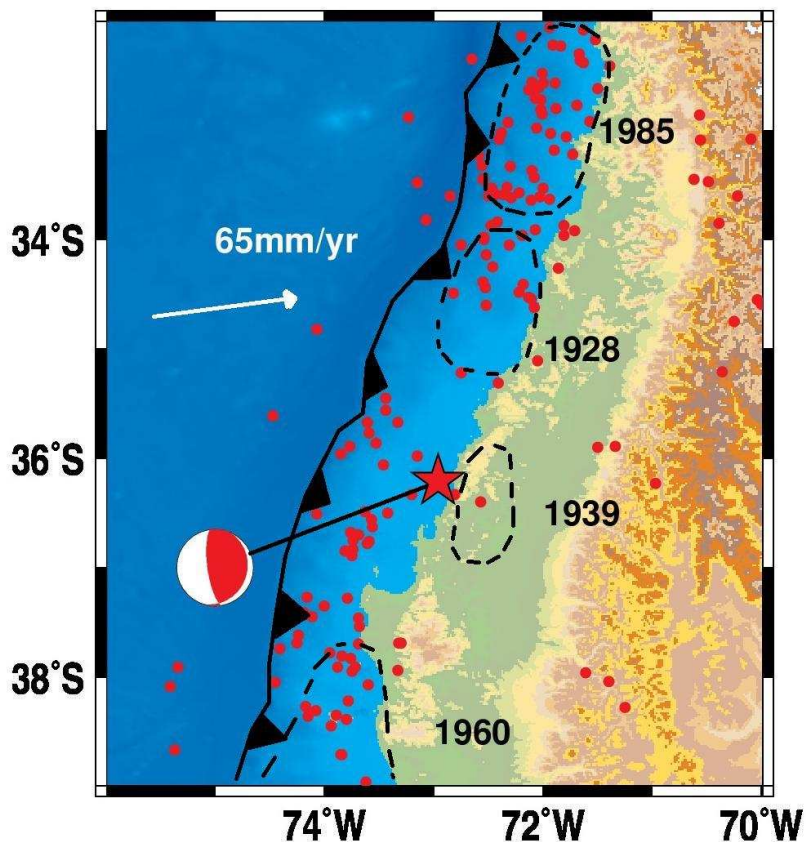


Figure 5.14: Map showing the tectonic setting of the 2010 Maule, Chile earthquake. Red star indicates the centroid location of the mainshock. Red beachball corresponds to its GCMT source model. Red circles show the seismicity ($M_w \geq 5.5$ in entire GCMT catalogue) of the study area. Black dotted lines indicate approximately the rupture areas of historic earthquakes.

Results obtained from a point source multiplets inversion using the GCMT origin

Table 5.9: Comparison of point $(\phi, \delta, \lambda, M_w)$ source model determined in this study with GCMT, W-phase, SCARDEC and other studies for the 2010 Chile earthquake. Uncertainties shown correspond to models with misfit values within a 1% tolerance with respect to the optimal misfit.

	$\phi(^{\circ})$	$\Delta\phi(^{\circ})$	$\delta(^{\circ})$	$\Delta\delta(^{\circ})$	$\lambda(^{\circ})$	$\Delta\lambda(^{\circ})$	M_w	ΔM_w
GCMT	19.0	–	18.0	–	116.0	–	8.8	–
W-phase	17.4	–	14.0	–	108.7	–	8.8	–
SCARDEC	24.0	–	15.0	–	115.0	–	8.8	–
Tong <i>et al.</i> (2010)	–	–	16.8	–	–	–	–	–
Vigny <i>et al.</i> (2011)	–	–	–	–	–	–	8.8	–
Politz <i>et al.</i> (2011a)	–	–	18.0	–	–	–	8.8	–
This study	13.6	8.6–20.0	14.8	12.0–21.9	110.5	109.0–119.4	8.8	8.7–8.9

time and location are presented in Table 5.9. Figure 5.15a shows the data fit for our optimal source model and Figures 5.15b–c show the earthquake source parameters and their associated uncertainties. The optimal model is obtained after 102 iterations and the generation of 3723 models (Figure 5.15d). Several spectral peaks show poorer fit due to their high noise level (Figure 5.15a). Table 5.9 shows that our estimates of moment magnitude, dip and rake angles are in good agreement with existing source models, while strike shows the largest variability especially when compared to SCARDEC, for which there is a difference of $\sim 10^{\circ}$. Figure 5.16 shows clear magnitude–dip and strike–rake tradeoffs affecting our inversions. For very shallow dipping earthquakes, such as the 2010 Maule earthquake, the strike and dip angles are not very stable parameters. In such cases, the strike and rake are poorly constrained and mutually correlated in a manner that their difference is constant (Han *et al.*, 2011, 2013). We have also attempted a finite source singlets inversion, however, the bilateral nature of the rupture propagation did not allow us to obtain robust results regarding the rupture duration and length, as when inverting for spatio-temporal kinematic parameters the optimal values persistently hit lower parameter space boundaries. This suggests low initial phases associated with opposite direction fault segments which tend to cancel each others rupture propagation (Lambotte *et al.*, 2007).

5.5 Discussion

In this Chapter we focused on six earthquakes in three different tectonic areas, the Sumatra-Andaman trench, the Japan and Kuril-Kamchatka trench and the Peru-Chile trench.

15 Earthquake source models obtained from ultra low-frequency normal mode data

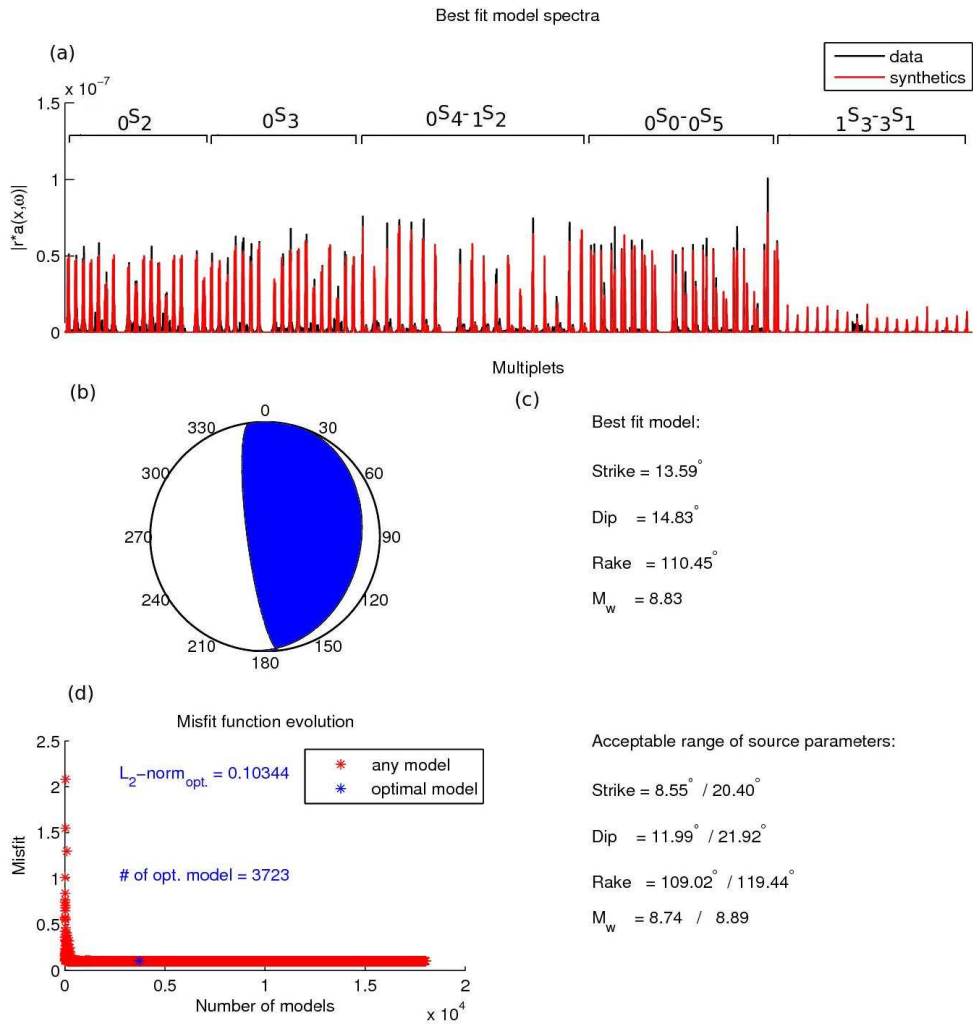


Figure 5.15: Results from a point source inversion for the 2010 Maule, Chile earthquake. The SAW12D 3-D mantle model is used to build the excitation kernels for the GCMT centroid location: (a) 240-hr optimal fit amplitude spectra of $0S_2$, $0S_3$, $0S_4$, $1S_2$, $0S_0$, $0S_5$, $1S_3-2S_2-3S_1$ multiplets; (b) optimal source mechanism; (c) optimal and acceptable range of source parameters (acceptable parameters correspond to source models yielding misfit values not exceeding the minimum misfit value by more than 1%); (d) misfit function evolution as a function of the number of models generated in the parameter search.

Our normal mode technique allows us to carry out source inversions by realistic normal mode spectra modelling, using either a point source approximation or a finite source representation. The application of the technique to large magnitude earthquakes highlights both the advantages and limitations of our approach for source model determinations. The use of the gravest normal modes ($f \leq 1$ mHz) brings independent insight into the rupture's bulk characteristics (e.g., Park *et al.*, 2005; Stein and Okal, 2005; Okal and Stein, 2009; Lambotte *et al.*, 2006, 2007). However, the need for very long and continuous high-quality recordings restricts our analysis to very large magnitude earthquakes ($M_w \geq$

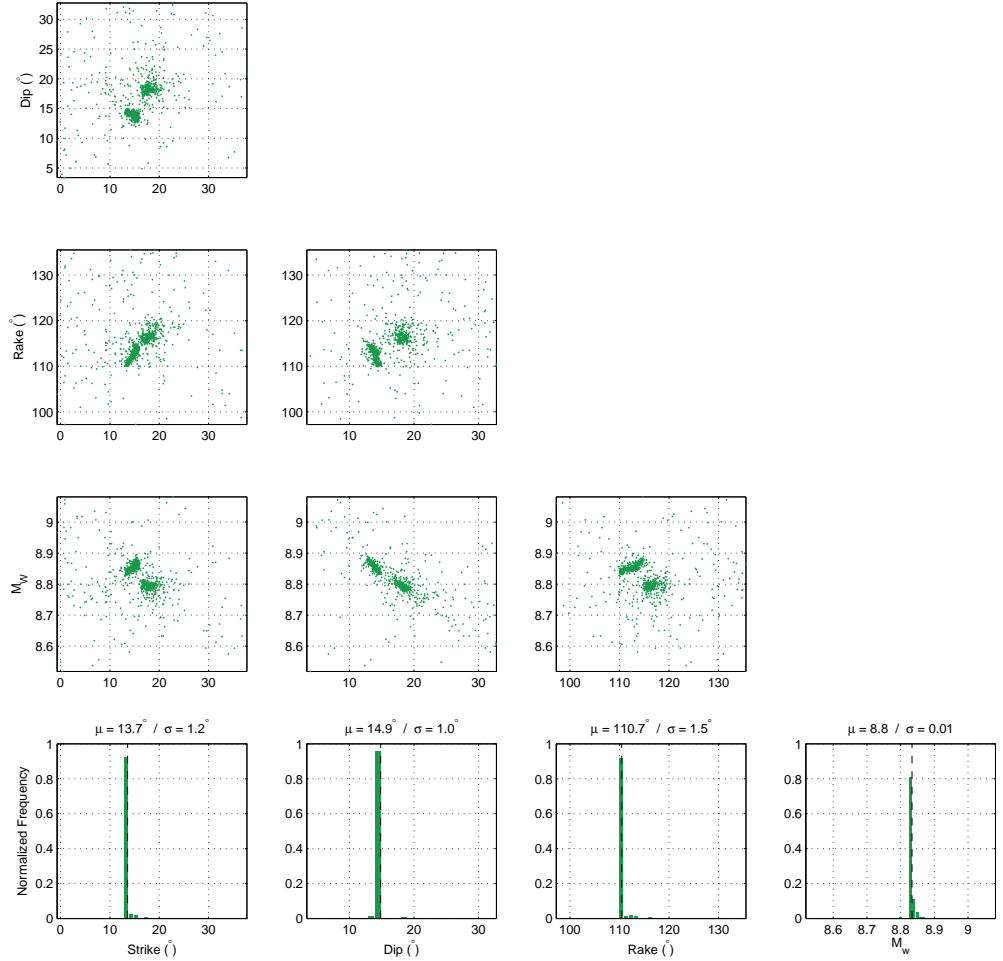


Figure 5.16: Tradeoff scatterplots from the ensemble of models produced by the Neighbourhood Algorithm for inversion results of Figure 5.15 for the 2010 Maule, Chile earthquake. The normalised histograms in the bottom row show the distribution of the inversion results (their mean μ and standard deviation σ values are also shown). Black dashed vertical lines correspond to the optimal source parameters obtained from the point source inversion.

8.3). Moreover, in its current form, our technique determines the bulk characteristics of unilateral ruptures only and assumes pure double-couple sources.

Figure 5.17 compares the source parameters obtained in this study with GCMT, W-phase, SCARDEC and other estimates reported in the literature using a variety of different data, such as body and surface waves (Walker *et al.*, 2005; Ammon *et al.*, 2005, 2011; Chu *et al.*, 2011; Honda *et al.*, 2011; Koper *et al.*, 2011; Lay *et al.*, 2011; Lee *et al.*, 2011; Wang and Mori, 2011; Yoshida *et al.*, 2011; Ishii *et al.*, 2005; Krüger and Ohrnberger, 2005; Ni *et al.*, 2005; Tsai *et al.*, 2005; Vallée, 2007), normal modes (Park *et al.*, 2005; Lambotte

15 Earthquake source models obtained from ultra low-frequency normal mode data

et al., 2006, 2007; Konca *et al.*, 2007), GPS/InSAR data (Vigny *et al.*, 2005; Chileh *et al.*, 2007; Politz *et al.*, 2011a,b; Tong *et al.*, 2010; Vigny *et al.*, 2011; Fujii *et al.*, 2011) and hydroacoustic/tsunami signals (Guilbert *et al.*, 2005; Konca *et al.*, 2008; Lorito *et al.*, 2008). Our source models for the 2004 Sumatra and 2011 Tohoku earthquakes shown in this figure correspond to both point (black asterisks) and finite (magenta asterisks) source inversion results. Source models for the remaining earthquakes correspond to point source inversion results (black asterisks).

For all the six earthquakes studied, overall the source parameters determined in this study agree well with the estimates from previous studies, which lie well within our source parameter error estimates (see Figure 5.17). Given that the majority of previous studies used very different and independent data types (notably body and surface waves as well as geodetic data), this good level of agreement is encouraging. Nevertheless, a number of complexities such as variations in fault geometry and slip across the fault may affect these comparisons, as they have different effects on different types of data. Moreover, differences in station distribution and Earth velocity structure used among our study and other seismic studies can also potentially explain the slight discrepancies observed.

We started with the well studied 2004 Sumatra-Andaman earthquake and we simultaneously determined its moment magnitude, fault geometry and bulk spatio-temporal kinematic characteristics using ultra low frequency normal mode singlets. We obtained a larger moment magnitude compared with GCMT and in excellent agreement with previous studies suggesting a slow slip component in the rupture (Stein and Okal, 2005; Park *et al.*, 2005). Moreover, our rupture duration and length estimates are consistent with body and surface wave studies, either using back-projection methods or defining the slip distribution (Ni *et al.*, 2005; Ammon *et al.*, 2005; Krüger and Ohrnberger, 2005; Tsai *et al.*, 2005; Vallée, 2007), and with Lambotte *et al.* (2006) and Lambotte *et al.* (2007) who also used ultra low frequency normal mode singlets, suggesting a rupture duration of 500–600 s and total rupture length of 1150–1250 km, yielding a mean rupture velocity of 2.1–2.7 km/s. These values are in very good agreement with our finite source inversion results (Table 5.3), which suggest an average rupture velocity of 2.45 km/s. Ishii *et al.* (2005) found a relatively higher average rupture velocity of 2.8 km/s and longer rupture length \sim 1300 km probably because they used high-frequency body-wave data.

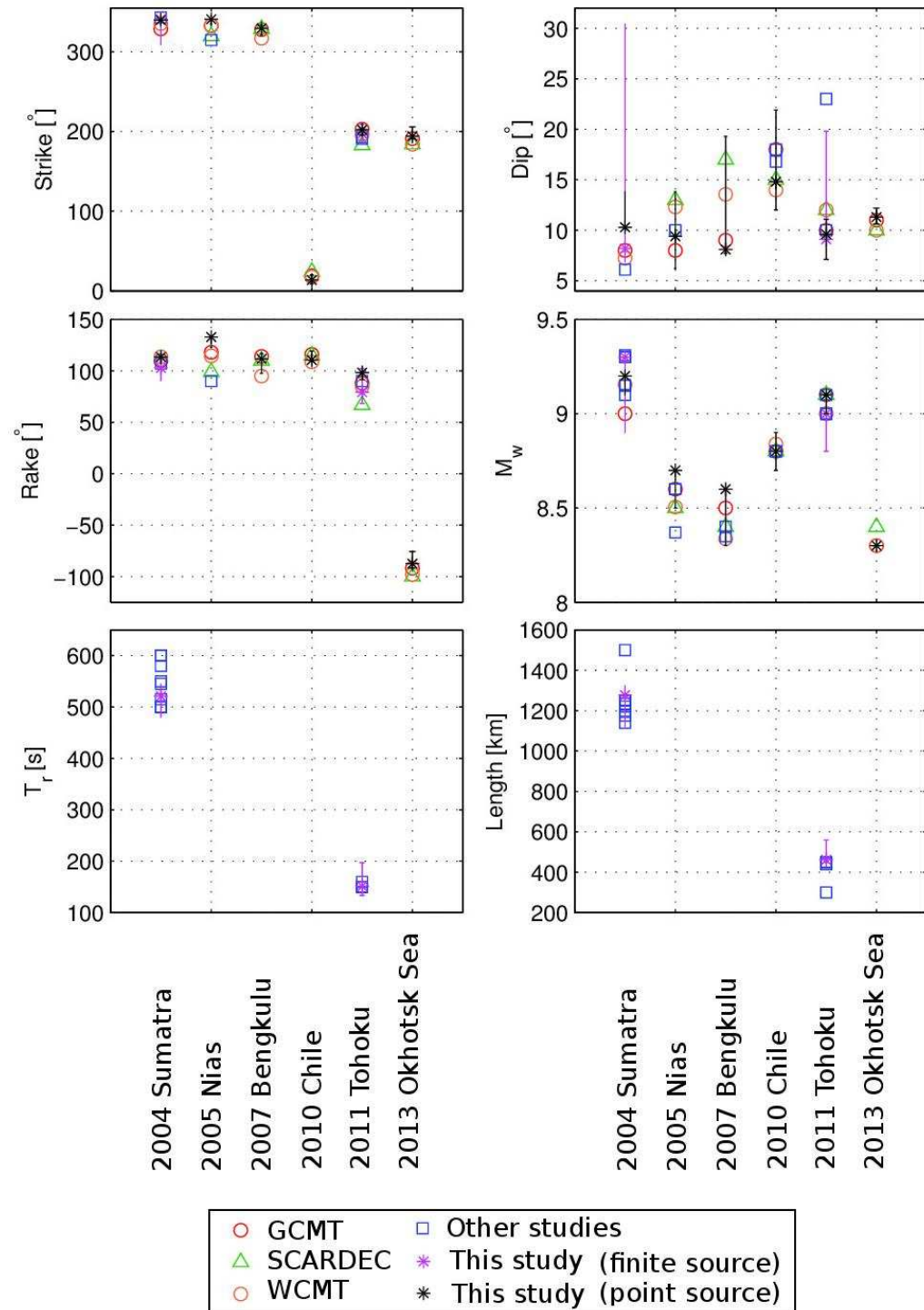


Figure 5.17: Comparisons of source parameters determined in this study (black asterisks – point source, magenta asterisks – finite source) with GCMT (red circles), SCARDEC (green triangles), W-phase (orange circles) and other source models published in the literature (blue squares). Error bars show source parameter uncertainties determined in this study.

154Earthquake source models obtained from ultra low-frequency normal mode data

Chileh *et al.* (2007) also found \sim 1500 km rupture length using GPS data. Overall, this earthquake was a good real earthquake validation exercise for our technique. Next, we moved on to the 2011 Tohoku earthquake by carrying out a finite source inversion. We present the first rupture duration (151 s) and length (461 km) estimates obtained from low frequency normal mode data (Table 5.7) which are in excellent agreement with previous studies (Honda *et al.*, 2011; Wang and Mori, 2011; Lay *et al.*, 2011; Yoshida *et al.*, 2011; Yagi and Fukahata, 2011b), suggesting \sim 150 s of source duration over \sim 450 km of total length, and an average rupture velocity of \sim 3 km/s in very good agreement with our average rupture velocity (3.05 km/s). Our findings also highlight the compact character of this unique seismic source which involved high static stress drop (up to 10 MPa) and a maximum slip of 50–60 m in a small region (Politz *et al.*, 2011b; Simons *et al.*, 2011). The rupture kinematics characterisation of the 2010 Chile and 2005 Nias earthquakes was limited by the bilateral rupture of these events. However, Lambotte *et al.* (2007) constrained the 2005 Nias overall rupture duration and length by forward modelling and they suggested a 40 s delay between the rupture initiation of the south fault segment with respect to the north. The determination of the spatio-temporal characteristics of smaller magnitude earthquakes in our data set was limited by the quality of the available data with respect to the very long time windows required from our technique.

The differences in fault strike between our estimates and those from other studies are generally smaller than 26° , with an average difference of 7.5° . On the other hand, most differences in fault rake do not exceed 43° , with the average of rake differences being 10.3° . A similar variability in these parameters was also observed in our synthetic tests (see Chapter 4) for the combined effects of noise in the data with unmodelled 3-D Earth structure. The observed larger differences for fault rake angle are likely due to the fact that the strike–rake tradeoff is a geometric tradeoff of shallow dipping faults (Han *et al.*, 2011, 2013), such as those associated with the earthquakes studied in this Chapter, where the rake angle is not sensitive in strike variations. A large variability is also shown from our heuristic error estimates for strike and rake angles. The largest variability in uncertainties observed in finite source inversion results ($\sim 10^\circ$ in strike and $\sim 30^\circ$ in rake), while point source inversion error estimates do not exceed $\sim 15^\circ$. This suggests that point source inversions (multiplets) constrain slightly better source parameters, compared

to finite source inversions (singlets), probably because of the wider frequency range of the data used. Moreover, source parameter error estimates can be also calculated in a statistical point of view ($\mu \pm 2\sigma$) directly from the ensemble of models (see for example Figures 5.7, 5.11, 5.13 and 5.16). These error estimates are always narrower around the optimal source parameters showing smaller variability, probably due to the large number of iterations allowed in the inversions. Nevertheless, these differences are comparable to errors in GCMT source parameters due to unmodelled 3-D Earth structure (Hjörleifsdóttir and Ekström, 2010). In addition, Ferreira *et al.* (2011) carried out surface wave CMT inversions of 32 shallow earthquakes with M_w 6.4–8.5, using different 3-D Earth models and theories. By comparing their results with InSAR source models, they found a median intraevent variability of 14° in strike and 30° in rake angle, which are larger than the uncertainties that we estimate in this study. They ascribe the large rake angle variability to the difficulty of long-period surface waves to constrain the dip-slip moment tensor components of shallow earthquakes.

Our estimates of fault dip angle and moment magnitude show smaller average discrepancies to results from other studies (2.5° in dip and 0.1 in M_w). Nevertheless, our dip angles are almost always systematically shallower than those from other studies (Figure 5.17), especially when compared to body wave techniques (e.g., SCARDEC), but in better agreement with GCMT estimates, which incorporate long-period mantle waves along with body waves for the earthquakes examined in this Chapter (Tables 5.3 – 5.9). On the other hand, as expected from the seismic moment – dip tradeoff (Kanamori and Given, 1981) affecting our shallow earthquake source inversions, our estimates of moment magnitude for the five thrust earthquakes considered are often slightly larger than in other studies; this is clearly observed in particular for the 2005 and 2007 Sumatra earthquakes (see Figure 5.17). Duputel *et al.* (2012a) report magnitude and dip angle uncertainties for the 2011 Tohoku earthquake. Their moment magnitude lies between 9.0–9.1 and the fault dip angle between $10\text{--}12^\circ$. These statistical error estimates compare well with our point source heuristic uncertainties obtained from the ensemble of the point source inversion ($7.1\text{--}11.1^\circ$) and our statistical error estimates ($9.6^\circ \pm 1.6^\circ$ in dip and 9.06 ± 0.04 in moment magnitude). Our finite source uncertainties show larger variability. Our heuristic dip angle uncertainties range $9.0\text{--}19.8^\circ$ and the moment magnitude ranges 8.8–9.0. Similarly,

15 Earthquake source models obtained from ultra low-frequency normal mode data

our statistical error estimations are $10.2^\circ \pm 4.2^\circ$ for the dip angle and 8.97 ± 0.10 for the magnitude (See Figure 5.11 and Table 5.7 for details). Hjörleifsdóttir and Ekström (2010) quantified errors in GCMT source determinations of shallow subduction zone earthquakes due to unmodelled 3-D Earth structure and noise in synthetic data. They found that the fault dip angle can be underestimated by about 5° and that the seismic moment is overestimated by about 20% even when body waves, are used in combination with surface wave and mantle wave data. Moreover, recent qualitative studies of source parameter uncertainties (Weston *et al.*, 2011) suggest a standard deviation of about 15° in dip between InSAR and long-period surface wave estimates. Furthermore, (Ferreira *et al.*, 2011) found an average intraevent variability of about 32° in fault dip estimates associated with the use of different Earth models and theories in long-period CMT surface wave inversions. From our tradeoff plots for the shallow thrust events considered (see Figures 5.7, 5.11, 5.16) we find an error of 0.03 in moment magnitude associated with every 2° in dip angle, which is in good agreement with the results of Tsai *et al.* (2011).

The need of additional seismic moment to fit low frequency normal modes compared to seismic moment inferred from higher frequency data could potentially indicate a slow rupture process if and only if the same fault geometry, especially the dip angle (seismic moment – dip tradeoff), is assumed. The above analysis presented in this Chapter did not indicate any frequency dependency of our results in comparison with source models obtained from shorter period data. The only exception is the 2004 Sumatra-Andaman earthquake, for which our work validated previous studies suggesting a slow slip component in the rupture process (e.g. Park *et al.*, 2005; Stein and Okal, 2005; Okal and Stein, 2009). The remaining earthquakes discussed in this Chapter show similar results with existing source models obtained by routine techniques using different frequency range seismic data (e.g. GCMT, SCARDEC, W-phase).

5.6 Conclusions

We have presented source models obtained from ultra low-frequency ($f \leq 1$ mHz) normal mode data for six global great earthquakes. Point source parameters ($\phi, \delta, \lambda, M_w$) and finite source parameters (T_r, L, V_r) have been successfully determined for the 2004 Sumatra-Andaman and 2011 Tohoku earthquakes. The good agreement between our

model for the 2004 Sumatra-Andaman event and those published in previous studies constitutes a good validation of our technique. On the other hand, our new model for the 2011 Tohoku event brings an alternative, independent confirmation of the compact nature of this event and of its average rupture speed, all important parameters for example for dynamic rupture studies (e.g. Aochi and Ide, 2011). Moreover, point source parameters have been obtained for the rest of the earthquakes studied, including the recent 2013 M_w 8.3 Okhotsk Sea earthquake. Overall, we find a good agreement between our new point source models and those from other studies using different types of data and techniques. This confirms that ultra low-frequency normal mode data alone can constrain the overall source process of large earthquakes well. In addition, we do not find any unexplained systematic differences between our results and those obtained using shorter period data, which suggests that the source processes of the earthquakes studied are not strongly frequency-dependent. Source parameter uncertainties have been also reported by using a misfit deterioration criterion with respect to the minimum misfit value, highlighting that the different parameters have different levels of uncertainties (e.g. $\sim 10^\circ$ in strike and $\sim 30^\circ$ in rake for finite source inversions). The grid searches carried out have also highlighted several tradeoffs between source parameters, notably: (i) Moment-dip angle tradeoffs associated with the shallow thrust earthquakes studied. Nevertheless, the small variability between our source parameters and others found in the literature shows that despite the tradeoff, our solutions are relatively well resolved. This is probably due to the fact that Earth's ellipticity, rotation and 3-D Earth structure are accurately taken into account in our modelling; (ii) Strike-rake tradeoffs leading to a relatively large variability in the rake angle; and, (iii) Strike-rupture length tradeoffs in the case of finite source inversions of unilateral rupture earthquakes, suggesting rupture over a longer fault as its orientation approaches N-S direction. Future incorporation of bilateral rupture modelling and allowing non-double-couple components in our source models could potentially enhance the technique's robustness towards more realistic source model representations. Overall, we have shown that the low-frequency Earth's normal modes excited by large magnitude earthquakes can be a robust, independent tool for the determination of earthquake source models and their bulk rupture characteristics.

Chapter 6

Discussion and conclusions

The key findings of the work presented in Chapters 3, 4 and 5, regarding earthquake source validation tests, source inversions using normal mode data, 3-D Earth structure effects and source parameter errors are discussed in this Chapter. Possible future work is also briefly discussed at the end of the Chapter.

6.1 Earthquake source validation

As discussed in various previous Chapters of this thesis, kinematic earthquake source models obtained routinely by different agencies and/or research groups for a given earthquake often show substantial discrepancies (e.g., Weston *et al.*, 2011, 2012). Different inversion techniques, data types, parameterisation and Earth structure models can yield significantly different results, and uncertainties are not routinely reported. Therefore, systematic assessments of the quality of existing source inversion techniques could help quantifying their robustness and estimating the errors associated with reported source models (e.g. Ferreira and Woodhouse, 2006; Hjörleifsdóttir and Ekström, 2010; Duputel *et al.*, 2012a).

Blind tests can significantly contribute to this effort. For example, a blind test exercise to investigate the robustness of different kinematic source inversion techniques was started by the EU FP7 SPICE (Seismic wave Propagation and Imaging in Complex media: a European network) project (<http://www.spice-rtn.org/>), in which several research groups derived kinematic variable slip rupture models from synthetic data calculated for an unknown input source model (Mai *et al.*, 2007, 2010). Noise was not

added to the synthetic data and the input fault geometry and seismic moment were provided. The kinematic models obtained by different research groups showed large discrepancies, with only a few studies achieving a good agreement between the input model and their solution. Since the end of SPICE project, the blind tests have continued as part of the source inversion validation project (<http://equake-rc.info/sivdb/wiki/index.cgi/Home>). This inspired many other efforts, such as the recently launched SCEC geodetic source inversion validation project (<http://www.geodynamics.org/cig/community/workinggroups/short/workshops/CDM2012/presentations/1ohman>), supported by the Southern California Earthquake Centre (SCEC), involving InSAR and GPS data.

Moreover, assessment of source models using sophisticated modelling techniques or realistic Earth structure to assess uncertainties (Ferreira and Woodhouse, 2006; Valentine and Trampert, 2012), and independent tests based on data not used in source model determinations (Ferreira *et al.*, 2011; Vallée *et al.*, 2011) can objectively quantify their robustness. The work presented in Chapter 3 carrying out new independent tests of source parameters determined using SCARDEC, a recent fast body-wave source inversion technique, addresses these issues. It goes beyond the previous work of Vallée *et al.* (2011) by using independent low-frequency normal mode data (up to 4.0 mHz) and for a larger number of earthquakes (34); thus, it provides a more general demonstration of the robustness of the SCARDEC technique. In addition, forward modelling of body waves using a purely numerical technique revealed that SCARDEC fault dip angles explain real body wave data as well or slightly better than GCMT dip angles, for the 3-D Earth structure considered (S20RTS and CRUST2.0, Ritsema *et al.*, 1999; Bassin *et al.*, 2000). SCARDEC dip angles also agree well with other studies (see Chapter 3 for details), seismic catalogues (e.g., WCMT, Duputel *et al.*, 2012b), and dip angle estimates obtained from the Slab1.0 subduction zone model (Hayes *et al.*, 2012). Hence, this work demonstrated the reliability of the SCARDEC method in a comprehensive and independent way, being well aligned and thus contributing to current efforts in source inversion validation tests (Mai *et al.*, 2007, 2010).

6.2 Spatio-temporal resolution of low frequency normal mode data

Body and surface wave data have been extensively used in earthquake kinematic rupture studies, as they can potentially resolve fine details of the seismic rupture process (e.g. Henry *et al.*, 2000; Yagi, 2004; Tsai *et al.*, 2005; Koper *et al.*, 2011). Body waves recorded at teleseismic distances can be used to determine fast preliminary source models using simple ray theory. In addition, recent back-projection techniques offer insights into rupture complexity (e.g. Ishii *et al.*, 2005; Kiser and Ishii, 2011; Wang and Mori, 2011). Surface wave inversion techniques are also appealing because of the relatively simple modelling involved, such as the great circle approximation and full ray theory (e.g. Ferreira and Woodhouse, 2006). In contrast, normal mode data have received less attention in source studies (Ben-Menahem *et al.*, 1972; Gilbert, 1973; Kedar *et al.*, 1994) as they require very long continuous time series and, due to their long wavelengths, they can only resolve overall bulk source characteristics. Furthermore, realistic modelling of the Earth's free oscillations taking into account mode coupling and splitting effects (e.g. Woodhouse and Dahlen, 1978) is more theoretically involved than classical ray theory approaches.

However, the giant 2004 M_w 9.3 Sumatra-Andaman earthquake brought new impetus to the study of the Earth's free oscillations. For example, several normal mode source studies showed that the seismic moment of this event was much larger than what was initially inferred by the GCMT using long-period mantle wave data (e.g., Park *et al.*, 2005; Stein and Okal, 2005). Moreover, Park *et al.* (2005) constrained simultaneously the rupture duration and the seismic moment of this earthquake by forward modelling of low-frequency normal mode data. Lambotte *et al.* (2006, 2007) showed that it is possible to derive bulk spatio-temporal rupture characteristics of unilateral rupture earthquakes (rupture duration and length) by modelling the initial phases of ultra low-frequency singlets excited by the 2004 Sumatra-Andaman earthquake.

Chapter 4 presented a novel normal mode technique for the simultaneous determination of fault geometry, moment magnitude and spatio-temporal rupture characteristics of unilateral earthquakes (rupture length and duration). While our rupture length and duration determinations have some similarities to previous studies, notably to the work of Lambotte *et al.* (2006, 2007), we do not fix the fault geometry or the seismic moment,

but we allow all parameters to vary in the inversions. Furthermore, the use of a 3-D Earth model for the forward modelling, allows us to better constrain the source models (Ferreira and Woodhouse, 2006), and hence, yield more realistic results. Synthetic tests showed that rupture duration determinations are relatively insensitive to data noise and to errors in the earthquake location and origin time, but that they are strongly affected by unmodelled 3-D Earth structure. On the other hand, rupture length determinations are strongly affected by all these factors, showing that accurate rupture length estimates based on our technique may only be achieved for very large magnitude earthquakes ($M_w \geq 8.8$) for which very high quality, low-noise data are available. Indeed, rupture duration and length estimates obtained in Chapter 5 for various real earthquakes are consistent with results from existing studies for the well studied 2004 Sumatra-Andaman earthquake (e.g., Ni *et al.*, 2005; Ammon *et al.*, 2005; Krüger and Ohrnberger, 2005; Tsai *et al.*, 2005; Lambotte *et al.*, 2006, 2007; Vallée, 2007), and for the 2011 Tohoku earthquake (e.g., Honda *et al.*, 2011; Wang and Mori, 2011; Lay *et al.*, 2011; Yoshida *et al.*, 2011; Yagi and Fukahata, 2011b), constraining their average rupture velocities to 2.5 km/s and 3.05 km/s, respectively.

Synthetic tests in Chapter 4 revealed an expected tradeoff between the seismic moment (and hence M_w) and the fault dip angle (Kanamori and Given, 1981), which appears clearly in our tradeoff plots (see Chapter 4 and Appendix B), highlighting the difficulty in estimating these source parameters for shallow earthquakes when using only normal mode data. Similar results were found in applications to real earthquakes (see Chapter 5). When systematically comparing our results for the five shallow thrust earthquakes considered in Chapter 5 with other source models, such as GCMT, SCARDEC and WCMT (see Tables 5.3 – 5.9), we find that our moment magnitudes are often slightly larger than in other studies, notably for the 2005 Nias and 2007 Bengkulu earthquakes (Figure 5.17).

Finally, synthetic tests on artificial thrust earthquakes presented in Chapter 4, showed the existence of a tradeoff between strike and rake. In contrast, our synthetic tests for a strike-slip artificial earthquake showed a dip – rake tradeoff. Tradeoff plots for the real earthquakes studied in Chapter 5 also showed the strike – rake tradeoff, except for the 2007 Bengkulu earthquake (Appendix D). The strike – rake tradeoff was also observed in the case of the deep, nearly horizontal fault, 2013 Okhotsk Sea earthquake (Figure 5.13) since it is rather a geometric tradeoff of shallow dipping faults, due to the fact that strike

and rake are poorly constrained and mutually correlated in a manner that their difference is constant (Han *et al.*, 2011, 2013).

Nevertheless, despite existing tradeoffs, our synthetic tests and tests with real earthquakes showed that source models obtained using ultra low-frequency normal mode data alone, yield source parameter uncertainties comparable or smaller to those reported in other studies (e.g., Ferreira and Woodhouse, 2006; Hjörleifsdóttir and Ekström, 2010). Hence, we showed clearly that despite being very low-frequency, this totally independent data can constrain various source parameters well. Existing tradeoffs are recognised and discussed, in comparison with other data types which also show tradeoffs, and unlike our study, are rarely thoroughly studied. Furthermore, uncertainties over all source parameters are reported in a systematic way.

6.3 Importance of 3-D structure

The assumed Earth structure is a key consideration in seismic source studies as it can strongly influence the retrieved source models (Ferreira and Woodhouse, 2006). Long-period body wave source studies based on teleseismic data (at epicentral distance of 30–90°) often use simplified 1-D Earth models (e.g. Hartzell and Liu, 1995; Yamanaka and Kikuchi, 2003; Vallée *et al.*, 2011), since the turning points of the seismic phases considered (e.g., P , PcP , S , ScS) are in the lower mantle, where the Earth's structure is relatively simple. In contrast, surface waves are sensitive to the uppermost part of the Earth (crust and upper mantle), which is highly laterally heterogeneous. Ferreira and Woodhouse (2007) found that local structure at the source can affect surface wave amplitude variations, while path effects are responsible for phase anomalies. Therefore, 3-D Earth models are preferred for source studies using surface waves (e.g. Ekström *et al.*, 2012). Normal modes are highly sensitive to 3-D Earth's structure, with different modes being sensitive to different parts of the Earth's interior. Notably, low angular order fundamental spheroidal modes (such as those used in this thesis) are sensitive to whole mantle structure, while higher angular order fundamental spheroidal modes are more sensitive to upper mantle structure. More specifically, the phase spectra of normal modes is particularly sensitive to 3-D Earth structure.

Since normal mode coupling in the frequency range 0–1 mHz is mainly controlled

by the Earth's rotation and ellipticity, not by Earth's structure (e.g. Masters *et al.*, 1983; Zürn *et al.*, 2000), one might expect no significant discrepancies between normal mode solutions obtained using 1-D and 3-D Earth models. However, synthetic tests presented in Chapter 4 showed that the use of the 1-D PREM model in inversions based on input synthetic data calculated for a 3-D Earth model leads to substantial underestimations of rupture duration and length. Moreover, neglecting the 3-D Earth structure leads to larger errors in fault geometry and M_w than other sources of uncertainties, such as noise in the synthetic data and spatio-temporal location errors. More importantly, the largest errors due to the use of 1-D structure are observed for rake angle, probably because for the shallow earthquakes tested in Chapter 4, the dip-slip components of the moment tensor, which are very sensitive to the fault dip and rake angles, are difficult to constrain using long-period data (e.g., Dziewonski *et al.*, 1981; Kanamori and Given, 1981). However, the source inversion errors found in this study due to unmodelled Earth's structure are similar or smaller than uncertainties from source inversions using other data types and methodologies reported in other previous studies (Ferreira and Woodhouse, 2006; Hjörleifsdóttir and Ekström, 2010; Ferreira *et al.*, 2011). The incorporation of 3-D mantle structure (model SAW12D) in our inversions carried out for the real earthquakes considered in Chapter 5 leads to source parameter estimates which are in good agreement with source models reported by routine source techniques, such as GCMT, WCMT, SCARDEC and other source models from individual studies (see details in Chapter 5). In addition, bulk rupture characteristics and average rupture velocities of the 2004 Sumatra-Andaman earthquake (2.5 km/s) and the 2011 Tohoku earthquake (3.05 km/s) are well constrained. Furthermore, this study gives the first purely normal mode source model of Tohoku earthquake, notably of rupture duration and length.

One potential limitation of this work may be the neglecting of 3-D anelasticity in the normal mode coupling (e.g., Millot-Langet *et al.*, 2003). However, this effect is strong for modes with almost overlapping degenerate eigenfrequencies (Woodhouse, 1980), such as the ${}_3S_1 - {}_1S_3$ supermultiplet used in point source inversions, and, more importantly, in $PKIKP$ – equivalent inner core modes (Tromp and Dahlen, 1990; Andrews *et al.*, 2006), which are not considered in this study. For the rest of the modes used in the inversions presented in Chapters 4 and 5, lateral variations in quality factors of the spherical model

PREM should not have a substantial effect.

6.4 Source parameter uncertainties

Quantitative knowledge of source parameter uncertainties is key for meaningful applications of earthquake source models, from their use in dynamic rupture simulations (e.g., Aochi and Ide, 2011), to Coulomb stress transfer (e.g., Toda *et al.*, 2011) and seismic hazard assessment studies. As discussed previously, possible sources of uncertainty in earthquake source parameter determinations include errors in the data, such as instrument miscalibrations and high noise levels, errors in the modelling due to unmodelled Earth structure and/or to the use of approximate forward modelling techniques.

Helffrich (1997) presented a statistical analysis of errors in CMT inversions, while Ferreira and Woodhouse (2006) quantified errors in CMT source parameter determinations due to the use of different forward modelling theories and models of Earth structure. Moreover, Hjörleifsdóttir and Ekström (2010) extensively tested the robustness of the GCMT method and quantified expected errors in source parameters due to Earth's structure uncertainties and data noise. Significant differences between source parameters obtained using InSAR and seismic data have been reported by Weston *et al.* (2011, 2012), and Ferreira *et al.* (2011) tested InSAR source models through comparisons with seismic solutions obtained using a variety of 3-D Earth models and two different forward modelling techniques. Earthquake source validation tests and systematic comparisons between SCARDEC source models, existing catalogues (e.g., GCMT, WCMT), source studies in the literature and geophysical constraints (Slab1.0, Hayes *et al.*, 2012) have been presented and discussed in Chapter 3. In addition, similar to Hjörleifsdóttir and Ekström (2010), the new normal mode source inversion technique presented in Chapter 4 has been tested against the effects of unmodelled Earth's structure, noise in synthetic data, spatio-temporal location errors and neglecting finite source effects.

Currently there are increased efforts to understand, quantify and systematically report uncertainties in source parameters. For example, Vallée *et al.* (2011); Valentine and Trampert (2012) developed heuristic, practical schemes for source model uncertainty quantifications based on numerical experiments. Moreover, some recent studies have addressed

uncertainties due to both data and modelling errors by calculating a more realistic covariance matrix and taking into account prior constraints (e.g., Yagi and Fukahata, 2011a; Duputel *et al.*, 2012a). In this thesis a heuristic approach is used to estimate earthquake source parameter uncertainties. Specifically, normal mode inversions carried out in Chapters 4 and 5 used a misfit threshold criterion to quantify uncertainties over the optimal source parameters, similar to the approaches used by Vallée *et al.* (2011); Valentine and Trampert (2012). Our uncertainty approach which is an inexpensive computationally procedure, although not a proper statistical calculation of errors, gives an estimation of the technique's resolution, and maps the sensitivity of normal mode data to changes in source parameters.

6.5 Conclusions

The giant 2004 M_w 9.3 Sumatra-Andaman earthquake re-sparked the interest of using the Earth's free oscillations in earthquake source studies. However, previous studies focused mostly on magnitude determinations (Park *et al.*, 2005; Stein and Okal, 2005) or kinematic spatio-temporal parameters (Lambotte *et al.*, 2006, 2007) using a fixed fault geometry. Furthermore, issues such as the influence of 3-D Earth structure, noise in data, parameter trade-offs and non-uniqueness in normal mode source inversions have not been previously fully investigated.

In this thesis we started by carrying out validation tests of a recent body-wave source inversion technique (the SCARDEC method) using: (i) independent normal mode data; and, (ii) accurate purely numerical modelling of body waves taking 3-D Earth structure into account. We showed that SCARDEC source parameters explain independent long-period, normal mode data reasonably well. Accurate forward modelling of body waves taking into account lateral variations in Earth's crust and mantle showed that the SCARDEC dip angles explain body wave data as well or slightly better than GCMT. Comparisons of SCARDEC dip angles with values from other individual earthquake studies and with subduction slab geophysical constraints showed also a good agreement. Comparing realistic source time functions obtained by SCARDEC with source duration estimates from other individual earthquake studies suggests that SCARDEC enables the rapid identification of classical tsunami earthquakes with anomalously large source durations

compared to their magnitudes, potentially complementary to existing routine ocean-wide tsunami warning techniques.

Next we developed a new Monte Carlo normal mode earthquake source inversion technique for the simultaneous determination of the rupture duration, length, M_w , fault strike, dip and rake of large magnitude earthquakes ($M_w > 8.0$) with unilateral rupture. Forward modelling of normal mode spectra is carried using Higher Order Perturbation Theory (HOPT) which enables the incorporation of Earth's rotation, ellipticity and 3-D structure in the calculations. The optimisation is carried out using the Neighbourhood Algorithm, which explores the model space and allows us to identify source parameter tradeoffs and quantify uncertainties in both an heuristic and a statistical manner. Synthetic experiments investigating the effects of finite rupture, noise in the data, uncertainties in Earth's structure and spatio-temporal location errors in the source inversions, emphasised the importance of taking into account realistic Earth's structure, notably for rupture duration and length determinations. In addition, important tradeoffs (moment magnitude – dip angle, strike – rake) have been observed, suggesting that rake angles may show substantial errors (up to 25°). Application of our new technique to real earthquake normal mode data for five shallow subduction earthquakes (2004 M_w 9.3 Sumatra-Andaman, 2005 M_w 8.6 Nias, 2007 M_w 8.5 Bengkulu, 2010 M_w 8.8 Chile, 2011 M_w 9.1 Tohoku) and the recent, nearly horizontal fault, deep, 2013 M_w 8.3 Okhotsk Sea earthquake showed an overall good agreement between source models obtained from this technique and those from existing catalogues (GCMT, WCMT, SCARDEC) and other individual studies. Furthermore, we obtained spatio-temporal constraints (rupture length and duration) consistent with those of Lambotte *et al.* (2006, 2007) for the 2004 Sumatra-Andaman earthquake and we presented the first bulk rupture characteristics for the 2011 Tohoku earthquake obtained from normal mode data, suggesting a rupture time of 151 s and a fault length of 461 km, highlighting the compact character of the earthquake's source compared to its magnitude.

Overall, we have shown that the low-frequency Earth's normal modes excited by large magnitude earthquakes can be a robust, independent tool for the validation of existing source models and the determination of earthquake source parameters and their bulk rupture characteristics, notably average rupture velocity. The latter is an important dynamic

source parameter that is not very easy to determine using other methods, as it's often strongly affected by constraints and assumptions in slip inversions (e.g., assumptions of constant rupture velocity), so it is important to obtain it in independent ways. Moreover, our results have shown that, for the earthquakes studied and for the frequency range considered, the source models are not frequency-dependent, a subject currently in debate (Koper *et al.*, 2012; Kiser and Ishii, 2011). Despite requiring very high quality long continuous time series and being associated with various source parameter tradeoffs, this thesis showed that low-frequency normal mode data are complementary to other data types used in routine source studies, especially for earthquakes with anomalously long source duration or slow slip, which may be undetected by existing techniques.

6.6 Future work

The work carried out in this thesis can potentially be further expanded in several ways, as follows:

- Bilateral rupture modelling of the initial phase could be investigated through synthetic tests prior to real earthquake applications. The current modelling algorithm could be expanded by including two fault segments with opposite rupture direction, allowing for a time delay between their rupture initiation. This yields a nine-dimensional parameter space with the three additional parameters being a second fault segment rupture duration and length, and the delay time between rupturing of the different direction fault segments. This can be done by calculating two initial phases, each one corresponding to different fault segments. However, Lambotte *et al.* (2007) who studied the bilateral rupture of the 2005 Nias earthquake, stated that the two opposite direction rupture segments will tend to cancel each other, and the use of long-period normal mode data does not provide enough resolution to allow their length identification, due to a tradeoff between the lengths of the two segments.
- In the current version of our normal mode technique a search over a parameter space for fault geometry and seismic moment is carried out, assuming a pure double-couple mechanism. An inversion of five independent moment tensor components

could be carried out instead still assuming a source type with no volume change ($M_{rr} + M_{\theta\theta} + M_{\phi\phi} = 0$), but allowing for a non-double-couple mechanism. This would require a different parameter space definition by searching over the moment tensor components, rather than searching over the actual source parameters. As a consequence, uncertainties would not refer directly to source parameters but to moment tensor components. Similarly, any tradeoffs observed amongst source parameters in the current study, may not appear between moment tensor components as the latter are defined by more than one parameter.

- It would be useful to test different 3-D Earth mantle and crustal models and, importantly, to address the issue of attenuation (Q) by using different 1-D Q models and by incorporating a 3-D anelasticity model into the modelling. From our synthetic tests we showed that initial phase estimates, and hence, rupture duration and length determinations are very sensitive to uncertainties in the Earth's structure. The use of higher resolution 3-D models, such as S20RTS (Ritsema *et al.*, 1999), would be a significant improvement to our technique. Moreover, the effect of the Earth's crust could also be studied by incorporating CRUST2.0 model (Bassin *et al.*, 2000) in the theoretical normal mode spectra calculations. Since very long time-series (up to 20 days) are used in our inversions, it is straightforward to consider the great importance of attenuation which affects the amplitudes of theoretical normal mode spectra calculations. Bearing in mind that our misfit function used by our inversion technique, depends strongly on the amplitude of the spectra, it is expected to affect directly the moment magnitude determinations, and given of the M_w – dip tradeoff, the dip angle determinations, too. In its current form, our technique uses normal mode quality factors based on 1-D PREM model. Although normal mode quality factor measurements are not an easy task, and different models often show large discrepancies, a 3-D anelasticity model, such as QR19 (Romanowicz, 1995), could potentially improve the robustness of our technique.
- The addition of other data types to the inversions such as long-period body and surface waveforms could potentially yield more robust results. Moreover, the incorporation of other data types could be combined with a search for centroid location

parameters and it could strengthen the robustness of non-double-couple mechanism determinations (Hjörleifsdóttir and Ekström, 2010). The determination of an earthquake's location is a non-linear problem, which is usually solved in a least-squares inversion. However, the use of the Neighbourhood Algorithm which performs a global search of the parameter space, could enable the determination of the earthquake's location and depth using pre-calculated kernels within some space boundaries. The use of long-period normal mode data alone, do not have enough resolution to robustly determine the depth of an earthquake (especially for shallow depth earthquakes), thus, the incorporation of surface and/or body wave data in our inversions would overcome this limitation.

- The source model uncertainty estimations using our normal mode inversion technique could be expanded by using the second stage of the Neighbourhood Algorithm (Sambridge, 1999b). The ensemble of models already determined can be analysed in a quantitative manner, by calculating Bayesian integrals and thus, the posterior probability density functions through Monte-Carlo integration. This would provide more quantitative measures of uncertainty, resolution and tradeoffs of the source parameters.

Appendix A

Supplementary material for Chapter 3

Table A.1: SCARDEC source parameters of the subduction earthquakes studied (strike - ϕ , dip - δ , rake - λ , moment magnitude - M_w , depth - Z) and their uncertainties for dip angle ($\Delta\delta$), depth (ΔZ) and moment magnitude (ΔM_w). The index numbers correspond to the earthquakes' GCMT codes (see chapter 3).

Index	ϕ	δ	$\Delta\delta$	λ	Z	ΔZ	M_w	ΔM_w
1	225.5	29.4	28.4 - 30.4	97.0	41.9	38.9 - 44.9	7.50	7.50 - 7.51
2	271.7	7.9	6.9 - 11.9	85.1	14.0	0.0 - 35.0	7.74	7.59 - 7.77
3	180.1	14.5	13.5 - 16.5	66.9	27.1	18.9 - 35.4	7.71	7.67 - 7.77
4	19.9	25.1	24.1 - 26.1	115.3	25.5	21.8 - 29.3	8.08	8.06 - 8.10
5	310.8	21.3	19.3 - 23.3	99.9	14.2	0.0 - 15.7	7.85	7.83 - 7.86
6	241.4	20.3	17.3 - 24.3	118.7	16.5	0.0 - 21.0	7.89	7.86 - 7.94
7	17.7	16.1	12.1 - 20.1	38.1	27.5	19.2 - 35.7	7.61	7.60 - 7.68
8	85.9	13.5	10.5 - 16.5	45.9	12.3	0.0 - 13.8	8.15	8.13 - 8.17
9	318.8	15.0	12.0 - 17.0	66.6	12.3	0.0 - 13.8	7.52	7.50 - 7.53
10	271.4	26.5	23.5 - 30.5	114.6	15.8	0.0 - 23.3	7.88	7.82 - 7.92
11	311.4	29.2	24.2 - 34.2	55.7	28.6	21.8 - 35.3	7.80	7.77 - 7.84
12	226.1	19.8	17.8 - 21.8	99.7	28.1	20.6 - 35.6	7.87	7.85 - 7.91
13	300.1	26.9	22.9 - 30.9	53.5	34.9	27.4 - 42.4	8.37	8.36 - 8.40
14	307.2	21.8	20.8 - 23.8	53.4	25.9	18.4 - 33.4	7.54	7.50 - 7.59
15	297.3	32.7	29.7 - 35.7	51.4	27.8	20.3 - 35.3	7.48	7.45 - 7.51
16	98.2	45.2	42.2 - 47.2	27.9	12.3	0.0 - 12.3	7.52	7.52 - 7.53
17	299.9	24.5	21.5 - 26.5	93.9	31.8	24.3 - 39.3	7.36	7.33 - 7.40
18	256.0	21.4	19.4 - 23.4	133.8	35.1	27.6 - 42.6	8.12	8.10 - 8.16
19	298.5	25.7	21.7 - 29.7	142.0	18.1	13.6 - 24.1	7.76	7.72 - 7.80
20	63.8	24.8	20.8 - 28.8	87.1	14.6	0.0 - 19.1	7.61	7.59 - 7.64
21	317.5	13.1	11.1 - 15.1	94.7	26.8	18.5 - 35.0	8.52	8.47 - 8.56
22	281.6	12.8	9.8 - 16.8	86.2	12.3	0.0 - 22.8	7.80	7.72 - 7.80
23	216.3	12.7	9.7 - 16.7	95.8	12.3	0.0 - 13.8	8.36	8.33 - 8.37
24	31.6	37.6	34.6 - 40.6	105.3	13.1	0.0 - 17.6	7.57	7.56 - 7.58
25	301.7	30.1	27.1 - 33.1	63.0	18.3	13.8 - 22.8	8.11	8.08 - 8.15
26	315.3	20.3	18.3 - 24.3	54.4	24.6	17.8 - 31.4	8.17	8.14 - 8.20
27	333.5	15.8	12.8 - 19.8	114.7	17.5	0.0 - 25.0	8.43	8.38 - 8.48
28	13.7	28.1	27.1 - 29.1	111.2	49.1	44.6 - 53.6	7.73	7.72 - 7.75
29	103.3	27.7	25.7 - 30.7	63.0	14.0	0.0 - 17.0	7.62	7.60 - 7.64
30	35.0	31.8	26.8 - 35.8	144.4	25.5	18.8 - 32.3	7.72	7.70 - 7.76
31	26.4	18.2	15.2 - 22.2	119.4	27.0	20.3 - 33.8	8.79	8.77 - 8.82
32	303.8	13.3	11.3 - 15.3	81.7	23.3	15.8 - 30.8	7.73	7.68 - 7.79
33	320.4	8.5	7.5 - 9.5	95.9	12.3	0.0 - 12.3	7.84	7.84 - 7.84
34	187.0	10.9	8.9 - 13.9	70.8	12.4	0.0 - 16.9	9.11	9.06 - 9.11

Table A.2: Numerical results of the misfit analysis for the GCMT and SCARDEC techniques. Amplitude msfits $m_{Amp.}^2$, real and imaginary FFT part misfits $m_{Re/Im}^2$ and the number of stations used at each component are shown.

Earthquake/Component	$m_{Amp.}^2$ <i>CMT</i>	$m_{Amp.}^2$ <i>SCARDEC</i>	$m_{Re/Im}^2$ <i>CMT</i>	$m_{Re/Im}^2$ <i>SCARDEC</i>	Number of stations
1997 Kamchatka (LHZ)	0.3118	0.3092	0.7095	0.7645	20
1997 Kamchatka (LHT)	0.5507	0.5567	1.0607	0.8431	10
2009 New Zealand (LHZ)	0.3416	0.3662	0.7236	0.7599	18
2009 New Zealand (LHT)	–	–	–	–	8
2010 N. Sumatra (LHZ)	0.3312	0.3689	0.7465	0.7109	17
2010 N. Sumatra (LHT)	–	–	–	–	9
1996 Minahassa (LHZ)	0.3154	0.3429	0.7544	0.6700	20
1996 Minahassa (LHT)	–	–	–	–	4
1996 Andreanof (LHZ)	0.3088	0.3359	0.7086	0.7860	13
1996 Andreanof (LHT)	0.6056	0.6500	1.0236	1.0220	10
1995 Kuril (LHZ)	0.2777	0.3601	0.7197	0.8291	17
1995 Kuril (LHT)	–	–	–	–	8
1995 Jalisco (LHZ)	0.2893	0.3217	0.9217	1.1523	20
1995 Jalisco (LHT)	0.5637	0.5462	0.9311	0.9819	10
2007 Peru (LHZ)	0.2612	0.2621	0.6613	0.7602	20
2007 Peru (LHT)	0.4822	0.4251	0.8285	0.8555	10
1995 Chile (LHZ)	0.2616	0.2176	0.6047	0.6420	17
1995 Chile (LHT)	0.3886	0.3637	0.7454	0.7847	10
2007 Solomon (LHZ)	0.2855	0.3156	0.8634	0.8593	17
2007 Solomon (LHT)	0.3375	0.3390	0.8296	0.8357	10
2003 Hokkaido (LHZ)	0.3051	0.3298	0.9318	0.9692	20
2003 Hokkaido (LHT)	0.5334	0.5582	0.9918	0.9604	10
2001a Peru (LHZ)	0.2405	0.2709	0.7619	0.8438	18
2001a Peru (LHT)	0.4366	0.4075	0.8312	0.8265	10
2007 Sumatra (LHZ)	0.3842	0.3812	0.8956	0.8928	20
2007 Sumatra (LHT)	0.5168	0.5283	1.0282	0.9645	10
2005 Sumatra (LHZ)	0.2427	0.2623	0.6697	0.7408	20
2005 Sumatra (LHT)	0.4274	0.4547	0.8750	0.9211	13

Table A.3: GCMT and SCARDEC source models compared with WCMT and other source models found in the literature for the 22 earthquakes with substantial dip angle differences studied in Chapter 3.

1994 Honshu						
Study	$\phi(^{\circ})$	$\delta(^{\circ})$	$\lambda(^{\circ})$	M_w	Depth (km)	Data
GCMT	179.0	12.0	67.0	7.7	27.7	Mantle waves
SCARDEC	180.1	14.5	66.9	7.7	27.1	Body waves
WCMT	178.2	16.9	64.1	7.7	—	W-phase
Tanioka <i>et al.</i> (1996)	180.0	9.0	75.0	—	22.0	Body waves
Sato <i>et al.</i> (1996)	155.0	13.0	45.0	—	—	Body waves
1995 Chile						
Study	$\phi(^{\circ})$	$\delta(^{\circ})$	$\lambda(^{\circ})$	M_w	Depth (km)	Data
GCMT	354.0	22.0	87.0	8.0	28.7	Mantle waves
SCARDEC	19.9	25.1	115.3	8.1	25.5	Body waves
WCMT	14.7	17.2	117.1	8.1	—	W-phase
Ruegg <i>et al.</i> (1996)	8.0	18.0	110.0	7.2	31.0	Body waves
Ruegg <i>et al.</i> (1996)	—	20.0–24.0	113.0	8.2	—	GPS data
Delouis <i>et al.</i> (1997)	3.0	17.0	97.0	—	35.0	Body waves
Carlo <i>et al.</i> (1999)	—	22.0	116.0	8.1	21.0–31.0	Surface waves
Ihmlé and Ruegg (1997)	—	—	—	8.0	—	Surface waves & Geodetic data
Klotz <i>et al.</i> (1999)	—	—	114.0	8.1	35.0	GPS data
1995 Jalisco						
Study	$\phi(^{\circ})$	$\delta(^{\circ})$	$\lambda(^{\circ})$	M_w	Depth (km)	Data
GCMT	302.0	9.0	92.0	8.0	15.0	Mantle waves
SCARDEC	310.8	21.3	99.9	7.9	14.2	Body waves
WCMT	291.4	15.8	68.4	7.9	—	W-phase
Escobedo <i>et al.</i> (1998)	306.0	26.0	94.0	7.5	24.0	Body waves
Mendoza and Hartzell (1999)	—	—	—	7.9	—	Body waves
Ortiz <i>et al.</i> (1998)	—	—	—	7.9	—	Tsunami data
Zobin (1997)	—	—	—	7.8	12.0–15.0	Body waves
Melbourne <i>et al.</i> (1997)	—	—	—	—	15.0	GPS

– *continued*

1995 Kuril						Data
Study	$\phi(^{\circ})$	$\delta(^{\circ})$	$\lambda(^{\circ})$	M_w	Depth (km)	
GCMT	225.0	12.0	95.0	7.9	25.9	Mantle waves
SCARDEC	241.4	20.3	118.7	7.9	16.5	Body waves
WCMT	230.1	18.9	103.2	7.8	–	W-phase
Hasegawa <i>et al.</i> (1994)	–	30.0	–	–	–	Earthquakes' relocation
1996 Minahassa						Data
Study	$\phi(^{\circ})$	$\delta(^{\circ})$	$\lambda(^{\circ})$	M_w	Depth (km)	
GCMT	36.0	6.0	54.0	7.9	15.0	Body & Mantle waves
SCARDEC	17.7	16.1	38.1	7.6	27.5	Body waves
WCMT	46.4	8.9	72.9	7.7	–	W-phase
Gómez <i>et al.</i> (2000)	53.0	7.0	68.0	7.6	16.0	Body waves
ERI	35.0	14.0	58.0	7.4	49.0	Surface waves
1996 Andreanof						Data
Study	$\phi(^{\circ})$	$\delta(^{\circ})$	$\lambda(^{\circ})$	M_w	Depth (km)	
GCMT	248.0	17.0	84.0	7.9	29.0	Mantle waves
SCARDEC	271.4	26.5	114.6	7.9	15.8	Body waves
WCMT	258.0	21.2	103.2	7.9	–	W-phase
Kisslinger and Kikuchi (1997)	–	–	–	7.7	35.0–55.0	Body waves
1997 Kamchatka						Data
Study	$\phi(^{\circ})$	$\delta(^{\circ})$	$\lambda(^{\circ})$	M_w	Depth (km)	
GCMT	202.0	23.0	74.0	7.8	33.6	Body & Mantle waves
SCARDEC	226.1	19.8	99.7	7.9	28.1	Body waves
WCMT	201.1	19.0	74.4	7.9	–	W-phase
Zobin and Levina (2001)	–	–	–	7.8	–	Body waves
2001a Peru						Data
Study	$\phi(^{\circ})$	$\delta(^{\circ})$	$\lambda(^{\circ})$	M_w	Depth (km)	
GCMT	310.0	18.0	63.0	8.4	29.6	Mantle waves
SCARDEC	300.1	26.9	53.5	8.4	34.9	Body waves
WCMT	317.3	16.0	72.0	8.4	–	W-phase
Bilek and Ruff (2002)	310.0	23.0	75.0	8.5	33.0	Body waves
Giovanni <i>et al.</i> (2002)	–	–	–	8.2	25.0	Body waves
Tavera <i>et al.</i> (2006)	–	28.0	–	8.1	29.0	Body waves
Robinson <i>et al.</i> (2006)	311.0	12.0	68.0	8.4	–	Surface waves
Robinson <i>et al.</i> (2006)	301.0	14.0	44.0	8.5	–	Mantle waves
Jordan <i>et al.</i> (1983)	–	30.0	–	–	–	Seismological & Geological data

– *continued*

2001b Peru						
Study	$\phi(^{\circ})$	$\delta(^{\circ})$	$\lambda(^{\circ})$	M_w	Depth (km)	Data
GCMT	306.0	14.0	52.0	7.6	25.0	Body & Mantle waves
SCARDEC	307.2	21.8	53.4	7.5	25.9	Body waves
WCMT	323.3	13.8	74.2	7.6	–	W-phase
2002 Mindanao						
Study	$\phi(^{\circ})$	$\delta(^{\circ})$	$\lambda(^{\circ})$	M_w	Depth (km)	Data
GCMT	314.0	25.0	70.0	7.5	28.7	Body & Mantle waves
SCARDEC	297.3	32.7	51.4	7.5	27.8	Body waves
WCMT	309.0	30.0	58.1	7.5	–	W-phase
2002 New Guinea						
Study	$\phi(^{\circ})$	$\delta(^{\circ})$	$\lambda(^{\circ})$	M_w	Depth (km)	Data
GCMT	106.0	34.0	43.0	7.6	19.5	Body & Mantle waves
SCARDEC	98.2	45.2	27.9	7.5	12.3	Body waves
WCMT	126.0	24.9	78.8	7.5	–	W-phase
2003 Jalisco						
Study	$\phi(^{\circ})$	$\delta(^{\circ})$	$\lambda(^{\circ})$	M_w	Depth (km)	Data
GCMT	308.0	12.0	110.0	7.5	26.0	Body & Mantle waves
SCARDEC	299.9	24.5	93.9	7.4	31.8	Body waves
WCMT	294.2	20.8	80.2	7.4	–	W-phase
Yagi <i>et al.</i> (2004)	300.0	20.0	93.0	7.5	–	Body waves
2003 Hokkaido						
Study	$\phi(^{\circ})$	$\delta(^{\circ})$	$\lambda(^{\circ})$	M_w	Depth (km)	Data
GCMT	250.0	11.0	132.0	8.3	28.2	Mantle waves
SCARDEC	256.0	21.4	133.8	8.1	35.1	Body waves
WCMT	245.4	15.6	125.3	8.2	–	W-phase
Ito <i>et al.</i> (2004)	246.0	16.0	124.0	7.9	29.0	Body waves
Yagi (2004)	250.0	20.0	130.0	17.0	8.1	Body waves
Honda <i>et al.</i> (2004)	246.0	18.0	127.0	8.2	29.0	Strong motion data
Miyazaki <i>et al.</i> (2004)	–	–	–	8.1	–	GPS
Koketsu <i>et al.</i> (2003)	–	–	–	8.2	–	Strong motion & Geodetic data
Yamanaka and Kikuchi (2003)	230.0	20.0	109.0	8.0	25.0	Body waves
Miura <i>et al.</i> (2004)	–	–	–	8.2	–	GPS
Katsumata <i>et al.</i> (2003)	–	20.0–30.0	–	–	–	Earthquakes' relocation
Hasegawa <i>et al.</i> (1994)	–	30.0	–	–	–	Earthquakes' relocation

– *continued*

2003 Rat Islands						
Study	$\phi(^{\circ})$	$\delta(^{\circ})$	$\lambda(^{\circ})$	M_w	Depth (km)	Data
GCMT	280.0	19.0	122.0	7.8	21.7	Body & Mantle waves
SCARDEC	298.5	25.7	142.0	7.8	18.1	Body waves
WCMT	285.9	21.1	125.5	7.7	–	W-phase
Yagi (2003)	270.0	6.0	116.0	7.8	12.0	Body waves
2005 Sumatra						
Study	$\phi(^{\circ})$	$\delta(^{\circ})$	$\lambda(^{\circ})$	M_w	Depth (km)	Data
GCMT	333.0	8.0	118.0	8.6	25.8	Mantle waves
SCARDEC	317.5	13.1	94.7	8.5	26.8	Body waves
WCMT	333.2	12.3	114.5	8.5	–	W-phase
Bukchin and Mostinskii (2007)	315.0	10.0	90.0	8.6	8.0-10.0	Surface waves
Konca <i>et al.</i> (2007)	–	10.0	–	8.6	–	Normal modes/GPS
Hsu <i>et al.</i> (2006)	–	8.0-12.0	–	–	22.0	GPS
Kreemer <i>et al.</i> (2006)	–	–	–	8.4	–	GPS
2007 Solomon						
Study	$\phi(^{\circ})$	$\delta(^{\circ})$	$\lambda(^{\circ})$	M_w	Depth (km)	Data
GCMT	333.0	37.0	121.0	8.1	14.1	Body, Surface & Mantle waves
SCARDEC	301.7	30.1	63.0	8.1	18.3	Body waves
WCMT	322.4	30.0	101.3	8.1	–	W-phase
Yagi (2007)	300.0	19.0	–	–	–	Body waves
Ji (2007)	305.0	25.0	–	–	–	Body waves
Tanioka <i>et al.</i> (2007)	315.0	35.0	–	–	–	Deformation data
Chen <i>et al.</i> (2009)	–	29.0	–	–	–	Geodetic data
2007 Peru						
Study	$\phi(^{\circ})$	$\delta(^{\circ})$	$\lambda(^{\circ})$	M_w	Depth (km)	Data
GCMT	321.0	28.0	63.0	8.0	33.8	Body, Surface & Mantle waves
SCARDEC	315.3	20.3	54.4	8.2	24.6	Body waves
WCMT	324.7	14.0	63.8	8.2	–	W-phase
Hébert <i>et al.</i> (2009)	343.0	39.0	97.0	8.0	40.0	Mantle waves (PDFM)
Hébert <i>et al.</i> (2009)	–	–	–	8.0	–	Body waves
Hébert <i>et al.</i> (2009)	–	–	–	8.0	–	Tsunami data
Biggs <i>et al.</i> (2009)	324.0	22.0	68.0	8.0	–	Surface waves
Biggs <i>et al.</i> (2009)	324.0	12.0	70.0	8.0	–	Body waves
Biggs <i>et al.</i> (2009)	–	–	–	8.2	–	InSAR
Motagh <i>et al.</i> (2008)	–	–	–	8.1	–	InSAR
Jordan <i>et al.</i> (1983)	–	30.0	–	–	–	Seismological & Geological data

– *continued*

2007 Sumatra						
Study	$\phi(^{\circ})$	$\delta(^{\circ})$	$\lambda(^{\circ})$	M_w	Depth (km)	Data
GCMT	328.0	9.0	114.0	8.5	24.4	Body, Surface & Mantle waves
SCARDEC	333.5	15.8	114.7	8.4	17.5	Body waves
WCMT	317.1	13.6	95.0	8.3	–	W-phase
Lorito <i>et al.</i> (2008)	–	–	–	8.4	20.0–30.0	Tsunami data
Konca <i>et al.</i> (2008)	–	–	–	8.4	25.0	GPS, InSAR & Body waves
2007 Chile						
Study	$\phi(^{\circ})$	$\delta(^{\circ})$	$\lambda(^{\circ})$	M_w	Depth (km)	Data
GCMT	358.0	20.0	98.0	7.7	37.6	Body, Surface & Mantle waves
SCARDEC	13.7	28.1	111.2	7.7	49.1	Body waves
WCMT	7.2	17.6	112.0	7.8	–	W-phase
Delouis <i>et al.</i> (2009)	0.0	20.0	105.0	–	–	Body waves
Peyrat <i>et al.</i> (2010)	358.0	26.0	109.0	–	–	Body waves
Béjar-Pizarro <i>et al.</i> (2010)	–	22.0	105.0	–	–	GPS
Béjar-Pizarro <i>et al.</i> (2010)	–	20.0	93.0	–	–	InSAR
2009 Irian Jaya						
Study	$\phi(^{\circ})$	$\delta(^{\circ})$	$\lambda(^{\circ})$	M_w	Depth (km)	Data
GCMT	99.0	23.0	47.0	7.7	15.2	Body, Surface & Mantle waves
SCARDEC	103.3	27.7	63.0	7.6	14.0	Body waves
WCMT	102.1	26.3	62.1	7.6	–	W-phase
2009 New Zealand						
Study	$\phi(^{\circ})$	$\delta(^{\circ})$	$\lambda(^{\circ})$	M_w	Depth (km)	Data
GCMT	25.0	26.0	138.0	7.8	23.5	Body, Surface & Mantle waves
SCARDEC	35.0	31.8	144.4	7.7	25.5	Body waves
WCMT	29.0	25.7	135.1	7.8	–	W-phase
2010 N. Sumatra						
Study	$\phi(^{\circ})$	$\delta(^{\circ})$	$\lambda(^{\circ})$	M_w	Depth (km)	Data
GCMT	307.0	7.0	88.0	7.8	17.6	Mantle waves
SCARDEC	303.8	13.3	81.7	7.7	23.3	Body waves
WCMT	314.8	9.3	97.6	7.7	–	W-phase

Appendix B

Supplementary material for Chapter 4 - Point source inversion synthetic tests

Table B.1: Input source parameters (inp.) and parameter space boundaries (min. and max.) over strike (ϕ), dip (δ), rake (λ), moment magnitude (M_w), rupture duration (T_r) and length (L) for the four different earthquakes tested (thrust, strike-slip, normal) in finite source synthetic tests. The parameter space ranges 40° in strike and rake, 30° in dip, 0.6 in moment magnitude, 100 s in rupture duration and 240 km in length. The same parameter space is used in our point source inversion tests for strike, dip, rake and M_w determinations. Input model beachballs are shown on top.

												
	min.	inp.	max.	min.	inp.	max.	min.	inp.	max.	min.	inp.	max.
$\phi(^{\circ})$	313.0	343.0	353.0	251.0	281.0	291.0	33.0	43.0	73.0	352.0	15.0	32.0
$\delta(^{\circ})$	1.0	6.1	31.0	59.0	84.0	89.0	34.0	59.0	64.0	1.0	18.0	31.0
$\lambda(^{\circ})$	97.0	107.0	137.0	7.0	17.0	47.0	-140.0	-115.0	-100.0	95.0	110.0	135.0
M_w	9.1	9.3	9.7	7.6	8.1	8.2	7.9	8.1	8.5	8.6	8.8	9.2
$T_r(s)$	455.0	545.0	555.0	0.0	90.0	100.0	0.0	60.0	100.0	150.0	230.0	250.0
$L(km)$	1104.0	1140.0	1344.0	2.0	240.0	242.0	36.0	220.0	276.0	400.0	600.0	640.0

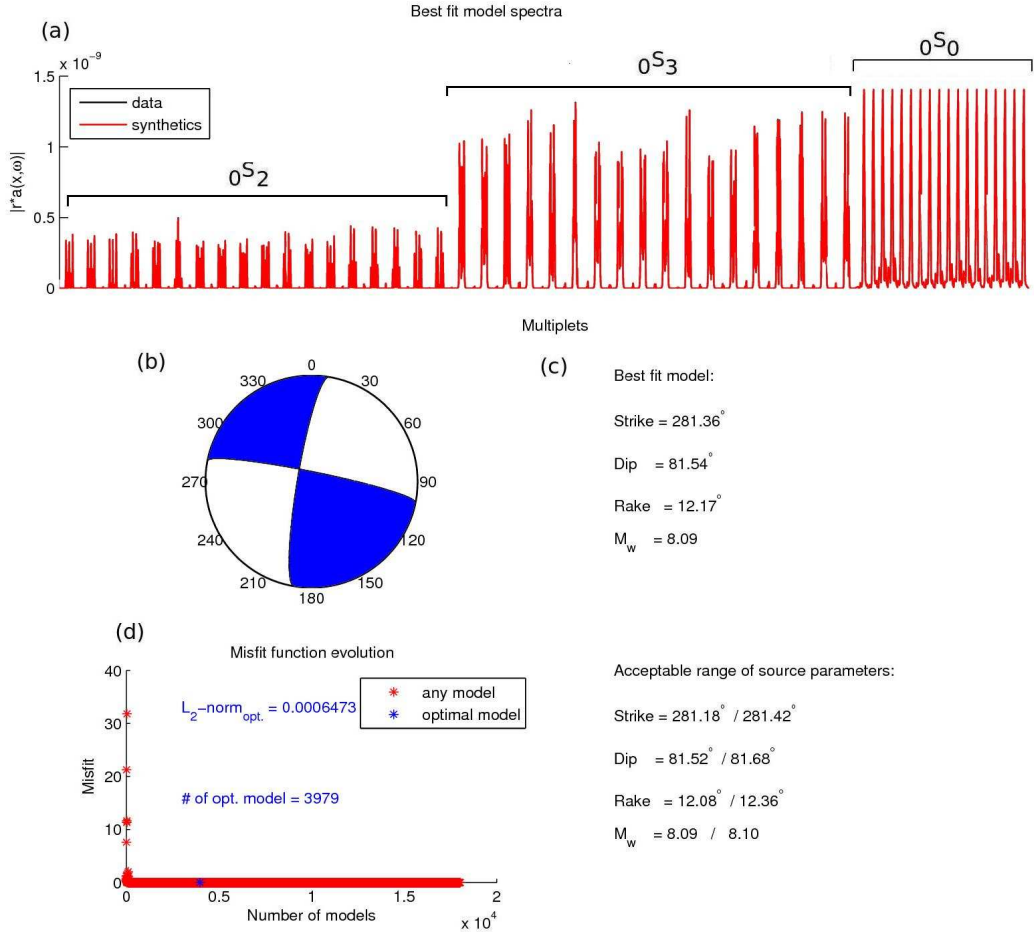


Figure B.1: Results from a point source inversion for the artificial 1998 Antarctic plate strike slip earthquake, using a combination of the amplitude and FFT misfits (97% amplitude and 3% FFT) using the GCMT location and fault geometry, assuming a total rupture duration of 90 s and rupture length of 240 km, based on the rupture model of Nettles *et al.* (1999), as the input model ($\phi = 281^\circ$, $\delta = 84^\circ$, $\lambda = 17^\circ$, $M_w = 8.1$, $T_r = 90$ s, $L = 240$ km). SAW12D 3-D model is used to build the synthetic data and the excitation kernels: (a) 480-hr optimal fit acceleration amplitude spectra of $0S_2$, $0S_3$ and $0S_0$ multiplets, (b) optimal source mechanism, (c) optimal and acceptable range of source parameters (acceptable parameters correspond to source models yielding misfit values not 1% larger than the lowest misfit associated with the optimal source model), (d) misfit function evolution.

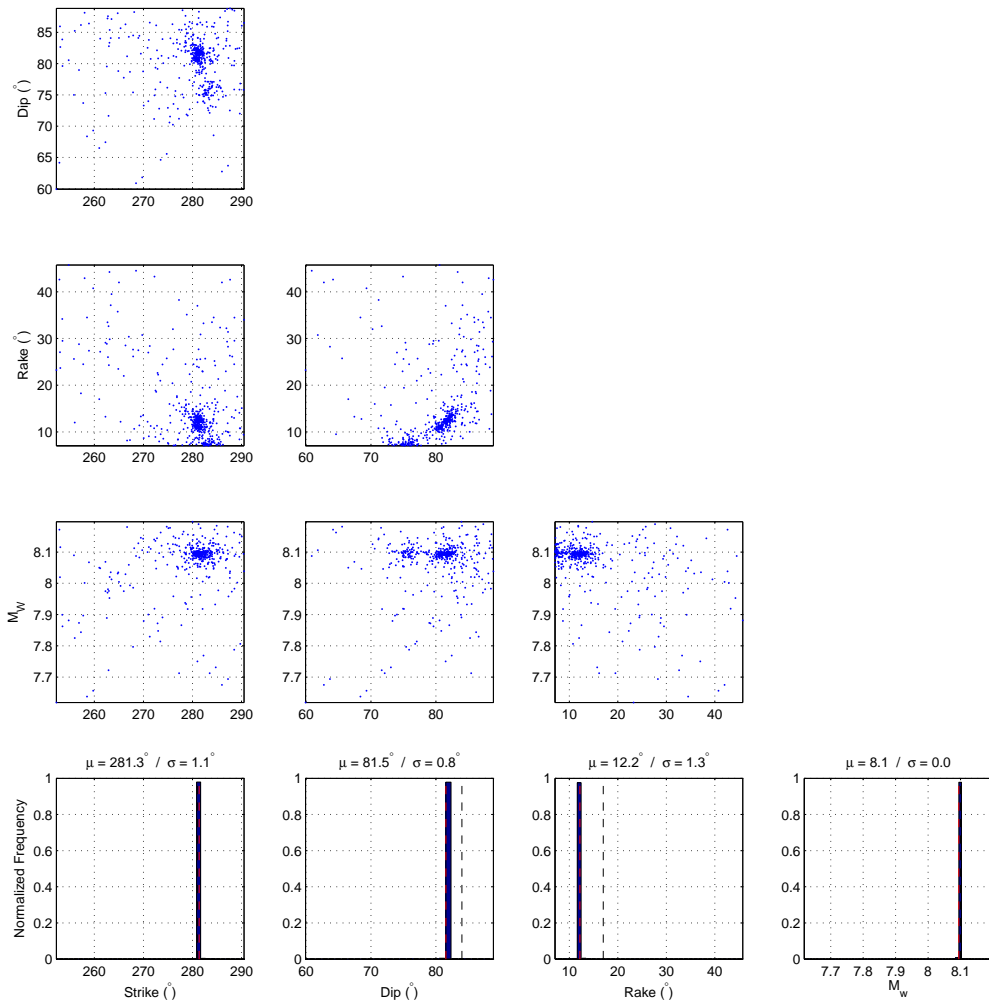


Figure B.2: Uncertainties and tradeoffs as shown from ensembles produced by Neighbourhood Algorithm and plotted as pairs of source parameters for the experiment of Figure B.1. Normalized frequency plots are shown at the bottom. The black dashed lines correspond to the input model ($\phi = 281^\circ, \delta = 84^\circ, \lambda = 17^\circ, M_w = 8.1$) and red dashed lines correspond to optimal models determined from the inversions. Mean (μ) and standard deviation (σ) values are also shown.

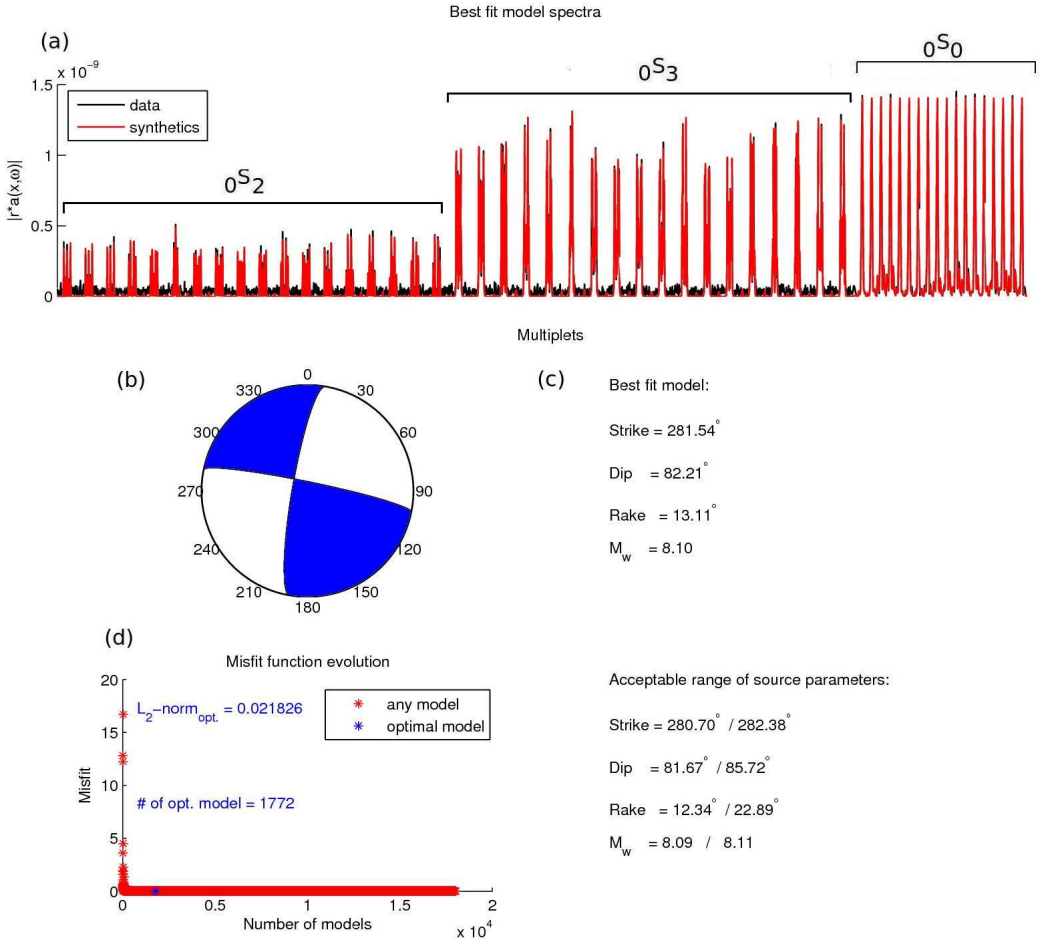


Figure B.3: Results from a point source inversion for the artificial 1998 Antarctic plate strike slip earthquake, using a combination of the amplitude and FFT misfits (97% amplitude and 3% FFT) using the GCMT location and fault geometry, assuming a total rupture duration of 90 s and rupture length of 240 km, based on the rupture model of Nettles *et al.* (1999), as the input model ($\phi = 281^\circ$, $\delta = 84^\circ$, $\lambda = 17^\circ$, $M_w = 8.1$, $T_r = 90$ s, $L = 240$ km). SAW12D 3-D model is used to build the synthetic data and the excitation kernels. White noise is also added to synthetic data: (a) 480-hr optimal fit acceleration amplitude spectra of $0S_2$, $0S_3$ and $0S_0$ multiplets, (b) optimal source mechanism, (c) optimal and acceptable range of source parameters (acceptable parameters correspond to source models yielding misfit values not 1% larger than the lowest misfit associated with the optimal source model), (d) misfit function evolution.

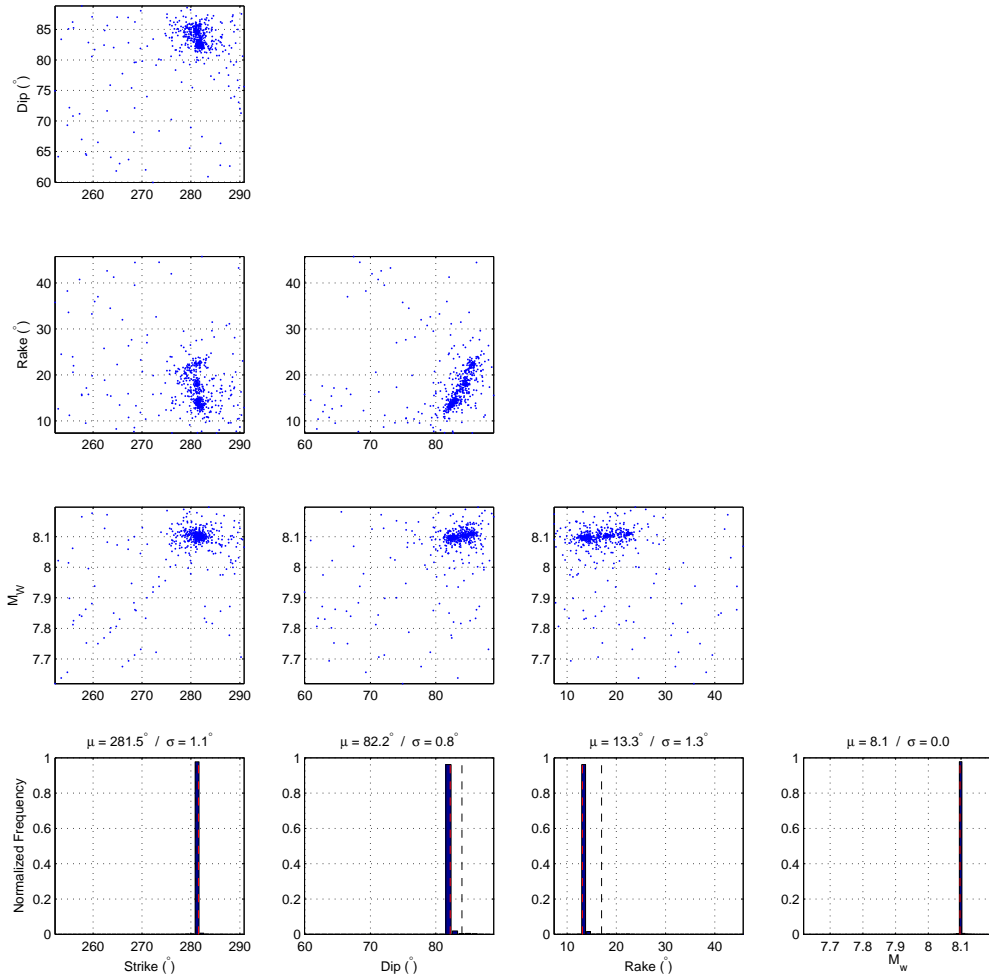


Figure B.4: Uncertainties and tradeoffs as shown from ensembles produced by Neighbourhood Algorithm and plotted as pairs of source parameters for the experiment of Figure B.3. Normalized frequency plots are shown at the bottom. The black dashed lines correspond to the input model ($\phi = 281^\circ, \delta = 84^\circ, \lambda = 17^\circ, M_w = 8.1$) and red dashed lines correspond to optimal models determined from the inversions. Mean (μ) and standard deviation (σ) values are also shown.

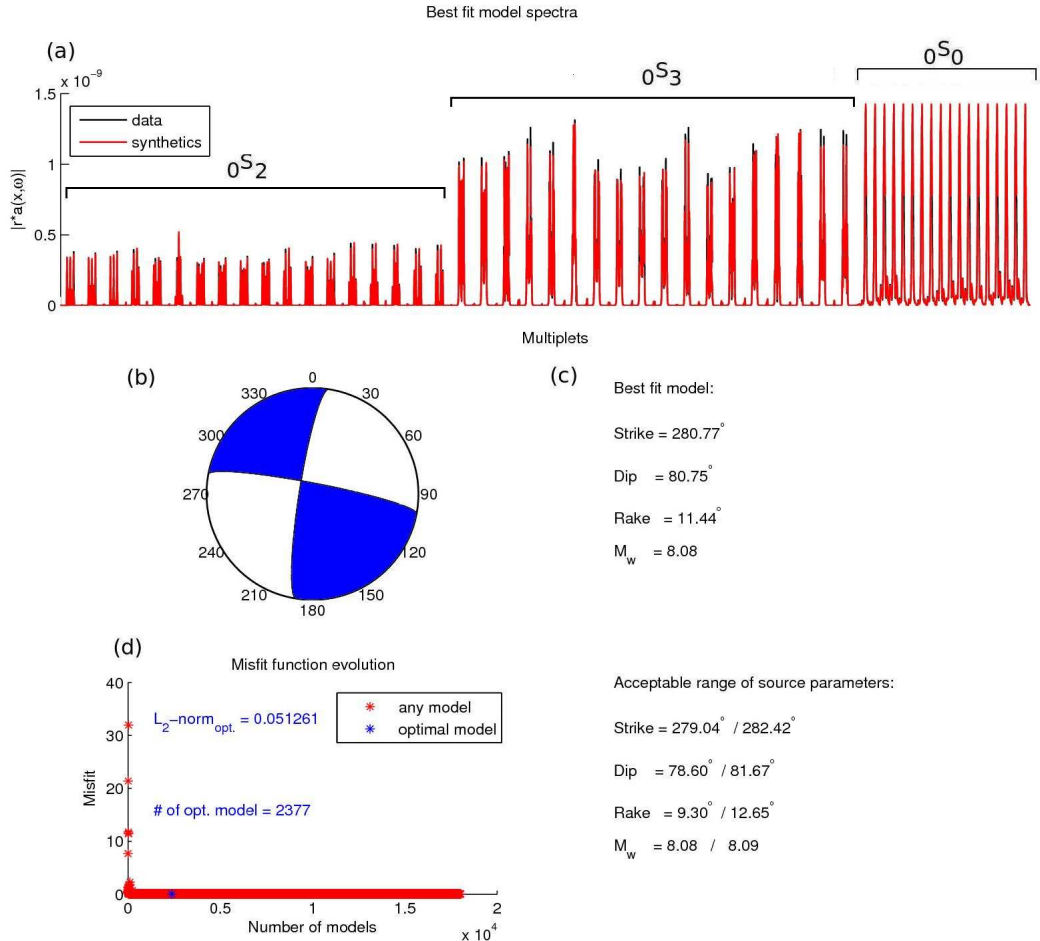


Figure B.5: Results from a point source inversion for the artificial 1998 Antarctic plate strike slip earthquake, using a combination of the amplitude and FFT misfits (97% amplitude and 3% FFT) using the GCMT location and fault geometry, assuming a total rupture duration of 90 s and rupture length of 240 km, based on the rupture model of Nettles *et al.* (1999), as the input model ($\phi = 281^\circ, \delta = 84^\circ, \lambda = 17^\circ, M_w = 8.1, T_r = 90$ s, $L = 240$ km). SAW12D 3-D model is used to build the synthetic data and PREM for the excitation kernels: (a) 480-hr optimal fit acceleration amplitude spectra of $0S_2$, $0S_3$ and $0S_0$ multiplets, (b) optimal source mechanism, (c) optimal and acceptable range of source parameters (acceptable parameters correspond to source models yielding misfit values not 1% larger than the lowest misfit associated with the optimal source model), (d) misfit function evolution.

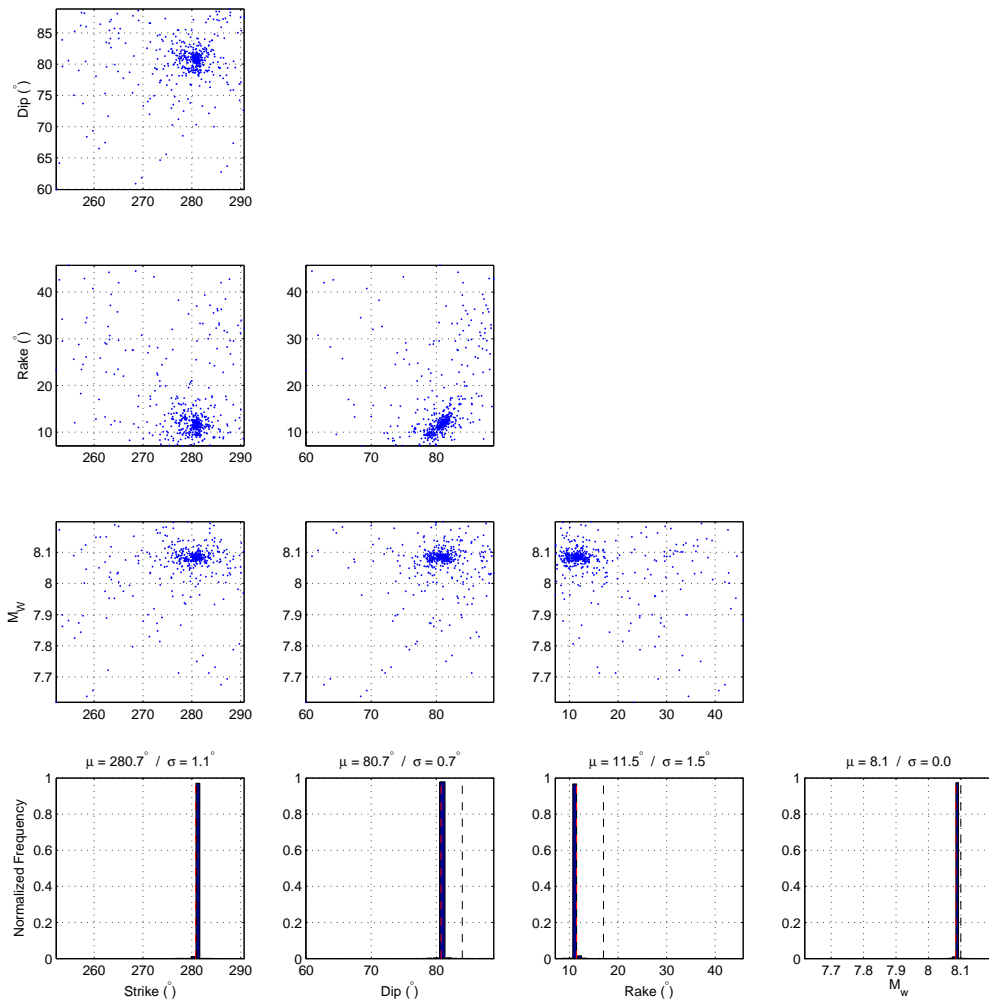


Figure B.6: Uncertainties and tradeoffs as shown from ensembles produced by Neighbourhood Algorithm and plotted as pairs of source parameters for the experiment of Figure B.5. Normalized frequency plots are shown at the bottom. The black dashed lines correspond to the input model ($\phi = 281^{\circ}, \delta = 84^{\circ}, \lambda = 17^{\circ}, M_w = 8.1$) and red dashed lines correspond to optimal models determined from the inversions. Mean (μ) and standard deviation (σ) values are also shown.

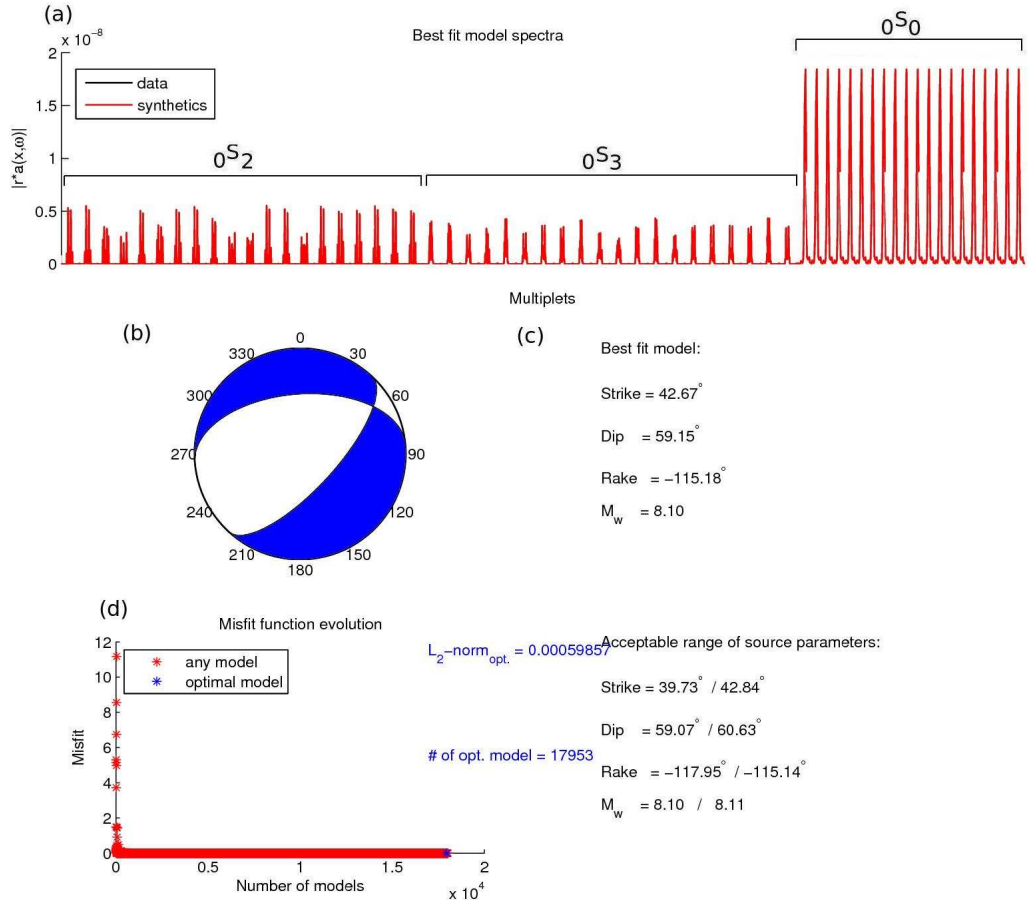


Figure B.7: Results from a point source inversion for the artificial 2007 Kuril normal faulting earthquake, using a combination of the amplitude and FFT misfits (97% amplitude and 3% FFT) using the GCMT location and fault geometry, assuming a total rupture duration of 60 s and rupture length of 220 km, based on the rupture model of Lay *et al.* (2009), as the input model ($\phi = 43^\circ$, $\delta = 59^\circ$, $\lambda = -115^\circ$, $M_w = 8.1$, $T_r = 60$ s, $L = 220$ km). SAW12D 3-D model is used to build the synthetic data and the excitation kernels: (a) 480-hr optimal fit acceleration amplitude spectra of $0S_2$, $0S_3$ and $0S_0$ multiplets, (b) optimal source mechanism, (c) optimal and acceptable range of source parameters (acceptable parameters correspond to source models yielding misfit values not 1% larger than the lowest misfit associated with the optimal source model), (d) misfit function evolution.

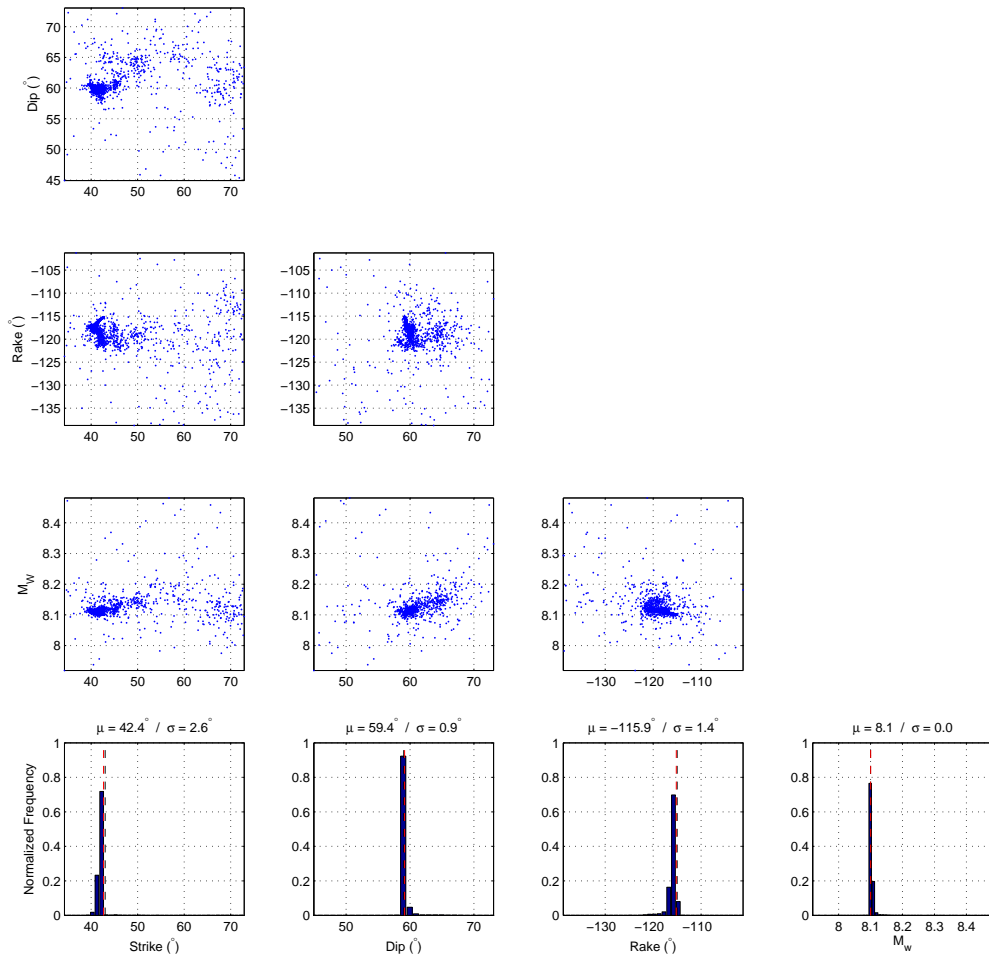


Figure B.8: Uncertainties and tradeoffs as shown from ensembles produced by Neighbourhood Algorithm and plotted as pairs of source parameters for the experiment of Figure B.7. Normalized frequency plots are shown at the bottom. The black dashed lines correspond to the input model ($\phi = 43^{\circ}, \delta = 59^{\circ}, \lambda = -115^{\circ}, M_w = 8.1$) and red dashed lines correspond to optimal models determined from the inversions. Mean (μ) and standard deviation (σ) values are also shown.

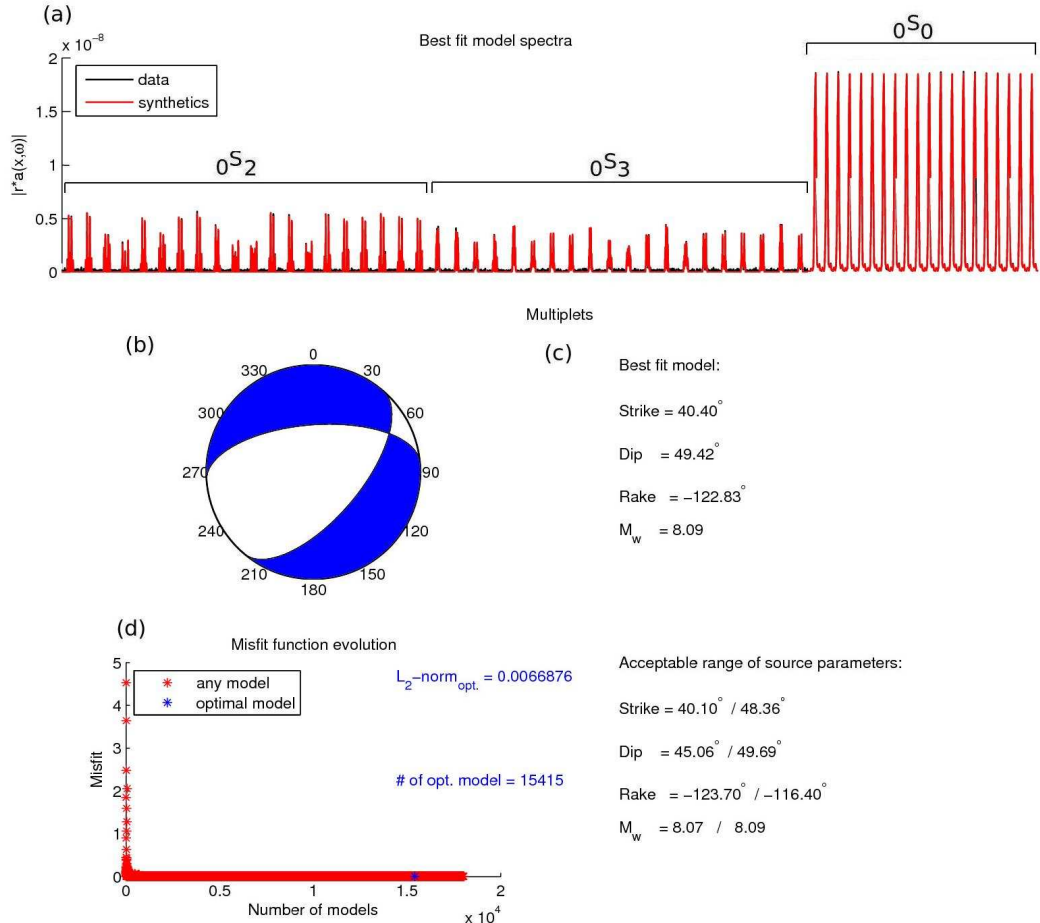


Figure B.9: Results from a point source inversion for the artificial 2007 Kuril normal faulting earthquake, using a combination of the amplitude and FFT misfits (97% amplitude and 3% FFT) using the GCMT location and fault geometry, assuming a total rupture duration of 60 s and rupture length of 220 km, based on the rupture model of Lay *et al.* (2009), as the input model ($\phi = 43^\circ$, $\delta = 59^\circ$, $\lambda = -115^\circ$, $M_w = 8.1$, $T_r = 60$ s, $L = 220$ km). SAW12D 3-D model is used to build the synthetic data and the excitation kernels. White noise is also added to synthetic data: (a) 480-hr optimal fit acceleration amplitude spectra of $0S_2$, $0S_3$ and $0S_0$ multiplets, (b) optimal source mechanism, (c) optimal and acceptable range of source parameters (acceptable parameters correspond to source models yielding misfit values not 1% larger than the lowest misfit associated with the optimal source model), (d) misfit function evolution.

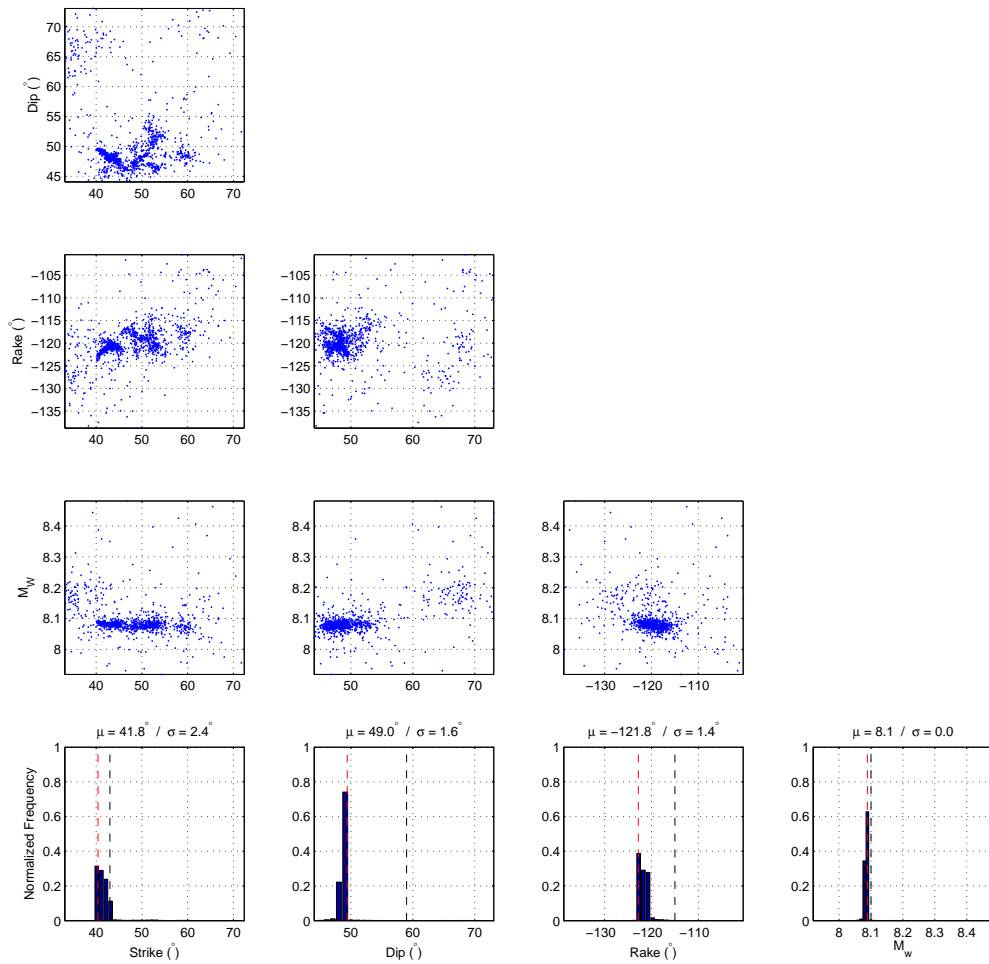


Figure B.10: Uncertainties and tradeoffs as shown from ensembles produced by Neighbourhood Algorithm and plotted as pairs of source parameters for the experiment of Figure B.9. Normalized frequency plots are shown at the bottom. The black dashed lines correspond to the input model ($\phi = 43^\circ, \delta = 59^\circ, \lambda = -115^\circ, M_w = 8.1$) and red dashed lines correspond to optimal models determined from the inversions. Mean (μ) and standard deviation (σ) values are also shown.

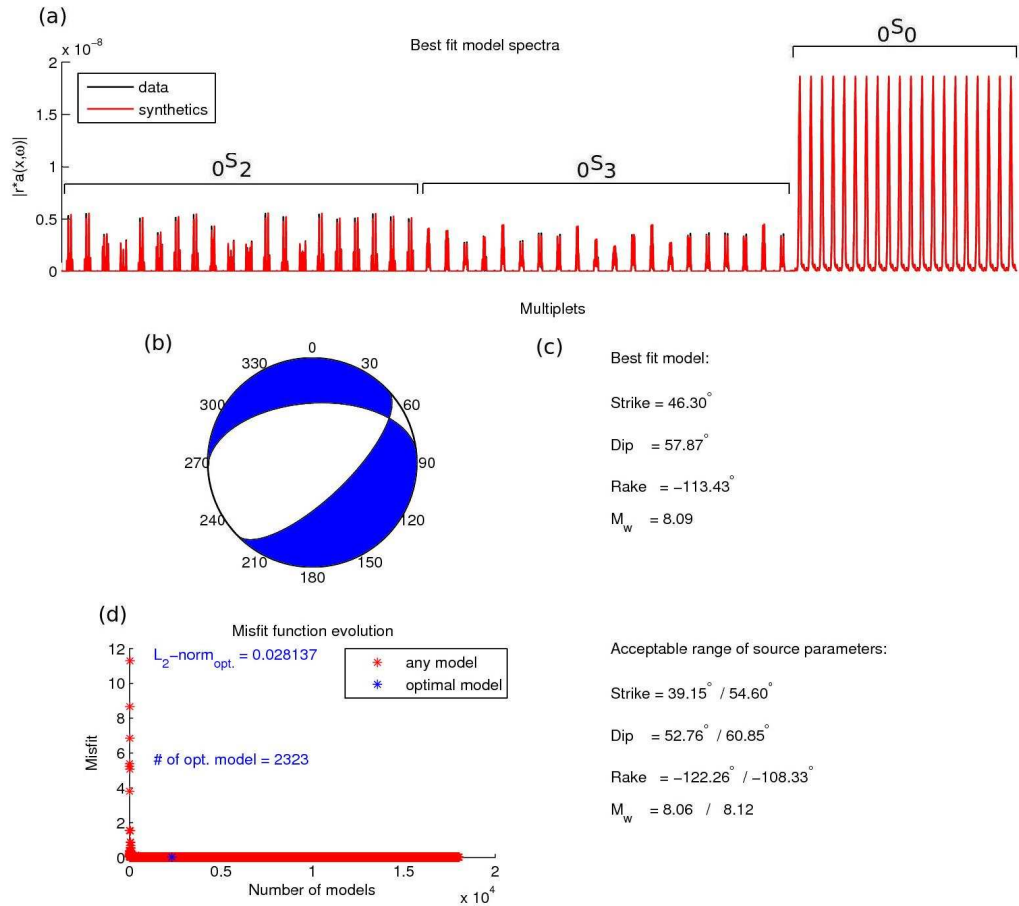


Figure B.11: Results from a point source inversion for the artificial 2007 Kuril normal faulting earthquake, using a combination of the amplitude and FFT misfits (97% amplitude and 3% FFT) using the GCMT location and fault geometry, assuming a total rupture duration of 60 s and rupture length of 220 km, based on the rupture model of Lay *et al.* (2009), as the input model ($\phi = 43^\circ$, $\delta = 59^\circ$, $\lambda = -115^\circ$, $M_w = 8.1$, $T_r = 60$ s, $L = 220$ km). SAW12D 3-D model is used to build the synthetic data and PREM for the excitation kernels: (a) 480-hr optimal fit acceleration amplitude spectra of $0S_2$, $0S_3$ and $0S_0$ multiplets, (b) optimal source mechanism, (c) optimal and acceptable range of source parameters (acceptable parameters correspond to source models yielding misfit values not 1% larger than the lowest misfit associated with the optimal source model), (d) misfit function evolution.

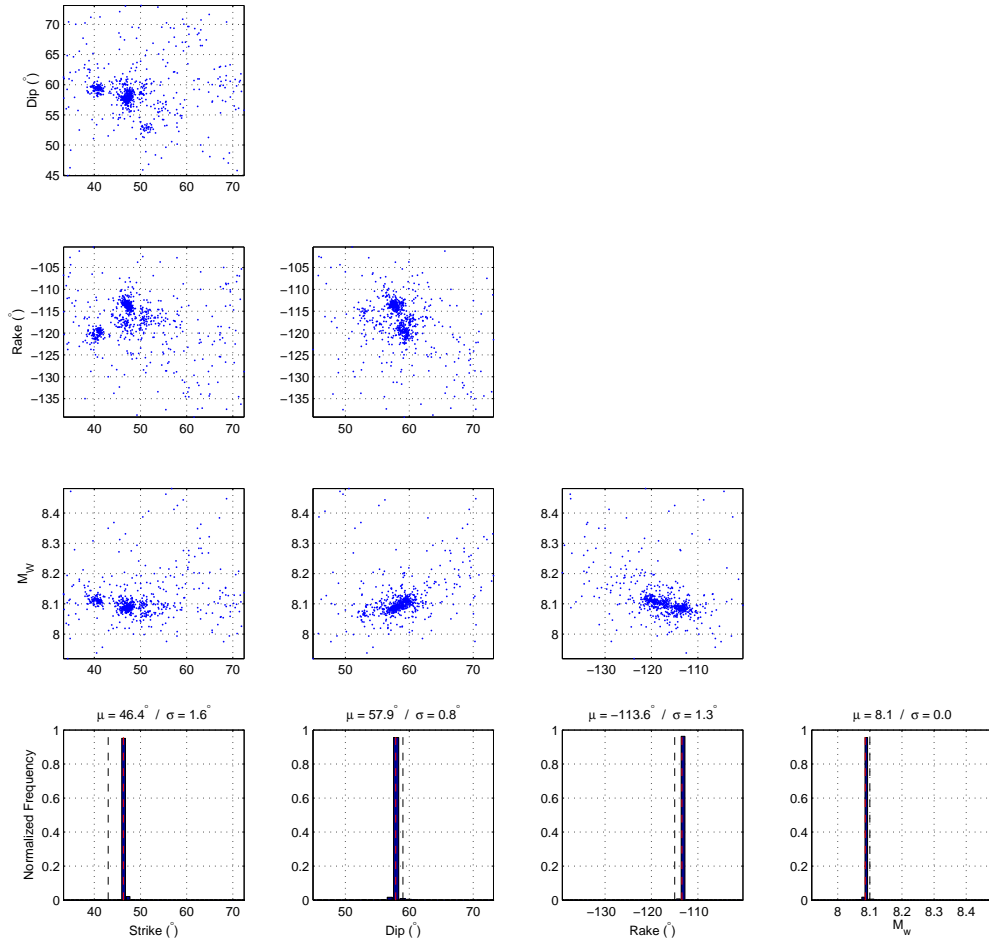


Figure B.12: Uncertainties and tradeoffs as shown from ensembles produced by Neighbourhood Algorithm and plotted as pairs of source parameters for the experiment of Figure B.11. Normalized frequency plots are shown at the bottom. The black dashed lines correspond to the input model ($\phi = 43^\circ, \delta = 59^\circ, \lambda = -115^\circ, M_w = 8.1$) and red dashed lines correspond to optimal models determined from the inversions. Mean (μ) and standard deviation (σ) values are also shown.

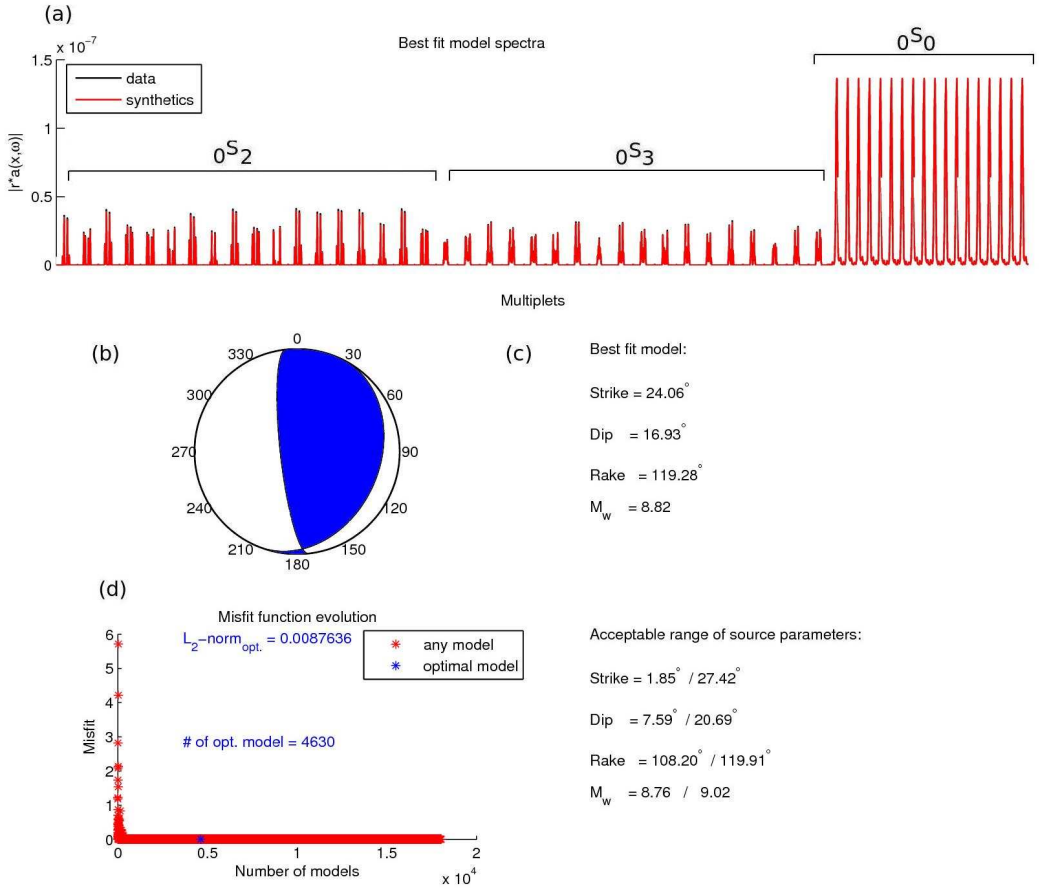


Figure B.13: Results from a point source inversion for the artificial 2010 Chile thrust earthquake, using a combination of the amplitude and FFT misfits (97% amplitude and 3% FFT) using an artificial unilateral rupture model based on the source model of Delouis *et al.* (2010) assuming a total rupture duration of 230 s and rupture length of 600 km, as the input model ($\phi = 15^\circ$, $\delta = 18^\circ$, $\lambda = 110^\circ$, $M_w = 8.8$, $T_r = 230$ s, $L = 600$ km). SAW12D 3-D model is used to build the synthetic data and the excitation kernels: (a) 480-hr optimal fit acceleration amplitude spectra of $0S_2$, $0S_3$ and $0S_0$ multiplets, (b) optimal source mechanism, (c) optimal and acceptable range of source parameters (acceptable parameters correspond to source models yielding misfit values not 1% larger than the lowest misfit associated with the optimal source model), (d) misfit function evolution.

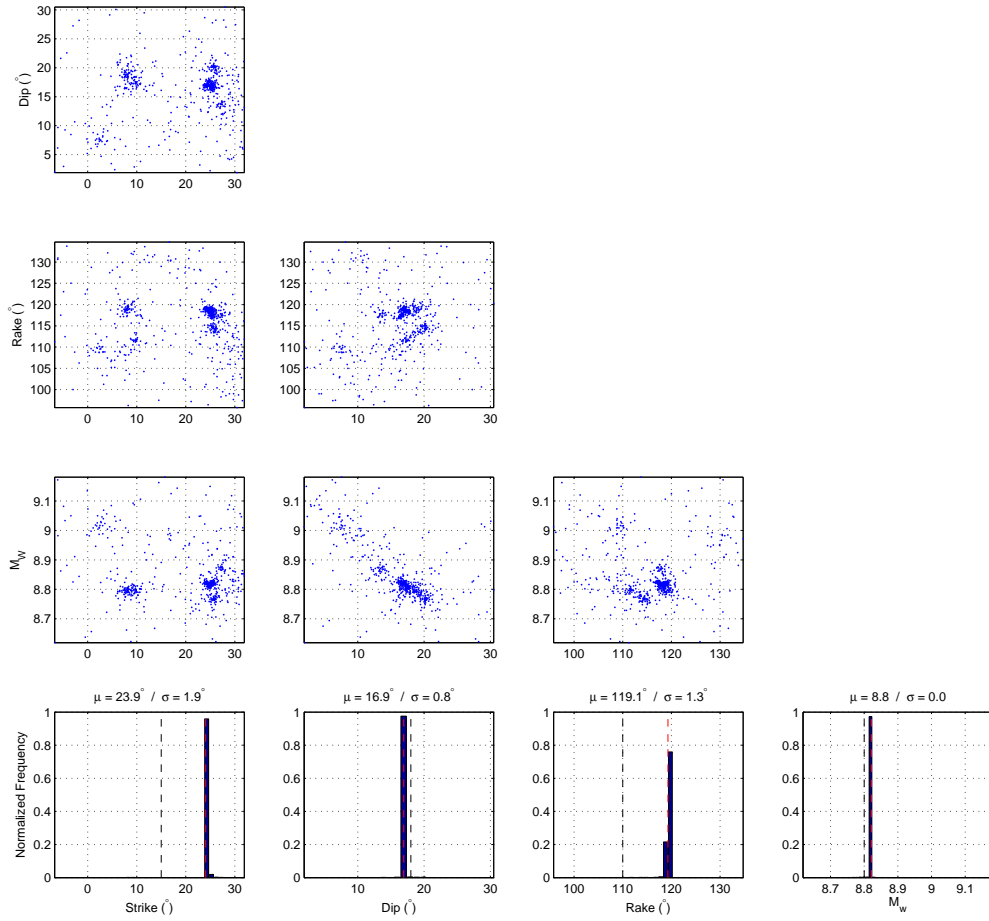


Figure B.14: Uncertainties and tradeoffs as shown from ensembles produced by Neighbourhood Algorithm and plotted as pairs of source parameters for the experiment of Figure B.13. Normalized frequency plots are shown at the bottom. The black dashed lines correspond to the input model ($\phi = 15^\circ, \delta = 18^\circ, \lambda = 110^\circ, M_w = 8.8$) and red dashed lines correspond to optimal models determined from the inversions. Mean (μ) and standard deviation (σ) values are also shown.

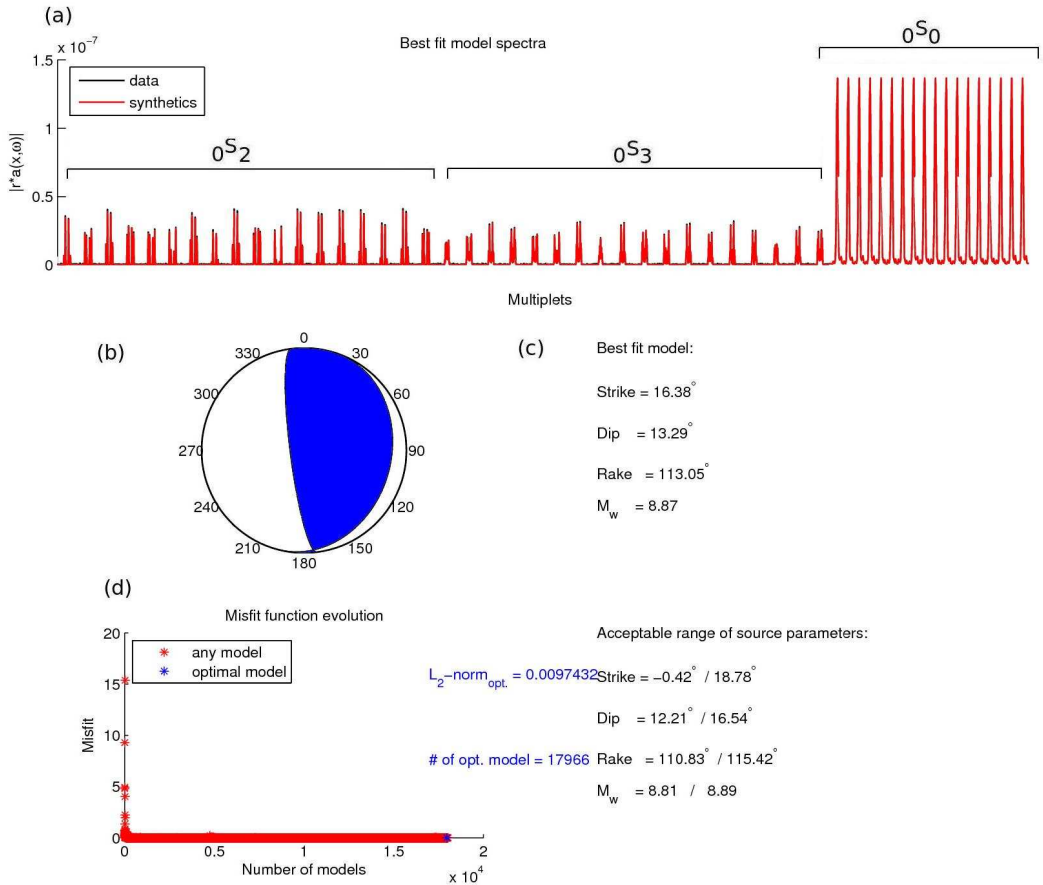


Figure B.15: Results from a point source inversion for the artificial 2010 Chile thrust earthquake, using a combination of the amplitude and FFT misfits (97% amplitude and 3% FFT) using an artificial unilateral rupture model based on the source model of Delouis *et al.* (2010) assuming a total rupture duration of 230 s and rupture length of 600 km, as the input model ($\phi = 15^\circ$, $\delta = 18^\circ$, $\lambda = 110^\circ$, $M_w = 8.8$, $T_r = 230$ s, $L = 600$ km). SAW12D 3-D model is used to build the synthetic data and the excitation kernels. White noise is also added to synthetic data: (a) 480-hr optimal fit acceleration amplitude spectra of $0S_2$, $0S_3$ and $0S_0$ multiplets, (b) optimal source mechanism, (c) optimal and acceptable range of source parameters (acceptable parameters correspond to source models yielding misfit values not 1% larger than the lowest misfit associated with the optimal source model), (d) misfit function evolution.

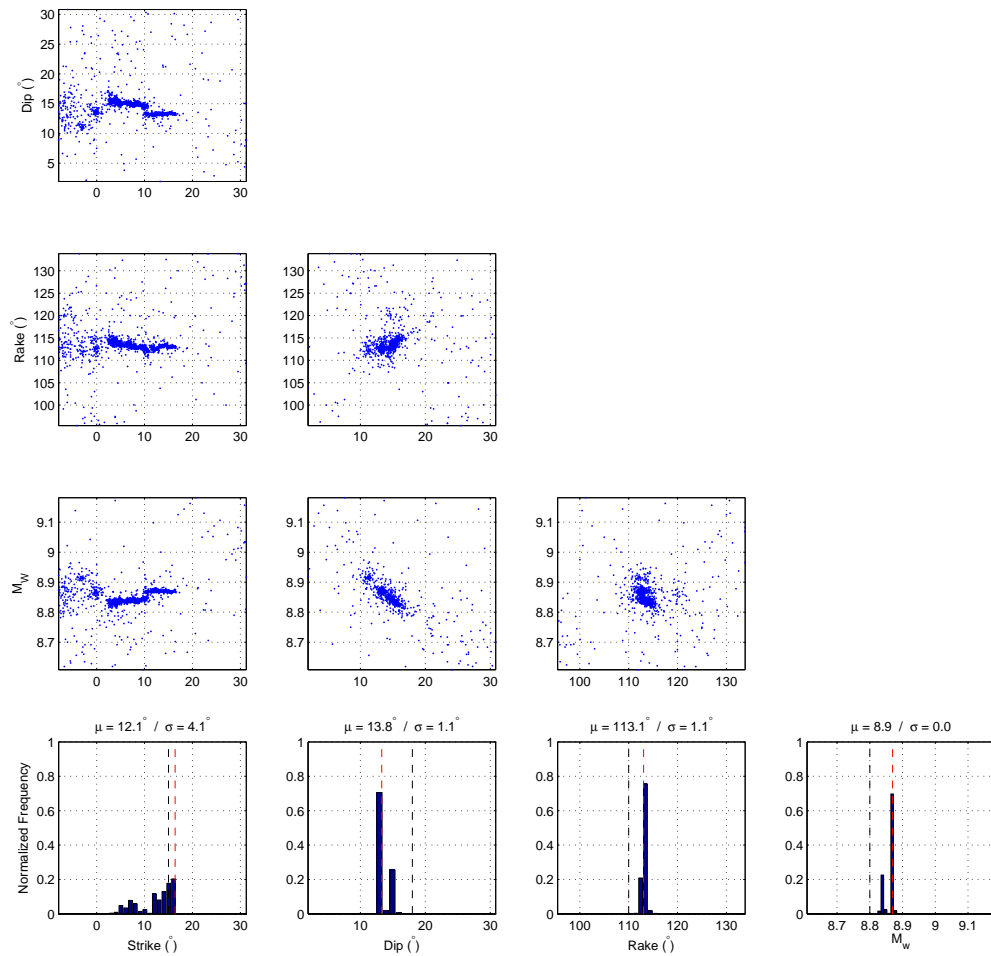


Figure B.16: Uncertainties and tradeoffs as shown from ensembles produced by Neighbourhood Algorithm and plotted as pairs of source parameters for the experiment of Figure B.15. Normalized frequency plots are shown at the bottom. The black dashed lines correspond to the input model ($\phi = 15^\circ$, $\delta = 18^\circ$, $\lambda = 110^\circ$, $M_w = 8.8$) and red dashed lines correspond to optimal models determined from the inversions. Mean (μ) and standard deviation (σ) values are also shown.

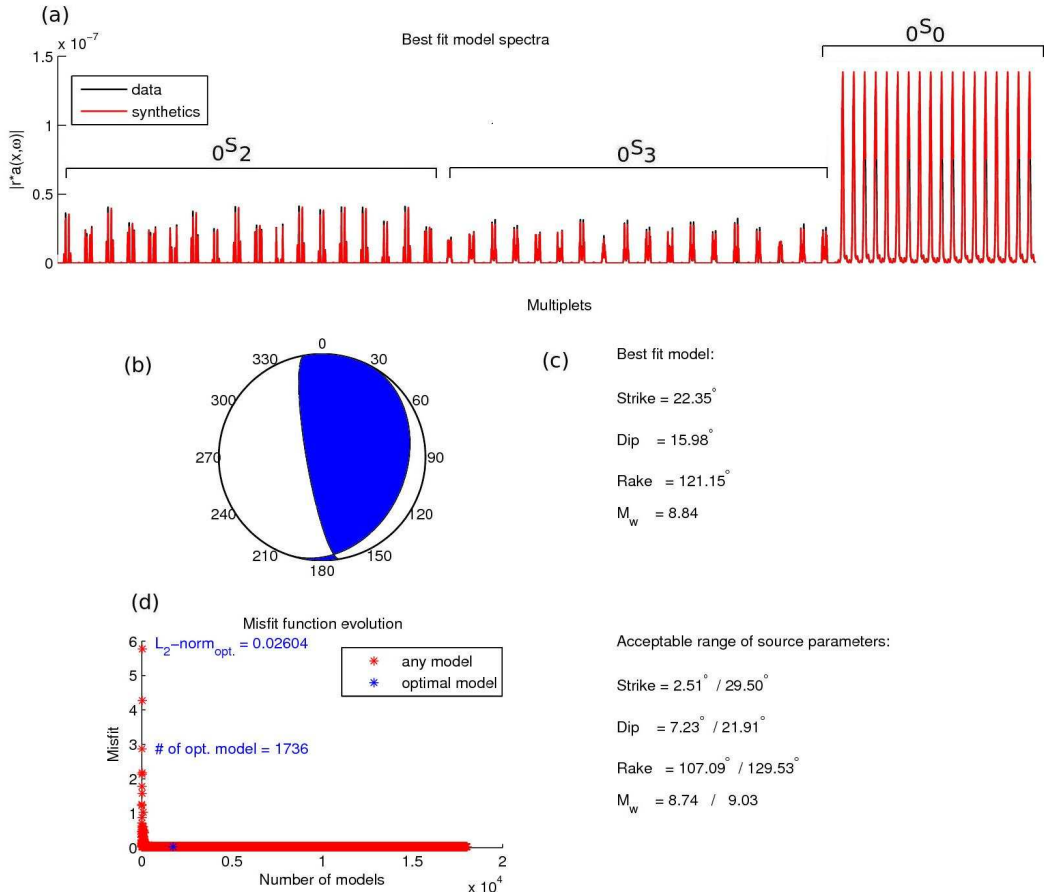


Figure B.17: Results from a point source inversion for the artificial 2010 Chile thrust earthquake, using a combination of the amplitude and FFT misfits (97% amplitude and 3% FFT) using an artificial unilateral rupture model based on the source model of Delouis *et al.* (2010) assuming a total rupture duration of 230 s and rupture length of 600 km, as the input model ($\phi = 15^\circ$, $\delta = 18^\circ$, $\lambda = 110^\circ$, $M_w = 8.8$, $T_r = 230$ s, $L = 600$ km). SAW12D 3-D model is used to build the synthetic data and PREM for the excitation kernels: (a) 480-hr optimal fit acceleration amplitude spectra of $0S_2$, $0S_3$ and $0S_0$ multiplets, (b) optimal source mechanism, (c) optimal and acceptable range of source parameters (acceptable parameters correspond to source models yielding misfit values not 1% larger than the lowest misfit associated with the optimal source model), (d) misfit function evolution.

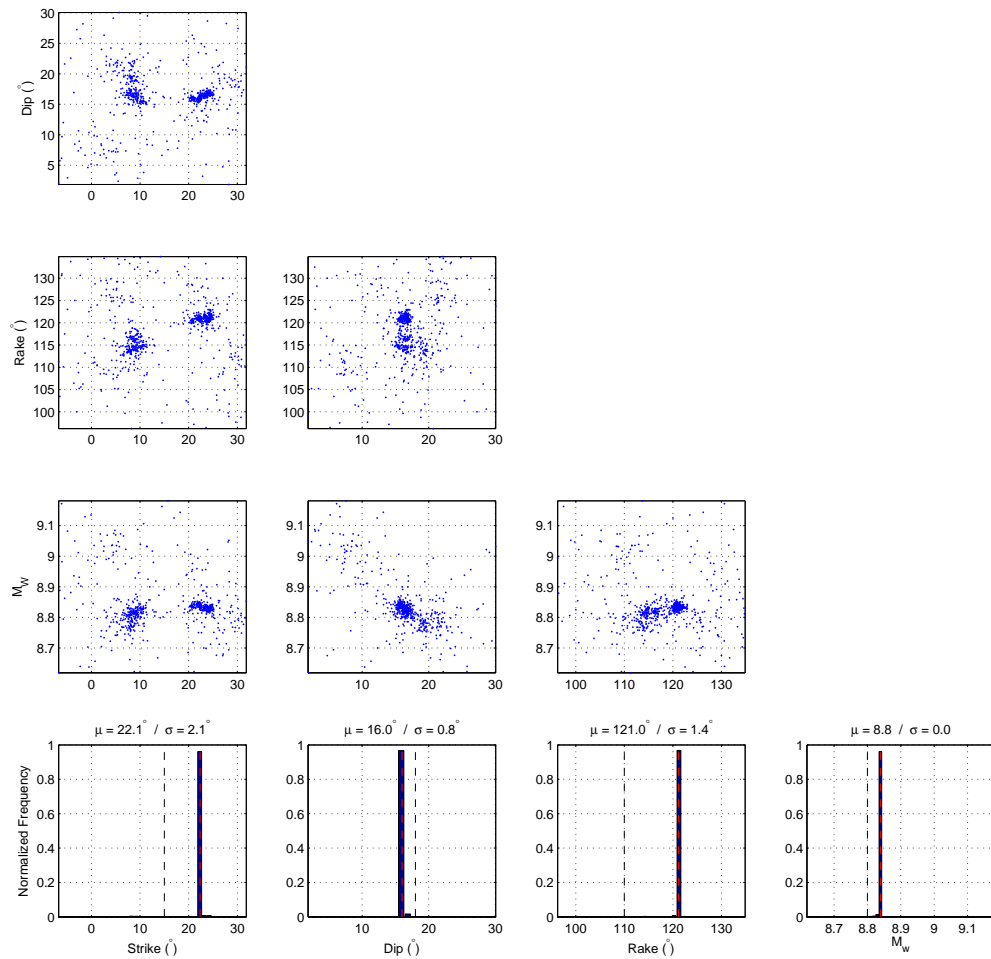


Figure B.18: Uncertainties and tradeoffs as shown from ensembles produced by Neighbourhood Algorithm and plotted as pairs of source parameters for the experiment of Figure B.17. Normalized frequency plots are shown at the bottom. The black dashed lines correspond to the input model ($\phi = 15^\circ, \delta = 18^\circ, \lambda = 110^\circ, M_w = 8.8$) and red dashed lines correspond to optimal models determined from the inversions. Mean (μ) and standard deviation (σ) values are also shown.

Appendix C

Supplementary material for Chapter 4 - Finite source inversion synthetic tests

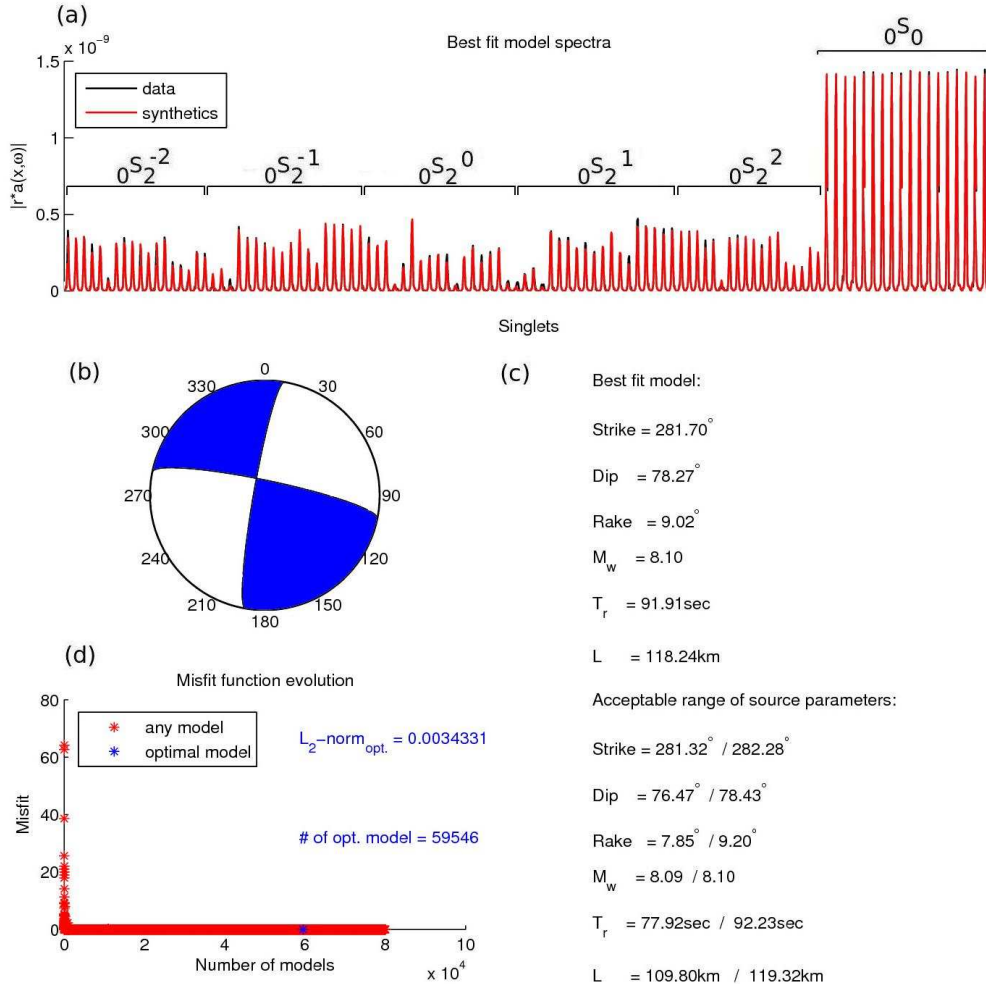


Figure C.1: Results from a finite source inversion for the artificial 1998 Antarctic plate strike slip earthquake, using a combination of the amplitude and FFT misfits (97% amplitude and 3% FFT) using the GCMT location and fault geometry, assuming a total rupture duration of 90 s and rupture length of 240 km, based on the rupture model of Nettles *et al.* (1999), as the input model ($\phi = 281^\circ, \delta = 84^\circ, \lambda = 17^\circ, M_w = 8.1, T_r = 90$ s, $L = 240$ km). SAW12D 3-D model is used to build the synthetic data and the excitation kernels. White noise is also added to synthetic data: (a) 480-hr optimal fit acceleration amplitude spectra of $0S_2^{0,\pm 1,\pm 2}$ and $0S_2^0$ singlets, (b) optimal source mechanism, (c) optimal and acceptable range of source parameters (acceptable parameters correspond to source models yielding misfit values up to 1% larger than the lowest misfit associated with the optimal source model), (d) misfit function evolution.

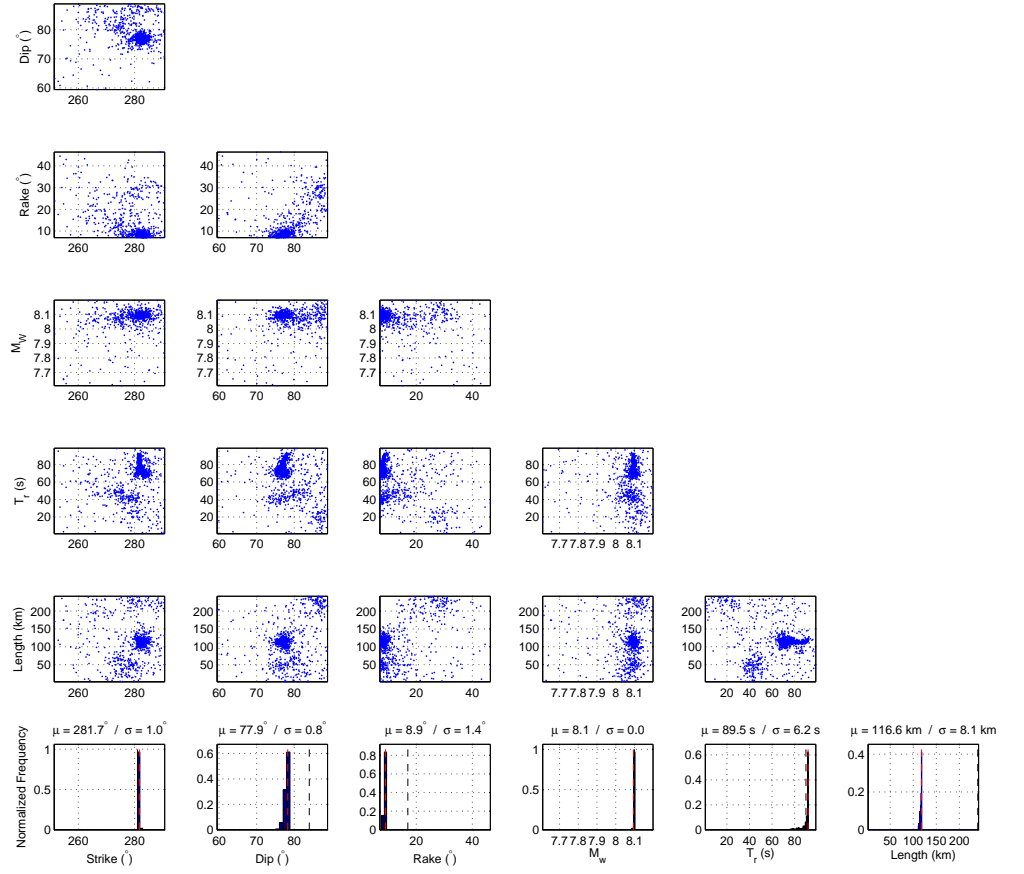


Figure C.2: Uncertainties and tradeoffs as shown from ensembles produced by Neighbourhood Algorithm and plotted as pairs of source parameters for the experiment of Figure C.1. Normalized frequency plots are shown at the bottom. The black dashed lines correspond to the input model ($\phi = 281^\circ, \delta = 84^\circ, \lambda = 17^\circ, M_w = 8.1, T_r = 90$ s, $L = 240$ km) and red dashed lines correspond to optimal models determined from the inversions. Mean (μ) and standard deviation (σ) values are also shown.

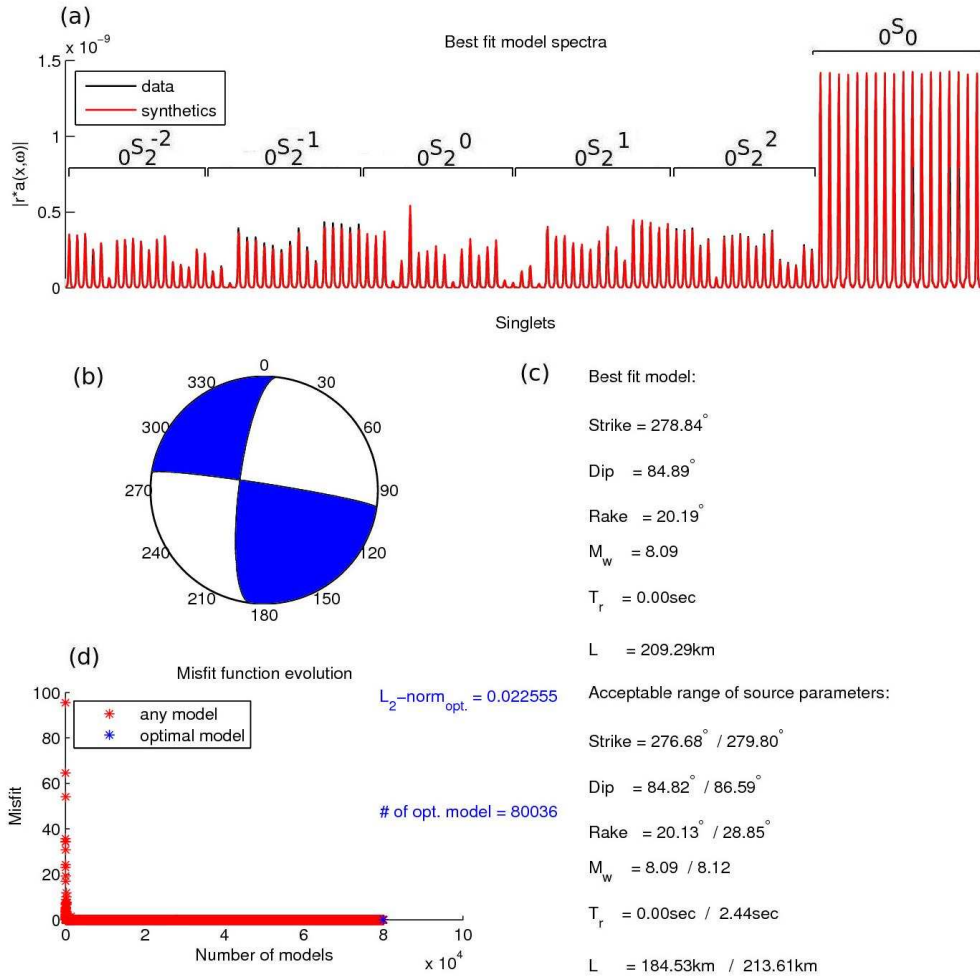


Figure C.3: Results from a finite source inversion for the artificial 1998 Antarctic plate strike slip earthquake, using a combination of the amplitude and FFT misfits (97% amplitude and 3% FFT) using the GCMT location and fault geometry, assuming a total rupture duration of 90 s and rupture length of 240 km, based on the rupture model of Nettles *et al.* (1999), as the input model ($\phi = 281^\circ$, $\delta = 84^\circ$, $\lambda = 17^\circ$, $M_w = 8.1$, $T_r = 90$ s, $L = 240$ km). SAW12D 3-D model is used to build the synthetic data and PREM for the excitation kernels: (a) 480-hr optimal fit acceleration amplitude spectra of $0S_2^{0,\pm 1,\pm 2}$ and $0S_0^0$ singlets, (b) optimal source mechanism, (c) optimal and acceptable range of source parameters (acceptable parameters correspond to source models yielding misfit values up to 1% larger than the lowest misfit associated with the optimal source model), (d) misfit function evolution.

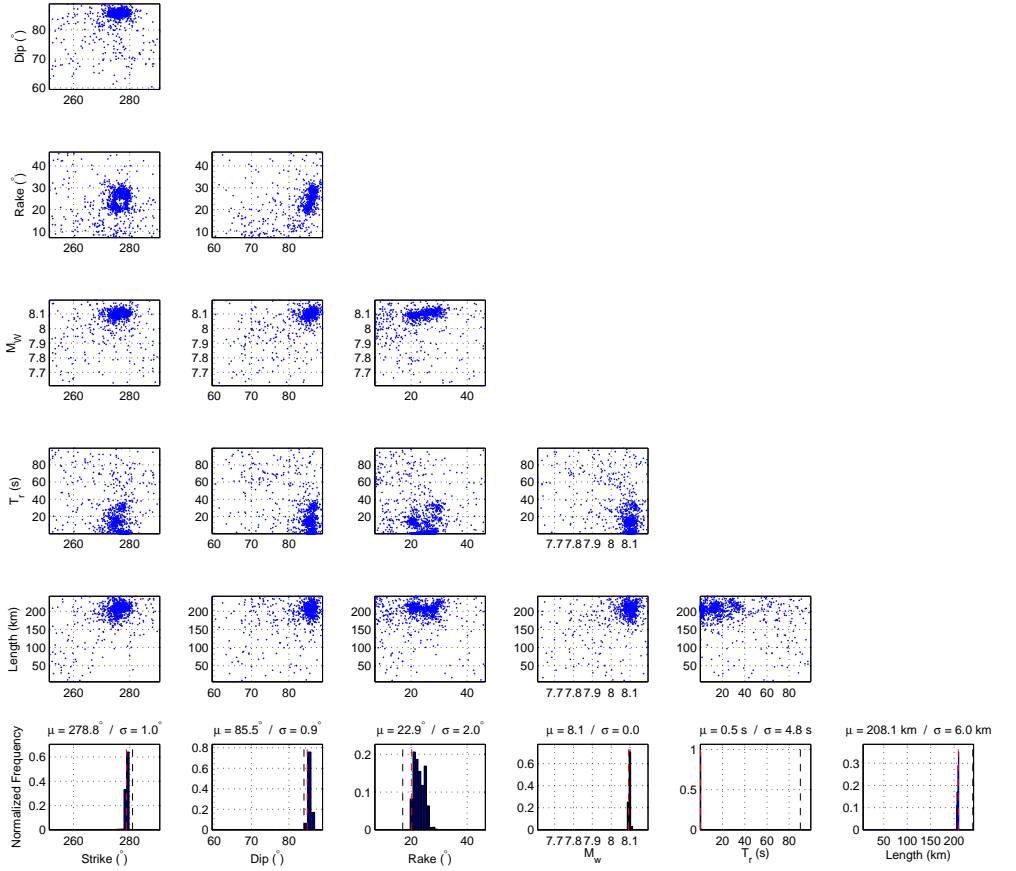


Figure C.4: Uncertainties and tradeoffs as shown from ensembles produced by Neighbourhood Algorithm and plotted as pairs of source parameters for the experiment of Figure C.3. Normalized frequency plots are shown at the bottom. The black dashed lines correspond to the input model ($\phi = 281^\circ, \delta = 84^\circ, \lambda = 17^\circ, M_w = 8.1, T_r = 90$ s, $L = 240$ km) and red dashed lines correspond to optimal models determined from the inversions. Mean (μ) and standard deviation (σ) values are also shown.

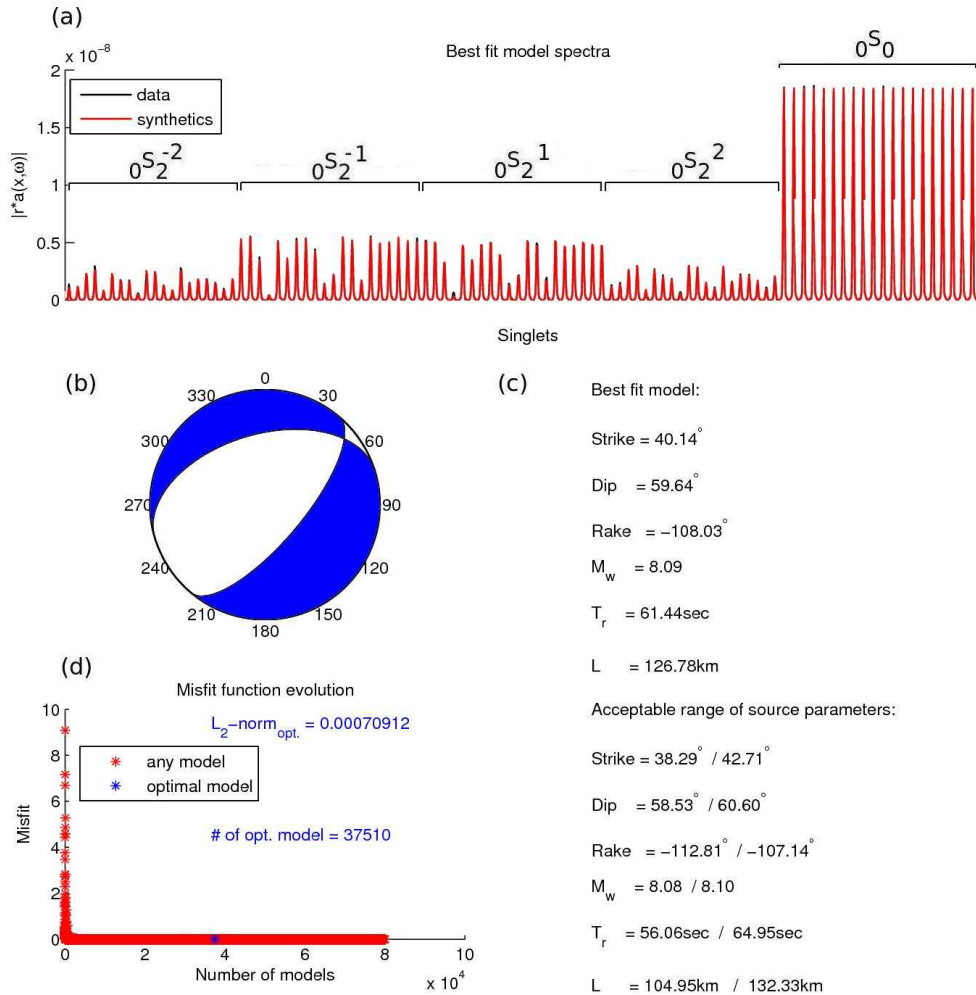


Figure C.5: Results from a finite source inversion for the artificial 2007 Kuril normal faulting earthquake, using a combination of the amplitude and FFT misfits (97% amplitude and 3% FFT) using the GCMT location and fault geometry, assuming a total rupture duration of 60 s and rupture length of 220 km, based on the rupture model of Lay *et al.* (2009), as the input model ($\phi = 43^\circ, \delta = 59^\circ, \lambda = -115^\circ, M_w = 8.1, T_r = 60$ s, $L = 220$ km). SAW12D 3-D model is used to build the synthetic data and the excitation kernels. White noise is also added to synthetic data: (a) 480-hr optimal fit acceleration amplitude spectra of $0S_2^{\pm 1, \pm 2}$ and $0S_0^0$ singlets, (b) optimal source mechanism, (c) optimal and acceptable range of source parameters (acceptable parameters correspond to source models yielding misfit values up to 1% larger than the lowest misfit associated with the optimal source model), (d) misfit function evolution.

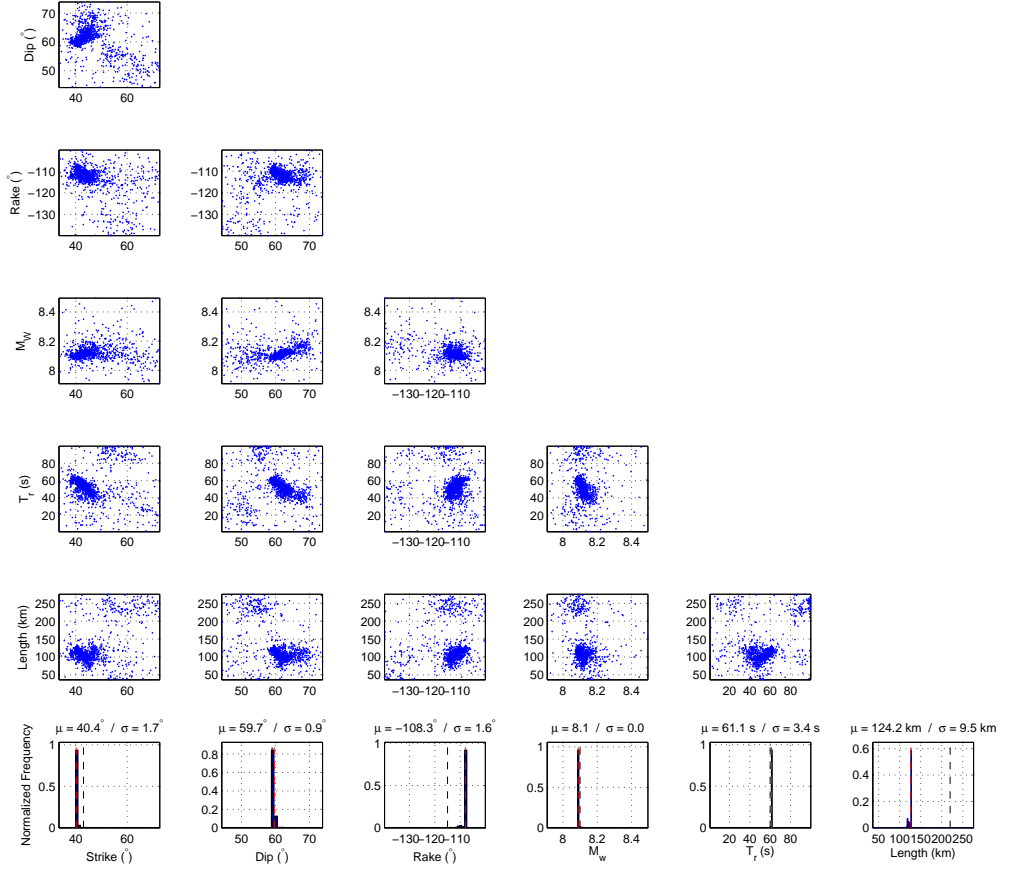


Figure C.6: Uncertainties and tradeoffs as shown from ensembles produced by Neighbourhood Algorithm and plotted as pairs of source parameters for the experiment of Figure C.5. Normalized frequency plots are shown at the bottom. The black dashed lines correspond to the input model ($\phi = 43^\circ, \delta = 59^\circ, \lambda = -115^\circ, M_w = 8.1, T_r = 60$ s, $L = 220$ km) and red dashed lines correspond to optimal models determined from the inversions. Mean (μ) and standard deviation (σ) values are also shown.

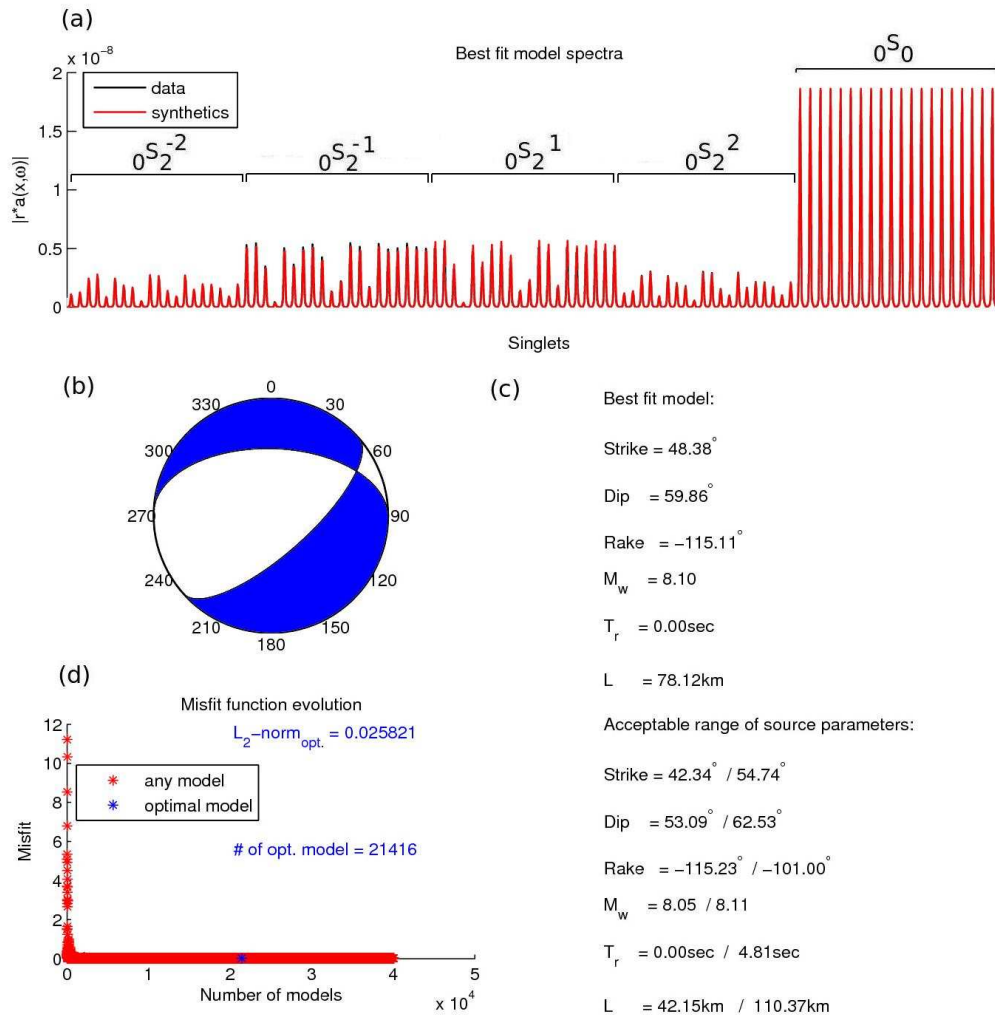


Figure C.7: Results from a finite source inversion for the artificial 2007 Kuril normal faulting earthquake, using a combination of the amplitude and FFT misfits (97% amplitude and 3% FFT) using the GCMT location and fault geometry, assuming a total rupture duration of 60 s and rupture length of 220 km, based on the rupture model of Lay *et al.* (2009), as the input model ($\phi = 43^\circ$, $\delta = 59^\circ$, $\lambda = -115^\circ$, $M_w = 8.1$, $T_r = 60$ s, $L = 220$ km). SAW12D 3-D model is used to build the synthetic data and PREM for the excitation kernels: (a) 480-hr optimal fit acceleration amplitude spectra of ${}_0S_2^{\pm 1, \pm 2}$ and ${}_0S_0^0$ singlets, (b) optimal source mechanism, (c) optimal and acceptable range of source parameters (acceptable parameters correspond to source models yielding misfit values up to 1% larger than the lowest misfit associated with the optimal source model), (d) misfit function evolution.

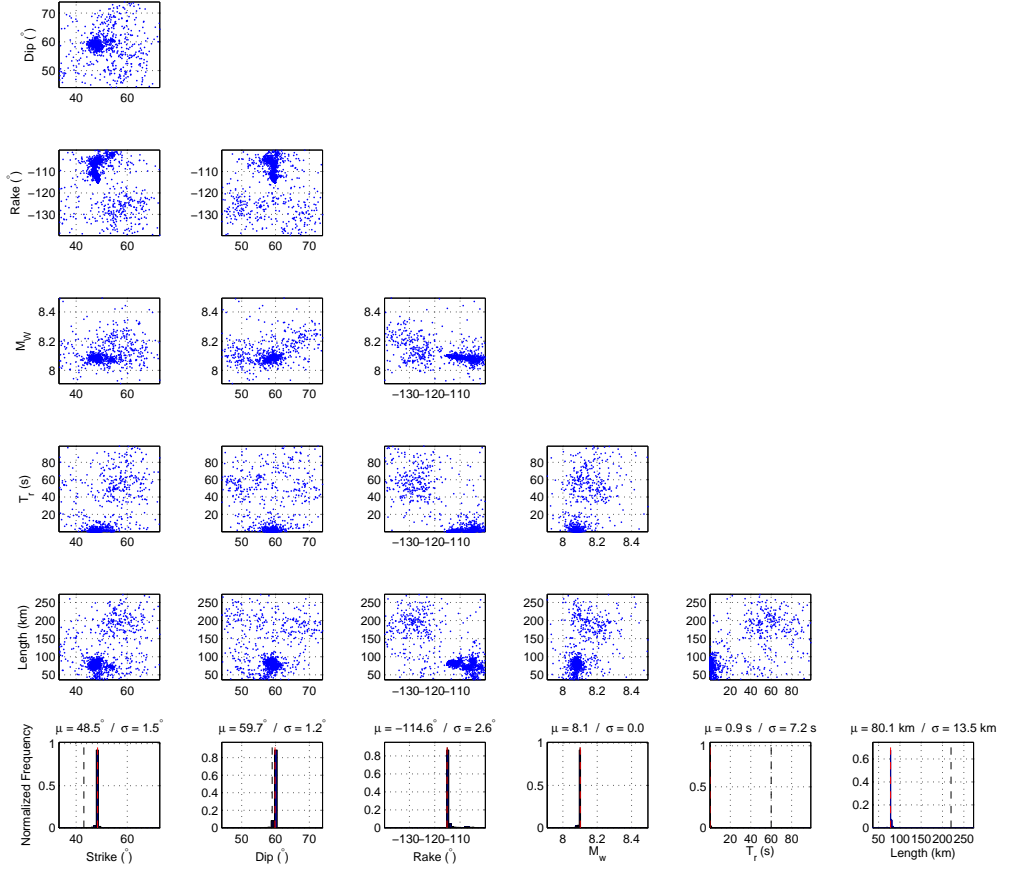


Figure C.8: Uncertainties and tradeoffs as shown from ensembles produced by Neighbourhood Algorithm and plotted as pairs of source parameters for the experiment of Figure C.7. Normalized frequency plots are shown at the bottom. The black dashed lines correspond to the input model ($\phi = 43^\circ, \delta = 59^\circ, \lambda = -115^\circ, M_w = 8.1, T_r = 60$ s, $L = 220$ km) and red dashed lines correspond to optimal models determined from the inversions. Mean (μ) and standard deviation (σ) values are also shown.

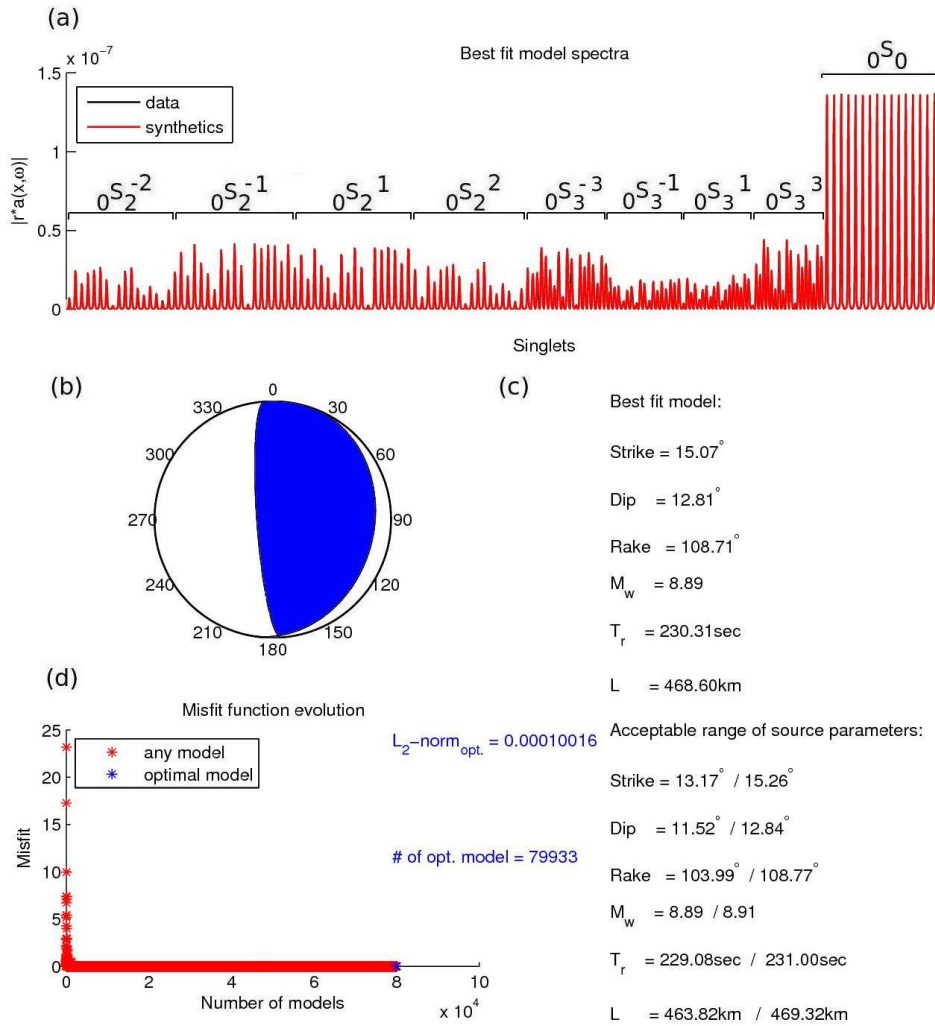


Figure C.9: Results from a finite source inversion for the artificial 2010 Chile thrust earthquake, using a combination of the amplitude and FFT misfits (97% amplitude and 3% FFT) using an artificial unilateral rupture model based on the source model of Delouis *et al.* (2010) assuming a total rupture duration of 230 s and rupture length of 600 km, as the input model ($\phi = 15^\circ$, $\delta = 18^\circ$, $\lambda = 110^\circ$, $M_w = 8.8$, $T_r = 230$ s, $L = 600$ km). SAW12D 3-D model is used to build the synthetic data and the excitation kernels. White noise is also added to synthetic data: (a) 480-hr optimal fit acceleration amplitude spectra of $0S_2^{\pm 1, \pm 2}$, $0S_3^{\pm 1, \pm 3}$ and $0S_0^0$ singlets, (b) optimal source mechanism, (c) optimal and acceptable range of source parameters (acceptable parameters correspond to source models yielding misfit values up to 1% larger than the lowest misfit associated with the optimal source model), (d) misfit function evolution.

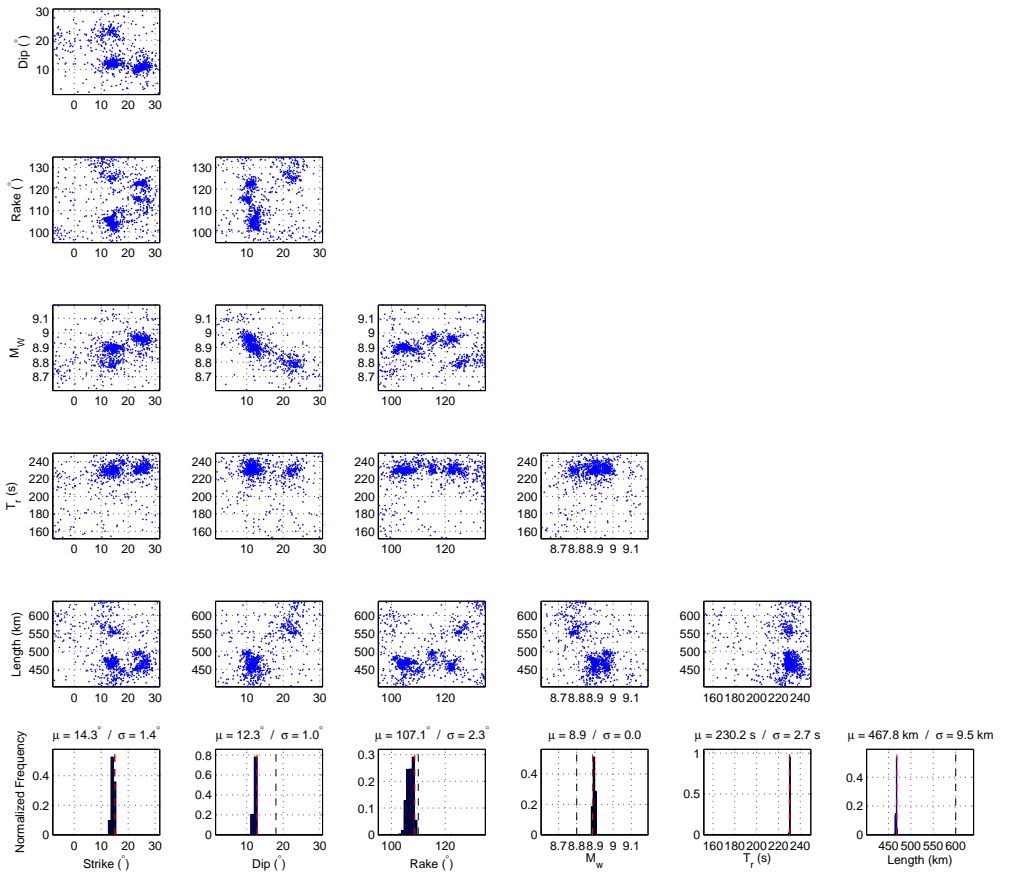


Figure C.10: Uncertainties and tradeoffs as shown from ensembles produced by Neighbourhood Algorithm and plotted as pairs of source parameters for the experiment of Figure C.9. Normalized frequency plots are shown at the bottom. The black dashed lines correspond to the input model ($\phi = 15^\circ, \delta = 18^\circ, \lambda = 110^\circ, M_w = 8.8, T_r = 230 \text{ s}, L = 600 \text{ km}$) and red dashed lines correspond to optimal models determined from the inversions. Mean (μ) and standard deviation (σ) values are also shown.

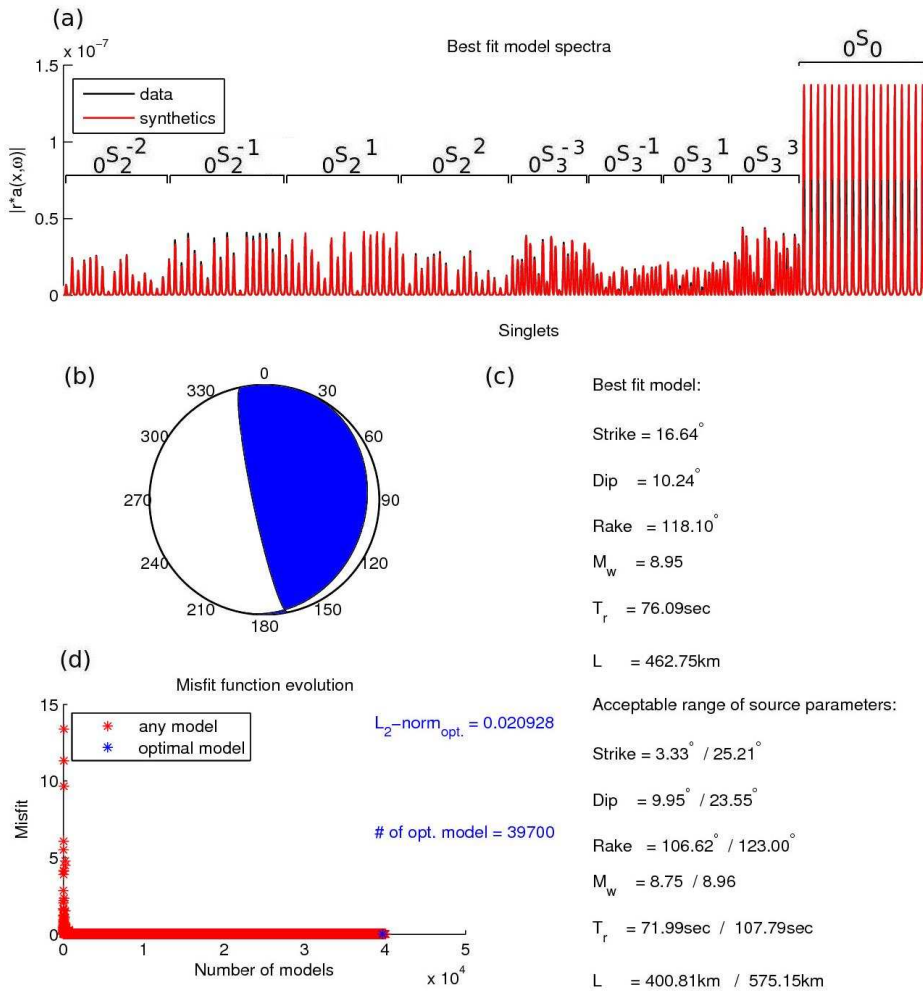


Figure C.11: Results from a finite source inversion for the artificial 2010 Chile thrust earthquake, using a combination of the amplitude and FFT misfits (97% amplitude and 3% FFT) using an artificial unilateral rupture model based on the source model of Delouis *et al.* (2010) assuming a total rupture duration of 230 s and rupture length of 600 km, as the input model ($\phi = 15^\circ$, $\delta = 18^\circ$, $\lambda = 110^\circ$, $M_w = 8.8$, $T_r = 230$ s, $L = 600$ km). SAW12D 3-D model is used to build the synthetic data and PREM for the excitation kernels: (a) 480-hr optimal fit acceleration amplitude spectra of $0S_2^{\pm 1, \pm 2}$, $0S_3^{\pm 1, \pm 3}$ and $0S_0^0$ singlets, (b) optimal source mechanism, (c) optimal and acceptable range of source parameters (acceptable parameters correspond to source models yielding misfit values up to 1% larger than the lowest misfit associated with the optimal source model), (d) misfit function evolution.

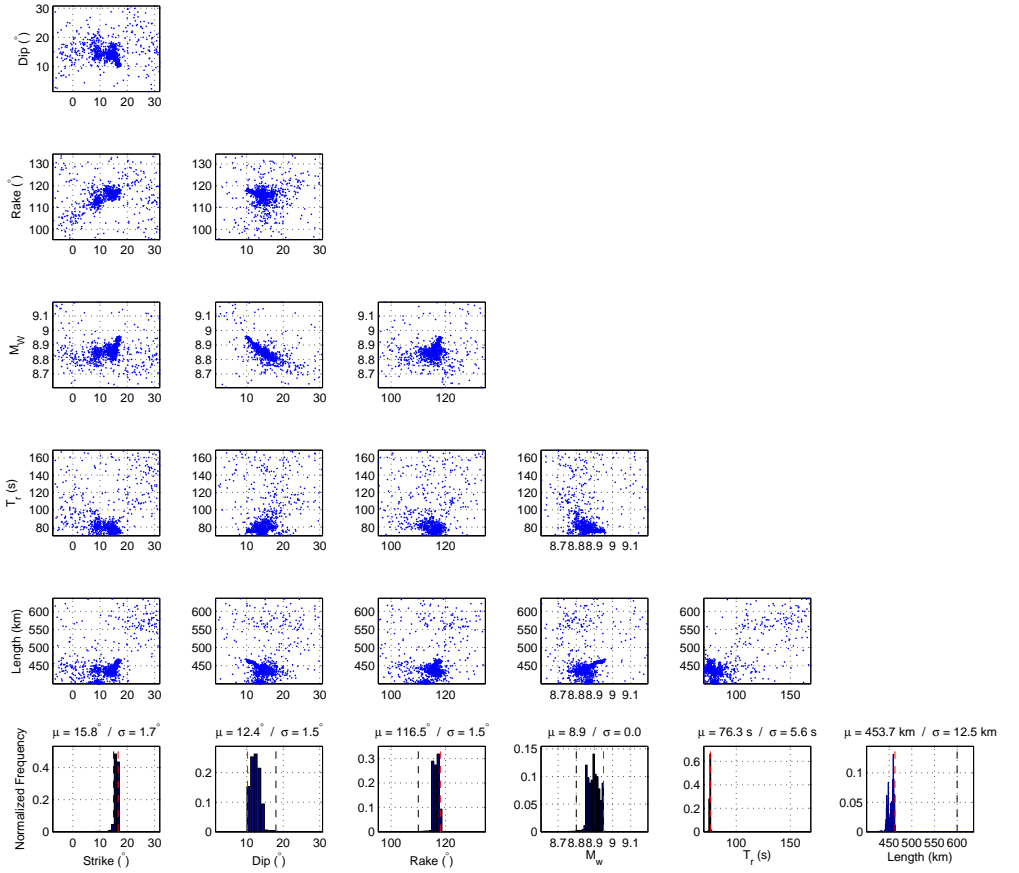


Figure C.12: Uncertainties and tradeoffs as shown from ensembles produced by Neighbourhood Algorithm and plotted as pairs of source parameters for the experiment of Figure C.11. Normalized frequency plots are shown at the bottom. The black dashed lines correspond to the input model ($\phi = 15^{\circ}$, $\delta = 18^{\circ}$, $\lambda = 110^{\circ}$, $M_w = 8.8$, $T_r = 230$ s, $L = 600$ km) and red dashed lines correspond to optimal models determined from the inversions. Mean (μ) and standard deviation (σ) values are also shown.

Appendix D

Supplementary material for Chapter 5

Table D.1: Parameter space boundaries (min. and max.) over strike (ϕ), dip (δ), rake (λ), moment magnitude (M_w), rupture duration (T_r) and length (L) of the six earthquakes studied in this Chapter. The parameter space ranges 40° in strike and rake, 30° in dip, 0.6 in moment magnitude, 100 s in rupture duration and 240 km in length. The same parameter space is used in our point source inversion tests for strike, dip, rake and M_w determinations.

	2004	Sumatra	2005	Nias	2007	Bengkulu	2011	Tohoku	2013	Okhotsk Sea	2010	Chile
	min.	max.	min.	max.	min.	max.	min.	max.	min.	max.	min.	max.
$\phi(^{\circ})$	309.0	349.0	313.0	353.0	308.0	348.0	183.0	223.0	171.0	211.0	359.0	39.0
$\delta(^{\circ})$	1.0	31.0	1.0	31.0	1.0	31.0	1.0	31.0	1.0	31.0	3.0	33.0
$\lambda(^{\circ})$	90.0	130.0	98.0	138.0	94.0	134.0	68.0	108.0	-112.0	-72.0	96.0	136.0
M_w	8.7	9.3	8.3	8.9	8.2	8.8	8.8	9.4	8.0	8.6	8.5	9.1
$T_r(s)$	460.0	560.0	—	—	—	—	133.2	223.2	—	—	—	—
$L(km)$	1100.0	1340.0	—	—	—	—	319.7	519.7	—	—	—	—

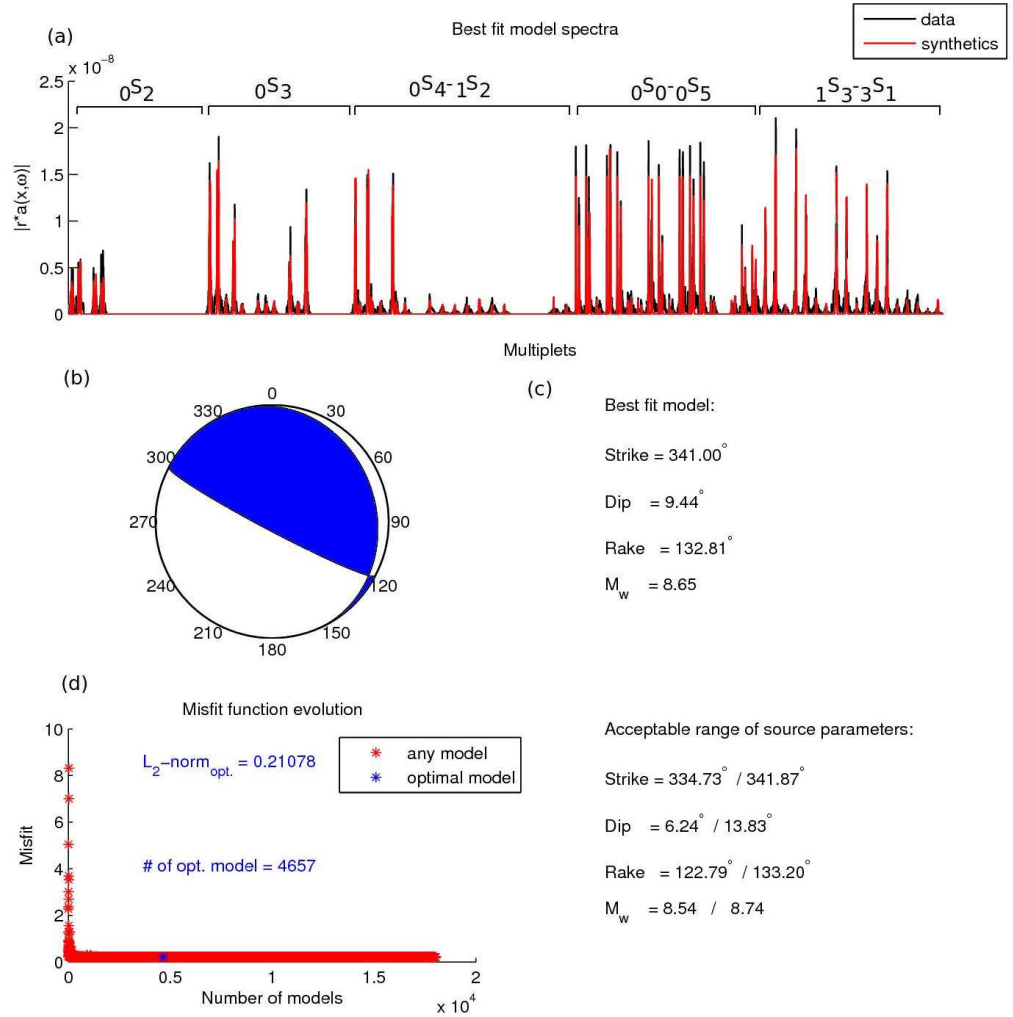


Figure D.1: Results from a point source inversion for the 2005 Nias earthquake. SAW12D 3-D model is used to build the excitation kernels: (a) 240-hr optimal fit amplitude spectra of $0S_2$, $0S_3$, $0S_4$, $1S_2$, $0S_0$, $0S_5$, $1S_3-2S_2-3S_1$ multiplets with respect to the GCMT centroid location, (b) optimal source mechanism, (c) optimal and acceptable range of source parameters (acceptable parameters correspond to source models yielding misfit values up to 1% larger than the lowest misfit associated with the optimal source model), (d) misfit function evolution.

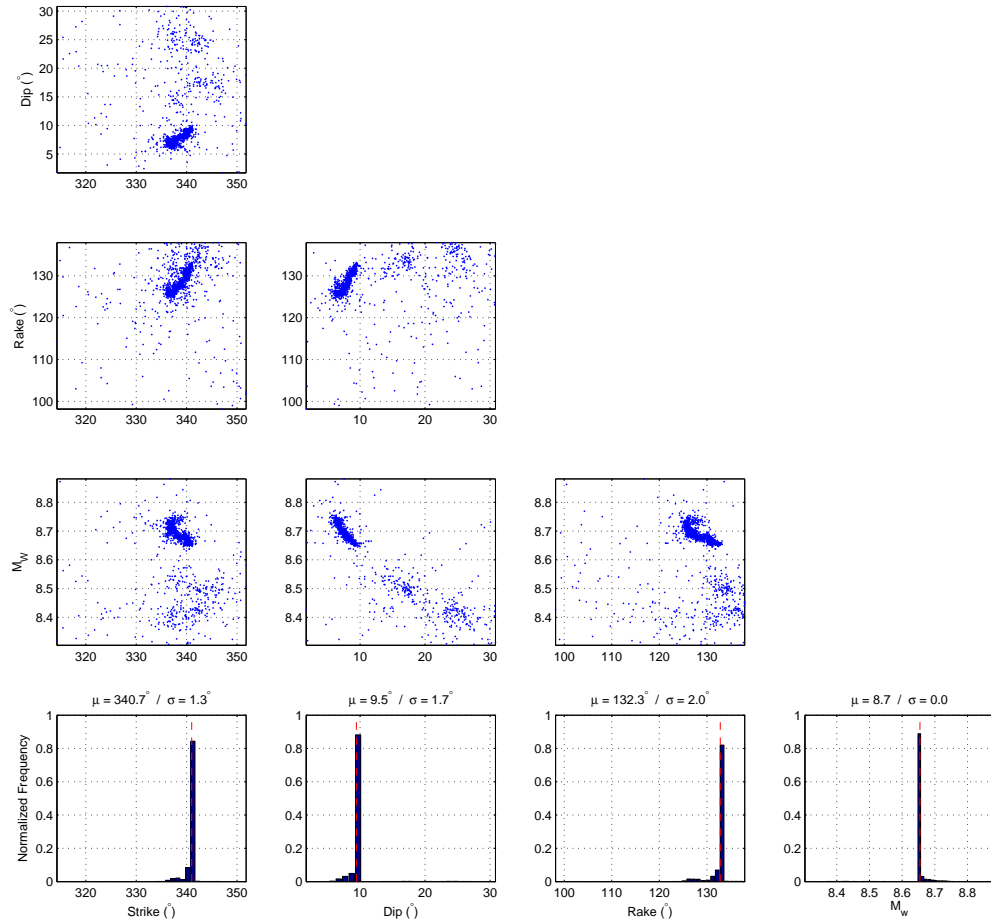


Figure D.2: Uncertainties and tradeoffs as shown from ensembles produced by Neighbourhood Algorithm and plotted as pairs of source parameters for inversion results of Figure D.1 for the 2005 Nias earthquake. Normalized frequency plots are shown at the bottom. Mean (μ) and standard deviation (σ) values are also shown on top of the normalized frequency plots. Red dashed lines show optimal source parameters obtained from point source inversion.

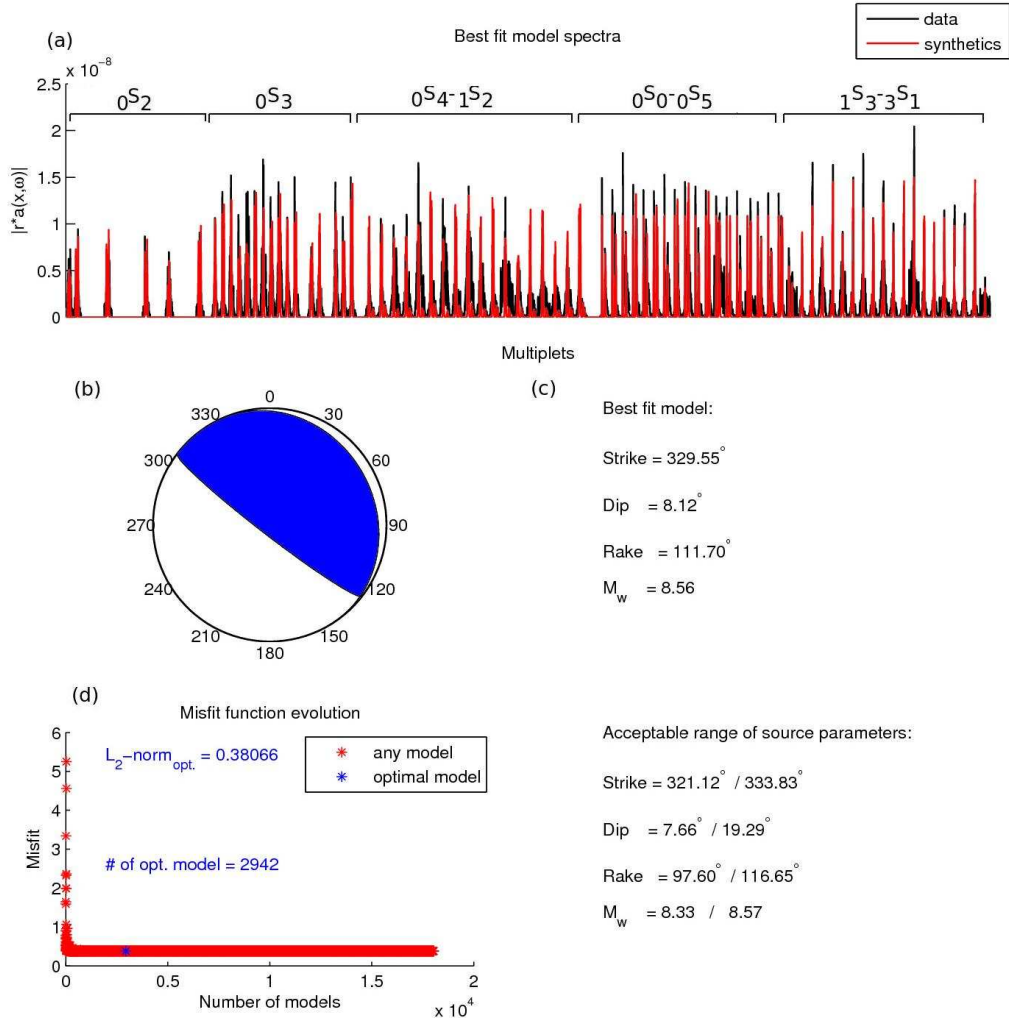


Figure D.3: Results from a point source inversion for the 2007 Bengkulu earthquake. SAW12D 3-D model is used to build the excitation kernels: (a) 240-hr optimal fit amplitude spectra of $0S_2$, $0S_3$, $0S_4$, $1S_2$, $0S_5$, $1S_3-2S_2-3S_1$ multiplets with respect to the GCMT centroid location, (b) optimal source mechanism, (c) optimal and acceptable range of source parameters (acceptable parameters correspond to source models yielding misfit values up to 1% larger than the lowest misfit associated with the optimal source model), (d) misfit function evolution.

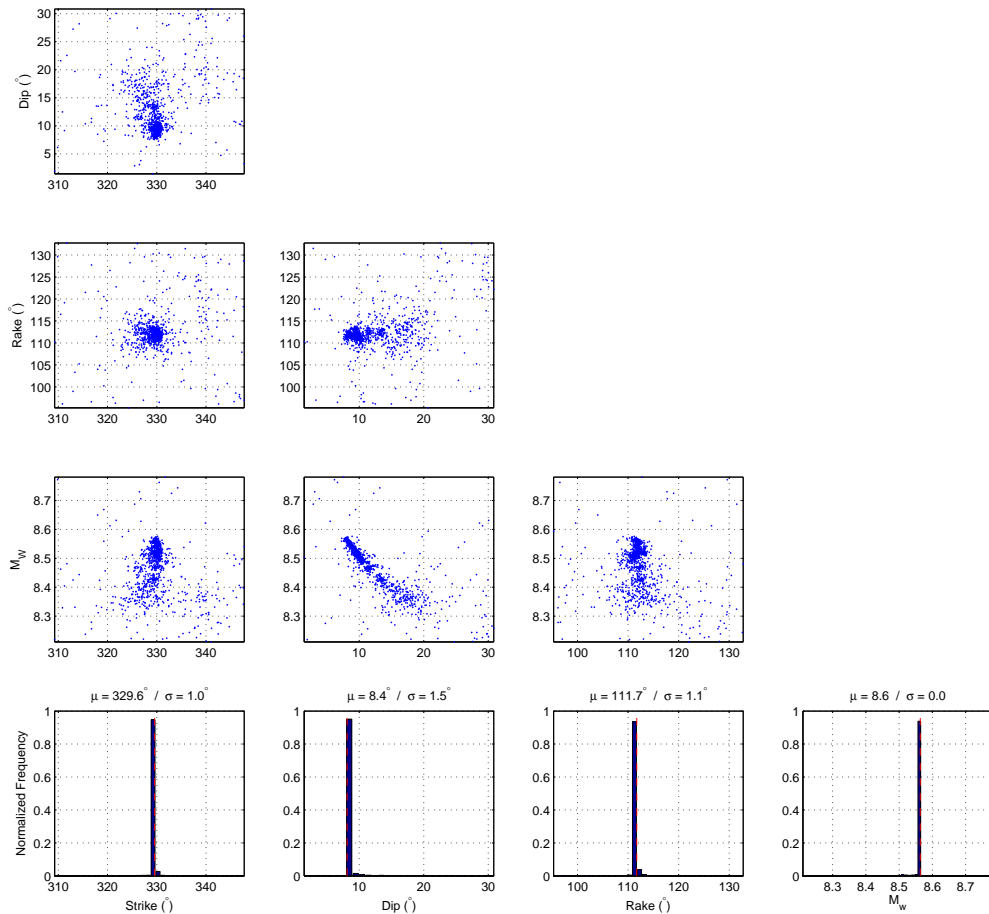


Figure D.4: Uncertainties and tradeoffs as shown from ensembles produced by Neighbourhood Algorithm and plotted as pairs of source parameters for inversion results of Figure D.3 for the 2007 Bengkulu earthquake. Normalized frequency plots are shown at the bottom. Mean (μ) and standard deviation (σ) values are also shown on top of the normalized frequency plots. Red dashed lines show optimal source parameters obtained from point source inversion.

References

Abe, K. (1970), Determination of seismic moment and energy from the Earth's free oscillation, *Phys. Earth. Planet. Int.*, 4, 49–61.

Abercrombie, R., M. Antolik, K. Felzer, and G. Ekström (2001), The 1994 Java tsunami earthquake: Slip over a subducting seamount, *J. Geophys. Res.*, 106(B4), 6595–6607.

Aki, K. (1966), Generation and propagation of G waves from the Niigata earthquake of June 16, 1964, *Bull. Earthquake Res. Inst. Tokyo Univ.*, 44, 73–88.

Aki, K. (1967), Scaling law of seismic spectrum, *J. Geophys. Res.*, 72, 1217–1231.

Aki, K., and P. G. Richards (2002), Quantitative Seismology, Second edition, *University Science Books, Sausalito, CA*.

Allmann, B. P., and P. M. Shearer (2009), Global variations of stress drop for moderate to large earthquakes, *J. Geophys. Res.*, 114, B01,310, doi:10.1029/2008JB005,821.

Ammon, C., T. Lay, H. Kanamori, and M. Cleveland (2011), A rupture model of the great 2011 off the Pacific coast Tohoku earthquake, *Earth Planets Space*, 63, 693–696.

Ammon, C. J., C. Ji, H.-K. Thio, D. Robinson, S. Ni, V. Hjörleifsdóttir, H. Kanamori, T. Lay, S. Das, D. Helmberger, G. Ichinose, J. Polet, and D. Wald (2005), Rupture Process of the 2004 Sumatra-Andaman earthquake, *Science*, 308, doi:10.1126/science.1112,260.

Ammon, C. J., H. Kanamori, and T. Lay (2008), A great earthquake doublet and seismic stress transfer cycle in the central Kuril islands, *Nature*, 451, doi:10.1038/nature06,521.

Ammon, C. J., H. Kanamori, T. Lay, and A. A. Velasco (2006), The 17 July 2006 Java tsunami earthquake, *Geophys. Res. Lett.*, 33(L24308), doi:10.1029/2006GL028,005.

Anatolik, M., A. Kaverina, and D. S. Dreger (2000), Compound rupture of the great 1998 Antarctic plate earthquake, *J. Geophys. Res.*, 105(B10).

Andrews, J., A. Deuss, and J. Woodhouse (2006), Coupled normal-mode sensitivity to inner-core shear velocity and attenuation, *Geophys. J. Int.*, 167, 204–212.

Aochi, H., and S. Ide (2011), Conceptual multi-scale dynamic rupture model for the 2011 off the Pacific coast of Tohoku earthquake, *Earth Planets Space*, 63(4), 761–765.

Arvidsson, R., and G. Ekström (1998), Global CMT analysis of moderate earthquakes, $Mw \geq 4.5$, using intermediate-period surface waves, *Bull. Seis. Soc. Am.*, 88(4), 1003–1013.

Backus, G., and J. Gilbert (1961), The rotational splitting of the free oscillations of the earth, *Proc. Natl. Acad. Sci.*, 47, 362–371.

Backus, G. E., and M. Mulcahy (1976), Moment tensors and other phenomenological descriptions of seismic sources, I. Continuous displacements, *Geophys. J. R. Astron. Soc.*, **46**, 341–361.

Bassin, C., G. Laske, and G. Masters (2000), The current limits of resolution for surface wave tomography in North America, *EOS*, **81**(F897).

Béjar-Pizarro, M., D. Carrizo, A. Socquet, R. Armijo, S. Barrientos, F. Bondoux, S. Bonvalot, J. Campos, D. Comte, J. B. de Chabalier, O. Charade, A. Delorme, G. Gabalda, J. Galetzka, J. Genrich, A. Nercessian, M. Olcay, F. Ortega, I. Ortega, D. Remy, J. C. Ruegg, M. Simons, C. Valderas, and C. Vigny (2010), Asperities and barriers on the seismogenic zone in North Chile: state-of-the-art after the 2007 Mw 7.7 Tocopilla earthquake inferred by GPS and InSAR data, *Geophys. J. Int.*, **183**, 390–406.

Ben-Menahem, A., M. Rosenman, and M. Israel (1972), Source mechanism of the Alaskan earthquake of 1964 from amplitudes of free oscillations and surface waves, *Phys. Earth and Planet. Int.*, **5**, 1–29.

Ben-Menahem, A., and S. J. Singh (1980), Seismic waves and sources, *Second Ed., Dover Publications, Mineda, New York*.

Benioff, H., F. Press, and S. Smith (1961), Excitation of the free oscillations of the Earth by earthquakes, *J. Geophys. Res.*, **66**(2), 605–619.

Biggs, J., D. Robinson, and T. Dixon (2009), The 2007 Pisco, Peru, earthquake (M8.0): seismology and geodesy, *Geophys. J. Int.*, **176**, 657–669.

Bilek, S., and E. R. Engdahl (2007), Rupture characterization and aftershock relocations for the 1994 and 2006 tsunami earthquakes in the Java subduction zone, *Geophys. Res. Lett.*, **34**(L20311), doi:10.1029/2007GL031,357.

Bilek, S., and L. Ruff (2002), Analysis of the 23 June 2001 Mw=8.4 Peru underthrusting earthquake and its aftershocks, *Geophys. Res. Lett.*, **29**(20).

Bilham, R., R. Engdahl, N. Feldl, and S. Satyabala (2005), Partial and complete rupture of the Indo-Andaman earthquake plate boundary 1847–2004, *Seism. Res. Lett.*, **76**, 229–311.

Borrero, J. C., R. Weiss, E. A. Okal, R. Hidayat, Suranto, D. Arcas, and V. V. Titov (2009), The tsunami of 2007 September 12, Bengkulu province, Sumatra, Indonesia: post-tsunami field survey and numerical modelling, *Geophys. J. Int.*, **178**, 180–194.

Bouchon, M. (1976), Teleseismic body wave radiation from a seismic source in a layered medium, *Geophys. J. R. astr. Soc.*, **47**, 515–530.

Bouchon, M., M. Toksoz, H. Karabulut, M.-P. Bouin, M. Dietrich, M. Aktar, and M. Edie (2002), Space and time evolution of rupture and faulting during the 1999 Izmit (Turkey) earthquake, *Bull. Seism. Soc. Am.*, **92**(1), 256–266.

Bourgeois, J., C. Petroff, H. Yeh, V. V. Titov, C. E. Synolakis, B. Benson, J. Kuroiwa, J. Lander, and E. Norabuena (1999), Geologic setting, field survey and modeling of the Chimbote, northern Peru tsunami of 21 February 1996, *Geophys. J. Int.*, **154**, 513–540.

Braatenberg, C., G. Romeo, Q. Taccetti, and I. Nagy (2006), The very-broad-band long-base tiltmeters of Grotta Gigante (Trieste, Italy): Secular term tilting and the great Sumatra-Andaman islands earthquake of December 26, 2004, *J. Geodyn.*, **41**, 164–174.

Briggs, R., K. Sieh, A. Meltzner, D. Natawidjaja, J. Galetzka, B. Suwargadi, Y.-J. Hsu, M. Simons, N. Hananto, I. Suprihanto, D. Prayudi, J.-P. Avouac, L. Prawirodirdjo, and Y. Bock (2006), Deformation and slip along the Sunda megathrust in the great 2005 Nias-Simeulue earthquake, *Science*, 311, 1897–1901.

Brominski, P. D., and P. Gerstoft (2009), Dominant source regions of the Earth's "hum" are coastal, *Geophys. Res. Lett.*, 36(L13303), doi:10.1029/2009GL038,903.

Bukchin, B., E. Clévédé, and A. Mostinskiy (2010), Uncertainty of moment tensor determination from surface wave analysis for shallow earthquakes, *J. Seismol.*, 14, 601–614.

Bukchin, B., and A. Mostinskii (2007), Integral source characteristics of the Sumatra earthquakes of December 26, 2004, and March 28, 2005, *J. Volcan. Seism.*, 1(4), 263–273.

Buland, R., J. Berger, and F. Gilbert (1979), Observations from the IDA network of attenuation and splitting during a recent earthquake, *Nature*, 277, 358–362.

Carlo, D., T. Lay, C. Ammon, and J. Zhang (1999), Rupture process of the 1995 Antofagasta subduction eaerthquake (Mw=8.1), *Pure and Appl. Geophys.*, 154(1999), 677–709.

Chen, T., A. V. Newman, L. Feng, and H. M. Fritz (2009), Slip distribution from the 1 April 2007 Solomon Islands earthquake: A unique image of near-trench rupture, *Geophys. Res. Lett.*, 36(L16307), doi:10.1029/2009GL039,496.

Chileh, M., J.-P. Avouac, V. Hjorleifsdottir, T.-R. A. Song, C. Ji, K. Sieh, A. Sladen, H. Hebert, L. Prawirodirdjo, Y. Bock, and J. Galetzka (2007), Coseismic slip and afterslip of the great (Mw 9.15) Sumatra-Andaman earthquake of 2004, *Bull. Seism. Soc. Am.*, 97(1A), S152–S173.

Chlieh, M., J. de Chabalier, J. Ruegg, R. Armijo, R. Dmowska, J. Campos, and K. Feigl (2004), Crustal deformation and fault slip during the seismic cycle in the North Chile subduction zone, from GPS and InSAR observations, *Geophys. J. Int.*, 158, 695–711.

Chu, R., S. Wei, D. V. Helmberger, Z. Zhan, L. Zhu, and H. Kanamori (2011), Initiation of the great Mw 9.0 Tohoku-Oki earthquake, *Earth and Planet. Sc. Lett.*, 308, 277–283.

Cifuentes, I., and P. Silver (1989), Low-frequency source characteristics of the great 1960 Chilean earthquake, *J. Geophys. Res.*, 94, 643–663.

Clévédé, E., and P. Lognonné (1996), Frechet derivatives of coupled seismograms with respect to an anelastic rotating Earth, *Geophys. J. Int.*, 58, 456–482.

Clévédé, E., and P. Lognonné (2003), Higher Order Perturbation Theory: 3D Synthetic Seismogram Package, *Int. Handbook Earth. Eng. Seism.*, 81B(1939).

Cohen, G., P. Joly, and N. Torjdman (1993), Construction and analysis of higher-order finite elements with mass lumping for the wave equation, *2nd Int. Conf. on Mathematical and Numerical Aspects of Wave Propagation*, (ed. R. Kleinman, SIAM, Philadelphia), 152–160.

Courtier, N., B. Ducarme, J. Goodkind, J. Hinderer, Y. Imanishi, N. Seama, H. Sun, J. Merriam, B. Bengert, and D. E. Smylie (2000), Global superconducting gravimeter observations and the search for the translational modes of the inner core, *Phys. Earth Planet. Int.*, 117, 3–20.

Dahlen, F. (1968), The normal modes of a rotating, elliptical Earth, *Geophys. J. R. Astr. Soc.*, *16*, 329–367.

Dahlen, F. (1974), Inference of the lateral heterogeneity of the Earth from the eigenspectrum, *Geophys. J. R. Astr. Soc.*, *38*, 143–167.

Dahlen, F. (1987), Multiplet coupling and the calculation of synthetic long-period seismograms, *Geophys. J. R. Astr. Soc.*, *91*, 241–254.

Dahlen, F. A. (1982), The effect of data windows on the estimation of free oscillation parameters, *Geophys. J. R. Astr. Soc.*, *58*, 609–623.

Dahlen, F. A., and J. Tromp (1998), *Theoretical Global Seismology*, Princeton Press, NJ.

Davis, P., M. Ishii, and G. Masters (2005), An assessment of the accuracy of gsn sensor response information, *Seism. Res. Lett.*, *76*(6), 678–683.

Delouis, B., T. Monfret, L. Dorbath, M. Pardo, L. Rivera, D. Comte, H. Haessler, J. Caminade, L. Ponce, E. Kausel, and A. Cisternas (1997), The Mw=8.0 Antofagasta (North Chile) earthquake of 30 July 1995: A precursor to the end of the large 1877 gap, *Bull. Seism. Soc. Am.*, *87*(2), 427–445.

Delouis, B., J.-M. Nocquet, and M. Vallée (2010), Slip distribution of the February 27, 2010 Mw = 8.8 Maule earthquake, central Chile, from static and high-rate GPS, InSAR, and broadband teleseismic data, *Geophys. Res. Lett.*, *37*(L17305), doi:10.1029/2010GL043,899.

Delouis, B., M. Pardo, D. Legrand, and T. Monfret (2009), The Mw 7.7 Tocopilla Earthquake of 14 November 2007 at the Southern Edge of the Northern Chile Seismic Gap: Rupture in the Deep Part of the Coupled Plate Interface, *Bull. Seism. Soc. Am.*, *99*(1), 87–94.

DeMets, C., R. Gordon, D. Argus, and S. Stein (1990), Current plate motions, *Geophys. J. Int.*, *101*(425–478).

Deuss, A., and J. Woodhouse (2001), Theoretical free oscillation spectra: the importance of wide band coupling, *Geophys. J. Int.*, *146*, 833–842.

Dragert, H., K. Wang, and T. S. James (2001), A silent slip event on the deeper Cascadia subduction interface, *Science*, *292*(5521), 1525–1528.

Duputel, Z., L. Rivera, L. Fukahata, and H. Kanamori (2012a), Uncertainty estimations for seismic source inversions, *Geophys. J. Int.*, *190*, 1243–1256.

Duputel, Z., L. Rivera, H. Kanamori, and G. Hayes (2012b), Wphase source inversion for moderate to large earthquakes (1990-2010), *Geophys. J. Int.*, *189*, doi: 10.1111/j.1365–246X.2012.05,419.x.

Duputel, Z., V. C. Tsai, L. Rivera, and H. Kanamori (2013), Using centroid time-delays to characterize source durations and identify earthquakes with unique characteristics, *Earth Planet. Sc. Lett.*, *374*, 92–100.

Dziewonski, A., and D. L. Anderson (1981), Preliminary reference Earth model, *Phys. Earth and Planet. Int.*, *25*(1981), 297–356.

Dziewonski, A. M., T. A. Chou, and J. H. Woodhouse (1981), Determination of earthquake source parameters from waveform data for studies of global and regional seismicity, *J. Geophys. Res.*, 86(B4), 2825–2852.

Dziewonski, A. M., and B. A. Romanowicz (1977), An exact solution to the problem of excitation of normal modes by a propagating fault, *Lincoln Laboratories, Massachusetts Institute of Technology, Semi-annual Report*, pp. 88–90.

Dziewonski, A. M., and J. H. Woodhouse (1983), An experiment in systematic study of global seismicity: centroid-moment tensor solutions for 201 moderate and large earthquakes in 1981, *J. Geophys. Res.*, 88, 3247–3271.

Dziewonski, A. M., and R. L. Woodward (1992), Acoustic imaging of the planetary scale, *Acoustical Imaging*, 19, 785–797.

Edmonds, A. R. (1960), Angular momentum in Quantum Mechanics, *Princeton Press, NJ*.

Ekström, G. (1989), A very broad band inversion method for the recovery of earthquake source parameters, *Tectonophysics*, 166, 73–100.

Ekström, G. (1995), Calculation of static deformation following the Bolivia earthquake by summation of Earth's normal modes, *Geophys. Res. Lett.*, 22(16), 2289–2292.

Ekström, G., M. Nettles, and A. M. Dziewonski (2012), The global CMT Project 2004–2010: Centroid-moment tensors for 13,017 earthquakes, *Phys. Earth and Planet. Int.*, 200–201, 1–9.

Engdahl, E. R., R. D. V. D. Hilst, and R. P. Buland (1998), Global teleseismic earthquake relocation with improved travel times and procedures for depth determination, *Bull. Seismol. Soc. Am.*, 88, 722–743.

Escobedo, D., J. Pachero, and G. Suárez (1998), Teleseismic body-wave analysis of the 9 October, 1995 (Mw=8.0), Colima-Jalisco, Mexico earthquake, and its largest foreshock and aftershock, *Geophys. Res. Lett.*, 25(4), 547–550.

Faccioli, E., F. Maggio, R. Paolucci, and A. Quarteroni (1997), 2D and 3D elastic wave propagation by a pseudo-spectral domain decomposition method, *J. Seism.*, 1, 237–251.

Ferreira, A. M. G., N. F. d Oreyde, J. H. Woodhouse, and W. Zürn (2006), Comparison of fluid tiltmeter data with long-period seismograms: Surface waves and Earth's free oscillations, *J. Geophys. Res.*, 111(B11307).

Ferreira, A. M. G., J. Weston, and G. J. Funning (2011), Global compilation of interferometric synthetic aperture radar earthquake source models: 2. Effects of 3-D Earth structure, *J. Geophys. Res.*, 116(B08409), doi:10.1029/2010JB008132.

Ferreira, A. M. G., and J. Woodhouse (2007), Source, path and receiver effects on seismic surface waves, *Geophys. J. Int.*, 168, 109–232.

Ferreira, A. M. G., and J. H. Woodhouse (2006), Long-period seismic source inversions using global tomographic models, *Geophys. J. Int.*, 166, doi:10.1111/j.1365–246X.2006.03,003.x.

Fitch, T. (1972), Plate convergence, transcurrent faults and internal deformation adjacent to Southeast Asia and the western Pacific, *J. Geophys. Res.*, 77, 4432–4460.

Fujii, Y., K. Satake, S. Sakai, M. Shinohara, and T. Kanazawa (2011), Tsunami source of the 2011 off the Pacific coast of Tohoku earthquake, *Earth Planets Space*, 63, 815–820.

Furlong, K. P., T. Lay, and C. J. Ammon (2009), A Great Earthquake Rupture Across a Rapidly Evolving Three-Plate Boundary, *Science*, 324, 226–229.

Gilbert, F. (1970), Excitation of the normal modes of the Earth by earthquake sources, *Geophys. J. R. Astron. Soc.*, 22, 223–226.

Gilbert, F. (1973), Derivation of source parameters from low-frequency spectra, *Philos. Trans. R. Soc. London*, 274, 369–371.

Gilbert, F., and A. M. Dziewonski (1975), An application of normal mode theory to the retrieval of structural parameters and source mechanisms from seismic spectra, *Philos. Trans. R. Soc. London*, 278, 187–269.

Giovanni, M., S. Beck, and L. Wagner (2002), The June 23, 2001 Peru earthquake and the southern Peru subduction zone, *Geophys. Res. Lett.*, 29(21).

Gómez, J., R. Madariaga, A. Walpersdorf, and E. Chalard (2000), The 1996 earthquakes in Sulawesi, Indonesia, *Bull. Seism. Soc. Am.*, 90(3).

Guilbert, J., J. Vergoz, E. Schisselé, A. Roueff, and Y. Cansi (2005), Use of hydroacoustic and seismic arrays to observe rupture propagation and source extent of the $M_w = 9.0$ Sumatra earthquake, *Geophys. Res. Lett.*, 32(L15310), doi:10.1029/2005GL022,966.

Han, S. C., R. Riva, J. Sauber, and E. Okal (2013), Source parameter inversion for recent great earthquakes from a decade-long observation of global gravity fields, *J. Geophys. Res.*, 118, 1240–1267.

Han, S. C., J. Sauber, and R. Riva (2011), Contribution of satellite gravimetry to understanding seismic source processes of the 2011 Tohoku-Oki earthquake, *Geophys. Res. Lett.*, 38, L24,312, doi:10.1029/2011GL049,975.

Hartzell, S., and P. Liu (1995), Determination of earthquake source parameters using a hybrid global search algorithm, *Bull. Seism. Soc. Am.*, 85(2), 516–524.

Hasegawa, A., S. Horiuchi, and N. Umino (1994), Seismic structure of the northeastern Japan convergent margin: A synthesis, *Journal of Geophys. Res.*, 99(B11), 22,295–22,311.

Hayes, G. P. (2011), Rapid source characterization of the 2011 $M_w 9.0$ off the Pacific coast of Tohoku earthquake, *Earth Planets Space*, 63, 529–534.

Hayes, G. P., D. J. Wald, and R. L. Johnson (2012), Slab1.0: A three-dimensional model of global subduction zone geometries, *J. Geophys. Res.*, 117(B01302), doi:10.1029/2011JB008,524.

Hébert, H., D. Reymond, Y. Krien, J. Vergoz, F. Schindelé, J. Roger, and A. Loevenbruck (2009), The 15 August 2007 Peru earthquake and tsunami: Influence of the source characteristics on the tsunami heights, *Pure and Appl. Geophys.*, 166(2009), 211–232.

Heinrich, P., F. Schindelé, and S. Guibourg (1998), Modeling of the February 1996 Peruvian tsunami, *Geophys. Res. Lett.*, 25(14), 2687–2690.

Helffrich, G. R. (1997), How good are routinely determined focal mechanisms? Empirical statistics based on a comparison of Harvard, USGS and ERI moment tensors, *Geophys. J. Int.*, *131*, 741–750.

Henry, C., and S. Das (2002), The Mw 8.2, 17 February 1996 Biak, Indonesia, earthquake: Rupture history, aftershocks, and fault plane properties, *Journal of Geophys. Res.*, *107*(B11).

Henry, C., S. Das, and J. H. Woodhouse (2000), The great March 25, 1998 Antarctic Plate earthquake: Moment tensor and rupture history, *J. Geophys. Res.*, *105*(B7), 16,097–16,118.

Hergert, T., and O. Heidbach (2006), New insights into the mechanism of postseismic stress relaxation exemplified by the 23 June 2001 Mw = 8.4 earthquake in southern Peru, *Geophys. Res. Lett.*, *33*(L02307), doi:10.1029/2005GL024,858.

Hjörleifsdóttir, V., and G. Ekström (2010), Effects of three-dimensional Earth structure on CMT earthquake parameters, *Phys. Earth and Planet. Int.*, *179*, 178–190.

Hjörleifsdóttir, V., H. Kanamori, and J. Tromp (2009), Modeling 3-D wave propagation and finite slip for the 1998 Balleny Islands earthquake, *J. Geophys. Res.*, *114*(B03301), doi:10.1029/2008JB005,975.

Honda, R., S. Aoi, N. Morikawa, H. Sekiguchi, T. Kunugi, and H. Fujiwara (2004), Ground motion and rupture process of the 2003 Tokachi-oki earthquake obtained from strong motion data of K-NET and KiK-net, *Earth Planets Space*, *56*, 317–322.

Honda, R., Y. Yukutake, H. Ito, M. Harada, T. Aketagawa, A. Yoshido, S. Sakai, N. S. N. Hirata, K. Obara, and H. Kimura (2011), A complex rupture image of the 2011 Tohoku earthquake revealed by the MeSO-net, *Earth Planets Space*, *63*, 583–588.

Houston, H. (2001), Influence of depth, focal mechanism, and tectonic setting on the shape and duration of earthquake source time functions, *J. Geophys. Res.*, *106*(B6).

Hsu, Y.-J., M. Simons, J.-P. Avouac, J. Galetzka, K. Sieh, M. Chlieh, D. Natawidjaja, L. Prawirodirdjo, and Y. Bock (2006), Frictional afterslip following the 2005 Nias-Simeulue earthquake, Sumatra, *Science*, *312*, 1921–1926.

Igel, H., M.-F. Nader, D. Kurrale, A. M. G. Ferreira, J. Wassermann, and K. U. Schreiber (2011), Observations of Earth's toroidal free oscillations with a rotation sensor: The 2011 magnitude 9.0 Tohoku-Oki earthquake, *Geophys. Res. Lett.*, *38*(L21303), doi:10.1029/2011GL049,045.

Ihmlé, P., and J. Ruegg (1997), Source tomography by simulated annealing using broad-band surface waves and geodetic data: application to the Mw=8.1 Chile 1995 event, *Geophys. J. Int.*, *131*, 146–158.

Ishii, M., P. M. Shearer, H. Houston, and J. E. Vidale (2005), Extent, duration and speed of the 2004 Sumatra-Andaman earthquake imaged by the Hi-net array, *Nature*, *435*, 933–936.

Ito, Y., H. Matsubayashi, H. Kimura, T. Matsumoto, Y. Asano, and S. Sekiguchi (2004), Spatial distribution for moment tensor solutions of the 2003 Tokachi-oki earthquake (MJMA=8.0) and aftershocks, *Earth Planets Space*, *56*, 301–306.

Ji, C. (2007), Preliminary result of the Sep 12, 2007 Sumatra earthquake, available at http://earthquake.usgs.gov/earthquakes/eqinthene.../2007/us2007aqbk/finite_fault.php.

Johnson, J. M., Y. Tanioka, K. Satake, and L. J. Ruff (1995), Two 1993 Kamchatka Earthquakes, *Pageoph.*, 144, 633–647.

Jordan, T., B. Isacks, R. Allmendinger, J. Brewer, V. Ramos, and C. Ando (1983), Andean tectonics related to geometry of subducted Nazca plate, *Geol. St. Am. Bull.*, 94, 341–361.

Kanamori, H. (1971), Seismological evidence for a lithospheric normal faulting: the Snariku earthquake of 1933, *Phys. Earth Planet. Inter.*, 4(289–300).

Kanamori, H. (1972), Mechanism of tsunami earthquakes, *Phys. Earth Planet. Inter.*, 6(346–359).

Kanamori, H. (1977), The energy release in great earthquakes, *J. Geophys. Res.*, 82, 2981–2987.

Kanamori, H. (1993), W phase, *Geophys. Res. Lett.*, 20(16), 1691–1694.

Kanamori, H., and D. L. Anderson (1975a), Amplitude of the Earth's free oscillations and long-period characteristics of the earthquake source, *J. Geophys. Res.*, 80, 1075–1078.

Kanamori, H., and D. L. Anderson (1975b), Theoretical basis of some empirical relations in Seismology, *Bull. Seis. Soc. Am.*, 65(5), 1073–1095.

Kanamori, H., and J. J. Cipar (1974), Focal process of the great Chilean earthquake, May 22, 1960, *Phys. Earth Planet. Int.*, 9, 128–136.

Kanamori, H., and J. W. Given (1981), Use of long-period surface waves for rapid determination of earthquake-source parameters, *Phys. Earth Planet. Inter.*, 27, 8–31.

Kanamori, H., and L. Rivera (2008), Source inversion of W phase: speeding up seismic tsunami warning, *Geophys. J. Int.*, 175, 222–238.

Kane, D. L., G. A. Prieto, F. L. Vernon, and P. M. Shearer (2011), Quantifying seismic source parameter uncertainties, *Bull. Seism. Soc. Am.*, 101(2).

Katsumata, K., N. Wada, and M. Kasahara (2003), Newly imaged shape of the deep seismic zone within the subducting Pacific plate beneath the Hokkaido corner, Japan-Kurile arc-arc junction, *J. Geophys. Res.*, 108(B12).

Kawakatsu, H. (1995), Automated near-realtime CMT inversion, *Geophys. Res. Lett.*, 22, 2569–2572.

Kedar, S., S. Watada, and T. Tanimoto (1994), The 1989 Macquarie Ridge earthquake: Seismic moment estimation from long-period free oscillations, *J. Geophys. Res.*, 99(B9).

Kennett, B. L. N., and E. R. Engdahl (1991), Travel times for global earthquake location and phase association, *Geophys. J. Int.*, 105, 429–465.

Kikuchi, M., and H. Kanamori (1982), Inversion of complex body waves, *Bull. Seism. Soc. Am.*, 72(2), 491–506.

Kiser, E., and M. Ishii (2011), The 2010 Mw 8.8 Chile earthquake: Triggering on multiple segments and frequency-dependent rupture behavior, *Geophys. Res. Lett.*, 38(L07301), doi:10.1029/2011GL047,140.

Kiser, E., and M. Ishii (2012), The March 11, 2011 Tohoku-oki earthquake and cascading failure of the plate interface, *Geophys. Res. Lett.*, 39(L00G25), doi:10.1029/2012GL051,170.

Kisslinger, C., and M. Kikuchi (1997), Aftershocks of the Andreanof islands earthquake of June 10, 1996, and local seismotectonics, *Geophys. Res. Lett.*, 24(15), 1883–1886.

Klotz, J., D. Angermann, G. Michel, R. Porth, C. Reigber, J. Reinking, J. Viramonte, R. Perdomo, V. Rios, S. Barrientos, R. Barriga, and O. Cifuentes (1999), GPS-derived deformation of the Central Andes including the 1995 Antofagasta Mw=8.0 earthquake, *Pure and Appl. Geophys.*, 154(1999), 709–730.

Koketsu, K., K. Hikima, S. Miyazaki, and S. Ide (2003), Joint inversion of strong motion and geodetic data for the source process of the 2003 Tokachi-oki, Hokkaido, earthquake, *Earth Planets Space*, 55.

Komatitsch, D., J. Ritsema, and J. Tromp (2002), The spectral-element method, Beowulf computing, and global Seismology, *Science*, 298, 1737–1742.

Komatitsch, D., and J. Tromp (1999), Introduction to the spectral element method for three-dimensional seismic wave propagation, *Geophys. J. Int.*, 139, 806–822.

Komatitsch, D., and J. Tromp (2002a), Spectral-element simulations of global seismic wave propagation-I. Validation, *Geophys. J. Int.*, 149, 390–412.

Komatitsch, D., and J. Tromp (2002b), Spectral-element simulations of global seismic wave propagation-II. 3D models, oceans, rotation and self-gravitation, *Geophys. J. Int.*, 150, 303–318.

Komatitsch, D., and J. P. Vilotte (1998), The spectral element method: an efficient tool to simulate the seismic response of 2D and 3D geological structures, *Bull. Seism. Soc. Am.*, 88, 368–392.

Komatitsch, D., J. P. Vilotte, R. Vai, J. M. Castillo-Covarrubias, and F. J. Sánchez-Sesma (1999), The spectral element method for elastic wave equation to 2D and 3D seismic problems, *Int. J. Num. Meth. Eng.*, 45, 1139–1164.

Konca, A., J.-P. Avouac, A. Sladen, A. Meltzner, K. Sieh, P. Fang, Z. Li, J. Galetzka, J. Genrich, M. Chlieh, D. Natawidjaja, Y. Bock, E. Fielding, C. Ji, and D. V. Helmberger (2008), Partial rupture of a locked patch of the Sumatra megathrust during the 2007 earthquake sequence, *Nature*, 456, 631–635.

Konca, A., V. Hjorleifsdottir, T.-R. A. Song, J.-P. Avouac, D. V. Helmberger, C. Ji, K. Sieh, R. Briggs, and A. Meltzner (2007), Rupture kinematics of the 2005 Mw 8.6 Nias-Simeulue earthquake from the joint inversion of seismic and geodetic data, *Bull. Seism. Soc. Am.*, 97(1A), S307–S322.

Koper, K., A. Hutko, T. Lay, C. Ammon, and H. Kanamori (2011), Frequency-dependent rupture process of the 11 March 2011 Mw 9.0 Tohoku earthquake: Comparison of short-period P wave backprojection images and broadband seismic rupture models, *Earth Planets Space*, 63, 599–602.

Koper, K., A. Hutko, T. Lay, and O. Sufri (2012), Imaging short-period seismic radiation from the 27 February 2010 Chile (Mw 8.8) earthquake by back-projection of P, PP, PKIKP waves, *J. Geophys. Res.*, 117(B02308), doi:10.1029/2011JB008,576.

Kreemer, C., G. Blewitt, and F. Maerten (2006), Co- and postseismic deformation of the 28 March 2005 Nias Mw 8.7 earthquake from continuous GPS data, *Geophys. Res. Lett.*, 33(L07307), doi:10.1029/2005GL025,566.

Krüger, F., and M. Ohrnberger (2005), Spatio-temporal source characteristics of the 26 December 2004 Sumatra earthquake as imaged by teleseismic broadband array, *Geophys. Res. Lett.*, 32(L24312), doi:10.1029/2005GL023,939.

Kuge, K., M. Kikuchi, and Y. Yamanaka (1999), Non-double-couple moment tensor of the March 25, 1998, Antarctic earthquake: Composite rupture of strike-slip and normal faults, *Geophys. Res. Lett.*, 26(22), 3401–3404.

Kurahashi, S., and K. Irikura (2011), Source model for generating strong ground motions during the 2011 off the Pacific coast of Tohoku earthquake, *Earth Planets Space*, 63, 571–576.

Kurrale, D., and R. Widmer-Schnidrig (2008), The horizontal hum of the Earth: A global background of spheroidal and toroidal modes, *Geophys. Res. Lett.*, 35(L06304), doi:10.1029/2007GL033,125.

Lamb, H. (1882), On the vibrations of an elastic sphere, *Proc. Lond. Math. Soc.*, 13, 189–212.

Lambotte, S., L. Rivera, and J. Hinderer (2006), Rupture length and duration of the 2004 Aceh-Sumatra earthquake from the phases of the Earth's gravest free oscillations, *Geophys. Res. Lett.*, 33(L023307), doi 10.1029/2005GL024,090.

Lambotte, S., L. Rivera, and J. Hinderer (2007), Constraining the overall kinematics of the 2004 Sumatra and the 2005 Nias earthquakes using the Earth's gravest free oscillations, *Bull. Seism. Soc. Am.*, 97(1A), pp.S128–S138.

Langston, C. A., and D. W. Helmberger (1975), A procedure for modelling shallow dislocation sources, *Geophys. J. R. Astron. Soc.*, 42, 117–130.

Lay, T., C. J. Ammon, A. R. Hutko, and H. Kanamori (2010), Effects of kinematic constraints on teleseismic finite-source rupture inversions: Great Peruvian earthquakes of 23 June 2001 and 15 August 2007, *Bull. Seism. Soc. Am.*, 100(3), 969–994.

Lay, T., C. J. Ammon, H. Kanamori, Y. Yamazaki, K. F. Cheung, and A. A. Hutko (2011), The 25 October 2010 Mentawai tsunami earthquake (Mw 7.8) and the tsunami hazard presented by shallow megathrust ruptures, *Geophys. Res. Lett.*, 38(L06302), doi:10.1029/2010GL046,552.

Lay, T., H. Kanamori, C. J. Ammon, A. R. Hutko, K. Furlong, and L. Rivera (2009), The 2006–2007 Kuril Islands great earthquake sequence, *J. Geophys. Res.*, 114(B11308), doi:10.1029/2008JB006,280.

Lay, T., H. Kanamori, C. J. Ammon, M. Nettles, S. Ward, R. Aster, S. Beck, S. Bilek, M. Brudzinski, R. Buttler, H. DeShon, G. Ekström, K. Satake, and S. Sipkin (2005), The great Sumatra-Andaman earthquake of 26 December 2004, *Science*, 308(1127), DOI: 10.1126/science.1112,250.

Lay, T., and T. C. Wallace (1995), *Modern Global Seismology*, Academic press.

Lee, S.-J., B.-S. Huang, M. Ando, H.-C. Chiu, and J.-H. Wang (2011), Evidence of large scale repeating slip during the 2011 Tohoku-Oki earthquake, *Geophys. Res. Lett.*, 38(L19306), doi:10.1029/2011GL049,580.

Li, X.-D., and B. Romanowicz (1996), Global mantle shear velocity model developed using nonlinear asymptotic coupling theory, *J. Geophys. Res.*, 101(B10), 22,245–22,272.

Lognonné, P. (1991), Normal modes and seismograms in an anelastic rotating Earth, *J. Geophys. Res.*, 98, 20,309–20,319.

Lognonné, P., and E. Clévédé (2002), Normal Modes of the Earth and Planets, *edited by W. H. K. Lee, H. Kanamori, and P. C. Jennings, Int. Assoc. of Seismol. and Phys. of the Earth's Inter.*, Boulder, Colo, pp. pp.125–147.

Lognonné, P., and B. Romanowicz (1990), Modelling of coupled normal modes of the Earth: The spectral method, *Geophys. J. Int.*, 102, 365–395.

Lomax, A. (2005), Rapid estimation of rupture extent for large earthquakes: application to the 2004, M9 Sumatra-Andaman mega-thrust, *Geophys. Res. Lett.*, 32(L10314).

Lorito, S., F. Romano, S. Atzori, X. Tong, A. Avallone, J. McCloskey, M. Cocco, E. Boschi, and A. Piatanesi (2011), Limited overlap between the seismic gap and coseismic slip of the great 2010 Chile earthquake, *Nature Geoscience*, p. doi:10.1038/NGE01073.

Lorito, S., F. Romano, A. Piatanesi, and E. Boschi (2008), Source process of the September 12, 2007, Mw 8.4 southern Sumatra earthquake from tsunami tide gauge record inversion, *Geophys. Res. Lett.*, 35(L02310).

Madariaga, R. (1972), Spectral splitting of toroidal free oscillations due to lateral heterogeneities of the Earth's structure, *J. Geophys. Res.*, 23, 4421–4431.

Mai, P. M., J. Burjanek, B. Delouis, G. Festa, C. Francois-Holden, D. Monelli, T. Uchide, and J. Zahradník (2007), Earthquake Source Inversion Blindtest: Initial Results and Further Developments, *EOS, Trans. Am. Geophys. Un.*, 88, 52.

Mai, P. M., M. T. Page, and D. Schorlemmer (2010), Source Inversion Validation: Quantifying Uncertainties in Earthquake Source Inversions, *EOS, Trans. Am. Geophys. Un.*, 91, 49.

Marson-Pidgeon, K. B., L. N. Kennett, and S. Sambridge (2000), Source depth and mechanism inversion at teleseismic distances using a Neighbourhood Algorithm, *Bull. Seism. Soc. Am.*, 90(6).

Masters, G., and F. Gilbert (1981), Structure of the inner core inferred from observations of its spheroidal shear modes, *Geophys. Res. Lett.*, 8, 569–571.

Masters, G., T.-H. Jordan, P.-G. Silver, and F. Gilbert (1982), Aspherical Earth structure from fundamental spheroidal-mode data, *Nature*, 298, 609–613.

Masters, G., J. Park, and F. Gilbert (1983), Observations of coupled spheroidal and toroidal modes, *J. Geophys. Res.*, 88(B12), 10,285–10,298.

Masters, T. G., and R. Widmer (1995), Free oscillations: frequencies and attenuations, *Global Earth Physics - A handbook of physical constants, AGU Reference Shelf 1*, 104–125.

McCaffrey, R., P. Zwick, Y. Bock, L. Prawirodirdjo, J. Genrich, S. Puntodewo, and C. Subarya (2000), Strain partitioning during oblique plate convergence in northern Sumatra: Geodetic and seismologic constraints and numerical modeling, *J. Geophys. Res.*, *105*, 28,363–28,376.

McCloskey, J., S. S. Nalbant, and S. Steacy (2005), Indonesian earthquake risk from coseismic stress, *Nature*, *434*, 291.

Mégnin, C., and B. Romanowicz (2000), The three-dimensional shear velocity structure of the mantle from the inversion of body, surface and higher-mode waveforms, *Geophys. J. Int.*, *143*, 709–728.

Melbourne, T., I. Carmichael, C. DeMets, K. Hudnut, O. Sanchez, J. Stock, G. Suarez, and F. Webb (1997), The geodetic signature of the M8.0 Oct. 9, 1995, Jalisco subduction earthquake, *Geophys. Res. Lett.*, *24*(6), 715–718.

Melbourne, T. I., and F. H. Webb (2002), Precursory transient slip during the 2001 Mw=8.4 Peru earthquake sequence from continuous GPS, *Geophys. Res. Lett.*, *29*(21), doi:10.1029/2002GL015,533.

Mendoza, C., and S. Hartzell (1999), Fault-slip distribution of the 1995 Colima-Jalisco, Mexico, earthquake, *Bull. Seism. Soc. Am.*, *89*(5), 1338–1344.

Millot-Langet, R., E. Clévédé, and P. Lognonné (2003), Normal modes and long period seismograms in a 3D anelastic elliptical rotating Earth, *Geophys. Res. Lett.*, *30*(5), 1202, doi:10.1029/2002GL016,257.

Miura, S., A. H. Y. Suwa, and T. Nishimura (2004), The 2003 M8.0 Tokachi-Oki earthquake - How much has the great event paid back slip debts?, *Geophys. Res. Lett.*, *31*(L05613).

Miyazaki, S., K. Larson, K. Xhoi, K. Hikima, K. Koketsu, P. Bodin, J. Haase, G. Emore, and A. Yamagiwa (2004), Modeling the rupture process of the 2003 September 25 Tokachi-Oki (Hokkaido) earthquake using 1-Hz GPS data, *Geophys. Res. Lett.*, *31*(L21603).

Morris, S., R. Geller, H. Kawakatsu, and S. Tsuboi (1987), Variational normal modes computations for three laterally heterogeneous earth models, *Phys. Earth. Planet. Inter.*, *47*, 275–318.

Motagh, M., R. Wang, T. Walter, R. Bürgmann, E. Fielding, J. Anderssohn, and J. Zschau (2008), Coseismic slip model of the 2007 August Pisco earthquake (Peru) as constrained by Wide Swath radar observations, *Geophys. J. Int.*, *174*, 842–848.

Nabelek, J. (1984), Determination of earthquake fault parameters from inversion of body waves, *Ph.D. thesis, Mass. Inst. of Technol.*, *361 pp.*, Cambridge, Mass.

Nakano, M., H. Kumagai, and H. Inoue (2008), Waveform inversion in the frequency domain for the simultaneous determination of earthquake source mechanism and moment function, *Geophys. J. Int.*, *173*, 1000–1011.

Nettles, M., G. Ekström, and H. Koss (2011), Centroid-moment tensor analysis of the 2011 off the Pacific coast of Tohoku earthquake and its larger foreshocks and aftershocks, *Earth Planets Space*, **63**, 519–523.

Nettles, M., T. C. Wallace, and S. L. Beck (1999), The March 25, 1998 Antarctic plate earthquake, *Geophys. Res. Lett.*, **26**(14), 2097–2100.

Newcomb, K. R., and W. R. McCann (1987), Seismic history and seismotectonics of the Sunda arc, *J. Geophys. Res.*, **92**, 421–439.

Newman, A. V., G. Hayes, Y. Wei, and J. Convers (2011), The 25 October 2010 Mentawai tsunami earthquake, from real-time discriminants, finite-fault rupture, and tsunami excitation, *Geophys. Res. Lett.*, **38**(L05302), doi:10.1029/2010GL046498.

Ni, S., H. Kanamori, and D. Helmberger (2005), Energy radiation from the Sumatra earthquake, *Nature*, **434**(7033), 582–585.

Ogata, Y., and S. Toda (2010), Bridging great earthquake doublets through silent slip: On- and off-fault aftershocks of the 2006 Kuril Island subduction earthquake toggled by a slow slip on the outer rise normal fault of the 2007 great earthquake, *J. Geophys. Res.*, **115**(B06318), doi:10.1029/2009JB006777.

Okal, E., S. Hongsresawat, and S. Stein (2012), Split-mode evidence for no ultraslow component to the source of the 2010 Maule, Chile, earthquake, *Bull. Seism. Soc. Am.*, **102**(1), 391–397.

Okal, E. A., and S. Stein (2009), Observations of ultra-long period normal modes from the 2004 Sumatra-Andaman earthquake, *Phys. Earth Planet. Inter.*, **175**, 53–62.

Ortiz, M., S. Singh, J. Pachero, and V. Kostoglodov (1998), Rupture length of the October 9, 1995 Colima-Jalisco earthquake (Mw 8.0) estimated from tsunami data, *Geophys. Res. Lett.*, **25**(15), 2857–2860.

Paolucci, R., E. Faccioli, and F. Maggio (1999), 3D response analysis of an instrumented hill at Matsuzaki, Japan, by a spectral method, *J. Seism.*, **3**, 191–209.

Park, J. (1986), Asymptotic coupled-mode expressions for multiplet amplitude anomalies and frequency shifts on a laterally heterogeneous Earth, *Geophys. J. R. Astr. Soc.*, **90**, 129–169.

Park, J., and F. Gilbert (1986), Coupled free oscillations of an aspherical dispersive rotating Earth: Galerkin theory, *J. Geophys. Res.*, **91**, 7241–7260.

Park, J., C. Lindberg, and F. Vernon (1987), Multitaper spectral analysis of high-frequency seismograms, *J. Geophys. Res.*, **92**(B12), 12,675–12,684.

Park, J., T. R. A. Song, J. Tromp, E. Okal, S. Stein, G. Roult, E. Clévétré, G. Laske, H. Kanamori, P. Davis, J. Berger, C. B. M. V. Camp, X. Lei, H. Sun, H. Xu, and S. Rosat (2005), Earth's free oscillations excited by the 26 December 2004 Sumatra-Andaman earthquake, *Science*, **308**, 1139–1144.

Patera, A. T. (1984), A spectral element method for fluid dynamics: Laminar flow in a channel expansion, *J. Comput. Phys.*, **54**, 468–488.

Patton, H., and G. Randall (2002), On the causes of biased estimates of seismic moment for earthquakes in central Asia, *J. Geophys. Res.*, **107**, doi: 10.1029/2001JB000,351.

Pavlov, V. M. (1994), On non-uniqueness of the inverse problem for a seismic source-II. Treatment in terms of polynomial moments, *Geophys. J. Int.*, 119, 487–4796.

Pekeris, C., and H. Jarosch (1958), The free oscillations of the Earth. In Benioff, H., Ewing, M., Howell, Jr., B.F. & Press, F., editors, *Contributions in Geophysics in honor of Beno Gutenberg*, pp. 171–192, Pergamon, New York.

Peyrat, S., R. Madariaga, E. Buforn, J. Campos, G. Asch, and J. P. Vilote (2010), Kinematic rupture process of the 2007 Tocopilla earthquake and its main aftershocks from teleseismic and strong-motion data, *Geophys. J. Int.*, 182, 1411–1430.

Piatanesi, A., and S. Lorito (2007), Rupture process of the 2004 Sumatra-Andaman earthquake from tsunami waveform inversion, *Bull. Seism. Soc. Am.*, 97(1A), 223–231.

Poiata, N., K. Koketsu, and H. Miyake (2010), Source processes of the 2009 Irian Jaya, Indonesia, earthquake doublet, *Earth Planets Space*, 62, 475–481.

Poisson, B., C. Oliveros, and R. Pedreros (2011), Is there a best source model of the Sumatra 2004 earthquake for simulating the consecutive tsunami?, *Geophys. J. Int.*, 185, 1365–1378.

Poisson, S. D. (1829), Mémoire sur l'équilibre et le mouvement des corps élastiques, *Mém. Acad. Roy. Sci. Inst. France*, 8, 357–570.

Polet, J., and H. Kanamori (2000), Shallow subduction zone earthquakes and their tsunamigenic potential, *Geophys. J. Int.*, 142, 684–702.

Politz, F., B. Brooks, X. T. abd M.G. Bevis, J. Foster, R. Bürgmann, R. S. Jr., C. Vigny, A. Socquet, J.-C. Ruegg, J. Campos, S. Barrientos, H. Parra, J. C. B. Soto, S. Cimbaro, and M. Blanco (2011a), Coseismic slip distribution of the February 27, 2010 Mw 8.8 Maule, Chile earthquake, *Geophys. Res. Lett.*, 38(L09309), doi:10.1029/2011GL047,065.

Politz, F., R. Bürgmann, and P. Banerjee (2011b), Geodetic slip model of the 2011 M9.0 Tohoku earthquake, *Geophys. Res. Lett.*, 38(L00G08), doi:10.1029/2011GL048,632.

Pollitz, F., P. Banerjee, K. Grijalva, B. Nagarajan, and R. Bürgmann (2008), Effect of 3-D viscoelastic structure on post-seismic relaxation from the 2004 M=9.2 Sumatra earthquake, *Geophys. J. Int.*, 173, 189–204.

Prawirodirdjo, L., Y. Bock, J. F. Genrich, S. S. O. Puntodewo, J. Rais, C. Subarya, and S. Sutisna (2000), One century of tectonic deformation along the Sumatran fault from triangulation and Global Positioning System surveys, *J. Geophys. Res.*, 105, 28,343–28,361.

Prawirodirdjo, L., R. McCaffrey, C. Chadwell, Y. Bock, and C. Subarya (2010), Geodetic observations of an earthquake cycle at the Sumatra subduction zone: Role of interseismic strain segmentation, *Geophys. Res. Lett.*, 115(B03414), doi:10.1029/2008JB006,139.

Priolo, E., J. M. Carcione, and G. Seriani (1994), Numerical simulation of interface waves by higher-order spectral modeling techniques, *J. Acoust. Soc. Am.*, 95, 681–693.

Reid, H. (1910), The Mechanics of the Earthquake, The California earthquake of 18 April, 1906: Report of the State Earthquake Investigation Commission, *Washington: Carnegie Institution, Tech. Rep. 2*.

Resovsky, J. S., and M. H. Ritzwoller (1998), New and refined constraints on three-dimensional Earth structure from normal modes below 3mHz, *J. Geophys. Res.*, **103**(B1), 783–810.

Ritsema, J., H. J. V. Heijst, and J. H. Woodhouse (1999), Complex shear velocity structure imaged beneath Africa and Iceland, *Science*, **286**, 243–259.

Ritzwoller, M., G. Masters, and F. Gilbert (1986), Observations of anomalous splitting and their interpretation in terms of aspherical structure, *J. Geophys. Res.*, **91**, 10,203–10,228.

Rivera, L., K. Sieh, D. Helmberger, and D. Natawidjaja (2002), A comparative study of the Sumatran subduction-zone earthquakes of 1935 and 1984, *Bull. Seism. Soc. Am.*, **92**, 1721–1736.

Robinson, D., S. Das, and A. Watts (2006), Earthquake rupture stalled by a subducting fracture zone, *Science*, **312**, 1203–1205.

Rogister, Y. (2003), Splitting of seismic-free oscillations and of the Slichter triplet using the normal mode theory of a rotating, ellipsoidal Earth, *Phys. Earth. Planet. Int.*, **140**, 169–182.

Romanowicz, B. (1995), A global tomographic model of shear attenuation in the upper mantle, *J. Geophys. Res.*, **100**, 12,375–12,394.

Rosat, S., J. Hinderer, and L. Rivera (2003), First observation of ${}_2S_1$ and study of the splitting of the football mode ${}_0S_2$ after the June 2001 Peru earthquake of magnitude 8.4, *Geophys. Res. Lett.*, **30**(21), doi:10.1029/2003GL018,304.

Ruegg, J., J. Campos, R. Armijo, S. Barrientos, P. Briole, R. Thiele, M. Arancibia, J. Canuta, T. Duquesnoy, M. Chang, D. Lazo, H. Lyon-Caen, L. Ortlieb, J. Rossignol, and L. Serrurier (1996), The Mw=8.1 Antofagasta (North Chile) earthquake of July 30, 1995: First results from teleseismic and geodetic data, *Geophys. Res. Lett.*, **23**(9), 917–920.

Ruegg, J., A. Rudolff, C. Vigny, J. de Chabalier, J. Campos, E. Kausel, S. Barrientos, and D. Dimitrov (2009), Interseismic strain accumulation measured by GPS in the seismic gap between Concepción-Constitución in Chile, *Phys. Earth Planet. Int.*, **175**(78–85).

Sambridge, M. (1999a), Geophysical inversion with a neighbourhood algorithm. I. Searching a parameter space, *Geophys. J. Int.*, **138**, 479–494.

Sambridge, M. (1999b), Geophysical inversion with a neighbourhood algorithm. II. Appraising the ensemble, *Geophys. J. Int.*, **138**, 727–746.

Sambridge, M., and B. L. N. Kennett (2001), Seismic event location: nonlinear inversion using a neighbourhood algorithm, *Pageoph*, **158**, 241–257.

Sato, T., K. Imanishi, and M. Kasuga (1996), Three-stage rupture process of the 28 December 1994 Sanriku-Oki earthquake, *Geophys. Res. Lett.*, **23**(1), 33–36.

Seriani, G. (1998), 3-D large-scale wave propagation modeling by spectral element method on Cray T3E multiprocessor, *Comp. Meth. Appl. Mech. Eng.*, **164**, 235–247.

Seriani, G., E. Priolo, J. M. Carcione, and E. Padovani (1992), High-order spectral element method for elastic wave modeling, *Expanded abstracts of the SEG*, (62nd Int. Mtng of the SEG, New-Orleans), 1285–1288.

Simons, M., S. Minson, A. Sladen, F. Ortega, J. Jiang, S. Owen, L. Meng, J.-P. Ampuero, S. Wei, R. Chu, D. Helmberger, H. Kanamori, E. Hetland, A. Moore, and F. Webb (2011), The 2011 magnitude 9.0 Tohoku-Oki earthquake: Mosaicking the megathrust from seconds to centuries, *Science*, 332(1421), DOI: 10.1126/science.1206731.

Sladen, A., H. Tavera, M. Simons, J. P. Avouac, A. O. Konca, H. Perfetini, L. Audin, E. J. Fielding, F. Ortega, and R. Cavagnoud (2010), Source model of the 2007 Mw 8.0 Pisco, Peru earthquake: Implications for seismogenic behavior of subduction megathrusts, *J. Geophys. Res.*, 115(B02405), doi:10.1029/2009JB006429.

Slichter, L. B. (1961), The fundamental free mode of the Earth's inner core, *Proc. Nat. Acad. Sci. USA*, 47, 186–190.

Smith, M., and G. Masters (1989), Aspherical structure constraints from free oscillation frequency and attenuation measurements, *J. Geophys. Res.*, 94, 1953–1976.

Stein, S., and J. Geller (1977), Amplitudes of the Earth's split normal modes, *J. Geophys. Res.*, 25, 117–142.

Stein, S., and E. A. Okal (2005), Speed and size of the Sumatra earthquake, *Nature*, 434, 581–582.

Stein, S., and M. Wysession (2003), An introduction to Seismology, earthquakes and Earth structure, *Balckwell publishing*.

Swenson, J. L., and S. L. Beck (1999), Source characteristics of the 12 November 1996 Mw 7.7 Peru subduction zone earthquake, *Pure Appl. Geophys.*, 154, 731–751.

Synolakis, C., and L. Kong (2006), Run-up measurements of the December 2004 Indian Ocean tsunami, *Earthq. Spectra*, 22(3), 67–91.

Takeuchi, H. (1959), Torsional oscillations of the Earth and some related problems, *Geophys. J. R. Astr. Soc.*, 2, 89–100.

Tanimoto, T. (2001), Continuous free oscillations: atmosphere-solid Earth coupling, *Annu. Rev. Earth Planet. Sci.*, 29, 563–584.

Tanimoto, T., and C. Ji (2010), Afterslip of the 2010 Chilean earthquake, *Geophys. Res. Lett.*, 37(L22312), doi:10.1029/2010GL045244.

Tanimoto, T., C. Ji, and M. Igarashi (2012), An approach to detect afterslips in giant earthquakes in the normal-mode frequency band, *Geophys. J. Int.*, 190, 1097–1110.

Tanioka, Y., and L. Ruff (1997), Source Time Functions, *Seism. Res. Lett.*, 68(3), 386–400.

Tanioka, Y., L. Ruff, and K. Satake (1996), The Sanriku-oki, Japan, earthquake of December 28, 1994 (Mw 7.7): Rupture of a different asperity from a previous earthquake, *Geophys. Res. Lett.*, 23(12), 1465–1468.

Tanioka, Y., N. Y., Y. Nishimura, T. Yoshinobu, Y. Nakamura, M. Murata, and S. Woodward (2007), Fault model of the 2007 Solomon earthquake estimated from the crustal deformation survey data, *AGU Fall Meeting 2007*, S13A-1044.

Tarantola, A. (1987), Inverse Problem Theory, *Elsevier, Amsterdam*.

Tavera, H., E. Fernández, I. Bernal, Y. Antayhua, C. Agüero, H. Salas, S. Rodríguez, L. Vilcapoma, Y. Zamudio, D. Protugal, A. Inza, J. Carpio, F. Ccallo, and I. Valdivia (2006), The southern region of Peru earthquake of June 23rd, 2001, *J. of Seism.*

Toda, S., and R. S. Stein (2000), Did stress triggering cause the large off-fault aftershocks of the 25 March 1998 Mw=8.1 Antarctic plate earthquake?, *Geophys. Res. Lett.*, 27(15), 2301–2304.

Toda, S., R. S. Stein, and J. Lin (2011), Widespread seismicity excitation throughout central Japan following the 2011 M=9.0 Tohoku earthquake and its interpretation by Coulomb stress transfer, *Geophys. Res. Lett.*, 38(L00G03), doi:10.1029/2011GL047,834.

Tong, X., D. Sandwell, K. Luttrell, B. Brooks, M. Bevis, M. Shimada, J. Foster, R. S. Jr, H. Parra, J. C. B. Soto, M. Blanco, K. E. J. Genrich, and D. Caccamise (2010), The 2010 Maule, Chile earthquake: Downdip rupture limit revealed by space geodesy, *Geophys. Res. Lett.*, 37(L24311), doi:10.1029/2010GL045,805.

Tromp, J. (1993), Support for anisotropy of the Earth's inner core, *Nature*, 366, 678–681.

Tromp, J., and F. Dahlen (1990), Free oscillations of a spherical anelastic Earth, *Geophys. J. Int.*, 103, 707–723.

Tromp, J., D. Komatitsch, and Q. Liu (2008), Spectral-element and adjoint methods in Seismology, *Commun. Comput. Phys.*, 3(1), 1–32.

Tsai, V. C., G. P. Hayes, and Z. Duputel (2011), Constraints on the long-period moment-dip tradeoff for the Tohoku earthquake, *Geophys. Res. Lett.*, 38(L00G17), doi:10.1029/2011GL049,129.

Tsai, V. C., M. Nettles, G. Ekström, and A. M. Dziewonski (2005), Multiple CMT source analysis of the 2004 Sumatra earthquake, *Geophys. Res. Lett.*, 32(L17304), doi:10.1029/2005GL023,813.

Valentine, A. P., and J. Trampert (2012), Assessing the uncertainties on seismic source parameters: Towards realistic error estimates for centroid-moment-tensor determinations, *Phys. Earth Planet. Inter.*, 210–211, 36–49.

Vallée, M. (2007), Rupture properties of the giant Sumatra earthquake imaged by empirical Green's function analysis, *Bull. Seism. Soc. Am.*, 97(1A), S103–S114.

Vallée, M., J. Charléty, A. M. G. Ferreira, B. Delouis, and J. Vergoz (2011), SCARDEC: a new technique for the rapid determination of seismic moment magnitude, focal mechanism and source time functions for large earthquakes using body-wave deconvolution, *Geophys. J. Int.*, 184, 338–358.

Vigny, C., W. Simons, S. Abu, R. Banphenyu, C. Satirapod, N. Choosakul, C. Subarya, K. Omar, H. Abidin, and B. Ambrosius (2005), Insight into the 2004 Sumatra-Andaman earthquake from GPS measurements in southeast Asia, *Nature*, 436, 201–206.

Vigny, C., A. Socquet, S. Peyrat, J.-C. Ruegg, M. Métois, R. Madariaga, S. Morvan, M. Lancieri, R. Lacassin, J. Campos, D. Carrizo, M. Bejar-Pizarro, S. Barrientos, R. Armijo, C. Aranda, M.-C. Valderas-Bermejo, I. Ortega, F. Bondoux, S. Baize, H. Lyon-Caen, A. Pavez, J. P. Villette, M. Bevis, B. Brooks, R. Smalley, H. Parra, J.-C. Báez, M. Blanco, S. Cimbaro, and E. Kendrick (2011), The 2010 Mw 8.8

Maule megathrust earthquake of central Chile, monitored by GPS, *Science*, 332, doi: 10.1126/science.1204,132.

Villaseñor, A., E. Bergman, T. Boyd, E. Engdahl, D. Frazier, M. Harden, J. Orth, R. Parkes, and K. Shedlock (1997), Toward a comprehensive catalog of global historical seismicity, *Eos Trans. AGU*, 78(50), 581–588.

Walker, K. T., M. Ishii, and P. M. Shearer (2005), Rupture details of the 28 March 2005 Sumatra Mw 8.6 earthquake imaged with teleseismic P waves, *Geophys. Res. Lett.*, 32(L24303).

Wang, D., and J. Mori (2011), Rupture process of the 2011 off the Pacific coast of Tohoku earthquake (Mw 9.0) as imaged with back-projection of teleseismic P-waves, *Earth Planets Space*, 63, 603–607.

Webb, S. C. (2007), The Earth's 'hum' is driven by ocean waves over the continental shelves, *Nature*, 445, doi:10.1038/nature05,536.

Wells, D., and K. Coppersmith (1994), New empirical relationships among magnitude, rupture length, rupture width, rupture area, and surface displacement, *Bull. Seism. Soc. Am.*, 84(4), 974–1002.

Wen, J., and X. Chen (2011), Study on the effect of parameters on source kinematic inversion, *Abstract S43C-2288 presented at 2011 AGU fall meeting, AGU, San Francisco, Calif., 5-9 December*.

Weston, J., A. M. G. Ferreira, and G. J. Funning (2011), Global compilation of interferometric synthetic aperture radar earthquake source models: 1. Comparisons with seismic catalogs, *J. Geophys. Res.*, 116(B08408), doi:10.1029/2010JB008,131.

Weston, J., A. M. G. Ferreira, and G. J. Funning (2012), Systematic comparisons of earthquake source models determined using InSAR and seismic data, *Tectonophysics*, 532–535, doi: 10.1016/j.tecto.2012.02.001.

Widmer, R., G. Masters, and F. Gilbert (1992a), Observably split multiplets – data analysis and interpretation in terms of large-scale aspherical structure, *Geophys. J. Int.*, 111, 559–576.

Widmer, R., W. Zürn, and G. Masters (1992b), Observation of low-order toroidal modes from the 1989 Macquarie Rise event, *Geophys. J. Int.*, 111, 226–236.

Widmer-Schnidrig, R. (2003), What can superconducting gravimeters contribute to normal-mode seismology?, *Bull. Seis. Soc. Am.*, 93(3), 1370–1380.

Woodhouse, J. (1983), The joint inversion of seismic waveforms for lateral variations in Earth structure and earthquake source parameters, in *Proc.'Enrico Fermi' Int. Sch. Phys.*, LXXXV, 366–397.

Woodhouse, J., D. Giardini, and X.-D. Li (1986), Evidence for inner-core anisotropy from splitting in free oscillation data, *Geophys. Res. Lett.*, 13, 1549–1552.

Woodhouse, J. H. (1980), The coupling and attenuation of nearly resonant multiplets in the Earth's free oscillation spectrum, *Geophys. J. R. Astr. Soc.*, 61, 261–283.

Woodhouse, J. H. (1996), Long period Seismology and the Earth's free oscillations, *Seismic modelling of Earth structure*, Eds. E. Boschi, G. Ekström and A. Morelli. *Instituto Nazionale di Geofisica. Editrice Compositori*.

Woodhouse, J. H., and F. A. Dahlen (1978), The effect of a general aspherical perturbation on the free oscillations of the Earth, *Geophys. J. R. Astron. Soc.*, **53**, 335–354.

Woodhouse, J. H., and T. P. Girnius (1982), Surface waves and free oscillations in region- alized Earth model, *Geophys. J. R. Astron. Soc.*, **68**, 653–673.

Yagi, Y. (2003), Source process of large and significant earthquakes in 2003, *Bull. Int. Inst. Seismol. Earthquake Eng., special volume*, 145–153.

Yagi, Y. (2004), Source rupture process of the 2003 Tokachi-oki earthquake determined by joint inversion of teleseismic body wave and strong ground motion data, *Earth Planets Space*, **56**, 311–316.

Yagi, Y. (2007), , http://www.geo.tsukuba.ac.jp/press_HP/yagi/EQ/20070401/.

Yagi, Y., and Y. Fukahata (2011a), Introduction of uncertainty of Green's function into waveform inversion for seismic source processes, *Geophys. Res. Lett.*, **186**, 711–720.

Yagi, Y., and Y. Fukahata (2011b), Rupture process of the 2011 Tohoku-oki earthquake and absolute elastic strain release, *Geophys. Res. Lett.*, **38**(L19307), doi:10.1029/2011GL048,701.

Yagi, Y., T. Mikumo, J. Pacheco, and G. Reyes (2004), Source rupture process of the Tecoman, Colima, Mexico earthquake of 22 January 2003, determined by joint inversion of teleseismic body-wave and near-source data, *Bull. Seism. Soc. Am.*, **97**(5), 1795–1807.

Yamanaka, Y., and M. Kikuchi (2003), Source process of the recurrent Tokachi-oki earthquake on september 26, 2003, inferred from teleseismic body waves, *Earth Planets Space*, **55**, e21–e24.

Yamanaka, Y., and M. Kikuchi (2004), Asperity map along the subduction zone in north- eastern Japan inferred from regional seismic data, *J. Geophys. Res.*, **109**(B07307), doi:10.1029/2003JB002,683.

Yamazaki, Y., T. Lay, K. F. Cheung, H. Yue, and H. Kanamori (2011), Modeling near-field tsunami observations to improve finite-fault slip models for the 11 March 2011 Tohoku earthquake, *Geophys. Res. Lett.*, **38**(L00G15), doi:10.1029/2011GL049,130.

Yoshida, Y., H. Ueno, D. Muto, and S. Aoki (2011), Source process of the 2011 off the Pacific coast of Tohoku earthquake with the combination of teleseismic and strong motion data, *Earth Planets Space*, **63**, 565–569.

Zachariasen, J., K. Sieh, F. W. Taylor, R. L. Edwards, and W. S. Hantoro (1999), Sub- mergence and uplift associated with the giant 1833 Sumatran subduction earthquake: Evidence from coral microatolls, *J. Geophys. Res.*, **104**, 895–920.

Zhang, H., G. Zengxi, and L. Ding (2011), Three sub-events composing the 2011 off the Pacific coast Tohoku earthquake (Mw 9.0) inferred from rupture imaging by back projecting teleseismic P waves, *Earth Planets Space*, **63**, 595–598.

Zhang, Y., Y.-T. Chen, and L. Xu (2012), Fast and robust inversion of earthquake source rupture process and its application to earthquake emergency response, *Earthq. Sci.*, **121**, doi:10.1007/s11,589–012–0838–2.

Zheng, Y., and T. Lay (2006), Low Vp/Vs ratios in the crust and upper mantle beneath the Sea of Okhotsk inferred from teleseismic $p_M P$, $s_M P$, and $s_M S$ underside reflections from the Moho, *J. Geophys. Res.*, **111**(B01305), doi:10.1029/2005JB003,724.

Zhou, R., F. Tajima, and P. Stoffa (1995), Earthquake source parameter determination using genetic algorithms, *Geophys. Res. Lett.*, **22**(4), 517–520.

Zobin, V. (1997), The rupture history of the Mw 8.0 Jalisco, Mexico, earthquake of 1995 October 9, *Geophys. J. Int.*, **130**, 220–228.

Zobin, V., and V. Levina (2001), The rupture process of the Mw 7.8 Cape Kronotsky, Kamchatka earthquake of 5 December 1997 and its relationship to foreshocks and aftershocks, *Bull. Seism. Soc. Am.*, **91**(6), 1619–1628.

Zürn, W., G. Laske, R. Widmer-Schnidrig, and F. Gilbert (2000), Observations of Coriolis coupled modes below 1mHz, *Geophys. J. Int.*, **143**, 113–118.